Chapter 3: Human influence on the climate system

Coordinating Lead Authors:
Veronika Eyring (Germany) and Nathan P. Gillett (Canada)

Lead Authors:
Krishna Achuta Rao (India), Rondrotiana Barimalala (South Africa/Madagascar), Marcelo Barreiro (Uruguay), Nicolas Bellouin (UK/France), Christophe Cassou (France), Paul J. Durack (USA/Australia), Yu Kosaka (Japan), Shayne McGregor (Australia), Seung-Ki Min (Republic of Korea), Olaf Morgenstern (New Zealand/Germany), Ying Sun (China)

Contributing Authors:
Gudfinna Adalgeirsdottir (Iceland), Lisa Bock (Germany), Chris Brierley (UK), John Dunne (USA), John Fyfe (Canada), Lee de Mora (UK), Peter J. Gleckler (USA), Peter Greve (Austria), Lukas Gudmundsson (Switzerland), Karsten Haustein (UK/Germany), Edward Hawkins (UK), Benjamin J. Henley (Australia), Marika M. Holland (USA), Chris Huntingford (UK), Colin Jones (UK), Masa Kageyama (France), Yeon-Hee Kim (Republic of Korea), Charles Koven (USA), Gerhard Krinner (France), Dan Lunt (UK), Adam Phillips (USA), Valeriu Predoi (UK), Malcolm J. Roberts (UK), Sophie Nowicki (USA), Jon Robson (UK), Jean-Baptiste Sallee (France), Andrew Schurer (UK), Jessica Tierney (USA), Blair Trewin (Australia), Xuebin Zhang (Canada)

Review Editors:
Tomas Halenka (Czech Republic), Jose A. Marengo Orsini (Brazil), Daniel Mitchell (UK)

Chapter Scientist:
Lisa Bock (Germany)

Date of Draft: 02/03/2020

Notes: TSU compiled version

Table of Contents

Executive Summary

The IPCC Second Assessment Report (1995) identified a discernible human influence on the climate. Since this initial assessment and throughout subsequent assessments (TAR, 2001; AR4, 2007 and AR5, 2013), the evidence for human influence on the climate system has progressively strengthened. AR5 concluded that human influence on the climate system is clear, evident from increasing greenhouse gas concentrations in the atmosphere, positive radiative forcing, observed warming, and physical understanding of the climate system. **This evidence is now even stronger.** {3.3-3.8}

It is *virtually certain* that human influence has warmed the global climate system. Combining the evidence from across the climate system increases the level of confidence in the attribution of observed climate change to human influence and reduces the uncertainties associated with assessments based on single variables. Large-scale indicators in the atmosphere, ocean and cryosphere show clear responses to anthropogenic forcing consistent with those expected based on model simulations and physical understanding. {3.8.1}

The *likely* range of human-induced warming in global-mean surface air temperature (GSAT) in 2010-2019 relative to 1850-1900 of 0.8-1.4°C encompasses the observed warming of 1.0-1.3°C[1], and it is *extremely likely* that human influence is the main driver[2] of the observed warming. The high level of confidence comes from strengthening evidence from studies using new attribution approaches that better account for observational, model and methodological uncertainties, and from the strong warming observed since the publication of the AR5. However, a more confident assessment is hindered by remaining uncertainty in the magnitude of internal climate variability and its representation in models. The *likely* range for human-induced warming expressed in terms of global mean surface temperature (GMST) is 0.8-1.3°C, again encompassing the best estimate and range of observed GMST warming of 1.0-1.2°C. Over the same period the *likely* range of GSAT warming due to well-mixed greenhouse gas increases from human activities is 0.9-2.0°C, and the *likely* range of GSAT change due to aerosols and other anthropogenic forcings is -0.7-0.2°C. It is *very likely* that human influence, dominated by greenhouse gases, was the main driver of warming of the troposphere since the start of comprehensive satellite observations in 1979, and *extremely likely* that human influence, dominated by stratospheric ozone depletion, was the main driver of the cooling of the lower stratosphere since 1979. {3.3.1}

Since AR5, further assessments have been made on model reproducibility of surface and atmospheric temperature trends. The CMIP5 and CMIP6 multi-model ensemble averages reproduce the observed surface temperature trend well on global and continental scales. However, we assess with *medium confidence* that most CMIP5 and CMIP6 models overestimate observed warming in the upper tropical troposphere during the satellite era. Based on the latest updates to satellite observations of stratospheric temperature, simulated and observed changes of global mean temperature through the depth of the stratosphere are more consistent than based on previous datasets, but some differences remain (*medium confidence*). {3.3.1}

The observed slower global mean surface temperature increase in the 1998-2012 period was temporary and with *high confidence* induced by variations in solar and volcanic forcing and internal variability, particularly Pacific Decadal Variability, that partly offset the anthropogenic warming tendency over this period. **Global upper to mid (0 to 2000 m) ocean heat content, which represents more than 90% of the Earth's energy imbalance continued to increase throughout this period (*very high confidence*)**. Using updated observational data sets and like-for-like comparison of simulated and observed merged near-surface air temperature and sea surface temperatures, all observed estimates of the 1998-2012 trend in GMST lie within the 5-95% range of CMIP6 trends. Therefore, the observed 1998-2012 trend is consistent with the CMIP6 multi-model ensemble of trends over the same period (*high confidence*).

[1] The ranges of observed GSAT and GMST warming quoted here are ranges for 2009-2018 taken from Chapter 2 and rounded to 1 decimal place. These will be updated to ranges for 2010-2019 in the Final Draft.

[2] In this chapter, 'main driver' means responsible for more than 50% of the change.

Since 2012, global mean surface temperature has warmed strongly, with the past five years (2014-2018) being the hottest five-year period in the instrumental record until 2018 (*high confidence*). {Cross-Chapter Box 3.1, 3.3.1; 3.5.1}

It is *likely* that human influence has contributed to[3] observed large-scale precipitation changes since 1950. New attribution studies find a detectable increase in high latitude precipitation over the Northern Hemisphere. Despite large decadal variability, there is *medium confidence* that rainfall over the wet regions of the tropics has increased due to enhanced greenhouse gas forcing. Yet, there is also growing evidence and *medium confidence* that this tropical precipitation increase has been partly muted by anthropogenic aerosols through a decreasing effect in the Northern Hemisphere summer monsoon region from the mid to late 20th century. There is *medium confidence* that ozone depletion has increased precipitation over the Southern Ocean and decreased it over southern midlatitudes during austral summer. This is an aspect of the strengthening of the Southern Annular Mode. However, even though there have been improvements, models still have deficiencies in simulating some characteristics of the precipitation patterns, in particular in the tropical oceans, and also in simulated runoff. {3.3.2, 3.3.3}

There is *medium confidence* that greenhouse gas increases and stratospheric ozone depletion have contributed to the expansion of the zonal mean Hadley cell in the Southern Hemisphere since around 1980. However, the expansion of the zonal mean Hadley cell in the Northern Hemisphere and changes in the Pacific Walker circulation strength have not exceeded the range of internal variability (*medium confidence*). Models capture the general characteristics of the tropospheric circulation, including monsoons. Systematic errors are, however, still present, for example in the frequency of blocking events in the North Atlantic, and rainfall associated with monsoons. {3.3.3}

It is *extremely likely* that anthropogenic forcing has made a substantial contribution to the ocean heat content (OHC) increase over the historical period that extends into the deeper ocean (*high confidence*). Since AR5 there is improved consistency between recent observed estimates and model simulations of changes in upper OHC, particularly when accounting for forcing discrepancies. Improved upper ocean (<700 m) observed estimates provide increased agreement and more confidence in the ability of models to accurately simulate the historical OHC change. Updated observations, like model simulations, show that warming extends throughout the entire water column (*high confidence*), with models partitioning industrial-era (1865 to 2017) heat uptake throughout the upper (0 – 700 m, 65%), intermediate (700 – 2000 m, 20%) and deep (>2000 m, 15%) layers. {3.5.1}

It is *extremely likely* that human influence has contributed to observed near-surface and subsurface oceanic salinity changes since the mid-20th century. The associated pattern of change corresponds to fresh regions becoming fresher and salty regions becoming saltier (*high confidence*). Changes to the coincident atmospheric water cycle and ocean-atmosphere fluxes (evaporation and precipitation) are the primary drivers of the basin-scale observed salinity changes (*high confidence*). The observed depth-integrated basin-scale salinity changes have been attributed to anthropogenic forcing, with CMIP5 models able to reproduce these patterns only in simulations that include greenhouse gases (*medium confidence*). The basin-scale changes are consistent across models and intensify on centennial scales from the historical period through to future projections (*high confidence*). {3.5.2}

It is *very likely* that anthropogenic forcings are the main driver of the observed global mean thermosteric sea level increase since 1970. Since the AR5, studies have highlighted that simulations that exclude anthropogenic greenhouse gases are unable to capture the thermosteric sea level rise of the historical period and that model simulations that include all forcings (anthropogenic and natural) most closely match observed estimates. Combining the attributable contributions from glaciers, ice sheet surface mass balance and thermal expansion, it is *very likely* that anthropogenic forcings are the main driver of the observed global mean sea level rise since 1970. {3.5.3, 3.5.1, 3.4.3}

[3] In this chapter the phrase 'human influence has contributed to' an observed change means that the response to human influence is nonzero and consistent in sign with the observed change.

Observations highlight changes in the circulation of both the Southern Ocean and the Atlantic Ocean, but the observational record is not long enough to determine if these changes are due to internal variability, solar and volcanic forcing or a response due to anthropogenic forcing. The mean zonal and overturning circulations of the Southern Ocean and the mean overturning circulation of the North Atlantic (AMOC) are broadly reproduced by CMIP5 and CMIP6 models. However, biases are apparent in the circulation strengths, which contribute to biases in the model representation of mean ocean temperature and salinity (*medium confidence*). {3.5.4}

It is *very likely* that anthropogenic forcing was the main driver of Arctic sea ice loss since 1979. There is new evidence that increases in anthropogenic aerosols have offset part of the greenhouse gas induced Arctic sea ice loss since the 1950s. In the Arctic, despite large differences in the mean sea ice state, loss of sea ice extent and thickness during recent decades is captured by all CMIP5 and CMIP6 models. By contrast, global climate models generally capture neither the observed increase in Antarctic sea ice extent during 1979-2015 nor the reduced sea ice extent observed since 2016, and there is *low confidence* in the understanding of the causes of these changes. {3.4.1}

It is *very likely* that anthropogenic influence contributed to the observed reductions in Northern Hemisphere springtime snow cover since 1950. The seasonal cycle in Northern Hemisphere snow cover is better reproduced by CMIP6 than CMIP5 models. Anthropogenic forcings *very likely* contributed to the observed retreat of glaciers. {3.4.2, 3.4.3}

The observed increased amplitude of the seasonal cycle of atmospheric CO_2 is *likely* attributable to fertilisation of plant growth by increased CO_2. There is *medium confidence* that Earth system models simulate the magnitude and large interannual variability of the land carbon sink well if they account for nutrient limitation on plant growth, but a possible underestimate by models of the role of warming of surface temperature in affecting plant growth prevents a more confident assessment. {3.6.1}

It is *virtually certain* that the uptake of anthropogenic CO_2 has substantially contributed to the acidification of the global ocean. The observed increase in CO_2 concentration in the subtropical and equatorial North Atlantic since mid-2000 is *likely* in part associated with an increase in ocean temperature, a response that corresponds to the expected weakening of the ocean carbon sink with warming. Consistent with AR5 there is *medium confidence* that deoxygenation in the surface ocean is due in part to anthropogenic forcing. There is *high confidence* that Earth system models simulate a realistic time evolution of the global mean ocean carbon sink. {3.6.2}

There is *high confidence* that anthropogenic forcings have modulated the Southern Annular Mode (SAM). Since AR5, further model evidence supports the assessment that ozone depletion and greenhouse gas increases have contributed to a positive trend of the SAM, particularly during austral summer in the last several decades. There is *medium confidence* that climate models reproduce the spatiotemporal features and trends of the summertime SAM observed during recent decades, with CMIP6 models outperforming CMIP5 models. {3.3.3}

There is no robust evidence that anthropogenic forcing has affected the principal modes of interannual climate variability and associated regional teleconnections beyond the range of internal variability, with the exception of the SAM. Further assessment since the AR5 confirms that climate and Earth system models are able to reproduce most aspects of the spatial structure and variance of the interannual modes of variability, which are intrinsic to the atmosphere (North Atlantic Oscillation, Northern Annular Mode) and coupled to the ocean (El Niño-Southern Oscillation and Indian Ocean Basin and Dipole modes), although some underlying processes are still misrepresented. Biases exist in the spatial structure, magnitudes, and seasonality in CMIP6 despite slight improvement. In the Tropical Atlantic basin, major errors in mean state and variability remain. For all of these modes, internal variability overwhelms the influence of anthropogenic forcing in the simulation of their changes over the historical era (*high confidence*). {3.7.1 to 3.7.5}

There is new evidence that anthropogenic aerosol changes have contributed to observed Atlantic Multidecadal Variability (AMV), but there is *low confidence* in the magnitude of this influence. Large

uncertainties remain in the identification of the human influence on AMV and Pacific Decadal Variability (PDV) due to the brevity of the observational records, difficulty in separating externally and internally driven decadal phenomena in observations, inconsistencies among proxy reconstructions, moderate model performance in reproducing these modes, and limited process understanding. In addition to the models' moderate skills in reproducing the decadal-to-multidecadal modes of variability and underlying mechanisms, there is evidence for an underestimation of the magnitude of PDV and for a crude representation of the intrinsic tropical-extratropical teleconnectivity associated with both PDV and AMV. {3.7.6, 3.7.7}

It is *virtually certain* that anthropogenic influences have caused increases in the frequency and severity of hot extremes and decreases in those of cold extremes at global and most continental scales. It is *likely* that anthropogenic influence is the main cause of the observed intensification of heavy precipitation in global land regions. {Cross-Chapter Box 3.2}

For most large-scale indicators of climate change, the mean climate simulated by the latest generation climate models underpinning this assessment has improved compared to the models assessed in the AR5 (*high confidence*). High resolution models exhibit reduced biases in some but not all aspects of surface and ocean climate (*medium confidence*). While a broad range of warming rates across models and a lengthening observational record mean that significant differences between the climate response in individual models and observations can often be identified, the multi-model mean captures most aspects of observed climate change well (*high confidence*).{3.8.2}

3.1 Scope and Overview

This chapter assesses the extent to which human influence on the climate system has affected its evolution and to what extent climate models are able to simulate observed changes and variability. This assessment informs our confidence in climate projections and is the basis for understanding what impacts of anthropogenic climate change are already occurring. Moreover, an understanding of the amount of human-induced global warming to date is key to assessing how close we are to exceeding targets to limit the global mean temperature increase to below 1.5°C or to well below 2°C above pre-industrial levels, as defined in the Paris Agreement of the United Nations Framework Convention on Climate Change (UNFCCC) 21st session of the Conference of the Parties (COP21, UNFCCC (2015)).

The evidence for human influence on the climate system has strengthened progressively over the course of the previous five IPCC assessments, from the Second Assessment Report that concluded 'the balance of evidence suggests a discernible human influence on climate' through to the Fifth Assessment Report (AR5) which concluded that 'it is *extremely likely* that human influence caused more than half of the observed increase in GMST from 1951 to 2010' (see also Section 3.3.1.1). In addition, significant uncertainties remained in the separation of the contribution of greenhouse gases and other anthropogenic forcings to observed temperature trends. These were related to uncertainties in forcings, particularly aerosol forcing, and the simulated response to those forcings (Bindoff et al., 2013). There was also *low confidence* in the assessed contribution of forcings to the reduced global mean temperature trend over the 1998-2012 period (Flato et al., 2013). AR5 concluded that climate models have continued to be developed and improved since the AR4 and were able to reproduce many features of observed climate. Nonetheless, several systematic biases were detected (Flato et al., 2013). In addition, this chapter builds on the assessment of attribution of global temperatures contained in the IPCC Special Report on Global Warming of 1.5°C (IPCC, 2018), and assessments of attribution of changes in the ocean and cryosphere in the IPCC Special Report on the Ocean and Cryosphere in Changing Climate (SROCC, IPCC (2019)).

This chapter assesses the evidence for human influence on observed large-scale indicators of climate change that are described in the Cross-Chapter Box 2.1 and assessed in Chapter 2. It takes advantage of the longer period of record now available in most observational datasets. The evaluation of human influence on the climate system requires an estimate of the expected responses to forcings and the contribution from internal climate variability, which are obtained primarily from climate and Earth system models. Since the AR5, a new set of coordinated model results from the World Climate Research Programme (WCRP) Coupled Model Intercomparison Project Phase 6 (CMIP6; Eyring et al. (2016a)) has become available. Together with updated observations of large-scale indicators of climate change (Chapter 2), CMIP simulations are a key resource for assessing human influences on the climate system. Pre-industrial control and historical simulations are of most relevance for model evaluation and assessment of internal variability. CMIP6 also includes an extensive set of idealized and single forcing experiments for attribution (Eyring et al., 2016; Gillett et al., 2016; Jones et al., 2016b). In addition to the assessment of model performance and human influence on the climate system during the instrumental era until present-day, this chapter also includes evidence from paleo-observations and simulations over past millennia (Kageyama et al., 2018). The assessment in this chapter is primarily based on studies using the CMIP6 model simulations, building on the evidence already assessed in the AR5 and Special Reports, as well as more recent studies using the CMIP5 model simulations. It provides the primary evaluation of large-scale indicators of climate change in this report, and is complemented by fitness-for-purpose evaluation in subsequent chapters.

Whereas in previous IPCC Assessment Reports the comparison of simulated and observed climate change was done separately in a model evaluation chapter and a chapter on detection and attribution, in AR6 these comparisons are integrated together. This has the advantage of allowing a single discussion of the full set of explanations for any inconsistency in simulated and observed climate change, including missing forcings, errors in the simulated response to forcings, and observational errors, as well as an assessment of the application of detection and attribution techniques to model evaluation. Where simulated and observed changes are consistent, this can be interpreted both as supporting attribution statements, and as giving confidence in simulated future change in the variable concerned. However, if a model's simulation of historical climate change has been tuned to agree with observations, or if the models used in an attribution

study have been selected or weighted on the basis of the realism of their simulated climate response, this information would need to be considered in the assessment and any attribution results correspondingly tempered: an integrated discussion of evaluation and attribution supports such a robust and transparent assessment.

This chapter starts with a brief description of methods for detection and attribution of observed changes in Section 3.2. The following sections address the climate system component-by-component, in each case assessing human influence and evaluating climate models' simulations of the relevant aspects of climate and climate change. This chapter assesses the evaluation and attribution of continental and ocean basin-scale large-scale indicators of climate change in the atmosphere and at the Earth's surface (Section 3.3), cryosphere (Section 3.4), ocean (Section 3.5), and biosphere (Section 3.6), and the evaluation and attribution of modes of variability (Section 3.7), the period of slower warming in the early 21st century (Cross-Chapter Box 3.1:) and large-scale analyses of changes in extremes (Cross-Chapter Box 3.2:). Model evaluation and attribution on sub-continental scales are not covered here, since these are assessed in the Atlas and Chapter 10, and extreme event attribution is not covered since it is assessed in Chapter 11. Section 3.8 assesses multivariate attribution and integrative measures of model performance based on multiple variables, as well as process representation in different classes of models. The chapter concludes with a discussion of the limits to the assessment in Section 3.9.

3.2 Methods

New methods for model evaluation that are used in this chapter are described in Section 1.4. These include new techniques for process-based evaluation of Earth system models against observations that have rapidly advanced since the publication of AR5 (Eyring et al., 2019b) as well as newly developed CMIP evaluation tools that allow a more rapid and comprehensive evaluation of the models with observations. In this chapter, we use the Earth System Model Evaluation Tool (ESMValTool, Eyring et al. (2019a); Righi et al. (2019)) and the NCAR Climate Variability Diagnostic Package (CVDP, Phillips et al., 2014) that is included in the ESMValTool to produce the figures in order to ensure traceability of the results and to provide an additional level of quality control. The code to produce the figures will be released as open source software at the time of the publication of AR6.

An introduction to recent developments in detection and attribution methods in the context of this report is provided in Cross-Chapter Box 1.5. Here we discuss new methods and improvements applicable to the attribution of changes in large-scale indicators of climate change which are used in this chapter.

3.2.1 Methods Based on Optimal Fingerprinting

Fingerprinting methods have been widely used for detection of climate change and attribution of the changes to different external drivers. Initially, these methods were applied to detect changes in global surface temperature (Hegerl et al., 1996), and were then extended to other climate variables at different time and spatial scales (e.g. Hasselmann, 1997; Allen and Tett, 1999b; Hegerl and Zwiers, 2011). These approaches assume that the observed change consists of a linear combination of externally forced signals plus internal variability, and are based on multivariate linear regression. The regressors are given by the expected space-time response patterns to different climate forcings (fingerprints), and the residuals represent internal variability. Fingerprints and internal variability are usually estimated from climate model simulations. A regression coefficient which is inconsistent with zero implies that a detectable change is identified in observations. When the confidence interval of regression coefficient includes unity and is inconsistent with zero, the magnitude of model simulated fingerprints are assessed to be consistent with the observations, implying that the observed changes can be attributed in part to a particular forcing. Variants of linear regression have been used to address uncertainty in the fingerprints due to internal variability (Allen and Stott, 2003) as well as the structural model uncertainty (Huntingford et al., 2006).

In order to improve the signal-to-noise ratio, optimisation is usually applied by normalizing observations and

model-simulated responses by internal variability. This procedure requires an estimate of the inverse covariance matrix of the internal variability, and some approaches have been proposed for more reliable estimation (Ribes et al., 2009). A signal can be spuriously detected due to too small noise, and model underestimation in simulating internal variability needs to be evaluated with care. Model-simulated variability is typically checked through comparing modelled variance from unforced simulations with the observed residual variance using a standard residual consistency test (Allen and Tett, 1999), or an improved one (Ribes and Terray, 2013). In this respect, Imbers et al. (2014) tested sensitivity of the detection and attribution results to the different representations of internal variability associated with short-memory and long-memory processes. Their results supported the robustness of previous detection and attribution statements for the global mean temperature change but also implicated the necessity of a wider variety of robustness tests.

Some recent studies focused on the improved estimation of the scaling factor (regression coefficient) and its confidence interval. In order to address the same covariance structure assumption made between model error and internal variability, Hannart et al. (2014) proposed an inference procedure of scaling factor estimation using a maximum likelihood method. Hannart (2016) further suggested an integrated approach to optimal fingerprinting where all uncertainty sources (i.e., observed error, model error, and internal variability) are treated in one statistical model, which does not require a preliminary dimension reduction. Katzfuss et al. (2017) introduced a similar integrated approach based on a Bayesian model averaging. On the other hand, DelSole et al. (2019) suggested a bootstrap method to better estimate confidence intervals of scaling factors even in a weak-signal regime. It is notable that some studies do not optimise fingerprints, as uncertainty in the covariance introduces a further layer of complexity, resulting in limited improvement in detection (Polson and Hegerl, 2017). Li et al. (submitted) note that failing to take account of uncertainty in the estimated covariance matrix can result in underestimated uncertainty intervals, particularly in studies using a small number of realisations of internal variability to estimate this matrix.

Another fingerprinting approach uses pattern similarity between observations and fingerprints, in which the leading empirical orthogonal function mode obtained from the time-evolving multi-model forced simulation is usually defined as a fingerprint (e.g. Bonfils et al., submitted; Marvel et al., 2019; Santer et al., 2013). Observations and model simulations are then projected onto the fingerprint to measure the degree of spatial pattern similarity with the expected physical response to a given forcing. This projection provides the signal time series, which is in turn tested against the internal variability noise estimated from long-term control simulations. As a way to extend this pattern-based approach to a high-dimensional detection variable, Sippel et al. (2019, 2020) proposed using the relationship pattern with a global climate change metric as a fingerprint. To solve the high-dimensional regression problem which makes regression coefficients not well constrained, they incorporated a machine learning technique based on a regularized linear regression, which maximizes a global warming signal by giving lower weight to regions with larger internal variability.

3.2.2 Other Probabilistic Approaches

Considering the difficulty in accounting for climate modelling uncertainties in the regression-based approaches, Ribes et al. (2017) introduced a new statistical inference framework based on an additivity assumption and likelihood maximization. The method was further developed by (Ribes et al., submitted), who linked it to Kriging, and applied it to narrow the uncertainty range in the estimated human-induced warming. Hannart and Naveau (2018), on the other hand, extended the application of standard causal theory (Pearl, 2009) to the context of detection and attribution by converting a time series into an event, calculating the probability of causation, and maximizing the causal evidence associated with the forcing. Application of these approaches to attribution of large-scale temperature changes supports the dominant anthropogenic contribution to the observed global warming.

Climate change signals can vary with time and discriminant analysis has been used to obtain more accurate estimates of time-varying signals, and has been applied to different variables such as seasonal temperatures (Jia and DelSole, 2012) and the South Asian monsoon (Srivastava and DelSole, 2014). The same approach was applied to separate aerosol forcing responses from other forcings (Yan et al., 2016b) and results

indicated that using joint temperature-precipitation spatial structure may be more accurate. Paeth et al. (2017) introduced a detection and attribution method applicable for multiple variables based on a discriminant analysis and a Bayesian classification method. Finally, a systematic approach has been proposed to translating quantitative analysis into a description of 'confidence' in the detection and attribution of a climate response to anthropogenic drivers (Stone and Hansen, 2016).

3.3 Human Influence on the Atmosphere and Surface

3.3.1 Temperature

3.3.1.1 Surface Temperature

Surface temperature change is the aspect of climate in which the climate research community has had most confidence over past IPCC Assessment Reports, largely because of relatively good long-term observations, a response to anthropogenic forcing which is large compared to variability in the global mean, allowing detection from just a day of observations (Sippel et al., 2020), and a strong theoretical understanding of the key thermodynamics driving its changes (Collins et al., 2010; Shepherd, 2014). AR5 assessed that it was *extremely likely* that human activities had caused more than half of the observed increase in global mean surface temperature from 1951 to 2010, and *virtually certain* that internal variability alone could not account for the observed global warming since 1951 (Bindoff et al., 2013). The AR5 also assessed with *very high confidence* that climate models reproduce the general features of the global-scale annual mean surface temperature increase over 1850-2011 and with *high confidence* that models reproduce global and Northern Hemispere (NH) temperature variability on a wide range of time scales (Flato et al., 2013). This section assesses the performance of the current generation of CMIP6 models in simulating the most important aspects of surface temperature and its change, and assesses the evidence from detection and attribution studies of human influence on surface temperature.

Paleoclimate context
Paleoclimate studies provide context in which to attribute past climate transitions to external forcings, lengthen the period over which natural variability is quantified, and provide quantitative metrics for model evaluation. Cross-chapter Box 2.1 describes the paleoclimate periods considered in this section.

In terms of attribution, AR5 assessed with *high confidence* that the 20th-century annual mean surface temperature warming reversed a 5000-year old cooling trend in NH mid-to-high latitudes caused by orbital forcing, attributing the reversal to anthropogenic forcing with *high confidence*. This trend reversal has since been dated to around 1800 for ocean temperatures (McGregor et al., 2015), 1830 for tropical ocean temperatures, mid-19th century for NH land temperatures, and 1900 for Southern Hemisphere (SH) temperatures (Abram et al., 2016; see also Section 2.3.1.1). Since AR5, the role of external forcings was detected in all NH continents (PAGES 2k-PMIP3, 2015) over the common era with good agreement between reconstructions and models. In contrast, the effect of external forcings was not detectable in the SH, where models and reconstructions disagree strongly (Neukom et al., 2018). Global or NH temperature changes over the common era are attributed from reconstructions mostly to volcanic forcing (Schurer et al., 2014; McGregor et al., 2015; Otto-Bliesner et al., 2016; Neukom et al., 2019), with solar forcing playing a small role (Schurer et al., 2014; Neukom et al., 2019). Attribution of warming to greenhouse gas forcing is made as early as the end of the 19th century (Schurer et al., 2014; Neukom et al., 2019), with volcanism contributing a detectable cooling in the early 19th century, a lack of volcanic activity contributing to early-20th century warming, and aerosols contributing a cooling throughout the 20th century, especially since the 1950s (Hegerl et al., 2019).

In terms of model evaluation, paleoclimate proxies have been used to evaluate modelled past climate temperature change patterns. The AR5 found consistent polar amplification of warming in reconstructed and modelled temperatures from past periods of high (Pliocene and Eocene) and low (Last Glacial Maximum, LGM) CO_2, although deficiencies were noted with the modelled patterns and seasonality (Masson-Delmotte et al., 2013). Since AR5, the understanding of uncertainties in proxies (Hollis et al., 2019) and the boundary

conditions used to simulate the Pliocene and Eocene warm periods (Haywood et al., 2016; Lunt et al., 2017) has improved, and model agreement with proxies has improved for these time periods (Haywood et al., submitted; Lunt et al., submitted; Zhu et al., 2019b) (Sections 7.4.4.1.2; 7.4.4.2.2). For the LGM, the AR5 noted that models overestimated tropical cooling indicated in the sea surface temperature (SST) proxies (Annan and Hargreaves, 2015; Harrison et al., 2015, 2016) (upper panel of Figure 3.1:) but more recent SST and surface air temperature (SAT) proxy reconstructions show much better agreement with the models (Cleator et al., 2019; Tierney et al., submitted) (lower panel of Figure 3.1:), thanks to a better understanding of SST proxies and new calibration models (Tierney et al., submitted). CMIP5 simulations of the mid-Holocene show regional biases similar to those in pre-industrial and historical simulations (Harrison et al., 2015; Ackerley et al., 2017), as well as underestimated Arctic warming (Yoshimori and Suzuki, 2019). There is no evidence of improved agreement for CMIP6 models for these time periods. Indeed CMIP6 mid-Holocene simulations find a mid-latitude, subtropical, and tropical cooling compared to pre-industrial (Brierley et al., submitted), whereas proxies indicate a warming (Kaufman et al., submitted; see also section 2.3.1.1.2). For the Last Interglacial, improved temporal resolution of proxies (Capron et al., 2017) and better appreciation of the importance of freshwater forcing (Stone et al., 2016) brought improved understanding for the reasons behind apparent model-data inconsistencies. A metric-based assessment of paleoclimate model simulations is carried out in Section 3.8.2.

[START FIGURE 3.1 HERE]

Figure 3.1: Last Glacial Maximum (LGM, 21 ka) anomalies in mean annual temperature over land and sea surface temperature in the Tropics (30S-30N) for paleoclimate reconstructions featured in AR5 (upper panel) and for updated estimates (lower panel). The coloured crosses show long-term modelled mean differences (experiment minus pre-industrial control) in the relative warming/cooling over tropical land and ocean where the model output has been sampled only at the locations for which there are temperature reconstructions. The black crosses show the paleo proxy reconstructions.

[END FIGURE 3.1 HERE]

Model evaluation

To be fit for detecting and attributing human influence on globally-averaged surface temperatures, climate models need to represent, from physically-based understanding, both the response of surface temperature to external forcings and the internal variability in surface temperature over various time scales. This section evaluates those aspects in the latest generation of climate models. See Chapter 10 for model evaluation in the context of regional climate information, and the Atlas for regional assessments of model performance.

AR5 assessed with *very high confidence* that CMIP5 models reproduced observed large-scale mean surface temperature patterns, although errors of several degrees appear in elevated regions, like the Himalayas and Antarctica, at the edge of North Atlantic sea-ice field, and in upwelling regions. CMIP5 models also showed overestimations of SST in subtropical stratocumulus regions and the Southern Ocean but underestimation in the equatorial Pacific (Lauer et al., 2017). This assessment is updated here with CMIP6 simulations. Figure 3.2: shows the annual-mean surface air temperature at 2 m for the CMIP6 multi-model mean and its comparison to a reanalysis for the period 1995-2014. The AR5 assessment remains valid, with the largest biases being again seen in the same regions. CMIP6 model development studies support that view by reporting that regional absolute biases in surface temperature of more than 6°C remain (Crueger et al., 2018; Kuhlbrodt et al., 2018; Lauer et al., 2018). Along the Equator, although Planton et al. (submitted) found reduced biases in SST in CMIP6 compared to CMIP5, the reduction is not statistically significant. A cold bias is again found along the Pacific equator, with too cold sea surface temperatures extending too far west (Lauer et al., 2018). The causes of temperature biases are model-dependent but for example relate to biases in downward shortwave radiation at the surface caused by errors in cloudiness (Lauer et al., 2018), errors in oceanic circulation (Kuhlbrodt et al., 2018), errors in the simulation of trade winds (Lauer et al., 2018), and errors in surface albedo and moisture propagated from the vegetation schemes (Séférian et al., 2016). Increasing horizontal resolution however shows promise of decreasing long-standing biases in surface temperature, specifically in the North Atlantic, tropical Pacific, and upwelling regions, although Southern

Ocean biases get larger (Bock et al., submitted). As shown, in panels d and e of Figure 3.2:, biases in the mean HighResMIP model are smaller than those in the mean of the corresponding lower-resolution version of the same models simulating the same period, see further discussion in Section 3.8.2.2.

In summary, CMIP6 models reproduce observed large-scale mean surface temperature patterns as well as their CMIP5 predecessors, but with little evidence for reduced systematic biases. This assessment is currently made with *medium confidence* while the CMIP6 database is being populated.

[START FIGURE 3.2 HERE]

Figure 3.2: Annual-mean surface (2 m) air temperature (°C) for the period 1995–2014. (a) Multi-model (ensemble) mean constructed with one realization of CMIP6 historical experiments. (b) Multi-model-mean bias as the difference between the CMIP6 multi-model mean and the climatology from the Fifth generation of ECMWF atmospheric reanalyses of the global climate (ERA5). (c) Multi-model-mean of the root mean square error of the seasonal cycle with respect to the climatology from ERA5. Also shown is the multi-model-mean bias as the difference between the multi-model mean of (d) low resolution and (e) high resolution simulations of the HighResMIP and the climatology from ERA5. (Figure from Bock et al. (submitted), their Figure 2, produced with ESMValTool v2.0.0b3.)

[END FIGURE 3.2 HERE]

AR5 assessed with *very high confidence* that models reproduce the general history of the increase in global-scale annual mean surface temperature since the year 1850, although AR5 also reported that an observed reduction in the rate of warming over the first 15 years of the 20th century was not reproduced by the models (see Cross-Chapter Box 3.1). Figure 3.3: shows time series of anomalies in annually- and globally-averaged surface temperature simulated by CMIP6 models for the period 1850 to 2014, with the baseline set to 1850-1900. Anomalies are shown instead of absolute temperatures to focus on simulated climate change, and because anomalies are less uncertain in observations. Results for CMIP6 shown in Figure 3.3: suggest that the history of surface temperature increase is well reproduced, including the increase in warming rates beginning in the 1960s and the temporary cooling that follows large volcanic eruptions. Virtually all CMIP6 modelling groups report improvements in their model's ability to simulate current climate compared to the CMIP5 version (Boucher et al., submitted; Dunne et al.; Gettelman et al., 2019; Golaz et al., 2019; Rind et al.; Swart et al., 2019; Voldoire et al., 2019b; Wu et al., 2019b). Yet, the CMIP6 multi-model mean shows very little early 20th century warming. It is also cooler over the period 1940-1990 than both observations (Figure 3.3:) and CMIP5 (Flynn and Mauritsen, submitted; Gillett et al., submitted). This bias is driven by biases of several tenths of degrees in individual models over that period, and may be due to an overestimate in aerosol radiative forcing (Andrews et al., submitted; Dittus et al., submitted; Flynn and Mauritsen, submitted). Indeed, several models had to reduce the strength of their simulated aerosol radiative forcing during development to ensure total radiative forcing remained positive (Danabasoglu et al., submitted; Mulcahy et al., 2018). The CMIP6 multi-model mean warms at the same rate as observations after 1970, although models with the largest transient climate sensitivities simulate exaggerated warming rates compared to observations after 1980 (Swart et al., 2019; Tokarska et al., submitted). Note however that the magnitude of the biases varies strongly both spatially and temporally across ensemble members of a given model, especially for the most variable models. According to Figure 3.3:, the CMIP6 multi-model mean tends to simulate too large a response to volcanic eruptions. CMIP5 models had a similar issue, which Lehner et al. (2016) explained by missed compensating effects on surface temperature change associated with ENSO, which was not simulated in its correct phase, rather than overestimated response to forcing. When interpreting model simulations of historical temperature change, it is important to keep in mind that some models are tuned towards representing the observed trend in global mean surface temperature (Hourdin et al., 2017). Figure 3.3: marks those models with an asterisk: these models are either tuned to reproduce observed warming directly, or indirectly by tuning equilibrium climate sensitivity. However, Bock et al. (submitted) found no significant difference in skill at reproducing observed warming between models that use observed warming in their tuning compared to models that do not. Model spread around the mean is larger for models that are not tuned to observed warming, as can be expected. Diversity in modelled radiative

forcing, especially for aerosols and land-use changes, may translate into biases in the simulation of historical temperature changes, so models that simulate those forcings may reproduce observed temperature change with less fidelity than physical climate models, in which those forcings are prescribed. Current CMIP6 data remain insufficient to assess whether that is the case. In summary, the CMIP6 results currently available suggest that CMIP6 models reproduce global-scale annual mean surface temperature change over the historical period less well than their CMIP5 counterparts, but *medium confidence* is placed on that assessment until CMIP6 historical simulations have been submitted in larger numbers.

[START FIGURE 3.3 HERE]

Figure 3.3: Observed and simulated time series of the anomalies in annual and global mean surface temperature. All anomalies are differences from the 1850–1900 time-mean of each individual time series. The reference period 1850–1900 is indicated by grey shading. Single simulations for CMIP6 models (thin lines); multi-model mean (thick red line). Observational data (thick black lines) are Hadley Centre/Climatic Research Unit gridded surface temperature data set 4 (HadCRUT4; Morice et al., 2012), and are merged surface temperature (2 m height over land and surface temperature over the ocean). (a) All models have been subsampled using the HadCRUT4 observational data mask (see Jones et al., 2013). (b) All models have been blended to GMST and subsampled using the HadCRUT4 observational data mask (Cowtan et al., 2015). (c) HighResMIP models are displayed with the reference period 1950-1979. Masking was done like in (a). Inset: the global mean surface temperature for the reference period of the subsampled fields. (Figure from Bock et al. (submitted), their Figure 1, produced with ESMValTool v2.0.0b3.)

[END FIGURE 3.3 HERE]

The application of climate models to detection and attribution studies requires that those models simulate realistic internal variability on multi-decadal timescales. An underestimate of variability in models would make conclusions from detection and attribution overconfident. AR5 found that CMIP5 models simulate realistic variability in global-mean surface temperature on decadal time scales, with variability on multi-decadal time scales being more difficult to evaluate because of the short observational record (Flato et al., 2013). Since AR5, new work has characterized the contributions of variability in different ocean areas to SST variability, with tropical modes of variability like ENSO dominant on time scales of 5 to 10 years, while longer time scales see the variance move poleward to the North Atlantic, North Pacific, and Southern oceans (Monselesan et al., 2015). There may however be sizeable interdependencies between ENSO and sea surface temperature variability in different basins (Kumar et al., 2014), and ENSO's influence on global surface temperature variability may not be confined only to decadal timescales (Triacca et al., 2014). Studies based on large ensembles of 20th and 21st century climate change confirm that internal variability has a substantial influence on global warming trends over a few decades (Kay et al., 2015; Dai and Bloecker, 2018) (FAQ 3.1). Although the equatorial Pacific seems to be the main source of internal variability on decadal timescales, Brown et al. (2016) link diversity in modelled oceanic convection, sea ice, and energy budget in high-latitude regions to overall diversity in modelled internal variability.

This renewed interest in internal variability stems in part from its importance in understanding the slowdown in global surface temperature warming rate in the early 21st century (see Cross-Chapter Box 3.1). Some evidence is emerging that decadal to multidecadal modes of variability, such as Pacific decadal variability (Section 3.7.6) (England et al., 2014; Thompson et al., 2014; Schurer et al., 2015) and Atlantic Multidecadal variability (Section 3.7.7) partly drive global scale temperature variations over the historical period, and that variability in these modes may be underestimated by CMIP5 models. But evidence, coming mostly from paleo studies, is more mixed on whether CMIP5 models also underestimate decadal and multi-decadal variability in global mean temperature in general. Schurer et al. (2013) found good agreement between internal variability derived from paleo reconstructions, estimated as the fraction of variance that is not explained by forced responses, and modelled variability, although the subset of CMIP5 models they used may have been associated with larger variability than the full CMIP5 ensemble. Zhu et al. (2019) showed agreement in the modelled and reconstructed temporal spectrum of global surface temperatures on annual to multi-millennial timescales, and Neukom et al. (2019) found that the largest 51-year trends in both

reconstructions of global mean temperature and fully forced climate simulations over the period 850 to 1850 were almost identical. Laepple and Huybers (2014) found good agreement between modelled and proxy-derived decadal ocean temperature variability, but underestimates of variance by models by at least a factor 10 at longer timescales. In the SH, Hegerl et al. (2018) reported internal variability in the early 20th century larger than that modelled. (Friedman et al., submitted) found model biases in interhemispheric SST contrast that may be consistent with underestimated cooling after early-20th century eruptions or underestimated Pacific decadal variability. In addition, new literature suggests that anthropogenic forcing itself may affect variability in surface temperatures, at least on an interannual basis, challenging a common assumption in detection and attribution techniques that forcing does not change the variability. Screen (2014) reported an observed decrease in variance in the Northern Hemisphere mid-latitude land temperature, largest in Autumn, associated with Arctic amplification, and qualitatively consistent with simulated future changes in variance (Cross-Chapter Box 10.1). Qian and Zhang (2015) and Santer et al. (2018b) found an anthropogenic influence on the seasonal cycle of surface and tropospheric temperatures, respectively. Figure 3.4: shows the standard deviation of zonal-mean surface temperature in CMIP6 pre-industrial control simulations and observed temperature datasets. Results are consistent with the CMIP5 generation, which showed the largest model spread where variability is also large, in the tropics and mid- to high-latitudes (Flato et al., 2013). But CMIP6 models tend to overestimate variability in the high latitudes.

[START FIGURE 3.4 HERE]

Figure 3.4: Global climate variability as represented by standard deviation of zonal-mean surface temperature of observed temperature datasets (in black: GISTEMP (dashed), Cowtan and Way (dot-dashed), HadCRUT4 (solid), and Berkeley Earth (long dashed)) and in CMIP6 pre-industrial control simulations (after Jones et al., 2013). Figure produced with ESMValTool v2.0.0b3.

[END FIGURE 3.4 HERE]

Figure 3.5:, taken from Parsons et al. (submitted), illustrates the large differences in GSAT variability in CMIP6 pre-industrial unforced control simulations. Surface temperatures in pre-industrial conditions are especially variable in the models on the top row, and some models substantially exceed the variability seen in CMIP5 models. Their variability in a small number of occurences approaches that observed under anthropogenically forced conditions (bottom-right panel of Figure 3.5:). Ribes et al. (submitted) reached similar conclusions. For the CNRM models, which are among the most variable, the large, low-frequency variability is attributed to a strong simulated Atlantic Multidecadal Variability (Séférian et al., 2019; Voldoire et al., 2019b), which is difficult to disprove because of the short observational record (Cassou et al., 2018; Section 3.7.7). Given a potential oceanic origin for the large internal variability in GSAT in some CMIP6 models, it is noteworthy that the 10 most variable models, shown on the two topmost rows of Figure 3.5:, share only two ocean models, either version 3.6 of Nucleus for European Modelling of the Ocean (NEMO) or versions of the Modular Ocean Model (MOM).

[START FIGURE 3.5 HERE]

Figure 3.5: Global mean surface air temperature (GSAT) anomalies in 29 CMIP6 control simulations, compared with GISTEMP GMST observations. Blue lines show annual means, and red lines show 25-year low-pass filtered means. Red numbers show standard deviations of interdecadal GSAT/GMST variations. (From Parsons et al. (submitted), their Figure 1, updated to correct a latitude weighting error.)

[END FIGURE 3.5 HERE]

Detection and attribution

AR5 assessed that it was *extremely likely* that human influence was the dominant cause of the observed warming since the mid-20th century, and that it was *virtually certain* that warming over the same period

cannot be explained by internal variability alone. Since AR5 and in anticipation of new CMIP6 simulations, most new attribution studies of changes in global surface temperature have focused on methodological advances. Those advances include improvements in the way observational and model uncertainties, and internal variability are accounted for in optimal fingerprinting (Ribes and Terray, 2013; Hannart, 2016; Ribes et al., 2017); formulating the attribution problem in a counterfactual framework (Hannart and Naveau, 2018); or reducing the dependence of the attribution on uncertainties in climate sensitivity and forcing by fitting an impulse-response model to observed temperatures (Otto et al., 2015; Haustein et al., 2017, 2019). Those studies make strongly confident attribution statements about global warming trends, finding that observed warming is consistent with the response to anthropogenic forcing and that natural forcings alone cannot explain the observed warming (Ribes et al., 2017); that anthropogenic forcing is a necessary and sufficient cause of the observed spatio-temporal anomalies of temperature change (Hannart and Naveau, 2018); that even the early 20th century was anthropogically-forced, much reducing the role of internal variability (Haustein et al., 2019); and that anthropogenic influence is detectable in a single day of observations (Sippel et al., 2020). The findings of those studies imply that the AR5 assessment could be strengthened, but based on expert judgement, those studies may also still underestimate the importance of the structural limitations of climate models, which probably do not represent all possible sources of internal variability, or use too simple climate models, which may underestimate the role of internal variability. While Li et al. (submitted) show that uncertainties in attributable warming may be underestimated in optimal detection studies which neglect uncertainties in the estimated covariance matrix of internal variability and use a small number of simulated realisations of internal variability to estimate this matrix (Gillett et al., 2013a; Jones et al., 2013), this source of uncertainty is explicitly considered by several recent studies (Hannart, 2016; Hannart and Naveau, 2018; Ribes et al., 2017, submitted), and moreover studies which validate their approaches by testing in an imperfect model framework also implicitly address this potential issue (Gillett et al., submitted; Ribes and Terray, 2013; Schurer et al., 2018). The influence of observational uncertainty on detection and attribution of global temperature changes has been studied in more detail than earlier studies, and Jones and Kennedy (2017) and Schurer et al. (2018) conclude that accounting for observational uncertainty inflates the uncertainty associated with the greenhouse gas regression scaling factor by 10-30%. Schurer et al. (2018) found that using blended SSTs over ocean and SAT over land from climate models, which is more comparable to observed global temperature estimates (Chapter 2), in an attribution analysis resulted in a greenhouse gas scaling factor 3-5% higher than using global mean SAT.

It is more difficult to attribute observed warming to individual forcing mechanisms, such as increases in greenhouse gas concentrations or changes in anthropogenic aerosol loading, than to anthropogenic forcings combined. A new analysis of the observed warming between 1901 and 1950 (Hegerl et al., 2018) finds that approximately half of this warming was externally forced by a combination of greenhouse gas increases and natural forcing, partially offset by aerosols, with the remaining warming due to internal variability, although they caution that observational uncertainty over this period is substantial. Indeed, a growing body of literature suggests that closely constraining the separate contributions of greenhouse gas changes and aerosol changes to observed temperature changes remains challenging. For example, although Jones et al. (2016a) attribute a warming of 0.87 to 1.22°C per century to well-mixed greenhouse gases, partially offset by a cooling of −0.54 to −0.22°C per century attributed to aerosols, they highlight the wide range covered by those two estimates, which they link to uncertainties in modelled patterns of change and internal variability. Ribes and Terray (2013) also conclude that the weak observational constraints on the contributions of greenhouse gas and aerosol forcing call for new attribution techniques. Linear addition of single-forcing responses implied by fingerprinting attribution techniques were found to hold for large-scale surface temperature changes in Bindoff et al. (2013) based on two studies. A more recent third study also finds additivity using the GISS climate model (Marvel et al., 2015).

IPCC SR1.5 notes that anthropogenic warming has essentially been equal to total warming since the early 2000s, based on the assessment by (Bindoff et al., 2013) that temperature changes by solar and volcanic forcings are small. By applying the method of Haustein et al. (2017), which accounts for forcing uncertainty and internal variability, and moderating their uncertainty estimates to account for additional forcing and model uncertainty, the IPCC SR1.5 assessed that GMST warming attributable to anthropogenic forcing has reached 1.0°C in 2017 with respect to the period 1850-1900, with a *likely* range of ±0.2°C.

Figure 3.6: shows two- and three-way fingerprinting regression coefficients for six CMIP6 models and the corresponding attributable warming ranges, derived using HadCRUT4 (Gillett et al., submitted). Some of those models have regression coefficients significantly less than 1, meaning that they significantly over-predict the temperature response to either greenhouse gases or aerosols, and some have regression coefficients significantly greater than 1, implying that they underpredict the response to these forcings. However, all models are consistent in attributing most of simulated warming to anthropogenic influences, and five of six models exhibit constrained three-way regression coefficients, with warming from increases in greenhouse gases concentrations offset by a cooling attributed to other anthropogenic influences, mostly aerosols. Using HadCRUT5 (Chapter 2) in place of HadCRUT4 in the analysis results in only very small changes in estimates of anthropogenic warming in globally-complete GSAT (Gillett et al., submitted).

[START FIGURE 3.6 HERE]

Figure 3.6: Upper panels show regression coefficients based a two-way regression (left) and three-way regression (right), of observed 5-yr mean global mean masked and blended surface temperature onto individual model response patterns, and a multi-model mean, labelled 'Multi'. Combined anthropogenic (ANT), natural (NAT), well-mixed greenhouse gases (GHG), and other anthropogenic (aerosols, ozone, land-use change, OTH) regression coefficients are shown. Regression coefficients are the scaling factors by which the model responses must be multiplied to best match observations. Regression coefficients consistent with one indicate a consistent magnitude response in observations and models, and regression coefficients inconsistent with zero indicate a detectable response to the forcing concerned. Note that three-way regression coefficients for MIROC6 are unconstrained. Lower panels show corresponding observationally-constrained estimates of attributable warming in globally-complete GSAT for the period 2010-2019, relative to 1850-1900, and the horizontal black line shows an estimate of observed warming in GSAT for this period. (Figure from Gillett et al. (submitted), their Figure S3.)

[END FIGURE 3.6 HERE]

Figure 3.7: shows 5-95% ranges in attributable trends in globally-complete global mean near-surface air temperature (GSAT) for the period 2009-2018 compared to 1850-1900 from five analyses: a multi-model regression analysis using CMIP6 simulations (Gillett et al., submitted), the method of Ribes et al. (submitted) also applied on CMIP6 simulations, the method of Haustein et al. (2017) directly applied, and in an implementation by Jenkins et al. (submitted) using three full-coverage observational datasets (GISTEMP, NOAA, and Cowtan/Way), and estimates derived using a simple climate model driven using assessed estimates of effective radiative forcing and transient and equilibrium climate sensitivity (see Section 7.3.5.4). The figure also shows the GSAT changes directly simulated in response to these forcings in six CMIP6 models. In all approaches, the warming attributable to natural causes is close to zero. In spite of their different methodologies and input datasets, the four attribution approaches yield very similar results, with the anthropogenic attributable warming range encompassing observed warming, and the natural attributable warming being close to zero. The warming driven by greenhouse gas increases is offset in part by cooling due to other anthropogenic forcing agents, mostly aerosols, although confidence in that attribution is lower than attributing to all anthropogenic drivers, as discussed above. Physically-based estimates made by Chapter 7, not constrained by observed warming, while more uncertain, are remarkably close to estimates from attribution studies despite being the products of a totally different approach, enhancing confidence in the magnitude and causes of attributable surface temperature warming.

[START FIGURE 3.7 HERE]

Figure 3.7: Coloured bands show assessed *likely* ranges of temperature change in GSAT, 2010-2019 relative to 1850-1900, attributable to anthropogenic forcings (ANT), well-mixed greenhouse gases (GHG), other anthropogenic forcings (aerosols, ozone, land-use change, OTH), and natural forcings (NAT), and in observations (Obs). The observed warming shown currently is for 2009-2018 but will be updated to 2010-2019 in the final draft. Bars show 5-95% ranges based on the individual studies indicated (Gillett et al., submitted; Haustein et al., 2017; Jenkins et al., 2019; Ribes et al., submitted), with the results from

Gillett et al. (submitted) corresponding to the multi-model attributable warming estimates shown in Figure 3.6:. The Jenkins et al. (submitted) range shown was calculated by subtracting 0.35 times an estimated anthropogenic warming rate of 0.17°C/decade (Haustein et al., 2017) from the Jenkins et al. (submitted) reported anthropogenic attributable warming in GSAT in 2018 of 1.04-1.37°C, to account for the difference in averaging period. The Chapter 7 best estimates and ranges are derived using assessed forcing timeseries and a two-layer energy balance model as described in Section 7.3.5.4. Chapter 7 uncertainty ranges account for uncertainties in climate properties and radiative forcings, without constraints based on observed climate change, but are approximate and will be updated in the final draft. Coloured circles show the raw simulated responses to the forcings concerned in each of the models indicated.

[END FIGURE 3.7 HERE]

The AR5 found *high confidence* for a major role for anthropogenic forcing in driving warming over each of the inhabited continents, except for Africa where they found only *medium confidence* because of limited data availability (Bindoff et al., 2013). Friedman et al. (submitted) detect an anthropogenically forced response of inter-hemispheric contrast in surface temperature change, with the Northern Hemisphere cooling more than the southern hemisphere until 1980 but then warming more from 1980 to 2012. CMIP5 models simulate the correct sign of the inter-hemispheric contrast when forced with all forcings but underestimate its magnitude. There has been limited new literature on continental-scale attribution since the AR5. Stone and Hansen (2016) proposed and developed an automated empirical approach for developing confidence levels associated with detection and attribution statements, based on the amount of modelling and observational evidence, and the results of a detection and attribution analysis. Figure 3.8: shows global surface temperature change in CMIP6 all-forcing and natural-only simulations globally, at continental scales, and separately over land and ocean surfaces. All-forcing simulations encompass observed temperature changes for all regions, while natural-only simulations fail to do so in recent decades except in Antarctica, based on the annual means shown. As stated above, warming results from a partial offset of greenhouse warming by aerosol cooling. That offset is stronger over land than ocean. Regionally, models show a large range of possible temperature responses to greenhouse gas and aerosol forcing, which complicates single-forcing attribution. This is particularly true in North America and Europe.

[START FIGURE 3.8 HERE]

Figure 3.8: Global, land, ocean and continental annual mean temperatures anomalies for CMIP6 historical (brown) hist-nat (green), hist-GHG (grey) and hist-aer (blue) simulations (multi-model means shown as thick lines, and minimum and maximum ranges shown as shaded area) and for Hadley Centre/Climatic Research Unit gridded surface temperature data set 4 (HadCRUT4, black). All models have been subsampled using the HadCRUT4 observational data mask (see Jones et al., 2013). Temperatures are shown with respect to 1850–1900, for Antarctica with respect to 1900–2010. (Figure produced with ESMValTool v2.0.0b3).

[END FIGURE 3.8 HERE]

In summary, since the publication of the AR5, new literature has emerged which better accounts for methodological and climate model uncertainties in attribution studies (Ribes et al., 2017; Hannart and Naveau, 2018), reporting results consistent with probabilities above 99% for human activities causing more than half the observed warming over the 1951-2010 period. Moreover, calculated anthropogenic warming and associated uncertainties calculated for 2017 relative to 1850-1900 (Haustein et al., 2017), and as assessed in the IPCC SR1.5 also imply probabilities over 99% that human activities caused more than half the observed warming trend under the assumption of normally distributed uncertainties. And finally, the strong observed warming that has occurred in the period since the publication of the AR5 (Chapter 2), and the improved understanding of the causes of the apparent slowdown in warming over the beginning of the 21st century and the difference in simulated and observed warming trends over this period (Cross-Chapter Box 3.1), further improve our confidence in the assessment of the dominant anthropogenic contribution to

observed warming. However, there is also new literature that raise further questions about model ability to simulate variability in surface temperatures over a range of time scales (e.g. Friedman et al., submitted; Parsons et al., submitted), and some CMIP6 models exhibit substantially higher multidecadal internal variability than that seen in CMIP5, which remains to be fully understood (Parsons et al., submitted; Ribes et al., submitted). The IPCC SR1.5 best estimate and *likely* range of anthropogenic attributable warming was 1.0±0.2°C in 2017 with respect to the period 1850-1900. Here, we derive ranges for attributable GSAT warming by finding the smallest ranges with a precision of 0.1°C which span all of the 5-95% ranges from the attribution studies shown in Figure 3.7:, and assess these ranges as *likely* rather than *very likely* to account for sources of uncertainty not considered in the studies, for example common errors in forcings across models. This leads to a *likely* range for anthropogenic attributable warming in 2010-2019 relative to 1850-1900 of 0.8 to 1.4°C in terms of GSAT. Using the 4.3% scaling factor assessed in Cross-Chapter Box 2.3, the *likely* anthropogenic attributable warming in terms of GMST is 0.8-1.3°C, which is also consistent with the range of 0.85-1.16°C directly calculated by Gillett et al. (submitted). Importantly, the range for anthropogenic attributable GMST warming encompasses the best estimate and range of observed GMST warming of 1.06 °C (0.95 – 1.17 °C) over the same period (Section 2.1.1.1.4). Natural attributable GSAT warming is −0.1 to 0.1°C. The *likely* range of GSAT warming attributable to well-mixed greenhouse gases is assessed in the same way to be 0.9 to 2.0°C while the GSAT change attributable to aerosols, ozone and land-use change is −0.7 to 0.2°C. Balancing progress in attribution techniques with remaining uncertainty in the magnitude of internal climate variability, we assess that it remains *extremely likely* that human influence is the main driver of the observed increase in global-mean surface air temperature, causing more than half of observed warming in 2010-2019 relative to 1850-1900.

The IPCC SR1.5 gave a *likely* range for human-induced warming rate of 0.1°C to 0.3°C per decade in 2017, with a best estimate of 0.2°C per decade (Allen et al., 2018). Since the SR1.5, the detection study of Ribes et al. (submitted), based on CMIP6 simulations constrained by observed warming, found a warming rate over the period 2010-2019 of 0.22 ± 0.05°C per decade attributable to anthropogenic forcing, with 0.23 ± 0.06°C per decade attributed to greenhouse gas forcing alone. The choice of SSP emission scenario to simulate the period 2015-2019 has an impact on estimated warming rates, so the SR1.5 uncertainty ranges of ±0.1°C represent a more conservative choice. For this reason, we retain the SR1.5 *likely* range for surface temperature warming rate of 0.1°C to 0.3°C per decade, with a best estimate of 0.2°C per decade.

3.3.1.2 Upper-Air Temperature

The AR5 (Bindoff et al., 2013) assessed that anthropogenic forcings, dominated by GHGs, *likely* contributed to the warming of the troposphere since 1961 and that anthropogenic forcings, dominated by the depletion of the ozone layer due to ozone-depleting substances, *very likely* contributed to the cooling of the lower stratosphere since 1979. Since the AR5, observational uncertainties in the radiosonde and satellite data have been further understood with more available data and longer coverage, and differences between models and observations in the tropical atmosphere have been investigated further.

Tropospheric temperature

The AR5 assessed with *low confidence* that most, though not all, CMIP3 and CMIP5 models overestimated the observed warming trend in the tropical troposphere during the satellite period 1979-2012, and that a third to a half of this difference was due to an overestimate of the SST trend during this period (Flato et al., 2013). Mitchell et al.(2013) and McKitrick and Christy (2018) demonstrated an inconsistency between CMIP5 simulated and observed temperature trends in the tropical troposphere with models suggesting more substantial warming than observations. However, Mitchell et al. (2013) found a smaller discrepancy in models forced with observed SSTs, and models and observations are consistent below 150 hPa when viewed in terms of the ratio of temperature trends aloft to those at the surface. Figure 3.9: shows that CMIP6 models forced by anthropogenic and natural forcings again overestimate temperature trends compared to radiosonde data in the tropical troposphere, although models show better consistency with observations in the lower troposphere. The largest difference can be seen between 300 and 100 hPa over the 1979-2014 period. Because of uncertainties from the observational data, the assessment of causes of observed trends in the upper troposphere and stratosphere is less confident than an assessment of overall atmospheric temperature

changes. Kamae et al. (2015) suggested that the recent slowdown of tropical upper tropospheric warming was associated with Pacific climate variability. Tuel (2019) found that most of the tropospheric temperature difference between CMIP5 models and the satellite-based trend over the 1970-2018 period are due to respective differences in SST warming trends in regions of deep convection. Moreover, Santer et al. (2017b) compared the global-mean mid-tropospheric temperatures from multiple Microwave Sounding Unit (MSU) datasets and climate model data during the satellite era and found that during the late twentieth century, the discrepancies between simulated and satellite-derived tropospheric temperature trends are consistent with internal variability, while during most of the early twenty-first century, simulated tropospheric warming is significantly larger than observed, which they relate to systematic deficiencies in some of the external forcings used after year 2000 in the models. However, we note that differences between simulated and observed upper tropospheric temperature trends persist in CMIP6 despite updated forcing estimates (Figure 3.9). Focused on the temperature of the mid-to-upper troposphere (TMT), Santer et al. (2017c) used updated and improved satellite retrievals to investigate model performance in simulating the TMT trends and vertical profiles of warming, and removed the influence of stratospheric cooling by regression. These factors were found to reduce the size of the discrepancy in TMT trends between models and observations over the satellite era, but a discrepancy remained.

Overall, these studies continue to find that CMIP5 and CMIP6 models indicated more warming than observations in the tropical mid- and upper-troposphere over the 1979-2012 period (McKitrick and Christy, 2018; Mitchell et al., 2013, submitted, Santer et al., 2017a, 2017c; Suárez-Gutiérrez et al., 2017), and that overestimated surface warming is partially responsible (Mitchell et al., 2013). Although accounting for internal variability and residual observational errors can reconcile models with observations (Mitchell et al., 2013; Suárez-Gutiérrez et al., 2017), studies also point to forcing errors in the CMIP5 simulations in the early 21st century as a possible contributor (Mitchell et al., 2013; Sherwood and Nishant, 2015; Santer et al., 2017a). It is unknown whether forcing also explains part of the CMIP6 model biases. Hence, we assess with *medium confidence* that CMIP5 and CMIP6 models continue to overestimate observed warming in the upper tropical troposphere during the satellite era, in part because of an overestimate of the SST trend pattern over this period.

[START FIGURE 3.9 HERE]

Figure 3.9: Vertical profiles of temperature trends in the tropics (20°S-20°N) for three periods between 1979 and 2014. The black lines show trends in the RICH1.5 and RAOBCORE1.5 radiosonde datasets, and ERA5/5.1 reanalysis. Red lines show trends in 18 CMIP6 models' historical simulations, and blue lines show trends in 18 CMIP6 models' simulations with prescribed sea surface temperatures. Panel a), b) and c) show trends over the periods 1979-2014, 1979-1997 (ozone depletion era), and 1998-2014 (ozone recovery era) respectively. (Figure from Mitchell et al. (submitted), their Figure 1.)

[END FIGURE 3.9 HERE]

The human influence on changes in tropospheric tempeature has received much attention in recent years. The AR5 assessed as *likely* that anthropogenic forcings, dominated by GHGs, contributed to the warming of the troposphere since 1961 (Bindoff et al., 2013). Since then, there has been further progress in detecting and attributing tropospheric temperature changes. Santer et al. (2014) found significant correlations between observed stratospheric aerosol optical depth and satellite estimated tropospheric temperature and short-wave fluxes at the top of the atmosphere. They show that simulations which do not consider the influence of volcanic eruptions in the early 21st century overestimate the observed tropospheric warming since 1998. Focused on the seasonal cycle of tropospheric temperatures, Santer et al. (2018) investigated the changes in the annual mean and annual cycle of tropospheric temperature. They found clear human influence in the changes of seasonal cyle based on multiple observationally-based datasets and multiple models. They applied a standard fingerprint method to determine if the model "human influence" fingerprint can be distinguished from the background noise of internal variability. They found satellite data and the anthropogenic forcing-driven climate models show consistent geographical large-scale changes of seasonal cycle amplitude, including amplitude increases at mid-latitudes in both hemispheres, decreases in amplitude

at high latitudes in the Southern Hemisphere, and small changes in the tropics. The model fingerprint of externally forced seasonal cycle changes is identified in five out of six satellite temperature datasets. Their attribution results are not affected by removing the global mean information and by excluding the sea ice region. Santer et al. (2019) also quantify the stochastic uncertainty in detection time of human-caused climate signals. They used two climate models with large-ensemble runs and estimate signal detection time in individual ensemble members. They found that the stochastic uncertainty is greater for tropospheric warming (8-15 years) than stratospheric cooling (1-3 years) because of larger noise and slower recovery time from the Pinatubo eruption in the troposphere. The detection time of the anthropogenic signal in the tropospheric warming can be affetected by both the model climate sensitivity and the model response to aerosol forcing. Pallotta and Santer (submitted) further conducted a multi-frequency analysis of simulated versus observed variability in tropospheric temperature. They found on timescles of 5-20 years, that CMIP5 climate models overestimate the observed natural variabilty in global mean tropospheric temperature. This thus indicates that the previous detection results about anthropogenic influence on the tropospheric warming may be conservative.

Based on these additional analyses, we assess that it is *very likely* that anthropogenic forcing, dominated by GHGs, was the main driver of the warming of the troposphere since 1979.

Stratospheric temperature

The AR5 concluded that the CMIP5 models simulated a generally realistic evolution of lower stratospheric temperatures (Bindoff et al., 2013; Flato et al., 2013) and better than the CMIP3 models, in part because they generally include time-varying ozone concentrations, unlike many of the CMIP3 models. Nonetheless, it was noted that there was a tendency for the simulations to underestimate stratospheric cooling compared to observations. Based on attribution studies using simulations from CMIP5 and from the Chemsitry-Climate Model Validation Avtivity (CCMVal), Bindoff et al. (2013) concluded that it was *very likely* that anthropogenic forcing, dominated by stratospheric ozone depletion due to ozone-depleting substances, had contributed to the cooling of the lower stratosphere since 1979. Since the AR5, Santer et al. (2017b) compared observed lower stratospheric temperature trends with those simulated by the CMIP5 models, and found a tendency for the models to underestimate the cooling, which they attributed to an underestimation of stratospheric ozone depletion in many CMIP5 models (Eyring et al., 2013; Young et al., 2013), differences in stratospheric water vapour evolution, and internal variability. Maycock et al. (2018a) compared lower stratospheric temperature trends over the 1979-2005 period in the coupled chemistry climate simulations of the Chemistry-Climate Model Initiative (CCMI) with satellite observations, and found that observed trends were within the range of simulated trends, and the models reproduced the levelling off of lower stratospheric temperatures in the 1998-2016 period due to the cessation of ozone depletion and onset of recovery. Young et al. (2013) compared temperature trends based on various satellite and radiosonde observations and climate (GCM) and chemistry-climate model (CCM) outputs, with a focus on the influence of ozone depletion in the Antarctic lower stratosphere since mid-1950s. They found that CCMs and CMIP5 models' simulation of Antarctic stratospheric cooling is consistent with recent radiosonde datasets to within modelling and observational uncertainties. In a modelling study, Aquila et al. (2016) found that in the lower stratosphere, the cooling trend due to increasing GHGs is roughly constant over the satellite era. Changes in concentrations of ozone-depleting substances (ODS), via their chemical effect on ozone which then affects heating, cause a significant stratospheric cooling only up to the mid-1990s. After that, a decrease in ODS caused a flattening of temperature, with more rapid fluctuations caused by the eruption of Mount Pinatubo and the solar cycle. Mitchell et al. (submitted) show that while the CMIP6 models simulate realistic trends in tropical lower stratospheric temperature over the whole 1979-2014 period, they tend to overestimate the cooling trend over 1979-1997 and underestimate it over 1998-2014 (Figure 3.9:), which they speculate may be due to possible deficiencies in prescribed stratospheric ozone changes.

Upper stratospheric temperature changes were not assessed in the context of attribution or model evaluation in AR5, but this is an area where there has been considerable progress over recent years, with new versions of both Stratospheric Sounding Unit (SSU) datasets released, which are in better agreement than previous versions (Maycock et al., 2018a, Karpechko and Maycock et al., 2018) (see also Section 2.3.1.1.4). Simulated temperature changes in the CCMI coupled chemistry models show good consistency with the reprocessed dataset from NOAA STAR SSU but are less consistent with the revised UK Met Office record.

The latter still shows stronger cooling than simulated in the chemistry-climate models (Maycock et al., 2018a). It has been shown that reanalyses indicate an upper-stratospheric cooling from 1979 to 2009 of about 3°C at 5hPa and 4°C at 1hPa that agrees well with the cooling in AMIP-type simulations using CMIP5 forcings (Simmons et al., 2014).The cooling in the reanalyses results from the assimilation of SSU and AMSU data. Mitchell (2016) used regularized optimal fingerprinting techniques to make an attribution analysis of annual mid to upper stratospheric temperature in response to external forcings. They found that anthropogenic forcing has caused an approximate cooling of 2-3 °C in the upper stratosphere over the period of 1979-2015, with GHGs contributing two thirds of this change and ozone depletion contributing one third. They find a temperature change in response to volcanic forcing is large (0.4-0.6 °C for Mount Pinatubo) in the upper stratosphere, although it is still smaller than the lower-stratospheric signal. Aquila et al. (2016) used chemistry climate models with added forcing factors and prescribed observed sea surface temperature to investigate the influence of different forcings on global stratospheric temperature changes. They find that the cooling of the stratosphere after 1979 is mainly due to changes in GHG concentrations in the middle and upper stratosphere. The changes of global temperature anomalies are mainly due to changes in solar irradiance and volcanically-induced ozone depletion and water vapour increases in the post-Pinatubo years. Therefore, in the upper stratosphere, both a standard detection and attribution approach (Mitchell, 2016) and chemistry-climate model studies (Aquila et al., 2016; Maycock et al., 2018a) indicate that about two-thirds of the global long-term cooling is attributed to GHGs and one third to ozone depletion. Chemistry-climate model results further show that the relatively rapid decreases in global upper stratospheric temperatures in the early 1980s and early 1990s are likely to be due to the combined influence of temperature decreases after the warming from major tropical volcanic eruptions and the declining phase of the 11-year solar cycle.

Based on the latest updates to satellite observations of stratospheric temperature, we assess that simulated and observed changes of global mean temperature through the depth of the stratosphere are more consistent than based on previous datasets, but some differences remain (*medium confidence*). Studies published since the AR5 increase our confidence in the simulated stratospheric temperature response to greenhouse gas and ozone changes, and support an assessment that it is *extremely likely* that anthropogenic forcing, dominated by stratospheric ozone depletion due to ozone-depleting substances, was the main driver of the cooling of the lower stratosphere since 1979, as expected from physical understanding.

3.3.2 Precipitation, Humidity and Streamflow

Paleoclimate context

A fact hindering detection and attribution studies in precipitation and other hydrological variables is the large internal variability of these fields relative to the anthropogenic signal. Moreover, the human influence can result in increases or decreases in precipitation. Paleoclimate records provide valuable context for observed trends in the 20th and 21st century and assist with the attribution of these trends to human influence (see also Sections 2.3.1.3.1 and 8.3.1.8). For example, many areas of the subtropics – such as the Mediterranean and the western United States – have experienced systematic drying in recent decades. This is an expected response as elevated greenhouse gases cause an increase in evaporative demand (Seager et al., 2014b, 2014a), but can be difficult to attribute due to the large internal variability of the water cycle. Records of tree ring width provide evidence that recent prolonged dry spells in the Levant, Mongolia, and Chile are unprecedented in the last millennium (*high confidence*) (Pederson et al., 2014; Cook et al., 2016a; Garreaud et al., 2017). Recent drought in the Mediterranean may be attributable to anthropogenic forcing (*medium confidence*) (Kelley et al., 2015; Gudmundsson and Seneviratne, 2016). Likewise, tree rings indicate that the 2012-2014 drought in California was exceptionally severe in the context of natural variability in the last millennium, and may have been exacerbated by the contribution of anthropogenic temperature rise (*medium confidence*) (Griffin and Anchukaitis, 2014; Williams et al., 2015). East Africa has been drying in recent decades (Hoell et al., 2017), a trend that is unusual in the context of the sedimentary paleorecord spanning the last millennium (Tierney et al., 2015). This may be a signature of anthropogenic forcing but cannot as of yet be distinguished from natural variability (Hoell et al., 2017; Philip et al., 2018). Tree rings also indicate the presence of prolonged megadroughts (droughts lasting two decades or more) in western North America throughout the last millennium that were more severe than 20th and 21st century events (*high confidence*) (Cook et al., 2004, 2010, 2015). These were with *medium confidence* associated with internal climate

variability (Coats et al., 2016; Cook et al., 2016b) and indicate that large-magnitude changes in the water cycle may occur irrespective of anthropogenic influence.

Paleoclimate records also provide context for the human influence on large-scale atmospheric circulation, such as the inter-tropical convergence zone (ITCZ), the Walker circulation, and monsoon systems. In AR5, it was determined with *high confidence* that orbital forcing produces strong interhemispheric rainfall variability evident in multiple types of proxies. These large-magnitude intensifications and weakenings in the monsoon systems involved in some cases orders-of-magnitude changes in precipitation (Harrison et al., 2014; Tierney et al., 2017) and thus are *virtually certain* to have been larger than changes observed in the 20th and 21st centuries. Paleoclimate modeling and limited data from past climate states with high CO_2 suggest that monsoon systems intensify under elevated greenhouse gases (*medium confidence*), providing context for present and future trends (Passey et al., 2009; Haywood et al., 2013; Zhang et al., 2013b). Paleoclimate data from the Pliocene epoch suggest that there was a reduction in the zonal and meridional gradients of SST in the tropical Pacific (Fedorov et al., 2006; Brierley, Chris M et al., 2009) with similar CO_2 as today. Some studies suggest that this higher concentration of CO_2 at that time (410 ppm) weakened the Walker circulation (Tierney et al., 2019), in agreement with theory (Vecchi et al., 2006; Vecchi and Soden, 2007) but in contradiction to recently-observed trends in the Pacific (L'Heureux et al., 2013; England et al., 2014) and the ambiguous trends across the last 100 years as a whole (Vecchi et al., 2006; Karnauskas et al., 2009; DiNezio et al., 2013). Other studies consider that present climate models cannot simulate the extent and patterns of Pliocene warmth due to unresolved climate feedbacks, which can change the simulated response of precipitation in the subtropics in the context of global warming (Burls and Fedorov, 2014, 2017).

3.3.2.1 Precipitation

The AR5 concluded that there was *medium confidence* that human influence had contributed to large-scale precipitation changes over land since 1950, including an increase in the NH mid to high latitudes. Moreover, AR5 concluded that observational uncertainties and challenges in precipitation modelling precluded a more confident assessment (Bindoff et al., 2013). Overall, they found that large-scale features of mean precipitation in CMIP5 models are in modest agreement with observations, but there are systematic errors in the Tropics.

Since AR5, Li et al. (2016b) found that CMIP5 models simulate the large scale patterns of annual mean land precipitation and seasonality, as well as reproduce qualitatively the observed zonal mean land precipitation trends: models capture the drying trends in the tropics and along 45°S and the wetting trend in the NH mid-to-high latitudes, but the amplitude of the changes are much smaller. Nevertheless, models do not appear to reproduce the zonal mean trends of seasonality, nor the trends of annual precipitation and seasonality over land, though internal variability and observational uncertainty may contribute to these apparent differences (Li et al., 2016b). The CMIP5 models have also been shown to adequately simulate the mean and interannual variability of the Global Monsoon (section 3.3.3.2), but maintain the double ITCZ bias in the equatorial Pacific (Lee and Wang, 2014; Ni and Hsu, 2018). CMIP5 models do better than CMIP3 models, in particular regarding the Global Monsoon domain and intensity (Lee and Wang, 2014). Regarding trends in precipitation intensity, models have also been shown to reproduce the compensation between precipitation extremes and the rest of the distribution (Thackeray et al., 2018), a characteristic found in the observational record (Gu and Adler, 2018). Regional performance is further assessed in chapters 8 and 10.

The simulation of annual mean rainfall patterns in the CMIP6 models reveals minor improvements compared to those of CMIP5 models (Figure 3.10:). The persistent biases include the double ITCZ in the tropical Pacific and the southward-shifted ITCZ in the equatorial Atlantic, which has been suggested to be the result of underestimating the sensitivity of precipitation to local SST (Good et al., submitted). There is some improvement in the overly intense Indian ocean ITCZ and the too dry South American continent except over the Andes. Moreover, CMIP6 models represent better the storm tracks (Priestley et al., submitted; also Section 3.3.3.3) reducing the precipitation biases in the North Atlantic and midlatitudes of the SH. As result, pattern correlations between simulated and observed annual mean precipitation range between 0.80 and 0.92 for CMIP6, compared to a range of 0.79 and 0.88 for CMIP5 (Bock et al., submitted). A recent study using

several coupled models showed that increasing the atmospheric resolution leads to a strong decrease in the precipitation bias in the tropical Atlantic (Vannière et al., 2019), see further discussion in Section 3.8.2.2.

Observational data sets have also improved. Osborne et al. (2015) identified a data problem in observed land precipitation around 1930, proposing a correction which made the precipitation record more consistent with the runoff record. Moreover, the corrected data set became consistent with the expected negative precipitation response to mid-20th century aerosol forcing.

[START FIGURE 3.10 HERE]

Figure 3.10: Annual-mean precipitation rate (mm day–1) for the period 1995–2014. (a) Multi-model-mean constructed with one realization of CMIP6 (included models: see Fig.3.3) historical experiments (b) Difference between multi-model mean and precipitation analyses from the Global Precipitation Climatology Project (GPCP) version 2.3 (Adler et al., 2003). (c) Multi-model-mean of the root mean square error of the seasonal cycle with respect to precipitation analyses from GPCP v2.3. Also shown is the Multi-model-mean bias as the difference between the multi-model mean of (d) low resolution and (e) high resolution simulations of the HighResMIP and precipitation analyses from GPCP v2.3. (Figure from Bock et al. (submitted), their Figure 3, produced with ESMValTool v2.0.0b3).

[END FIGURE 3.10 HERE]

AR5 concluded that models can successfully reproduce to first-order patterns of past climate changes during the Last Glacial Maximum (LGM) and mid-Holocene; including the impacts of changes in monsoon circulation on precipitation patterns (Braconnot et al., 2012; Flato et al., 2013). Further analysis of CMIP5 models confirmed these results but has also revealed systematic offsets from the paleoclimate record (DiNezio and Tierney, 2013; Hargreaves and Annan, 2014; Harrison et al., 2014, 2015; Bartlein et al., 2017; Scheff et al., 2017; Tierney et al., 2017). For example, the differences between reconstructed and CMIP5 simulated changes in mid-Holocene rainfall over the African monsoon region is more than 50% (Perez-Sanz et al., 2014; Harrison et al., 2016; Tierney et al., 2017). As result, Harrison et al. (2014) concluded that CMIP5 models do not perform better in simulating rainfall than earlier model versions despite higher resolution and complexity. However, prescribing changes in vegetation and dust was found to improve the match to the paleoclimate record (Pausata et al., 2016; Tierney et al., 2017) suggesting that vegetation feedbacks in the CMIP5 models may be too weak (*low confidence*) (Hopcroft et al., 2017). Brierley et al. (submitted) compared the simulated annual precipitation changes by CMIP6 models during the mid-Holocene with pollen based reconstructions. They conclude that CMIP6 models do not show a robust signal in area averaged rainfall over most regions where quantitative reconstructions exist, which is not incompatible with reconstructions (Figure 3.11:). These results are similar to CMIP5. Over the Sahara/Sahel region, where reconstructions suggest positive anomalies during the mid-Holocene, CMIP6 models simulate a more robust and stronger rainfall increase, showing some improvement over CMIP5.

Liu et al. (2018) evaluated the terrestrial moisture changes that occurred during the LGM and concluded that the multi-model median from CMIP5 is consistent with available paleo-records in some regions, but not in others. CMIP5 models accurately reproduce an increase in moisture in the western United States, related to an intensified winter storm track and decreased evaporative demand (Oster et al., 2015; Ibarra et al., 2018; Lora, 2018). On the other hand, CMIP5 models show a wide variety of responses in the tropical Indo-Pacific region, with only a few matching the pattern of change inferred from the paleoclimate record (DiNezio and Tierney, 2013; DiNezio et al., 2018). The variable response across models is related to the effect of the exposure of the tropical shelves during glacial times, which variously intensifies or weakens convection in the rising limb of the Walker cell, depending on model parameterization (DiNezio et al., 2011). For the Last Interglacial, PMIP4 (CMIP6) models reproduce the proxy-based increased precipitation relative to pre-industrial in the North African, South Asian and North American regions, but not in Australia (Scussolini et al., 2019).

[START FIGURE 3.11 HERE]

Figure 3.11: Comparison between simulated annual precipitation changes and pollen-based reconstructions. Six regions where multiple quantitative reconstructions exist are chosen. These are Northern Europe (NEU), Central Europe (CEU), the Mediterranean (MED), the Sahara/Sahel (SAH), East Asia (EAS) and Eastern North America (ENA). The distribution of reconstructions within the region are shown by boxes and whiskers. The area-averaged change in mean annual precipitation simulated by CMIP6 (individually identifiable) and CMIP5 (blue) within each region is shown for comparison. (Figure from Brierley and PMIP4 (submitted), their Figure 11).

[END FIGURE 3.11 HERE]

The observed trend for precipitation averaged over NH land areas throughout the 20th century is negligible (Wu et al., 2013). Also, no significant trend is found in the global precipitation mean value during the satellite era (Adler et al., 2017), consistent with model simulations (Wu et al., 2013). This has been suggested to be due to the negative effect of anthropogenic sulfates and volcanic forcing that opposed the positive influence of rising global mean temperatures due to greenhouse gases (Salzmann, 2016; Richardson et al., 2018). The precipitation change expected from ocean warming is also partly offset by the fast atmospheric adjustment to increasing greenhouse gas concentration as long as the concentration are not stabilized (Section 8.2.1). Over the ocean the negligible trend may be due to the cancelling effects of CO_2 and aerosols (Richardson et al., 2018).

A gridpoint based analysis of precipitation trends over land regions since 1901 (Knutson and Zeng, 2018) comparing observed and model simulated trends finds that detectable anthropogenic increasing trends have occurred prominently over many middle to high latitude regions of both hemispheres. The observed trends in many cases are significantly stronger than modeled in the CMIP5 historical runs for the 1901-2010 period (though not for 1951-2010), suggesting possible deficiencies in models with capturing past forced trend behavior over the past century in precipitation trends.

The observed precipitation increase in the NH high latitudes over the period 1966-2005 was attributed to anthropogenic forcing by a study using CMIP5 models (Wan et al., 2015) supporting the AR5 assessment. Initial results from CMIP6 also support the role of anthropogenic forcing in the precipitation increase observed in NH high latitudes(see Figure 3.12:).

[START FIGURE 3. 12 HERE]

Figure 3.12: Global and zonal average changes in annual mean precipitation (mm day-1) over areas of land where there are observations, expressed relative to the base-line period of 1961–1990, simulated by CMIP6 models forced with both anthropogenic and natural forcings (brown) and natural forcings only (blue). Multi-model means are shown in thick solid lines and shading shows minimum and maximum ranges of the individual model simulations. Observations (gridded values derived from Global Historical Climatology Network station data, updated from Zhang et al. (2007) are shown as a black solid line. (Figure produced with ESMValTool v2.0.0b2.)

[END FIGURE 3.12 HERE]

For the SH extratropics, Solman and Orlanski (2016) found that the observed summertime rainfall increase (decrease) over high (mid) latitudes during 1979-2010 are quasi-zonally symmetric and related to changes in eddy activity. The latter were in turn associated with the poleward shift of the westerlies due mostly to ozone depletion. Positive rainfall trends in the subtropics, particularly over southeastern South America and northern and central Australia, have been also attributed to ozone depletion (Kang et al., 2011; Gonzalez et al., 2014) and greenhouse gases (Vera and Diaz, 2014). During austral winter wetting and drying conditions at high and middle latitudes, respectively, are not zonally homogeneous, and both changes in eddy activity

and increased lower troposphere humidity contributed. Solman and Orlanski (2016) associate these climate changes to increase in GHG concentration levels. Recently, Blazquez and Solman (2017) have shown that CMIP5 models represent very well the dynamical forcing and the frequency of frontal precipitation in the SH winter extratropics, but the amount of precipitation due to fronts is overestimated. Chapter 10 validates in more detail the simulation of fronts in climate models.

In the tropics and subtropics Polson and Hegerl (2017) found that the effect of external forcing on precipitation following the wet gets wetter, dry gets drier paradigm is robust if one takes into account the seasonal and interannual movement of the regions (Allan, 2014). A follow-up study found that the forced signal is already detectable over wet regions, but not over dry ones in the period 1988-2018 (Figure 3.13:; Schurer et al., submitted). Other studies suggest that this paradigm does not necessarily hold over dry regions where moisture is limited (Greve et al., 2014; Kumar et al., 2015, see also section 8.2.2.1). Based on long-term island precipitation records, Polson et al. (2016) identified significant increases in precipitation in the tropics and decreases in the subtropics, which are consistent with those simulated by the CMIP5 models. Barkhordarian et al. (2018) attributed the observed reduced springtime precipitation in tropical South America during 1983-2012 to elevated GHGs and land use. Polson et al. (2014) found that anthropogenic aerosols were the dominant influence in the decrease of NH summer monsoon precipitation during the second half of the 20th century. Moreover, Undorf et al. (2018) identified remote aerosol emissions from North America and Europe as the main source regions to explain changes over West African monsoon. For South Asian monsoon local emissions are also needed to explain precipitation changes.

Over the oceans, observations show coherent large-scale patterns of fresh ocean regions becoming fresher and salty ocean regions saltier across the globe, which has been related through modeling studies to changes in precipitation-evaporation and is consistent with the wet gets wetter, dry gets drier paradigm (see Section 3.5.2.2; Durack, 2015; Durack et al., 2012, 2013; Grist et al., 2016; Hegerl et al., 2015; Levang and Schmitt, 2015; Skliris et al., 2014; Zika et al., 2015).

[START FIGURE 3. 13 HERE]

Figure 3.13: Wet (top) and dry (bottom) region tropical mean (30S-30N) annual precipitation anomalies with respect to 1988-2018 (mm) for observations (GPCP - in black) and CMIP6 model simulations (single simulations light blue/red with multi-model-mean in dark blue/red). Wet and dry region annual values are calculated as the mean over 4 seasons (OND, JFM, AMJ, JAS). The regions are defined by the wettest third and driest third by surface area, calculated for the observations and for each model separately for each season (following Polson and Hegerl 2017). Scaling factors (right) are calculated for the combination of the wet and dry region mean, where the observations and all the model simulations are first standardised using the mean standard deviation of piControl simulations. Two total least squares regression methods are used: noise in variables (following Polson and Hegerl 2017) which estimates a best estimate and a 5-95% confidence interval using the piControls (circle and thick green line) and the piControls with double the variance (thin green line); and the bootstrap method (DelSole et al., 2019) 5-95% confidence interval purple line, best estimate purple circle.

[END FIGURE 3.13 HERE]

Land precipitation was found to show enhanced seasonality (Chiang et al., 2013), consistent with the simulated response to anthropogenic forcing (Dwyer et al., 2014). However, observed trends in seasonality depend on data set used (Li et al., 2016b; Marvel et al., 2017), and Marvel et al. (2017) found inconsistent trends in the amplitude of the seasonal cycle of precipitation in global satellite precipitation observations and CMIP5 models. On the other hand, Marvel et al. (2017) found that observed changes to the annual cycle phase are consistent with model estimates of forced changes. These phase changes are mainly characterized by earlier onset of the wet season on the equatorward flanks of the extratropical storm tracks, particularly in the SH.

Overall, several new studies detect an anthropogenic influence on precipitation over the continents and

oceans in the high latitudes and tropics, and we therefore now assess that it is *likely* that human influence has contributed to observed large-scale precipitation changes since 1950. Despite large decadal variability, there is *medium confidence* that rainfall over the wet regions of the tropics has increased due to enhanced greenhouse gas forcing. Yet, there is also growing evidence and *medium confidence* that this tropical precipitation increase has been partly muted by anthropogenic aerosols through a decreasing effect in the Northern Hemisphere summer monsoon region from the mid to late 20th century. There is *medium confidence* that ozone depletion has increased precipitation over the Southern Ocean and decreased it over southern midlatitudes during austral summer. Owing to observational uncertainties and inconsistent results between studies, we conclude that there is *low confidence* in the attribution of changes in the seasonality of precipitation.

3.3.2.2 Atmospheric Water Vapour

The AR5 concluded that an anthropogenic contribution to specific humidity is found with *medium confidence* at and near the surface. A levelling off of atmospheric water vapour over land in the last two decades that needed better understanding, and remaining observational uncertainties precluded a more confident assessment (Bindoff et al., 2013). Sections 4.1.1.12 and 8.3.1.4 show that there have been significant advances in the understanding of the processes controlling land surface humidity. In particular, there has been a focus on the role of oceanic moisture transport and land-atmosphere feedbacks in explaining the observed trends in relative humididty.

Water vapor is the most important natural greenhouse gas and its amount is expected to increase in a global warming context leading to further warming. Particularly important are changes in the upper troposphere because there water vapor regulates the strength of the water-vapor feedback (section 7.1.15). CMIP5 models have been shown to have a wet bias in the tropical upper troposphere and a drier-than-observed lower troposphere, with the former bias and model spread being larger than the latter (Jiang et al., 2012; Tian et al., 2013). Water vapor biases in models are dominated by errors in relative humidity throughout the troposphere, which are in turn closely related to errors in large scale circulation; temperature errors dominate near the tropopause (Takahashi et al., 2016). Section 7.1.1.5 discusses this topic in more detail for CMIP6 models.

Using satellite data as well as CMIP5 model output, Chung et al. (2014) demonstrated that the moistening observed in the upper troposphere over the period 1979–2005 cannot be explained by natural causes and results principally from an anthropogenic warming of the climate. This increase in water vapour is accompanied by a reduction in mid-tropospheric relative humidity and clouds in the subtropics and mid-latitude in both models and observations related to changes in the Hadley cell (Lau and Kim, 2015; also section 3.3.3.1).

Dunn et al. (2017) confirmed earlier findings that global mean surface relative humidity increased during 1973-2000, followed by a steep decline, and specific humidity correspondingly increased and then remained approximately constant, with none of the CMIP5 models capturing this behaviour. They noted biases in the mean state of the CMIP5 models' surface relative humidity (and ascribe the failure to the representation of land surface processes and their response to CO_2 forcing), concluding that these biases preclude any detection and attribution assessment. A recent study has, however, identified an anthropogenically-driven decrease in relative humidity over the NH midlatitude continents in summer during 1951-2005 (Douville and Plazzotta, 2017). This drying was underestimated by CMIP5 models with potential implications for the projected 21st century changes in these regions.

Based on new evidence we assess that it is *likely* that human influence has contributed to tropical moistening in the upper troposphere since 1979 with *medium confidence*. Owing to the limited number of studies and model biases we conclude that there is *low confidence* in the attribution of changes in the surface humidity.

3.3.2.3 Streamflow

Stream flow is to-date the only variable of the terrestrial water cycle with enough *in-situ* observations to allow for detection and attribution analysis at continental to global scales. Based on evidence from a few formal detection and attribution studies, particularly on the timing of peak streamflow, and the qualitative evaluation of studies reporting on observed and simulated trends, AR5 concluded that there is *medium confidence* that anthropogenic influence on climate has affected streamflow in some middle and high latitude regions. AR5 also noted that observational uncertainties are large and that often only a limited number of models were considered.

Section 2.3.1.3.6 assesses that there have not been significant trends in global average streamflow over the last century, though regional trends have been observed, driven in part by internal variability. Only a limited number of studies have systematically compared observed streamflow trends at continental to global scales with changes simulated by global circulation models (GCM) in a detection and attribution setting. Yang et al., (2017) did not find a significant correlation between observed runoff changes and changes simulated in CMIP5 models in most grid cells, consistent with the assessment that observed changes are dominated by internal variability. In a pan-European assessment, Gudmundsson et al. (2017) attribute the spatio-temporal pattern of decreasing streamflow in southern Europe and increasing streamflow in northern Europe to anthropogenic climate change, but also concluded that additional effects of human water withdrawals could not be excluded. Focussing on continental runoff during 1958-2004, Alkama et al. (2013) found a significant change only when using reconstructed data over all rivers, indicating a large uncertainty in the estimate of the global streamflow trend due to different statistical methods used and opposite changes over different continents. Gedney et al. (2014) detect the influence of aerosols on streamflow in North America and Europe, with aerosols having driven an increase in streamflow due to reduced evaporation (see Chapter 8 for details on processes). There is also evidence for a detectable anthropogenic contribution toward earlier winter-spring streamflows in north-central US (Kam et al., 2018) and in western Canada (Najafi et al., 2017). From a model evaluation perspective, Sheffield et al. (2013) report that CMIP5 models reproduce spatial variations in runoff in North America well, though they tend to underestimate it.

Recently Gudmundsson et al. (2019) performed a global detection and attribution study and found that some regions are drying and others are wetting. Moreover, the simulated streamflow trends are consistent with observations only if anthropogenic climate change is considered, and the simulated effects of water and land management cannot reproduce the trends. The effects of volcanic eruptions in driving reduced streamflow have also been detected in many regions of the world (Iles and Hegerl, 2015).

In summary, there is *medium confidence* that anthropogenic climate change has altered local and regional streamflow in various parts of the world and that the associated global-scale trend pattern is inconsistent with pre-industrial control simulations. Moreover, recent results suggest that human interventions and water withdrawals, while interfering with the streamflow, cannot explain the observed trends.

3.3.3 Atmospheric Circulation

3.3.3.1 Tropospheric Overturning Circulation in the Tropics

The tropical tropospheric circulation features meridional and zonal overturning circulations, called Hadley and Walker circulations. In the zonal mean, the downwelling branch of the Hadley circulation cell is located in the subtropics and is often used as an indicator of the meridional extent of the tropics. In the zonal-vertical section, the major rising branch of the Walker cell is located over the Maritime continent with secondary upwelling regions over northern South America and Africa. The zonal component of the surface trade winds over most of the equatorial Pacific and Atlantic is associated with the Walker circulation.

AR5 found *medium confidence* that the depletion of stratospheric ozone had contributed to Hadley cell widening in the Southern Hemisphere in austral summer. It also mentioned that in contrast to a simulated weakening in response to GHG forcing, the Walker circulation had actually strengthened since the early

1990s, precluding any detection of human influence.

Hadley cell width

Since AR5, studies identify dependence on metrics of the trends in the edge latitude of Hadley cells (Davis and Birner, 2017; Waugh et al., 2018). Grise et al. (2019) find that a metric based on surface zonal winds, which are well constrained by surface observations, best compares reanalyses with CMIP5 models. With this method and new reanalysis products, the CMIP5 historical simulation ensembles simulate comparable mean states and variability of the edge latitude of Hadley cells to those observed (Grise et al., 2019). Furthermore, the CMIP5 (Davis and Birner, 2017; Grise et al., 2018) and CMIP6 (Figure 3.14:) historical simulation ensembles capture the observed poleward shifting trend of the zonal-mean Hadley cell edges since around 1980. The models confirm the contribution from human influence to this widening trend, mostly through GHG increase and stratospheric ozone depletion (Gerber and Son, 2014; Nguyen et al., 2015; Tao et al., 2016a), although the mechanism remains inconclusive (Staten et al., 2018). However, a growing body of literature has found an important contribution from internal variability, including the Pacific Decadal Variability (PDV; Section 3.7.6), on the observed Hadley cell expansion for this period (Allen et al., 2014; Allen and Kovilakam, 2017; Mantsis et al., 2017; Amaya et al., 2018; Grise et al., 2018). Indeed, the simulated ensemble-mean expansion is much weaker than in reanalyses (Davis and Birner, 2017; Grise et al., 2018; Nguyen et al., 2015). In the annual mean, internal variability contributed to the observed zonal-mean Hadley cell expansion since 1980 at least comparably with human influence (Allen and Kovilakam, 2017; Amaya et al., 2018). The human-induced change has not yet emerged out of the range of internal variability in the Northern Hemisphere (Quan et al., 2018; Grise et al., 2019), whereas for 3 out of the 4 reanalyses assessed in Figure 3.14: the trend in the Southern Hemisphere boundary is outside the 5-95th percentile range of internal variability in CMIP6. For the Southern Hemisphere summer when the simulated human influence is strongest, the trend in 2 out of the 4 reanalyses fall outside the 5-95th percentile range of internal variability (Grise et al., 2018, 2019; Tao et al., 2016). Regionally, while Kim et al. (2017b) find that the observed shift of the South Atlantic Hadley Cell edge exceeds the 95th percentile of internal variability in CMIP5 piControl simulations based on a sea level pressure (SLP)-based metric, this is not detected in other metrics in (Grise et al., 2019). It is also noteworthy that many CMIP5 models underrepresent the magnitude of the PDV (Section 3.7.6), implying potential overconfidence on the detection of human influence on the Hadley cell expansion. Yet, CMIP6 models less suffer from this bias (Section 3.7.6).

Walker circulation strength

Historical CMIP5 simulations reproduce the mean state of the Walker circulation with reasonable fidelity, evidenced by the spatial pattern correlations of equatorial zonal mass stream function between models and observations being larger than 0.88 (Ma and Zhou, 2016). On average, historical CMIP5 simulations also simulate a weakening of the Pacific Walker circulation throughout the 20th century (DiNezio et al., 2013; Sandeep et al., 2014; Kociuba and Power, 2015). This weakening is accompanied by reduction and enhancement of convective activity over the Maritime Continent and the central Equatorial Pacific, respectively, and weakening of equatorial zonal SST gradient across the eastern Indian Ocean through the Pacific (DiNezio et al., 2013; Sandeep et al., 2014; Kociuba and Power, 2015), consistent with CMIP3 (Vecchi et al., 2006; Vecchi and Soden, 2007). However, observations show substantial decadal variability in Walker circulation strengthen (Section 2.3.1.4.1). Studies based on in-situ observations of sea level pressure show weakening of the Pacific Walker circulation since the late 19th century (DiNezio et al., 2013; Bordbar et al., 2017) and the 1950s (further confirmed by surface wind and cloudiness; Bellomo and Clement, 2015; Tokinaga et al., 2012), whereas L'Heureux et al. (2013) find strengthening since 1950-2011 based on blended sea level pressure data from in-situ observations and reanalyses. Trends since around 1980 in in-situ and satellite observations and reanalyses exhibit strengthening of the Pacific Walker circulation and SST gradient (L'Heureux et al., 2013; Boisséson et al., 2014; England et al., 2014; Kociuba and Power, 2015; Ma and Zhou, 2016). While these trends since around 1980 are contrary to CMIP5 ensemble mean, AGCM simulations forced by observed SST reproduce the Walker circulation strengthening (Boisséson et al., 2014; Ma and Zhou, 2016), suggesting dominance of internal variability (Bordbar et al., 2017). Yet, this Pacific Walker circulation strengthening found in reanalyses is outside of the CMIP5 ensemble spread (England et al., 2014; Kociuba and Power, 2015). This may be caused by overestimation of the strengthening in reanalyses (Chung et al., 2019) or underestimation of the magnitude of the PDV in CMIP5 models (Kociuba and Power, 2015; Section 3.7.6). DiNezio et al. (2013) compare the observed weakening trend of

the Walker circulation trend over the period 1870-2004, which may be subject to large observational uncertainty, with CMIP5 trends, finding that the models underestimate the weakening trend. Models suggest that while greenhouse gas increases drive a weakening of the Walker circulation, aerosols drive a strengthening (DiNezio et al., 2013; Takahashi and Watanabe, 2016; Hua et al., 2018), but large uncertainties remain (Hua et al., 2018; Oudar et al., 2018).

Contrary to the model ensemble mean trends, and reflecting long-term changes observed in the Walker circulation, the equatorial zonal SST gradient from the eastern Indian Ocean through the Pacific has strengthened since 1900 (Coats and Karnauskas, 2017) and since the 1950s (Seager et al., 2019), although observational uncertainties are large (Deser et al., 2010; Tokinaga et al., 2012). CMIP5 historical simulations fail to capture the trend since the 1950s (Seager et al., 2019), which Seager et al. (2019) attribute to mean state biases in the models changing the sign of the zonal SST gradient response to greenhouse gas forcing. Yet, Watanabe et al. (submitted) find that large ensemble simulations by a few coupled models capture the observed strengthening since the 1950s, due in part to the realistic magnitude of PDV, suggesting an important contribution from internal variability. Coats and Karnauskas (2017) also find that the anthropgenic influence on the SST gradient is yet to emerge out of internal variability even on centennial timescales.

In summary, there is *medium confidence* that greenhouse gas increases and stratospheric ozone depletion have contributed to the observed zonal-mean Hadley cell expansion in the Southern Hemisphere since around 1980. However, the Hadley cell expansion in the Northern Hemisphere and changes in the Pacific Walker circulation strength are within the range of internal variability (*medium confidence*). The latter assessment is supported by studies since AR5, which identify the important role of the PDV and other internal variability on long-term changes in both the zonal-mean Hadley cell extent and Walker circulation strength. However, differing views in the literature regarding human influence on the Walker circulation changes and limited process understanding prevent higher confidence. The fact that detection of human influence on the Southern Hemisphere zonal-mean Hadley cell expansion is sensitive to the choice of reanalysis datasets, along with the sensitivity to metric choice and limited understanding on the mechanism, makes the confidence level of the former assessment medium despite increasing model evidence on the role of human influence.

[START FIGURE 3.14 HERE]

Figure 3.14: 1980-2013 trend of subtropical edge latitude of the Hadley cells in (a) the Northern Hemisphere for annual mean and (b-c) Southern Hemisphere for (b) annual mean and (c) DJF. Positive values indicate northward shifts. Histograms are based on historical (red) and 34-year segments of piControl (grey) simulations of CMIP6. Horizontal lines indicate MME means of historical simulations of CMIP6 (red) and CMIP5 (blue; extended with RCP4.5) along with reanalyses. The edge latitude is defined where the surface zonal wind velocity changes sign from negative to positive, as described in the Appendix of Grise et al., (2018). Produced with 22 CMIP6 models (192 members of historical and 338 segments of piControl simulations) and 20 CMIP5 models (99 members).

[END FIGURE 3.14 HERE]

3.3.3.2 Global Monsoon

Monsoons are seasonal transitions of regimes in atmospheric circulation and precipitation in association with redistribution of moist static energy (Biasutti et al., 2018). The global monsoon encompasses all the monsoon systems with specific metrics (Wang and Ding, 2008). Assessments of regional monsoon changes are made in Chapters 8 and 10.

AR5 assessed that CMIP5 models better reproduce monsoons than CMIP3 models but biases remain in domains and intensity (*high confidence*). There were no detection and attribution assessment statements on the decreasing trend of global monsoon precipitation over land from the mid-20th century to the 1980s or the increasing trend of global monsoon precipitation afterwards. Paleoclimate information on monsoons was

mostly regional.

Reproducing monsoons in terms of domain, precipitation amount, and timings of onset and retreat remains difficult. While CMIP5 historical simulations correctly capture global monsoon domains and intensity based on summer and winter precipitation difference, they underestimate the extent and intensity of East Asian and North American monsoons while overestimating those of western North Pacific monsoon (Lee and Wang, 2014; Yan et al., 2016a). Wang et al. (submitted) report that CMIP6 models better reproduce the global monsoon domain and precipitation (Figure 3.15:), albeit with biases in annual mean precipitation in Southern Hemisphere monsoons and timing of onset. Notable inter-model differences are identified in CMIP5, with the MME mean outperforming individual models (Lee and Wang, 2014). Common biases are identified across CMIP5 models in the Northern Hemisphere summer monsoon. Thermodynamical biases associated with the South Asian summer monsoon are suggested to arise from overly smoothed model topography in CMIP5 models (Boos and Hurley, 2012). However, in AGCMs with increasing resolution of up to ~20 km, improvements in monsoon precipitation are not universal across regions and models, and overall improvements are unclear (Johnson et al., 2016; Ogata et al., 2017; Zhang et al., 2018b).

Proxy evidence shows that global monsoon has varied with orbital forcing and GHGs (Chapter 2 Section 2.3.1.4.2; Mohtadi et al., 2016; Seth et al., 2019). In model simulations for the mid-Pliocene, when globally averaged temperature was higher than present day in the equilibrium response to CO_2, precipitation is larger in West African and South and East Asian monsoon than under the pre-industrial conditions, consistent with proxy evidence (Zhang et al., 2015; Sun et al., 2016b; Corvec and Fletcher, 2017), while proxy evidence is missing for the Southern Hemisphere monsoons. Models are also able to capture interhemispherically contrasting changes for the Last Interglacial in response to orbital forcing and GHGs, with wetter West African and Asian monsoons and a drier South American monsoon as revealed from proxies (Govin et al., 2014; Gierz et al., 2017; Pedersen et al., 2017). During the mid-Holocene, global monsoons were stronger especially in the Northern Hemisphere with an expansion of the West African monsoon domain (Biasutti et al., 2018). CMIP5 PMIP simulations can qualitatively capture the stronger Northern Hemisphere monsoon (Jiang et al., 2015), but underestimate the expansion found in a proxy reconstruction (Harrison et al., 2015), which can be improved by imposing vegetation and dust changes (Pausata et al., 2016). Besides, while the models simulate a mid-Holocene decrease in the monsoons in Southern Africa and northern Australia proxy evidence suggests an increase, especially in southern Africa (Jiang et al., 2015). These studies indicate that models can qualitatively reproduce past global monsoon changes seen in proxies, but issues remain in hemispheric and regional monsoon changes and quantitative reproduction. Studies on last millennium simulations show that simulated global monsoon precipitation increases with global mean temperature, while changes in monsoon circulation and hemispheric monsoon precipitation depend on forcing sources (Liu et al., 2012; Chai et al., 2018).

In the instrumental records, global summer monsoon precipitation intensity (measured by summer precipitation averaged over the monsoon domain) decreased from the 1950s to 1980s, followed by an increase (Chapter 2 Section 2.3.1.4.2; Figure 3.15:), mainly due to Northern Hemispheric land contributions. Model simulations over the instrumental era (Polson et al., 2014; Zhang et al., 2018c) and last millennium (Liu et al., 2012; Chai et al., 2018) show that GHG increases act to enhance Northern Hemisphere summer monsoon precipitation intensity. Since the mid-20th century, however, this effect was overwhelmed by influence from anthropogenic aerosols (Polson et al., 2014; Guo et al., 2015; Zhang et al., 2018c). Besides these human influences, the global monsoon is sensitive to internal variability and natural forcing including ENSO and volcanic aerosols on interannual time scales and PDV and Atlantic Multidecadal Variability (AMV; Section 3.7.7) on decadal to multidecadal time scales (Liu et al., 2016; Wang et al., 2013, 2018; but note the possibility that AMV in the 20th century has been partly driven by aerosols; see Section 3.7.7). A CMIP5 multi-model study by Zhang et al. (2018b) finds that observed 1951-2004 trends of the global and Northern Hemisphere summer land monsoon precipitation intensity are well captured by historical simulations, and CMIP6 models show similar results for global land summer monsoon precipitation (Figure 3.15c). They also find that the multi-model ensemble mean trend of historical simulations, dominated by anthropogenic aerosol forcing contributions, emerges out of the 90% range of internally-driven trends in piControl simulations. However, it should be noted that CMIP5 models tend to underrepresent the PDV magnitude (Section 3.7.6). An enhancement in global summer monsoon precipitation since the 1980s is also

captured by the CMIP6 models (Figure 3.15:c). This tendency is accompanied by intensification of the Northern Hemisphere summer monsoon circulation, which appears to be outside the range of increase simulated by the CMIP6 ensemble (Figure 3.15:d). An important contribution of AMV to the subsequent enhancements in global monsoon precipitation and circulation has been pointed out (Kamae et al., 2017). However, it is unclear whether human influence has made a significant contribution to these increases directly through GHG increases or aerosol changes or indirectly via aerosol forcing on AMV.

In summary, there is *medium confidence* that anthropogenic aerosols contributed to weakening of global land summer monsoon precipitation intensity from the mid- to late 20th century. Although there is possibility that GHG increases have contributed to the subsequent intensification of global land summer monsoon since the late 20th century, evidence is *limited* on whether this human-induced change has emerged out of the range of internal variability. The assessment on the mid- to late 20th century change is supported by multi-model detection and attribution studies which find the important role of anthropogenic aerosols in the weakening trend, but the confidence level is inhibited by the strong influences of multidecadal modes of variability which are often underrepresented in CMIP5 (Section 3.7.6 and 3.7.7). In addition, while CMIP5 models can capture the domain and precipitation intensity of the global monsoon and its changes found in paleoclimate proxies, biases remain in their regional representations, and they are unsuccessful in quantitatively reproducing changes in paleo reconstructions (*high confidence*). CMIP6 models better reproduce the domain and precipitation intensity of the global monsoon, but with *low confidence* due to *limited evidence*.

[START FIGURE 3.15 HERE]

Figure 3.15: (a-b) Climatological summer-winter range of precipitation rate (scaled by annual mean precipitation rate; shading) and 850 hPa wind velocity (arrows) based on (a) GPCP and ERA5 and (b) MME mean of CMIP6 historical simulations for 1979-2014 (1 member each). Hatched regions are the monsoon domain based on the definition by (Wang and Ding, 2008) (c-d) 20-year running means of (c) summertime precipitation rate averaged over the monsoon regions over land (mm day–1) and (d) the NH summer monsoon circulation index defined as the vertical shear of zonal winds between 850 and 200 hPa levels averaged over 0º-20ºN, 120ºW-120ºE (Wang et al., 2013; m s^{-1}). Summer and winter are defined for individual hemispheres: May through September for NH summer and SH winter, and November through March for NH winter and SH summer. Produced with 40 CMIP6 models (each 1 member).

[END FIGURE 3.15 HERE]

3.3.3.3 Extratropical Jets, Storm Tracks and Blocking

Extratropical jets are wind maxima in the upper troposphere marking zones of baroclinic instability. Anomalies in the position of these jets are often associated with storms, blocking, and weather extremes. Extratropical storms result from such baroclinic instability; they are essential aspects of the equator-to-pole transport of heat that is a characteristic of the Earth's climate. Blocking refers to long-lived, stationary high-pressure systems that are often associated with a poleward displacement of the jet. Section 11.7.2 and chapter 10 discuss these features in more detail.

AR5 concluded that models were able to capture the general characteristics of extratropical cyclones and storm tracks, although it also noted that most models underestimated cyclone intensity, that biases in cyclone frequency were linked to biases in sea surface temperatures, and that resolution can play a significant role in the quality of the simulation of storms. Similarly for blocking, AR5 found with *high confidence* that its simulation was improved due to increases in resolution. AR5 did not specifically assess changes in southern-hemisphere storm track characteristics or blocking.

Since AR5, new research using CMIP5 and CMIP6 models has confirmed that increasing the model resolution usually improves the simulation of cyclones and blocking and seasons (Davini et al., 2017; Davini and D'Andrea, submitted; Priestley et al., submitted; Schiemann et al., 2017; Zappa et al., 2013) and that the model performance with respect to the simulation of cyclones and that of blocking events are correlated

(Zappa et al., 2014), suggesting biases in either are aspects of the same underlying problem in models (Figure 3.16:). In the North Pacific basin the annual-mean blocking frequency is now well simulated compared to earlier evaluations but substantial errors of the blocking frequency remain in the Euro-Atlantic sector (Davini and D'Andrea, 2016; Dunn-Sigouin and Son, 2013; Mitchell et al., 2017; Woollings et al., 2018b; Figure 3.16). While there is a resolution dependence in the size of this bias, even at very high resolution blocking in the Euro-Atlantic sector remains underestimated, and there is evidence of a compensation of errors as the resolution is increased (Schiemann et al., 2017). Davini and D'Andrea (submitted) show that while the simulation of blocking improves with increasing resolution in CMIP3, CMIP5, and CMIP6 models, other model deficiencies are also contributing, particularly to the underestimation of Euro-Atlantic blocking.

Regarding the simulation of storm tracks, for the North Pacific storm track CMIP6 simulations simulations indicate large remaining underestimations of cyclone frequencies during summer (JJA) which for the low-resolution models have essentially remained unchanged versus CMIP5, and only a small resolution dependence of this bias (Priestley et al., submitted). During winter (DJF), both CMIP5 and CMIP6 models tend to place the North Pacific storm track too far equatorward, leading to an overestimation of cyclones between 30 and 40°N in the Pacific and an underestimation to the north of it. Both low- and high-resolution models show this pattern, but low-resolution models generally simulate fewer cyclones throughout the North Pacific (Priestley et al., submitted).

In winter, the North Atlantic storm track remains displaced to the south and east in many models, leading to underestimations of cyclone frequencies near the North American coast and overestimations in the eastern North Atlantic. Higher-resolution CMIP6 models perform slightly better in this regard than low-resolution models. In summer (JJA), cyclone frequencies throughout the extratropical North Atlantic, which were substantially underestimated in CMIP5, have improved in CMIP6 high-resolution models. In low-resolution CMIP6 models, the problem is essentially unchanged (Priestley et al., submitted).

For the Southern Hemisphere (not considered in AR5), (Priestley et al., submitted) find considerable improvements in the placement of the Southern Ocean storm track during summer (DJF) in CMIP6 models versus CMIP5. Relative to CMIP5, both low- and high-resolution CMIP6 models have increased track densities south of about 55°S and decreases between about 40 and 55°S, in better agreement with observations than CMIP5 models. CMIP5 models simulate a storm track that is positioned substantially too far equatorward. This remains the case in CMIP6 high-resolution models, although the degree of misplacement is reduced. In CMIP6 low-resolution models, an opposite bias occurs, with mostly insignificant overestimations of the cyclone track density occurring near the Antarctic coast and underestimations in some lower-latitude regions. In winter (JJA), the biases found in CMIP5 are only slightly improved on in CMIP6, with models continuing to underestimate the broad maximum cyclone track density in the south-eastern Indian Ocean and overestimating the minimum in the south-western South Pacific.

For the Northern Hemisphere, new research since AR5 has found trends in the occurrence of extratropical cyclones. An observed reduction in cyclone activity by about 4% per decade in the Northern Hemisphere in summer (Chang et al., 2016, Chapter 2) may be associated with human-induced warming. Although there is a mechanistic explanation for this effect (mainly decreasing baroclinic instability due to larger warming in the Arctic than at lower latitudes), CMIP5 models generally underestimate this trend (Chang et al., 2016), and there is a general paucity of studies examining this effect. Furthermore, feedback mechanisms associated with clouds may be responsible for substantial inter-model spread (Chang et al., 2016; Voigt and Shaw, 2016). In boreal winter, recent studies have suggested a potential influence of the rapid Arctic warming on observed intensification of Northern Hemisphere storm track activity in the past few decades, while some other studies question this possibility (Cross-chapter Box 10.1).

For the Southern Hemisphere, studies using CMIP5 and other models imply that both ozone depletion and increasing greenhouse gases have caused substantial atmospheric circulation change since the 1960s when concentrations of ozone-depleting substances started to increase (Eyring et al., 2013; Iglesias-Suarez et al., 2016; Karpechko et al., 2018; Son et al., 2018). In particular, ozone depletion, during austral summer, has

been linked to a poleward shift of the westerly jet and Southern-Hemisphere circulation zones and a southward expansion of the tropics (Kang et al., 2011), which is associated with a strengthening trend of the Southern Annular Mode (SAM; Section 3.7.2). This has been well reproduced by climate models with prescribed historical ozone concentration or interactive ozone chemistry (Gerber and Son, 2014; Son et al., 2018; Figure 3.17:). There is limited evidence that ozone depletion has also affected stratospheric and tropospheric variability, especially the frequency, duration, and intensity of SAM anomalies (Dennison et al., 2015). For autumn, a role for SSTs in the tropical Pacific Ocean has been proposed, driving a continuing strengthening of the SAM in summer/autumn despite a levelling-off of ozone depletion (Clem et al., 2017) (Schneider et al., 2015).

There is only one contiguous blocking region in the Southern Hemisphere, with the blocking frequency maximizing in the South Pacific and minimizing in the southern Indian Ocean regions (Parsons et al., 2016). CMIP5 simulations agree relatively well with ERA-Interim in this region regarding the frequency and distribution of blocking events (Parsons et al., 2016). The blocking frequency is anticorrelated with the amplitude of the SAM. Ozone depletion, through stratosphere-troposphere coupling, may have caused an increase in the blocking frequency in the South Atlantic sector (Dennison et al., 2016); this finding requires confirmation using a multi-model approach.

In summary, there is *low confidence* that an observed decrease in the frequency of Northern Hemisphere extratropical cyclones is linked to anthropogenic influence. In the Southern Hemisphere, there is *high confidence* that human influence has contributed to the observed poleward shift of the jet in austral summer, while *confidence* is *low* for human influence on the historical blocking activity. The low confidence statements are due to the limited number of studies available. The shift of the Southern Hemisphere jet is correlated with modulations of the SAM, and justification for the associated high-confidence statement on attribution of changes in the SAM is provided in Section 3.7.2. Models have medium performance in reproducing the extratropical jets, storm track and blocking activity, with increased resolution sometimes corresponding to better performance, but important shortcomings remain, particularly for the Euro-Atlantic sector of the Northern Hemisphere (*high confidence*).

[START FIGURE 3.16 HERE]

Figure 3.16: Instantaneous Northern-Hemisphere blocking frequency (% of days) in the extended northern winter season (DJFM) following the (D'Andrea et al., 1998) definition of blocking, for the years 1961-2000. Reproduced from (Davini and D'Andrea, submitted), their figure 11. Note the good simulation of Pacific blocking but a persistent remaining underestimation of the blocking frequency in the Euro-Atlantic sector. The lower two panels show the results from two HighResMIP models. (Figure produced with ESMValTool v2.0a1.)

[END FIGURE 3.16 HERE]

[START FIGURE 3.17 HERE]

Figure 3.17: Long-term mean (thin black contour) and linear trend (colour) of zonal mean DJF zonal winds for (a) ERA-Interim and (b) CMIP6 over 1979-2014. Only one ensemble member per model is included. (Figure produced with ESMValTool v1.0.)

[END FIGURE 3.17 HERE]

3.3.3.4 Stratospheric Sudden Warming Activity

Sudden stratospheric warmings (SSWs) are stratospheric weather events associated with anomalously high temperatures at high latitudes. Section 2.3.1.4.1 discusses the definition and observational aspects of SSWs.

Seviour et al. (2016), analyzing stratosphere-resolving CMIP5 models, find that models, on average, reproduce the observed frequency of vortex splits (one form of SSWs) but with a wide range of model-specific biases. There is a correlation between the quality of the mean state and the bias in SSW frequency. SSWs are generally associated with SLP anomalies, although the resultant mean anomaly in the models differs substantially from what is found in reanalyses (Seviour et al., 2016). Unlike high-top models, low-top models, which make up more than half of the CMIP5 ensemble, underestimate the frequency of SSWs (Osprey et al., 2013; Kim et al., 2017a).

Some studies find an increase in the frequency of SSWs under increasing GHGs (e.g. Kim et al., 2017a; Schimanke et al., 2013; Young et al., 2013). However, this behaviour is not robust across ensembles of chemistry-climate models (Mitchell et al., 2012; Ayarzagüena et al., 2018). There is an absence of studies specifically focusing on simulated trends in SSWs during recent decades, possibly because large interannual variability would mask any trend. Such an absence of a trend and considerably large variability would be consistent with a recent reconstruction of SSWs extending back to 1850, based on surface observations of the NAO (Domeisen, 2019), although this timeseries does have limitations as it is not based on direct observations of SSWs.

In summary, an anthropogenic influence on the frequency or other aspects of SSWs has not yet been robustly detected. There is *low confidence* in the ability of models to simulate any such trends over the historical period because of large natural interannual variability and also due to common substantial biases in the simulated mean state that impact on the simulated frequency of SSWs.

3.4 Human Influence on the Cryosphere

3.4.1 Sea Ice

3.4.1.1 Arctic Sea Ice

The AR5 concluded that "anthropogenic forcings are *very likely* to have contributed to Arctic sea ice loss since 1979" (Bindoff et al., 2013), based on studies showing that models can reproduce the observed decline only when including anthropogenic forcings and formal attribution studies. Since the beginning of the modern satellite era in 1979, Northern Hemisphere sea ice extent has exhibited significant declines in all months with the largest reduction in September (see Figure 3.18: and Section 2.3.2.1.1 for more details on observed changes). CMIP5 models also simulate Northern Hemisphere sea ice loss over the satellite era but with large differences among models (e.g., Massonnet et al., 2012; Stroeve et al., 2012). The envelope of simulated ice loss across model simulations encompasses the observed change, although observations fall at the low end of the CMIP5 distribution. In contrast, available CMIP6 models on average capture the observed Arctic sea ice decline well, albeit with large inter-model spread (Figure 3.18:). Notz et al. (submitted) found that CMIP6 models better capture the sensitivity of Arctic sea ice area to the global warming. For more information on comparisons with observations, see Section 9.3.1.1. Ivanova et al. (2016) evaluated the regional distribution of sea ice in the CMIP5 models, proposing and evaluating metrics based on the longitudinal distribution of sea ice, to reduce the effects of the compensating errors which may be occuring when evaluating models on the basis of the hemispheric mean sea ice extent (see also Section 9.3.1.1 for details on the physical processes associated with regional changes in Arctic sea ice).

Since AR5, there have been several new detection and attribution studies on Arctic sea ice. Kirchmeier-Young et al. (2017) compared the observed time series of the September sea ice extent (SIE) over the period 1979-2012 with those from different large ensembles (CanEAM2, CESM1, IPSL, and CMIP5) using an optimal fingerprinting technique. They detected anthropogenic signals which were separable from natural forcing due to solar irradiance variations and volcanic aerosol, supporting previous findings (Figure 3.18; Kay et al., 2011; Min et al., 2008; Notz and Marotzke, 2012; Notz and Stroeve, 2016). Using selected CMIP5 models and three independently derived sets of observations, Mueller et al. (2018) detected fingerprints from greenhouse gases, natural, and other anthropogenic forcings simultaneously in the September Arctic SIE over the period 1953-2012. They further showed that about a quarter of the greenhouse gas-induced decrease in SIE has been offset by an increase due to other anthropogenic forcing

(mainly aerosols). Similarly, Gagné et al. (2017a) suggested that the observed increase in Arctic sea ice concentration during 1950-1975 was primarily due to the cooling contribution of anthropogenic aerosols forcing based on single model simulations. Gagné et al. (2017b) identified a detectable increase in Arctic SIE in response to volcanic eruptions using CMIP5 and four observational datasets.

Differences in sea ice loss among the models (Figure 3.18:) have been attributed to a number of factors (see Section 9.3.1.1 for more information on physical processes associated with sea ice loss). These factors include the late 20th century simulated sea ice state (Massonnet et al., 2012), the magnitude of changing ocean heat transport (Mahlstein and Knutti, 2011), and the rate of global warming (e.g., Gregory et al., 2002; Mahlstein and Knutti, 2012; Rosenblum and Eisenman, 2017). Sea ice thermodynamic considerations indicate that the magnitude of sea ice variability and loss depends on ice thickness (Bitz, 2008; Massonnet et al., 2018) and hence the climatology simulated by different models may influence their projections of change. This allows for the possibility of using observational constraints to sub-select models and thereby narrow projection uncertainty (e.g. Knutti et al., 2017; Massonnet et al., 2012; Senftleben et al., 2019) although other studies suggest that this is difficult due to the short observational record (Stroeve and Notz, 2015).

An important consideration in comparing Arctic sea ice loss in models and observations is the role of internal variability. Using ensemble simulations from a single model, Kay et al. (2012) suggested that internal variability could account for about half of the observed September ice loss. More recently, large ensemble simulations have been performed with many more ensemble members (Kay et al., 2015). These enable a more robust characterization of internal variability in the presence of forced anthropogenic change. Using such large ensembles, some studies discussed the influence of internal variability on Arctic sea-ice trends (Swart et al., 2015) and the timing of ice-free summer conditions (Jahn et al., 2016). Song et al., (2016) also compared thre trends in the forced and unforced simulations using multiple climate models and found that the natural internal variability explains no more than 42.3% of the observed September sea ice melting trend, confirming previous studies (Stroeve et al., 2012). Based on the large ensembles of CESM and CanESM, September Arctic sea ice extent variance first increases and then decreases as SIE declines from its pre-industrial value (Kirchmeier-Young et al., 2017; Mueller et al., 2018) consistent with previous work (Goosse et al., 2009), but neither study found a strong sensitivity of detection and attribution results to the change in variability. Further work has indicated that internally-driven summer atmospheric circulation trends with enhanced ridging over the Arctic Ocean play an important role in the observed Arctic sea ice loss (Ding et al., 2017) and a fingerprint analysis using the CESM large ensemble suggests that this internal variability accounts for 40-50% of the observed September ice decline (Ding et al., 2019). Internally-generated decadal-scale tropical variability and associated atmospheric teleconnections have likely contributed to the changing atmospheric circulation in the Arctic and the associated rapid sea ice decline from 2000 to 2014 (Meehl et al., 2018).

Some recent studies evaluated the human contribution to recent record minimum SIE events in the Arctic. Analysing CMIP5 simulations, Zhang and Knutson (2013) found that the observed 2012 record low in September Arctic SIE is inconsistent with internal climate variability alone. Based on several large ensembles, Kirchmeier-Young et al. (2017) concluded that the observed 2012 SIE minimum is extremely unlikely in a scenario excluding human influence. Fučkar et al. (2016) showed that the underlying climate change has contributed to the record low March Arctic SIE in 2015.

Based on the new attribution studies since AR5, we conclude that it is *very likely* that anthropogenic forcings mainly due to greenhouse gas increases have contributed substantially to Arctic sea ice loss since 1979, explaining at least half of the observed decreasing trend in summer sea-ice extent. There is new evidence that increases in anthropogenic aerosols have offset part of the greenhouse-gas-induced Arctic sea ice loss since the 1950s. Despite large differences in the mean sea ice state in the Arctic, Arctic sea ice loss is captured by all CMIP5 models and available CMIP6 models. Nonetheless, large inter-model differences in the Arctic sea ice decline remain, limiting our ability to quantify forced changes and internal variability contributions.

[START FIGURE 3.18 HERE]

Figure 3.18: Climatology (x-axis) and trend (y-axis) in Arctic sea ice extent in September (left) and Antarctic sea ice extent in February (right) for 1979-2014 from CMIP5 (upper) and CMIP6 (lower) models. All individual models (ensemble means) and the multi-model mean values are compared with the observations (HadISST, NSIDC NASA Team, and NSIDC Bootstrap). Solid line indicates a linear regression slope which is statistically significant at 5% level.

[END FIGURE 3.18 HERE]

3.4.1.2 Antarctic Sea Ice

AR5 concluded that "there is *low confidence* in the attribution of the observed increase in Antarctic SIE since 1979" (Bindoff et al., 2013) due to the limited understanding of the external forcing contribution as well as the role of internal variability. Based on a least squares regression, Antarctic sea ice extent has exhibited a small increase in all months over the 1979-2017 period (Figure 3.19:). However, these trends are often not statistically significant and starting in late 2016, anomalously low sea ice has been present (see also Section 2.3.2.1.2). The mean hemispheric sea ice changes result from much larger, but partially compensating, regional changes with increases in the western Ross Sea and Weddell Sea and declines in the Bellingshausen and Amundsen Seas (Hobbs et al., 2016). Observed regional trends have been particularly large in austral fall (see Section 2.3.2.1.2, and also Section 9.3.2.1 for more details of regional changes and related physical processess). Starting in austral spring of 2016 the ice extent decreased strongly (Turner et al., 2017) and has since remained anomalously low (Figure 3.19:). This decrease has been associated with anomalous atmospheric conditions associated with teleconnections from warming in the eastern Indian Ocean and a negative Southern Annular Mode (Chenoli et al., 2017; Stuecker et al., 2017; Schlosser et al., 2018; Meehl et al., 2019; Purich and England, 2019; Wang et al., 2019a). A decadal-scale warming of the near-surface ocean that resulted from strengthened westerlies also contributed to and helped to sustain the sea ice loss (Meehl et al., 2019).

CMIP5 climate models generally simulate ice loss over the satellite era since 1979 (Mahlstein et al., 2013; Turner et al., 2013) in contrast to the observed change, and CMIP6 models also simulate Antarctic ice loss (Roach et al., submitted; Figure 3.19:). A number of studies have suggested that this discrepancy may be in part due to the role of internal variability in the observed change (Mahlstein et al., 2013; Polvani and Smith, 2013; Zunz et al., 2013; Meehl et al., 2016a; Turner et al., 2016), including teleconnections associated with tropical Pacific variability (Meehl et al., 2016a) and changing surface conditions resulting from multi-decadal ocean circulation variations (Singh et al., 2019). However, when the spatial pattern is considered, trends in the summer and autumn (from 1979-2005) appear outside the range of internal variability (Hobbs et al., 2015). This suggests that the models may have an unrealistic simulation of the Antarctic sea ice forced response or internal variability of the system. Discrepancies among the models in simulated sea ice variability (Zunz et al., 2013), the sea ice climatological state (Roach et al., 2018), upper ocean temperature trends (Schneider and Deser, 2018), Southern hemisphere westerly wind jet trends (Purich et al., 2016), or the sea ice response to Southern Annular Mode variations (Ferreira et al., 2014; Holland et al., 2017; Kostov et al., 2017; Landrum et al., 2017) may all play some role in explaining these differences with the observed trends. Increased fresh water fluxes caused by mass loss of the Antarctic ice sheet (either by melting at the front of ice shelves or via iceberg calving) have been suggested as a possible mechanism driving the multidecadal Antarctic sea ice expansion (Bintanja et al., 2015; Pauling et al., 2016). A recent study based on decadal predictability suggests that initializing the state of the Antarctic bottom water cell can reproduce the observed Antarctic sea ice increase (Zhang et al., 2017), consistent with the suggestion that multidecadal variability associated with variations in deep convection has contributed to the observed increase in Antarctic sea ice since 1979 (Latif et al., 2013; Zhang et al., 2017, 2019) (see also Section 3.4.1.2). A comprehensive assessment of these mechanisms using a multi-model ensemble of simulations is still outstanding, and confidence in our understanding of this process remains *low*.

There have been several studies which aimed to identify causes of the observed Antarctic SIE changes.

Gagné et al. (2015) assessed the consistency of observed and simulated changes in Antarctic SIE for an extended period using recovered satellite-based estimates, and found that the observed trends since the mid-1960s are not inconsistent with model simulated trends. Studies based on the satellite period also indicate that the observed trends are largely within the range of simulated internal variability (Hobbs et al., 2016). A few distinct factors that led to the weak signal-to-noise ratio in Antarctic SIE trends have been further identified, which include large multi-decadal variability (Monselesan et al., 2015), the short observational record (e.g., Abram et al., 2013), and the limited model performances at representing the complex Antarctic climate system as discussed above (Bintanja et al., 2013; Uotila et al., 2014).

In conclusion, the multidecadal increase and the subsequent abrupt decrease of Antarctic sea ice extent for 1979-2015 and 2016-2019, respectively, are not generally captured by global climate models, and there is *low confidence* in the attribution of these changes in Antarctic sea-ice extent.

[START FIGURE 3.19 HERE]

Figure 3.19: Seasonal evolution of observed and simulated Arctic (left) and Antarctic (right) sea ice extent (SIE) over 1979–2017. SIE anomalies relative to the 1979–2000 means from observations (OBS from HadISST, NASA Team, and Bootstrap, top) and historical (ALL, middle) and hist-nat (NAT, bottom) simulations from CMIP5 and CMIP6 multi-models. These anomalies were obtained by computing non-overlapping 3-year mean sea ice anomalies for March (February for Antarctic SIE), June, September, and December separately. CMIP5 ALL runs are extended by using RCP4.5 scenario runs after 2005 while CMIP6 ALL runs are extended by using SSP2-4.5 scenario runs after 2014. CMIP5 NAT runs ends in 2012. Number in bracket represents the number of models used. The multi-model mean is obtained by taking the ensemble mean for each model first and then averaging over models. Grey dots indicate multi-model mean anomalies stronger than inter-model spread (beyond ± 1 standard deviation). Units: 10^6 km^2.

[END FIGURE 3.19 HERE]

3.4.2 Snow Cover

Seasonal snow cover is a defining climate feature of the northern continents. Feedbacks linked to snow include the planetary albedo, snow melt and associated hydrological impacts, thermal insulation by snow, and vegetation feedbacks associated with snow. A variety of human activities are impacted by the presence of snow, e.g. transport. It is therefore of considerable interest that climate models correctly represent snow cover. Snow cover is discussd in more detail in Section 9.5.4.

AR5 noted the strong linear correlation between Northern Hemisphere snow cover extent (SCE) and annual-mean surface air temperature in CMIP5 models. It was assessed as *likely* that there had been an anthropogenic contribution to observed reductions in Northern Hemisphere snow cover since 1970. AR5 assessed that CMIP5 models reproduced key features of observed snow cover well, including the seasonal cycle of snow cover over northerly regions of Eurasia and North America, but had more difficulties in more southerly regions with intermittent snow cover. AR5 also found that CMIP5 models underestimate the observed reduction in spring snow cover over this period (see also Brutel-Vuilmet et al., 2013; Thackeray et al., 2016; see Figure 3.20). This behaviour has been linked to how the snow-albedo feedback is represented in models (Thackeray et al., 2018). The CMIP5 multi-model ensemble has been shown to represent the snow-albedo feedback more realistically than CMIP3, although some individual models present in both ensembles have not improved or even got worse (Thackeray et al., 2018). There is still a systematic overestimation of the albedo of boreal forest covered in snow (Li et al., 2016c; Thackeray et al., 2015). Consequently the snow albedo feedback might have been overestimated by CMIP5 models (Xiao et al., 2017). This suggests that processes other than snow albedo might be implicated in the underestimated trend in springtime snow cover. This is dealt with in more detail in Chapter 9.

[START FIGURE 3.20 HERE]

Figure 3.20: Time series of Northern Hemisphere March-April mean snow cover extent (SCE) from observations [OBS: Brown and Robinson (2011), 20CR2, and GLDAS2 data], CMIP5 (upper) and CMIP6 (lower) models' simulations of the response to natural plus anthropogenic forcing (ALL), natural forcing only (NAT), and pre-industrial control simulations (CTL). 5-year mean anomalies are shown for the 1923-2017 period (left) and 1951-2015 period (right) with the *x*-axis representing the centre years of each 5-year mean. CMIP5 ALL simulations are extended by using RCP4.5 scenario simulations after 2005 while CMIP6 ALL simulations are extended by using SSP2-4.5 scenario simulations after 2014. ALL and NAT results are based on ensemble means for each model while CTL results are based on all available non-overlapping segments. Shading indicates the 5-95% range of CMIP5 ALL simulations and min-max range of CMIP6 ALL simulations. Blue dotted lines represent min-max ranges of NAT simulations while green dotted lines indicate 5-95% ranges of CTL simulations. Number in brackets indicate the number of models used. Anomalies are relative to the average over 1971-2000. For models, SCE is restricted to ice-free land (ice-free fraction ≥ 25%). Greenland is excluded from the spatial averages as it contains essentially perennial snow cover. (Updated from Najafi et al. (2016), their Figure 3).

[END FIGURE 3.20 HERE]

Like the CMIP5 models, the CMP6 models capture the negative trend in spring snow cover that has occured in recent decades (Figure 3.20:). Until about 1980, the models produce a generally stable February-March SCE, but after that, produce a substantial decline, reaching a loss of about 2×10^6 km^2 in 2012-2017 relative to the 1971-2000 average. Compared to earlier studies which evaluted trends for 1979-2005 (Brutel-Vuilmet et al., 2013), both CMIP5 and CMIP6 models show improved agreement with the observations by simulating stronger declining trends during recent years.

Several CMIP5-based studies have consistently attributed the observed Northern Hemisphere spring SCE changes (Hori et al., 2017) to anthropogenic influences (Rupp et al., 2013; Najafi et al., 2016), the observed changes being inconsistent with natural variability alone. Similarly, spring snow mass (SWE: Snow Water Equivalent) changes on the scale of the Northern Hemisphere have been attributed to greenhouse gas forcing (Jeong et al., 2017). In the Arctic (Brown et al., 2017), SWE changes are not expected to emerge from noise before the mid-21st century. Using individual forcing simulations from multiple CMIP6 models, Paik and Min (submitted) detected greenhouse gas influence in the observed decrease of early spring SCE during 1925-2019, which was found to be separable from the responses to other forcings.

In summary, it is *very likely* that anthropogenic influence contributed to the observed reductions in Northern Hemisphere springtime snow cover since 1950. There is evidence for some progress in representing the seasonality and geographical distribution of snow cover in CMIP6 in comparison to CMIP5 simulations. Both CMIP5 and CMIP6 models simulate strong declines in spring-time SCE during recent years, in general agreement with observations, causing the multi-model mean decreasing trend in spring-time SCE to now better agree with observations than in earlier evaluations, with anthropogenic signals robustly detected. Evidence has yet to emerge that interactions between vegetation and snow, found problematic in CMIP5, have indeed improved in CMIP6 models (Section 9.5.3). This lack of process understanding means there is *medium confidence* in the simulation of snow cover over the northern continents in CMIP6 model simulations. The models consistently link snow extent to surface-air temperature (Figure 9.24). With surface air warming linked to anthropogenic influences, particularly greenhouse gas increases, this provides additional evidence that reductions in snow cover are also caused by human activities.

3.4.3 Glaciers and Ice Sheets

While Chapter 9 (Sections 9.4 and 9.5) discusses process understanding of glaciers and ice sheets, as well as evaluation of standalone models, our focus here is on the evaluation of glaciers and ice sheets in the context of global climate models, as well as attribution of their large-scale changes. Land surface ice in the form of glaciers has been included in CMIP climate and Earth system models as components of the land sub-models

(LSMs) for many years. However, their representation is simplified and is omitted altogether in the less complex modelling systems. The Antarctic and Greenland ice sheets were absent in global climate models that pre-date CMIP6 (Eyring et al., 2016), however some preliminary analyses that used results from CMIP5 to drive offline models were included in AR5 (Church et al., 2013b). In CMIP3 (Meehl et al., 2007) and CMIP5 (Taylor et al., 2012) land ice area fraction, a component of LSMs, was defined as a time-independent quantity, and in most model configurations was preset at the simulation initialization as a permanent land feature. In CMIP6 considerable progress has been made in improving and evaluating the representation of modelled land ice. For glaciers, an example is the expansion of the Joint UK Land Environment Simulator (JULES) LSM to enable elevated tiles. These more accurately simulate the altitudinal atmospheric affects on glaciers, in addition to enhancing model tiles to simulate a multi-layered snowpack (Shannon et al., 2019a). For ice sheets, for the first time in CMIP, CMIP6 includes a coordinated effort in simulating temporally evolving ice sheets within the Ice Sheet Model Intercomparison Project (ISMIP6, Nowicki et al. (2016)).

Our understanding of aspects of the global water storage contained in the cryosphere (glaciers and ice sheets) and their contribution to sea-level rise (SLR), has improved since AR5 both in models and observations (Huss and Hock, 2015; Bamber et al., 2018; Cazenave et al., 2018; Goelzer et al., 2018; Farinotti et al., 2019; Hock et al., 2019b; Meredith et al., 2019; Shepherd et al., 2019a; Wouters et al., 2019; Zemp et al., 2019) (see also Sections 9.4.1 (Greenland; *virtually certain* mass loss since the 1990s); 9.4.2 (Antarctica; *very likely* mass loss since at least the early 1990s); 9.5.1 (Glaciers; *very high confidence* in global glacier retreat since 1850)). Current knowledge suggests cryospheric contributions to the global SLR budget are 22% from glaciers and 18% from ice sheets for 1971 to 2015 (see Box 9.2).

3.4.3.1 Glaciers

Glaciers are defined as perennial surface land ice masses independent of the Antarctic and Greenland ice sheets. Glaciers occur most often in high latitude cold regions where climate and topographic characteristics allow snow to accumulate over many years. After initially falling on the land surface, snow transforms into firn (snow that persists for more than a year) and finally to ice, which flows and possibly slides downhill under gravitational pull (Section 9.5). AR5 assessed that anthropogenic influence had *likely* contributed to the retreat of glaciers observed since the 1960s (Bindoff et al., 2013), based on a high level of scientific understanding and robust estimates of observed mass loss, internal variability and glacier response to climatic drivers.

The representation of glaciers in climate models is captured by the land sub-component LSMs, and for CMIP6 a small number of LSMs are being used (Shannon et al., 2019). In addition to ongoing glacier and land ice developments in climate and Earth system models participating in CMIP6, independent collaborative research efforts such as GlacierMIP (Hock et al., 2019a; Marzeion et al., submitted) that exist outside of the CMIP project are also underway. The GlacierMIP project aims to systematically compare several preceding modelling efforts. When contrasted to the relative abundance of ice sheet models, only very few models that are capable of modelling glaciers on a global scale have been documented in the literature (e.g. Maussion et al., 2018, 2019; for a review see Radić and Hock (2014)). A key limitation to glacier model evaluation is the poor observed record of global glacier changes prior to the development and release of the Randolf Glacier Inventory (Pfeffer et al., 2014; RGI Consortium, 2017) which led to highly simplified approaches and the extrapolation of results to regions of no data coverage (Hock et al., 2019a).

While direct attribution of glacier changes from the CMIP5 output is not possible, offline simulations forced by a subset of CMIP5 historical simulations have been undertaken. The CMIP5 boundary forcing fields of air temperature and precipitation were used to drive a model that represents all global glaciers outside of Antarctica over the period 1851 to 2010. The conclusion of this work was that 25 ± 35% of the global glacier mass loss was attributable to anthropogenic influence, with this number increasing to 69 ± 24% over the 1991 to 2010 period (Marzeion et al., 2014). A similar more regional study that considered 85 Northern Hemisphere glacier systems also concluded that there is a discernible human influence on glacier mass balance, with CMIP5 historical and greenhouse gas-only simulations showing a glacier reduction, whereas natural-only forced simulations showed a glacier accretion (Hirabayashi et al., 2016). In addition, statistical

assessment of the role of climate change in glacier retreat concludes that observed length changes would not have occurred without anthropogenic climate change (Roe et al., 2017).

In summary, based on new evidence since the AR5, we conclude that the recent observed retreat of global glaciers is *very likely* attributable to anthropogenic influences.

3.4.3.2 Ice Sheets

Ice sheets are defined as a mass of glacial ice that extends over a region covering more than 50,000 km^2. The persistent ice sheets of Antarctica are the largest cryospheric mass store, followed by the ice sheets of Greenland, which combined are two orders of magnitude larger than glaciers, the next largest global reservoir. These structures contain more than 99% of the freshwater (ice) on Earth. Ice sheets play an active role in sea level rise, with the Antarctic and Greenland ice sheets containing 58.3 m and 7.36 m of sea level equivalent (SLE) respectively (Vaughan et al., 2013). AR5 assessed that it is *likely* that anthropogenic forcing contributed to the surface melting of Greenland since 1993, but that there was *low confidence* in attributing the causes of the observed mass of loss from the Antarctic ice sheet since 1993 (Bindoff et al., 2013).

Ice sheet models have been developed in parallel to CMIP, with intercomparison activities extending across multiple decades, including the EISMINT (Huybrechts et al., 1996; Payne et al., 2000; Saito et al., 2006), ISMIP-HOM (Pattyn et al., 2008) and MISMIP (Pattyn et al., 2012) projects and the Sea level Response to Ice Sheet Evolution (SeaRISE) project (Bindschadler et al., 2013; Nowicki et al., 2013). With CMIP6, ice sheet modelling is formally contributing through ISMIP6 (Nowicki et al., 2016), marking the first time that coupled ice-sheet-climate models have been part of the project. It is likely that at least 3 ice-sheet-climate models will be contributing to CMIP6, with PISM coupled to the HTESSEL LSM (Bueler and Brown, 2009; Winkelmann et al., 2011; Balsamo et al., 2015) land model in EC-Earth3-GrIS, CISM (Lipscomb et al., 2013) in the CESM2 and various NorESM2 variants through the CLM LSM, and GRISLI (Boone et al., 2017; Napoly et al., 2017) in CNRM-CM6-1 in the Surfex LSM.

Detection and attribution studies targeting the Antarctic and Greenland ice sheets remain challenging (Kjeldsen et al., 2015). This is in part due to the short observational record (1992-present) (Shepherd et al., 2012, 2018, 2019b; Bamber et al., 2018; Cazenave et al., 2018; Mouginot et al., 2019; Rignot et al., 2019) and the challenges this poses to the evaluation of modelling efforts (Chapter 9.4.1 (Greenland) and 9.4.2 (Antarctica)). The latter require not only dynamic ice sheet models, but also appropriate atmospheric and oceanic conditions to use as a boundary forcing to drive the models (Nowicki and Seroussi, 2018). Since the AR4 and AR5, a new generation of ice sheet models has been developed, with recent improvements and current challenges reviewed for Antarctica (Pattyn et al., 2017) and Greenland (Goelzer et al., 2017). Ice sheet models are being coupled as dynamic components of CMIP-class climate models, such that scenario projections are becoming possible in a coupled framework (Vizcaino et al., 2015) as well as being used for improving our understanding of interactions and feedbacks between ice sheets and the Earth system (Fyke et al., 2018). In parallel to these developments, community efforts leveraging CMIP5 boundary forcing fields with standalone ice sheet models, such as SeaRISE (Bindschadler et al., 2013; Nowicki et al., 2013), laid the foundations for an effort that was more closely aligned with CMIP, resulting in ISMIP6 (Nowicki et al., 2016). However, insufficient new attribution literature has appeared since AR5 to justify updating our attribution assessment for the ice sheets.

Due to the limited attribution literature available since the AR5, our assessment remains that it is *likely* that anthropogenic forcing contributed to the surface melting of Greenland since 1993, but that there is *low confidence* in attributing the causes of the observed mass of loss from the Antarctic ice sheet since 1993.

3.5 Human Influence on the Ocean

The global ocean plays an important role in the climate system, as it is responsible for transporting and storing large amounts of heat (Section 3.5.1), freshwater (Section 3.5.2) and carbon (Section 3.6.2) that are exchanged with the atmosphere. Therefore, accurate ocean simulation in climate models is essential for skilful representation of the climatic response to anthropogenic warming, including the rate of warming, sea level rise and the representation of coupled modes of climate variability. Since AR5 (Flato et al., 2013; Rhein et al., 2013) ocean model development has advanced considerably, and a move toward more systematic evaluation, facilitated by the Coordinated Ocean-Ice Reference Experiments (COREs) (Griffies et al., 2009) have expanded ocean multi-model assessment. With the application of the CORE-II interannual forcing protocol (1948-2007), studies have focused on model intercomparison for sea level (Griffies et al., 2014), the North Atlantic mean state, meridional overturning and their variability (Danabasoglu et al., 2014, 2016), the Southern Ocean water mass structure, Antarctic Circumpolar Current (ACC) and meridional overturning (Downes et al., 2015; Farneti et al., 2015), North and equatorial Pacific Ocean circulation (Tseng et al., 2016), the Arctic Ocean, sea ice and freshwater (Ilicak et al., 2016; Wang et al., 2016b, 2016a), and the Indian Ocean's mean state and seasonal cycle (Rahaman et al., 2020).

With CMIP6, the importance of ocean modelling is highlighted by the inclusion of the Ocean Model Intercomparison Project (OMIP) as a CMIP6-Endorsed MIP (Griffies et al., 2016; Tsujino et al., submitted). Ongoing model developments since AR5 have focused on improving the realism of the simulated ocean in coupled models, with horizontal nominal resolutions increasing to 25 - 100 km (from about 200 km in CMIP5), and increased vertical resolutions in some modelling systems of up to 1 m near-surface levels (from the highest resolution 10 m in CMIP5) aimed at improving representation of the diurnal cycle coupling to the atmosphere (e.g. Bernie et al. 2005, 2007, 2008). A recent comparison using a hierarchy of GFDL ocean models with horizontal resolutions representing the CMIP5 contribution (nominal 1°) down to an eddy-permitting (0.1°), showed that the highest resolution model was able to recover the spatial distribution and variability magnitude in sea surface height when compared to the satellite based AVISO measurements, considerably improving upon the coarse resolution simulation (Griffies et al., 2015). General improvements to simulated ocean fidelity with increasing resolution is an expectation for all ocean modelling systems (Hewitt et al., 2017) and significant progress has been made in the ocean-only OMIP-2 eddy-resolving (~10 km) simulations, however inter-model differences remain (Chassignet et al., submitted).

When evaluating simulated ocean fields, it is useful to consider available observational products, and their representativeness when compared to a 1-degree horizontal, 5 m vertical, and monthly-mean temporal resolution CMIP simulation. Measurement representativeness error has been a consideration of the data assimilation community for many years, first for the atmosphere (Daley, 1993; Janjić and Cohn, 2006) and more recently for the ocean (Oke and Sakov, 2008; Storto and Masina, 2017; Janjić et al., 2018). Many observed ocean surface properties such as sea surface temperature (SST) and sea surface salinity (SSS) are based on remotely sensed satellite retrievals reflecting swath passes of the surface ocean skin properties (top cm), achieving global measurement coverage over a 7-day or similar time period. The swath measurements are composited to provide weekly or monthly maps, with the resulting observational products representing the surface layer (top centimetres), much shallower than a typical simulated ocean model top layer (0 to 10 m), but with comparable horizontal resolution of approximately 100 km. In the case of in-situ observations, additional complexities arise, as ocean profiles are point source measurements, which are often treated in composite observational analyses as representative of larger temporal and spatial scales. For instance, gridded products developed from Argo float profiles (Roemmich et al., 2019) aim to reproduce monthly mean maps of the upper 2000 m ocean state, often representative of 1-degree spatial resolution, whereas Argo floats provide a point source measurement in space and time, which may be influenced by ocean eddies, or fronts and other observed features that are present at very high temporal and spatial scales in the real world. Consequently, an Argo profile is not truly representative of a 1-degree grid cell and thus consideration must be made when contrasting gridded observational products which include such influences and model simulations, as such features are not explicitly resolved by the resolution of a typical CMIP-class model. Numerous techniques exist to map ocean circulation from measurements of ocean density (Bryden et al., 2005), gravity (Wahr et al., 2002), and surface wind and sea level measurements (Bonjean and Lagerloef, 2002). However, direct measurements of ocean circulation are sparse relative to other ocean variables. This

temporal and spatial scale mismatch of the observed, relative to the modelled ocean adds a level of complexity when attempting to relate the variable frequencies of observed point measurements from in-situ and remote platforms, to those of CMIP-class models which most often are assessed using grid-box averaged fields and regular, most often monthly output frequencies.

In this section we assess the broad- or basin-scale properties of the simulated ocean, with a focus on evaluation of the modelled realism in ocean properties, and the detection and attribution of a human-induced signal in changes to observed and simulated ocean properties over the period of observational coverage. Observed changes to ocean temperature (Section 2.3.3.1), salinity (Section 2.3.3.2), sea level (Section 2.3.3.3) and ocean circulation (Section 2.3.3.4) are reported in Chapter 2. A more process-based understanding of the changes reported here, alongside the assessment of variability and changes of ocean properties with spatial scales smaller than ocean basin scales, are presented in Chapter 9 (ocean temperature and salinity Section 9.2.2, ocean circulation Section 9.2.3 and sea level in Sections 9.2.4 and 9.6). Discussion of extreme events with ocean relevance are captured in Chapter 9 (Marine heatwaves Cross-Chapter Box 9.1) and Chapter 11 (the role of SST extremes).

3.5.1 Ocean Temperature

Ocean temperature and heat content are key physical variables considered for climate model evaluation and are the primary indicators of a changing ocean climate. This section assesses the performance of climate models in representing the mean state ocean temperature and heat content (Section 3.5.1.1), with a particular focus on the tropical oceans given the importance of air-sea coupling in these areas (Section 3.5.1.2). Simulations are evaluated with respect to available observational data. These are followed by an assessment of detection and attribution studies of changes in ocean temperature and heat content (Section 3.5.1.3). Changes in global surface temperature are assessed in Section 3.3.1.1.

3.5.1.1 Sea Surface and Zonal Mean Ocean Temperature Evaluation

In CMIP3 and CMIP5 models, large SST biases are found in the mid and high latitudes with marginal improvement in some of the CMIP5 models (Flato et al., 2013). In CMIP6, the Northern Hemisphere mid-latitude surface temperature biases appear to be marginally improved in the multi-model mean in contrast to CMIP5, despite large biases in a few models (Figure 3.21:, Figure 3.24: a,c). The inter-model standard deviation of the zonal mean SST error has decreased south of 50°N, relative to CMIP5 (Figure 3.24: c). On the other hand, the Southern Oceans warm surface temperature bias remains (Figure 3.21:a; Beadling et al., submitted), and is potentially larger in CMIP6 than in CMIP5 models (Figure 3.21:, Figure 3.24: a,c). Several other large biases appear to remain largely unchanged in CMIP6: i) in the equatorial regions, large warm biases remain along the eastern continental boundary of the tropical Atlantic and Pacific Oceans (Figure 3.21:a); and ii) large warm and cold biases remain in the Northern Hemisphere western boundary current regions of the Atlantic and Pacific Oceans (Figure 3.21:a).

In CMIP5, the multi-model mean zonally averaged ocean temperature shows warm biases between 200 m and 2000 m over most latitudes, whereas cold biases are simulated in the deep ocean (>2000 m) and near the surface. In CMIP6 the multi-model mean zonally averaged ocean temperature shows biases that are broadly consistent with those reported in CMIP5 for the near surface (<200 m) and mid-depth (between 200 and 2000 m). However, there are also several prominent differences, the mid-depth warm bias that occurred north of ~55°S have increased in CMIP6 relative to CMIP5, and the Southern Ocean mid-depth which displayed a cold bias in CMIP5 shows a warm bias in CMIP6 (Figure 3.22:a). Focusing on the deep ocean (>2000 m), CMIP6 models show a prominent warm bias (Figure 3.22:a), which contrasts to a cold bias reported in CMIP5 (Flato et al., 2013). While we note that an updated observational temperature dataset is being used in this assessment (WOA09 in AR5 to WOA18 in AR6), the deep ocean warm bias remains and is approaching double the magnitude (~0.5°C) of the equivalent CMIP5 multi-model ensemble mean. Assessing CMIP6 basin zonal mean biases allows a more effective analysis of the source basin(s) for the temperature biases (Figure 3.22:c,e,g). The warm temperature bias initiates between 200 and 400 m depth in

all three basins, however, is most prominent in the Atlantic Ocean at most depths and latitudes. Exceptions to this are the prominent warming of the extratropical Pacific region between the observed 5°C and 10°C isotherms, and the tropical Indian Ocean between 200 and 400 m depth. The cool near surface tropical bias is most prominent in the Pacific Ocean, however similar features are also present in the Atlantic (Figure 3.22:c,e,g).

Since AR5, there has been growing evidence on the improved representation of surface and deeper ocean mean temperature, by increasing the horizontal resolution both in the ocean and the atmosphere in coupled climate models (e.g. Small et al., 2014; Hewitt et al., 2016; Iovino et al., 2016; Roberts et al., 2019). High resolution ocean model components are shown to lead to an overall decrease in the surface temperature biases in some locations (e.g., Roberts et al., 2019a). Decreased biases are most prevalent over the central and western equatorial Pacific, as well as in the equatorial Atlantic (Figure 3.21:b; Haarsma et al., 2016), however the overall spread is larger than that of the CMIP6 models (Figure 3.24:c,d). Increasing model resolution also improves the simulation of eddy activity, thus, increases in the vertical eddy transport, and reduces the temperature drifts in the deeper ocean (Griffies et al., 2015; von Storch et al., 2016)**.** On the other hand, the zonal mean SST from the high resolution simulations does not differ from that of the standard resolution CMIP6 simulations except in the Southern Ocean (Figure 3.24:c).

[START FIGURE 3.21 HERE]

Figure 3.21: Multi-model mean bias of (a) sea surface temperature (°C) and (b) surface salinity as the difference between the CMIP6 multi-model mean constructed with one realization of CMIP6 historical experiments and the climatology from the World Ocean Atlas 2013 for the period 1995–2014. (Figure produced with ESMValTool v2.0.0b3.)

[END FIGURE 3.21 HERE]

[START FIGURE 3.22 HERE]

Figure 3.22: (a,c,e,g) Potential temperature (degrees C) and (b,d,f,h) salinity (PSS-78) for each of the ocean basins, global (GLO; a,b), Atlantic (ATL; c,d), Pacific (PAC; e,f) and Indian (IND; g,h). Shown in colour are the time-mean differences between the CMIP6 historical ensemble climatological mean and observations, zonally averaged for each basin (excluding marginal and regional seas). The observed climatological values are obtained from the World Ocean Atlas 2018 (WOA18; Prepared by the Ocean Climate Laboratory, National Oceanographic Data Center, Silver Spring, MD, USA), and are shown as labelled black contours for each of the basins. White contours show regions in potential temperature (left column) where the differences exceed positive or negative 1, 2, or 3 (degrees C), and regions in salinity (right column) where the differences exceed positive or negative 0.25, 0.5, 0.75 or 1 (PSS-78). The simulated annual mean climatologies are obtained for 1984 to 2014 from available CMIP6 historical simulations, whereas WOA18 synthesizes observed data from 1874 to 2018 in calculations of the decadally averaged annual mean; however, the median time for gridded observations most closely resembles the more modern era. Multiple realizations from individual models are first averaged to form a single model ensemble climatology, before construction of the CMIP6 multi-model mean from these fields. A total of 20 available CMIP6 models have contributed to the temperature panels (left column) and 21 models to the salinity panels (right column).

[END FIGURE 3.22 HERE]

[START FIGURE 3.23 HERE]

Figure 3.23: Time series of simulated and observed global ocean heat content anomalies (with respect to 1971). CMIP5 historical simulations and observations for both the upper 700 m of the ocean (a) as well as for the total ocean heat content (b). The 0 to 700 m and total heat content observational estimates (thick lines) are respectively described in AR5 Figure 3.2 and AR5 Box 3.1, Figure 1. Simulation drift has been

removed from all CMIP5 runs with a contemporaneous portion of the quadratic fit to each corresponding pre-industrial control run (Gleckler et al., 2012). Units are 10^{22} Joules.

[END FIGURE 3.23 HERE]

3.5.1.2 Tropical Sea Surface Temperature Evaluation

Tropical Pacific Ocean

In CMIP5, mean state biases in the tropical Pacific Ocean including the excessive equatorial cold tongue, erroneous mean thermocline depth and slope along the equator were improved relative to CMIP3, but still remained. Misrepresentation of the interaction between the atmosphere and ocean via the Bjerknes feedback, vertical mixing parameterization, and a bias in winds were among the suggested reasons for the persistent biases (Li et al., 2014; Zhu and Zhang, 2018). Moving to CMIP6, a clear reduction of the cold bias in the equatorial cold tongue has been reported (Grose et al., submitted; Planton et al., submitted), however, this bias reduction is not statistically significant when considered across the entire multi-model ensemble (Planton et al., submitted). It is also noteworthy that the longitude of the 28°C isotherm is closer to observed in CMIP6 than in CMIP5, with a coincident reduction in the CMIP6 inter-model standard deviation (Grose et al., submitted) (Figure 3.24:b,d). This latter result implies that there is an improvement in the representation of the tropical Pacific mean state in CMIP6 models.

The CMIP6 HighResMIP multi-model mean shows further reduction of the cold bias in the equatorial cold tongue (Roberts et al., 2018, 2019a). The significance of the improvements is currently not known as the model spread remains large (Figure 3.24:b,d), model diversity is limited, and the observed and model comparison periods are different (Bock et al., submitted).

Tropical Atlantic Ocean

Fundamental features such as the mean zonal SST gradient in the tropical Atlantic are not reproduced in CMIP5 (see Figure 3.24:). Studies have proposed that weaker than observed alongshore winds, underestimation of stratocumulus clouds, coarse model resolution, and insufficient oceanic cooling due to a deeper thermocline depth and too weak vertical velocities at the base of the mixed layers in the eastern basin, underpin these tropical Atlantic SST gradient biases (Hourdin et al., 2015; Richter, 2015). These SST gradient biases still remain in CMIP6, on average the cold bias in the western part of the basin is reduced while the warm bias in the eastern part has increased (Figure 3.24:b,d; Richter and Tokinaga, submitted). Several CMIP6 models, however, display large reductions in biases of the zonal SST gradient, such that the eastern equatorial Atlantic warm SST and westerly wind biases are mostly eliminated in these models (Richter and Tokinaga, submitted). The high resolution (HighResMIP) CMIP6 models appear to show a better representation of the zonal SST gradient (Figure 3.24:b,d), but some lower resolution models also perform well suggesting that the resolution is not the only factor for bias reduction in Tropical Atlantic (Richter and Tokinaga, submitted).

Tropical Indian Ocean

The tropical Indian Ocean mean state appears to be reasonably well simulated both in CMIP5 and CMIP6 (see Figure 3.24:b,d). However, CMIP5 models show a large spread in the thermocline depth, particularly in the equatorial part of the basin (Saji et al., 2006; Fathrio et al., 2017a), which have been linked to the parameterization of the vertical mixing and the wind structure, which then lead to a misrepresentation of the ventilation process (Schott et al., 2009; Richter, 2015; Shikha and Valsala, 2018). A common problem with the CMIP5 models is therefore a warm bias in the subsurface, mainly at depths around the thermocline.

In the CMIP6 multi-model mean, the western tropical Indian Ocean shows a slightly warmer bias compared to CMIP5 (see Figure 3.24:b,d; Grose et al., submitted). Similarly, for HighResMIP, the bias does not differ significantly from that of the lower resolution models. However, the inter-model standard deviation is large over the Indian Ocean basin and so any improvement due to increased horizontal resolution is not significant across the model ensemble.

In summary, for the purposes of evaluating basin-scale properties, the CMIP5 and CMIP6 models are appropriate tools for investigating ocean temperature and OHC responses to forcing. In each successive phase of CMIP (CMIP3, CMIP5 and CMIP6) the fidelity of ocean temperature simulation has improved, and near-surface and subsurface biases have reduced. This provides some confidence in the utility of CMIP-class models for detection and attribution studies, for both OHC and thermosteric sea level applications (Section 3.5.3).

[START FIGURE 3.24 HERE]

Figure 3.24: (a) Zonally averaged sea surface temperature (SST) error in CMIP6 models. (b) Equatorial SST error in CMIP6 models. (c) Zonally averaged multi-model mean SST error for CMIP6 (green curve), CMIP5 (red curve) and HighresMIP (purple curve), together with inter-model standard deviation (shading). (d) Equatorial multi-model mean SST in CMIP6 (green curve), CMIP5 (red curve) and HighresMIP (purple curve) together with inter-model standard deviation (shading) and observations (black). Model climatologies are derived from the 1979-1999 mean of the historical simulations. The Hadley Centre Sea Ice and Sea Surface Temperature (HadISST) (Rayner et al., 2003) observational climatology for 1979-1999 is used as the reference for the error calculation in (a), (b) and (c); and for observations in (d).

[END FIGURE 3.24 HERE]

3.5.1.3 Ocean Heat Content Change Attribution

Observed OHC changes are discussed in Section 2.3.3.1, where it is reported that it is *virtually certain* that the global upper ocean (0-700 m) and *very likely* that the global intermediate ocean (700-2000 m) warmed substantially between 1971 to present. Further, ocean layer warming contributions are reported as approximately 64% (0 – 700 m), 27% (700 – 2000 m) and 9% (2000 – 6000 m) for the 1971 to 2018 period (Box 7.2). CMIP5 model simulations replicate this partitioning fairly well for the industrial-era (1865 to 2017) throughout the upper (0 – 700 m, 65%), intermediate (700 – 2000 m, 20%) and deep (>2000 m, 15%) layers (Figure 3.25:a; Durack et al., 2018; Gleckler et al., 2016). The spatial distribution of these changes for different ocean depths are assessed in Section 9.2.2.

Overall, CMIP5 and observational estimates show an increase in OHC over time (see Figure 3.23:) (Flato et al., 2013). The AR5 concluded that anthropogenic forcing has *very likely* made a substantial contribution to upper ocean warming. Below 700 m, limited measurements restricted the assessment of OHC changes in AR5 and prevented a robust comparison between observations and models.

The recent increase in ocean sampling by Argo to 2000 m (Roemmich et al., 2015; Riser et al., 2016; von Schuckmann et al., 2016) and the resulting improvements in the recent estimates of ocean heat content (Balmaseda et al., 2013; Durack et al., 2014a; Cheng et al., 2017) allow a more quantitative assessment of the global OHC changes to extend into the intermediate ocean (700 to 2000 m) over the more recent period (from 2005 to the present) (Durack et al., 2018). SROCC assessed that it is *virtually certain* that both the upper and intermediate ocean warmed from 2004 to 2016, with an increased rate of warming since 1993 (Bindoff et al., 2019). The reported long-term OHC increase is further supported by a recent independent study that focuses on the well sampled Argo period (2006 to 2017) and uses a new method to partition OHC change into the addition of excess heat versus heat redistribution for the global ocean. A robust globally consistent warming is reported, with increased magnitude in the Atlantic and western subtropical Indian and Pacific Oceans contrasted to the global mean (Zika et al., submitted). In addition, the observed upper OHC continued to increase through the so called “hiatus” period (Nieves et al., 2015; Liu et al., 2016b), which highlights that the “hiatus” was a pause in global surface warming only (Cross-Chapter Box 3.1:).

The multi-model mean of both CMIP5 and CMIP6 historical simulations forced with time varying natural and anthropogenic forcing shows robust increases in OHC in the upper (0 – 700 m) and intermediate (700 – 2000 m) ocean (*high confidence*) (Figure 3.25:) (Bilbao et al., 2019; Cheng et al., 2016, 2019; Garry et al., submitted; Gleckler et al., 2016; Tokarska et al., 2019), with temporary surface and subsurface cooling

during large volcanic eruptions (e.g. Balmaseda et al., 2013), which are also captured in the upper-ocean, and global mean OHC (Figure 3.25:). Simulated OHC changes are consistent with the updated observational analyses and improved estimates of OHC over the period of 1960 to 2018 (Domingues et al., 2008; Ishii and Kimoto, 2009; Purkey and Johnson, 2010; Roemmich et al., 2012, 2015; Cheng et al., 2017) (also see Section 2.3.3). In addition, deep observed estimates (2000 – 6000 m), also share remarkable similarity to the rate of coincident simulated changes. The rate of ocean heat uptake, both in the observed estimates and simulations, has doubled in the past few decades (Figure 3.25:), with over a third of the accumulated heat stored below 700 m (Cheng et al., 2016, 2019; Gleckler et al., 2016; Durack et al., 2018). The Southern Ocean shows the strongest ocean heat uptake that penetrates to deeper layers, whereas OHC increase in the Pacific and Indian Oceans occur in the upper layers (Bilbao et al., 2019; Garry et al., submitted). This provides further evidence that a robust increase in OHC has occurred over the observed record (*high confidence*), and globally averaged, this warming has extended into the deep ocean (*medium confidence*).

With newly developed methods for OHC estimation (Gebbie and Huybers, 2019; Zanna et al., 2019), observational reconstructions have been generated to replicate the model-based historical period (1850-2014). The agreement between the new OHC observational reconstructions and simulations further confirms that there is *high confidence* that the upper and intermediate (0 to 2000 m) OHC has increased since 1960 and there is *medium confidence* that the deep ocean OHC (below 2000 m) has increased since 1992. Further, due to the enhanced ocean observing network since 2005, there is *high confidence* that ocean heat uptake has been accelerating in the past two decades.

Since AR5, the attribution of OHC increase to anthropogenic forcings has been supported by more evidence from independent detection and attribution studies. By separating natural and anthropogenic forcings in the CMIP5 multi-model mean, it is shown that contributions from natural forcings alone cannot explain the observed changes in OHC both in upper and intermediate ocean layers (Gleckler et al., 2016; Bilbao et al., 2019; Tokarska et al., 2019).

Recently, new studies have focused on separating the importance of different anthropogenic forcings (aerosols, ozone, greenhouse gases) to ocean warming. Overall, the global OHC changes have been attributed to greenhouse gases alone, and the warming signal in the greenhouse gas forcing experiments is shown to penetrate deeper in the North Atlantic than other basins (Tokarska et al., 2019). More evidence from other independent studies show that the Indo-Pacific Warm Pool warming and expansion are dominantly caused by greenhouse gas forcing, with natural fluctuations only having a small effect (Weller et al., 2016), whereas, temperature changes in the Southern Ocean are attributed to both greenhouse gas emissions and ozone depletion (Swart et al., 2018).

In summary, there is strong evidence and understanding on the increase in global OHC. It is *extremely likely* that anthropogenic forcing has made a substantial contribution to the OHC increase over the historical period that extends into the deeper ocean (*high confidence*). Updated observations, like model simulations, show that warming extends throughout the entire water column (*high confidence*).

[START FIGURE 3.25 HERE]

Figure 3.25: (a) Ocean heat uptake (percentage of total 1865-2017 change) for the CMIP5 multi-model mean layers. The three shaded wedges are combined similarly to the AR5 change in global inventory (Rhein et al. (2013); Box 3.1, Figure 1). The thick vertical grey bar represents a +/- one standard deviation spread from the CMIP5 simulations about the year (1999) at which the multi-model heat uptake reaches 50% of the net (1865-2017) industrial-era increase, and the thick horizontal grey bar indicates the CMIP5 +/- one standard deviation spread om the year at which 50% of the total accumulated heat is reached. Black (forcing included) and grey (forcing not included) triangles represent major twentieth- and twenty-first-century volcanic eruptions with magnitude (volcanic explosivity index [VEI] represented by symbol size. (b) The inset box displays the upper and intermediate layer warming for the years 1998 to 2017, with an adjustment for the 0 to 2000 m total warming by -0.19 W m^{-2}, the estimated discrepancy between CMIP5 modelled and the observed volcanic forcing (Ridley et al., 2014). When observed 0 to 2000 m ocean warming is compared across five independent available estimates these rates of change are approximately

equal. (Figure from Durack et al., 2018, their Figure 2).

[END FIGURE 3.25 HERE]

3.5.2 Ocean Salinity

While ocean assessments have primarily focused on temperature changes due to poor measurement coverage of other oceanic variables, improving observational salinity products since the early 2000s has led to a recent increase in the assessment of long-term ocean salinity change and variability from AR4 (Bindoff et al., 2007) to AR5 across both models and observations (Flato et al., 2013; Rhein et al., 2013). AR5 assessed that it was *very likely* that anthropogenic forcings have made a discernible contribution to surface and subsurface oceanic salinity changes since the 1960s. SROCC augmented these insights, noting that observed high latitude freshening and warming have very likely made the surface ocean less dense with stratification increase of between 2.18 and 2.42% from 1970 to 2017 (Bindoff et al., 2019). A recent observational analysis has expanded on these assessments, suggesting a very marked summertime density contrast enhancement across the mixed layer base of 7.4 to 13.9% per decade, driven by changes to tempeature and salinity, which is an order of magnitude larger than previous estimates (Sallée et al., submitted). An idealised ocean modelling study suggests that the enhanced stratification can account for a third of the salinity enhancement signal since 1990 (Zika et al., 2018). Thus, there has been an expansion of observed broad- and basin-scale salinity changes assessment literature since AR5, with many new studies reproducing the key patterns of long-term salinity change reported in AR5 (Rhein et al., 2013), and linking these through modelling studies to coincident changes to evaporation-precipitation patterns at the ocean surface (Sections 2.3.1, 3.3.2).

Unlike SSTs, simulated sea surface salinity (SSS) does not provide a direct feedback to the atmosphere. While a direct feedback is not simulated, some recent work has identified indirect radiative feedbacks through sea-salt aerosol interactions (Ayash et al., 2008; Amiri-Farahani et al., 2019; Wang et al., 2019b) and these have been found to have an effect of strengthening tropical cyclones and hurricanes and increasing precipitation (Balaguru et al., 2012, 2016; Grodsky et al., 2012; Reul et al., 2014; Jiang et al., 2019). The absence of a direct feedback is one of the primary reasons why salinity simulation is difficult to constrain in ocean modelling systems, and why deviations from the observed near-surface salinity mean state between models and observations are often apparent (Durack et al., 2012; Shi et al., 2017).

Due to the recent availability of a number of surface salinity satellite products (SMOS, Aquarius and SMAP) (Berger et al., 2002; Lagerloef et al., 2008; Tang et al., 2017), recent modelling studies have been investigating the role of surface salinity in the diurnal cycle and atmosphere-ocean coupling (Fine et al., 2015; Large and Caron, 2015; Song et al., 2015; Bellenger et al., 2017). Following dedicated observational campaigns (see Chapter 1), modelling studies have also started investigating the processes that maintain the high mean salinity regime in the North Atlantic in a global ocean model (Qu et al., 2011, 2013; Bryan and Bachman, 2015), in addition to more idealized studies that were focused on the role of land-ocean geometries in setting the salinity mean state in the global ocean (Nilsson et al., 2013; Ferreira and Marshall, 2015).

3.5.2.1 Sea Surface and Depth-profile Salinity Evaluation

When compared to the assessment of simulated SST, simulated SSS has not been systematically investigated at global- to basin-scales. For CMIP3, there was reasonable agreement between the basin-scale patterns of salinity, with a comparatively fresher Pacific when contrasted to the salty Atlantic, and basin salinity maxima features aligning well with the corresponding evaporation-precipitation field (Durack et al., 2012). Similar features are also reproduced in CMIP5 along with realistic variability in the upper layers, but less than observations at 300 m and deeper, especially in the poorly sampled Antarctic region (Pierce et al., 2012). In a regional study, only considering the Indian Ocean, CMIP5 SSS was assessed and it was shown that model biases were primarily linked to biases in the precipitation field, with ocean circulation biases

playing a secondary role (Fathrio et al., 2017b).

For the first time in AR5, alongside global zonal mean temperature, global zonal mean salinity through depth was assessed for the CMIP5 models. This showed a strong upper ocean (< 300 m) negative fresh bias of order 0.3 PSS-78, with a tendency toward a positive salty bias (< 0.25 PSS-78) in the Northern Hemisphere intermediate layers (200 to 2000 m) (Flato et al., 2013). These biases are also present in CMIP6, albeit with slightly smaller magnitudes (Figure 3.22:b). Here we expand the global zonal mean bias assessment to consider the three independent ocean basins individually, which allows for an assessment as to which biases and which basin features are dominating the global zonal mean. The basin with the most pronounced biases is the Atlantic which shares the strong upper ocean (<300 m) fresh bias, of order 0.3 PSS-78 just like the global zonal mean, but shows a marked subsurface salinity bias that exceeds 0.5 PSS-78 in equatorial waters between 300 – 500 m. Like the global mean, the high latitude Atlantic >60°N/S expresses a surface enhanced fresh bias, which has a much larger magnitude (~1 PSS-78) in the high northern region (Figure 3.22:d). The Pacific Ocean shares the strongest similarity to the global bias, with a similar upper ocean (<300 m) fresh bias, of a smaller magnitude than the Atlantic, except for a strong off-equator feature associated with the subtropical salinity maximum subsiding at 30°S. Lower magnitude positive salinity biases (~ 0.3 PSS-78) are present in both hemispheres between 100 and 2500 m, deeper in the Southern Hemisphere (Figure 3.22:f). The Indian Ocean shows similar features to the Southern Hemisphere Pacific, with a marked upper ocean (< 500 m) fresh bias of order 0.3 PSS-78, and a strong near-surface positive bias of order 0.4 PSS-78 (Figure 3.22:h). For the Southern Ocean in CMIP5, considerable fresh biases exist through the water column, and are most pronounced in the ventilated layers representing the subtropical, mode and intermediate water masses (Sallée et al., 2013b) and these features are reproduced, with a slightly larger magnitude in CMIP6 (Figure 3.22:b,d,f,h). The structure of the biases in CMIP6 multi-model mean (which averages across many simulations with differing subsurface geographies) strongly reflect the same biases evident in the CMIP5 multi-model mean, but with slightly smaller magnitudes. It must be noted that assessing each simulation field independently yields a subsurface salinity structure and salinity minima subduction pathways that approximate observations, albeit with large regional differences expressed across models that contributed to CMIP5 (Sallée et al., 2013b, 2013a).

In summary, in each successive phase of CMIP (CMIP3, CMIP5 and CMIP6) the fidelity of ocean salinity simulation has improved, and near-surface and subsurface biases have been reduced. This provides confidence in the utility of CMIP-class models for detection and attribution of ocean salinity studies.

3.5.2.2 Salinity Change Attribution

AR5 (Bindoff et al., 2013; Rhein et al., 2013) concluded that it was *very likely* that anthropogenic forcings had made a discernible contribution to surface and subsurface ocean salinity changes since the 1950s and 1960s. They highlighted that the spatial patterns of salinity trends, along with the mean fields of salinity and evaporation-precipitation (E-P) are all similar, with an enhancement to Atlantic Ocean salinity, and freshening in the Pacific and Southern Oceans. Since AR5 all subsequent work focused on assessing observed and modelled salinity changes has confirmed these results.

Considerable changes to observed broad- or basin-scale ocean near-surface salinity fields have been reported (see Section 2.3.3.2), and these have been linked to changes in the evaporation-precipitation patterns at the ocean surface through model simulations, expressing a pattern of change where climatological mean fresh regions become fresher and corresponding salty regions becoming saltier (Durack et al., 2012, 2013; Lago et al., 2015; Skliris et al., 2016; Zika et al., 2015, 2018; Figure 3.26:). The depth-integrated effect of mean salinity changes as captured in halosteric sea level for the top 0 to 2000 m has also been assessed, and these results mirror near-surface patterns (Durack et al., 2014b; Figure 3.27:). Further investigations using observations and models together have tied the long-term patterns of surface and subsurface salinity changes to coincident changes to the evaporation-precipitation field over the ocean (Durack et al., 2012, 2013; Durack, 2015; Lago et al., 2015b; Levang and Schmitt, 2015; Zika et al., 2015, 2018; Grist et al., 2016), however the rate of these changes through time continues to be an active area of active research (Sallée et al., submitted; Skliris et al., 2014, 2016, Zika et al., 2015, 2018).

Climate change detection and attribution assessments have considered salinity, with the first of these assessed in AR5 (Bindoff et al., 2013). Since this time, the positive detection conclusions (Stott et al., 2008; e.g., Pierce et al., 2012; Terray et al., 2012) have been supported by a number of more recent and independent assessments which have replicated the multi-decadal basin-scale patterns of change in observations and models (Figure 3.26:; Durack, 2015; Durack et al., 2014b; Levang and Schmitt, 2015; Skliris et al., 2016). Depth-integrated basin responses, contrasting the Pacific and Atlantic basins (freshening Pacific and enhanced salinity Atlantic) were also shown to be replicated in all historical (natural and anthropogenic) simulations, with this basin contrast absent in CMIP5 natural only simulations that excluded the greenhouse gas forcing (Durack et al., 2014b; Figure 3.27:).

While observational sparsity considerably limits quantifying all regional changes, a recent study by Friedman et al. (2017) assessed salinity changes in the Atlantic Ocean from 1896 to 2013 and confirmed the pattern of mid-to-low latitude enhanced salinity, and high latitude North Atlantic freshening over the period exists, even after removing the effects of variability modes NAO and AMO.

Considering the bulk of evidence, it is *extremely likely* that human influence has contributed to observed near-surface and subsurface salinity changes across the globe since the mid-20th century. All available multi-decadal assessments have confirmed that the associated pattern of change corresponds to fresh regions becoming fresher and salty regions becoming saltier (*high confidence*). Changes to the coincident atmospheric water cycle and ocean-atmosphere fluxes (evaporation and precipitation) are the primary drivers of the basin-scale observed salinity changes (*high confidence*). This result is supported by all available observational assessments, along with a growing number of CMIP5 and idealised climate modelling studies targeted at assessing ocean and water cycle changes. The basin-scale changes are consistent across models and intensify on centennial scales from the historical period through to future projections (*high confidence*).

[START FIGURE 3.26 HERE]

Figure 3.26: Maps of 50-year salinity trends for the near-surface ocean. (a) the 1950-2000 observational change and (b) the corresponding 1950-2000 climatological mean (Durack and Wijffels, 2010) (analysis period 1950-2008). (c) Modelled changes for the 1950-2000 period from the CMIP5 historical experiment multi-model mean. Black contours bound the climatological mean salinity associated with each map, and white contours bound the salinity trend in increments of 0.25 (PSS-78). (Figure from Durack, 2015, their Figure 7).

[END FIGURE 3.26 HERE]

[START FIGURE 3.27 HERE]

Figure 3.27: Long-term trends in 0 to 2000 dbar total halosteric (salinity-driven) sea level anomaly, and the contrast of basin-integrated results for the Pacific and Atlantic Oceans compared to CMIP5 models. Units are mm year-1. Maps of 0 to 2000 dbar halosteric anomalies (left column, a3, b3 and c3) from (Ishii and Kimoto, 2009, a3), (Durack and Wijffels, 2010, b3) and the CMIP5 historical multi-model mean (c3). Blue colours show a halosteric contraction (enhanced salinity) and orange a halosteric expansion (reduced salinity). Stippling is used to mark regions where the two observational estimates do not agree in their sign (a3, b3) and where less than 50% of the contributing models do not agree in sign with the multi-model mean map from the ensemble. Basin-integrated halosteric (right column, top panel A) and thermosteric (right column, panel B) anomalies for the Pacific, where Pacific anomalies are presented on the x-axis and Atlantic on the y-axis. Observational estimates are presented in the red (Ishii and Kimoto, 2009) and black (Durack and Wijffels, 2010) diamonds, CMIP5 historical models are shown in grey diamonds, with the multi-model mean in dark grey, and CMIP5 historicalNat models are shown in green diamonds with the multi-model mean in dark green. (Figure from Durack et al. (2014b), their Figures 1 and 4).

[END FIGURE 3.27 HERE]

3.5.3 Sea Level

In the AR5, the observed sea level budget was closed by considering all contributing factors (see Box 9.2) including ocean warming, mass contributions from terrestrial storage, glaciers and ice caps, and the Antarctic and Greenland ice sheets (Church et al., 2013a). The SROCC found that the observed global mean sea level (GMSL) rise is consistent within uncertainties with the sum of the estimated observed contributions for 1993–2015 and 2006–2015.

3.5.3.1 Sea Level Evaluation

A complication with modelling sea level change is that many of the necessary components, such as glaciers, ice sheets and land water storage required to close the observed budget were only partially resolved or missing from CMIP5 modelling systems (see Section 9.6 / Box 9.2). Consequently, most CMIP-based analyses of sea level change have focused on the thermosteric sea level changes (thermal expansion due to warming) and the ocean dynamic sea level change, which are simulated in the CMIP5-generation of models. Other contributions are computed using dedicated models, driven by CMIP output where possible. With the introduction of background volcanic forcing in the model control simulations (Eyring et al., 2016), modelled estimates of thermal expansion during the historical period have improved and agree better with the observed estimates. This agreement led the SROCC to assess a *high confidence* level in the simulated thermal expansion using climate models and *high confidence* in their ability to project future thermal expansion.

While CMIP5 models did not include all necessary components, some meta-studies have used offline mass inputs to account for glacier and terrestrial contributions. Slangen et al. (2017) and Meyssignac et al. (2017) suggest including corrections to several contributions to sea level changes including to the Greenland surface mass balance and glacier contributions, based on differences between CMIP5-driven model results and reanalysis-driven results. This helps close the gap between models and observations for the 20th century globally, as well as better agreement with tide gauge observations in terms of interannual and multi-decadal variability at the regional scale.

In CMIP6, ice sheets (see Section 3.4.3.2) are included for the first time in ISMIP6 (Nowicki et al., 2016). There is also scope for new insights of terrestrial water contributions from land surface (and sub-surface) modelling in the Land Surface, Snow and Soil moisture Model Intercomparison Project (LS3MIP; van den Hurk et al., 2016), providing a more comprehensive assessment of land surface snow and soil moisture feedbacks, as well as diagnosing systematic biases in land models. In parallel, the GlacierMIP project (Hock et al., 2019a; see Section 3.4.3.1) is also underway, and will provide more quantitative guidance and a comprehensive assessment of the uncertainties and best estimates of the sea level budget.

3.5.3.2 Sea Level Change Attribution

The SROCC concluded with *high confidence* that the dominant cause of global mean sea level rise since 1970 is anthropogenic forcing. Prior to that, the AR5 had concluded that it is *very likely* that there is a substantial contribution from anthropogenic forcings to the global mean sea level rise since the 1970s. Since the AR5, several studies have identified a human contribution to observed sea level change, manifest in thermosteric sea level which can be separated into global mean and spatial pattern assessments.

For the global mean thermosteric sea level change, Slangen et al. (2014) showed the importance of anthropogenic (combined greenhouse gas and aerosol forcings) to explain the magnitude of the observed changes considering the full depth of the ocean between 1957-2005 and natural forcings in order to capture the variability (see also Figure 3.28:). Over the 1950-2005 time period, Marcos and Amores (2014) found the human influence on thermosteric sea level rise in the 0-700m global ocean to be 87%. Both thermosteric and regional dynamic patterns of sea level change in individual forcing experiments from CMIP5 were considered by Slangen et al. (2015) who showed that responses to anthropogenic forcings are significantly different from both internal climate variability and inter-model differences and that although GHG and

anthropogenic aerosol forcings produce opposite global mean sea level responses, there are differences in response on regional scales. Based on these studies, we conclude that it is *very likely* that anthropogenic forcings are responsible for most of the observed global mean thermosteric sea level change since 1970.

In an attribution study of the sea-level contributions of glaciers, Marzeion et al. (2014) found that between 1991 to 2010, the anthropogenic fraction of global glacier mass loss was 69 ±24%. Slangen et al. (2016) considered all quantifiable components of the global mean sea level budget and showed that anthropogenic forced changes account for 69 ± 31% during 1970 to 2005, whereas natural forcings combined with internal climate variability have a much smaller impact only contributing 9 ± 18% of the change over the same period. These studies reveal that about 70% of the combined change in glaciers, ice sheet surface mass balance and thermal expansion since 1970 can be attributed to anthropogenic forcing, and that this percentage has increased over the course of the 20th century. Detection studies on GMSL change in the 20th century (Becker et al., 2014; Dangendorf et al., 2015) found that observed total GMSL change in the 20th century was inconsistent with internal climate variability. Dangendorf et al. (2015) identified that for 1900 to 2011 it is *virtually certain* (P = 0.99) that at least 45% is human-induced and *extremely likely* (P = 0.95) that at least 61% is human-induced. A study that semi-empirically coupled GMST to sea-level change concluded it was *very likely* that at least 41% of the 20th century sea-level rise would not have happened in the absence of the century's increasing GMST and that there was a 95% probability that by 1970 GMSL was higher than that which would have occurred in the absence of increasing GMST (Kopp et al., 2016).

We note that current detection and attribution studies do not yet include all processes that are important for sea-level change, such as ice sheet dynamical changes, local subsidence or direct human interventions in landwater storage such as groundwater extraction. However, based on the body of literature available, we conclude that most of the observed GMSL rise since 1970 is *very likely* caused by anthropogenic forcings.

[START FIGURE 3.28 HERE]

Figure 3.28: Comparison of global annual mean thermosteric sea level anomalies for CMIP6 historical (purple), natural-forcing only (green), well-mixed GHG only (red) and aerosol only (blue) simulations (multi-model means shown as thick lines, and individual model simulations as thin lines) and for observed thermosteric sea level anomalies (Zanna et al. (2019), black). Anomalies are shown with respect to 1985–2004. Numbers within brackets denote number of models used in producing the multi-model mean.

[END FIGURE 3.28 HERE]

3.5.4 Ocean Circulation

Circulation of the ocean, whether it be wind or density driven, plays a prominent role in the heat and freshwater transport of the Earth system (Buckley and Marshall, 2016). Thus, its accurate representation is crucial for the realistic representation of water mass properties, and replication of observed changes driven by atmosphere-land-ocean coupling. Here, we assess the ability of the models to reproduce the observed large-scale ocean circulation and the detection and attribution of anthropogenic-driven its changes, while noting that the process based understanding of these circulation changes and circulation changes occuring at smaller scales are reported in Chapter 9.2.3.

3.5.4.1 Atlantic Meridional Overturning Circulation (AMOC)

The Atlantic Meridional Overturning Circulation (AMOC) represents a largescale flow of warm salty water northward at the surface and a return flow of colder water southward at depth and, as such, its mean state plays an important role in transporting heat in the climate system, while its variability can act to redistribute heat (see Chapter 2.3.3.4.1 and Chapter 9.2.3.1 for more details).

AR5 concluded that while climate models suggested that an AMOC slowdown would occur in response to anthropogenic forcing, the short direct observational AMOC record precluded it from being used to support this model finding. The SROCC increased the confidence in historical AMOC changes, concluding with *medium confidence* that the AMOC weakened over the historical period. This increased confidence was based on the agreement between three different lines of evidence (CMIP5 climate model simulations, historical reconstructions using SST fingerprints and paleoclimatic evidence) that all supported an AMOC weakening during the historical period.

The CMIP5 and CMIP6 model ensembles simulate the general features of the AMOC similarly, but there is a large spread in the latitude and depth of the maximum overturning, and the maximum AMOC strength. In CMIP5 maximum AMOC strength ranges from 13 to 31 Sv (Sverdrups = 10^6 m^3 s^{-1} (Zhang and Wang, 2013) and deviations of AMOC strength have been related to global-scale sea surface temperature biases (Wang et al., 2014). Despite the additional six years or so of observations since the AR5 was prepared, the evaluation of the AMOC in models continues to be severely hampered by the geographically sparse and temporally short observational record. The longest continuous observational estimates of the AMOC are at 26°N by the RAPID-MOCHA array (Smeed et al., 2018). Basic evaluation of the AMOC at 26°N shows that the CMIP5 and CMIP6 multi-model mean overturning strength is comparable with RAPID (Reintges et al., 2017; Weijer et al., submitted), but the model range is large (12-29 Sv for CMIP5 and 10-22Sv for CMIP6) (see Figure 3.29:a). Both coupled and ocean-only models also underestimate the depth of the AMOC cell (Danabasoglu et al., 2014; Weijer et al., submitted; Figure 3.29:a). Paleo-climatic evidence has also raised questions regarding the accuracy of the representation of the strength and depth of the modelled AMOC during past periods (Otto-Bliesner et al., 2007; Muglia and Schmittner, 2015).

The short length of the observed time-series (about 14 years long for RAPID), sparse observations, and observational uncertainties (Sinha et al., 2018), as well as significant observed variability on interannual and longer time scales, also makes comparison of variability with models challenging. RAPID observations show that overturning at 26°N is 2.5 and 3.0 Sv weaker in the multi-year averages of 2008-2011 and 2012-2016 relative to the 2004-2007 period, respectively (Smeed et al., 2014, 2018) (see Section 2.3.3.4.1). CMIP5 models do produce a forced weakening of AMOC over the 2012-2016 period relative to 2004-2007, but at 26°N the multi-model mean response is 0.92 Sv, which is substantially weaker than the reported observed 3 Sv AMOC decline over the same period. The discrepancy between modelled and the RAPID observed AMOC changes has led studies to suggest that the observed weakening over 2004-2015 is largely due to internal variability (Yan et al., 2018). However, comparison of observed RAPID AMOC variability with modelled variability also reveals that CMIP5 models appear to underestimate the interannual and decadal timescale variability (Roberts et al., 2014; Yan et al., 2018), and similar results are found analysing the CMIP6 models (Figure 3.29:b,c). It is currently unknown why models underestimate this variability, but it may partly stem from underestimated surface wind variability and biases in the major atmospheric modes of variability over the North Atlantic, such as the NAO (see Section 3.3.3.3). This underestimation of AMOC variability likely also has implications for detection and attribution, the relationship between AMOC and AMV (see Section 3.7.7), and near-term predictions. There is also emerging evidence, based on analysis of freshwater transports, that the AMOC in CMIP5-era models is too stable, largely due to systematic biases in ocean salinity (Liu et al., 2017; Mecking et al., 2017). Such a systematic bias may potentially be linked with the underestimation of both simulated AMOC internal variability through eddy-mean flow interactions that are poorly represented in standard CMIP-class model resolution (Leroux et al., 2018), and externally forced change.

Instrument-based reconstructions suggest the AMOC weakened during the 20th century (Chapter 2) (Ezer et al., 2013; Caesar et al., 2018). Over the same period, the CMIP5 multi-model mean showed no significant net forced response in AMOC (Cheng et al., 2013). The CMIP6 multi-model mean opposes the observed estimate (Weijer et al., submitted), as despite a near zero long term trend, a clear increase of the AMOC is seen over ~1940-1985 period (Menary et al., submitted; Figure 3.29:e). Models suggest that the AMOC is sensitive to natural (Menary and Scaife, 2014; Swingedouw et al., 2017) and anthropogenic external forcing (Caesar et al., 2018; Menary et al., 2013, submitted; Undorf et al., 2018a). However, the response between models can be different and, hence, the relative importance of the influences of external forcings on AMOC's evolution in models is uncertain. Although there is general agreement that the influence of GHG

acts to a weaken the modelled AMOC (Delworth and Dixon, 2006), changes in solar, volcanic and anthropogenic aerosol emissions can often lead to temporary increases in AMOC on decadal-to-multidecadal timescales (Delworth and Dixon, 2006; Menary et al., 2013). The simulated net forced response in AMOC is, therefore, often a balance between different forcing factors (Delworth and Dixon, 2006; Menary et al., submitted). The differing AMOC response of CMIP5 and CMIP6 models during the historical period has been associated with stronger aerosol effective forcing in the CMIP6 models (Menary et al., submitted), such that the aerosol induced AMOC increase during the 1940-1985 period overcomes the GHG induced decline (Figure 3.29:e). However, there remains considerable uncertainty over the realism of the CMIP6 AMOC response during the 20th century due to disagreement among the differing lines of observational evidence. For example, indirect proxies of observed AMOC suggest that AMOC weakened over the period 1870–2015 (Caesar et al., 2018; Thornalley et al., 2018). Ocean reanalysis (Jackson et al., 2019) and forced ocean model simulations (Robson et al., 2012; Danabasoglu et al., 2016) generally beginning in the late 1950s do suggest a peak in AMOC in the 1990s, but their short length precludes an assessment of 20th century trends. The mechanisms of AMOC strengthening in the forced ocean model simulations is reportedly associated with atmospheric circulation changes, and primarily the North Atlantic Oscillation (NAO) (Robson et al., 2012; Danabasoglu et al., 2016). However, there is little evidence for a significant role of external forcing in driving the observed interannual to multidecadal variations of the NAO over the 20th century from CMIP5 and CMIP6 models (Section 3.7.1; Figure 3.32:). Significant questions also remain about the veracity of the forced AMOC response and, as discussed above, along with the relative importance of internal variability which is depicted by the extent of the box and whiskers, relative to the mean (Figure 3.29:d).

In summary, models do not currently help us to understand the role of anthropogenic forcing in the recently observed reduction in AMOC as the changes currently sit outside of the range of forced AMOC trends and outside of the range of modelled internal variability. Thus, we have *low confidence* that anthropogenic forcing has had an impact on observed changes in AMOC strength in the post-2004 period. Chapter 2 identified agreement from proxy evidence for a century-or longer-term decline in the AMOC, however, *low confidence* was placed on these findings (Section 2.3.3.4.1). In addition to this, there remains considerable uncertainty over the realism of the CMIP6 AMOC response during the 20th century due to disagreement among the differing lines of model simulation evidence (i.e., reanalysis, forced ocean simulations and historical CMIP6 simulations). Thus, we have *low confidence* that anthropogenic forcing has had an impact on observed changes in AMOC strength during the historical period (1860-2014).

[START FIGURE 3.29 HERE]

Figure 3.29: (a) AMOC streamfunction profiles at 26.5°N from the historical CMIP5 (1860-2004) and CMIP6 (1860-2014) simulations compared with the mean overturning observed with the RAPID data (2004-2018, black line). Overturning maxima are indicated by diamonds and the RAPID, CMIP5 MMM and CMIP6 MMM values are given in the legend. (b) Distribution of 8-year AMOC trends from individual CMIP6 historical simulations and the observed 2004-2012 trend (grey line). (c) Distribution of interannual AMOC variability from individual CMIP6 model historical simulations, along with the combined distributions of all available CMIP5 and CMIP6 models. The grey line is the observed value for 2009/2010 minus 2008/2009 (following Roberts et al., 2014). All annual means are for April-March. (d-f) distribution of linear AMOC trends calculated over various time periods (see panel titles) over the historical period in CMIP6 simulations forced with: Anthropogenic greenhouse gas forcing only (GHG), Natural forcing only (NAT), Anthropogenic Aerosol forcing only (AER) and all forcing combined (Historical; HIST). (b-d) Boxes indicate 25th to 75th percentile, whiskers indicate 1st and 99th percentiles, and dots indicate outliers, while the horizontal black line and text value are the multi-model mean trends. (a-c) were produced with one historical ensemble member per model where the AMOC variable was available (listed), while (d-f) were produced with the AMOC detection and attribution simulation data sets utilised by Menary et al. (submitted). (Figure produced with ESMValTool v2.0a1.)

[END FIGURE 3.29 HERE]

3.5.4.2 Southern Ocean Circulation

The Southern Ocean circulation provides the principal connections between the world's major ocean basins through the circulation of the Antarctic Circumpolar Current (ACC), while also largely controlling the connection between the deep and upper layers of the global ocean circulation, through its upper and lower overturning cells.

AR5 reported, that in spite of changes in overlying surface winds, there was no direct evidence to support an intensification of the ACC (AR5 Section 3.6.4, and 3.6.5.2) and findings since then also agree that ACC transport has been stable since the 1990s (Section 9.2.3.2). However, post AR5 observational advances revealed that the observed magnitude of ACC mean transport is *likely* higher than reported in AR5. SROCC reported that that it is *unlikely* that the ACC meridional position has shifted in recent decades, in contrast to AR5.

The modelled strength of the ACC clearly improved from CMIP3, in which the models tended to underestimate the strength of the ACC, to CMIP5 (Meijers et al., 2012). This improvement in the realism of ACC strength continues from CMIP5 to CMIP6, with the modelled ACC strength converging toward the magnitude of observed estimates of net flow through the Drake Passage (Beadling et al., submitted). There is, however, a small number of models that still display an ACC that is much weaker than that observed, while several models also display much more pronounced ACC decadal variability than that observed (Beadling et al., submitted). The increased realism of the ACC was at least partly related to noted improvements in all metrics of the Southern Ocean's surface wind stress forcing (Beadling et al., submitted). The most notable wind stress forcing improvements were found in the strength and the latitudinal position of the zonally-averaged westerly wind stress maximum (Beadling et al., submitted; Bracegirdle et al., submitted).

SROCC concluded that there is *low confidence* in an increase of the Southern Ocean's upper cell overturning circulation due to large decadal variability and indirect measurements, and *medium confidence* that the lower overturning cell had slowed since the 1950s, decreasing the production of Antarctic Bottom Water. While the two-cell structure of the overturning circulation appears to be well captured by CMIP5 models (Sallée et al., 2013b; Russell et al., 2018), they tend to underestimate the intensity of the lower cell overturning, and overestimate the intensity of the upper cell overturning (Sallée et al., 2013b). As the lower overturning cell is closely related to Antarctic Bottom Water formation and deep convection, both fields also display substantial errors in CMIP5 models (Heuzé et al., 2013, 2015). Changes in the CMIP6 model representation of the Southern Ocean's overturning circulation is curently unknown due to lack of literature.

More generally, some of the climate model biases in characterizing Southern Ocean circulation come from inherent limitations in representing important processes at play in the horizontal and vertical overturning circulation of the Southern Ocean (Chapter 9.2.3.2). For instance, Southern Ocean mesoscale eddies are wholly paramerterised in the current generation of climate models and despite their small spatial scales they are a key element for establishing the ACC and upper overturning cell, as well as for their future evolution under changing atmospheric forcing (Kuhlbrodt et al., 2012; Downes and Hogg, 2013; Gent, 2016; Downes et al., 2018; Poulsen et al., 2018).

SROCC reported that there is *low confidence* that the ACC or the Southern Ocean's upper overturning branch have displayed significant changes during the relatively short observational period, and *medium confidence* that the production of Antarctic Bottom Water reduced over this time. These Southern Ocean circulation assessments remain valid (Section 2.3.3.4 and 9.2.3.2). Models display continued improvement in the representation of the ACC strength from CMIP3 to CMIP6 (Beadling et al., submitted; Meijers et al., 2012). However, limitations in the representation of Antarctic Bottom Water formation remain in CMIP5 and it is currently unclear whether these biases have been improved in CMIP6. Model studies assessing the potential drivers of the decreased Antarctic Bottom Water production during the historical period are not available at this time. It is noted that existing model biases place important limits in the correct representation of the ACC and Southern Ocean overturning cells, as well as in their representation of associated water-masses.

In summary, while there have been improvements across successive phases of the CMIP project (CMIP3 to CMIP6) in representation of the Southern Ocean circulation, substantial observational uncertainty precludes attribution of Southern Ocean circulation changes. Overall, the mean zonal and overturning circulations of the Southern Ocean and the mean overturning circulation of the North Atlantic (AMOC) are broadly reproduced by CMIP5 and CMIP6 models. However, we assess that some biases are apparent in the circulation strengths, which contribute to biases in the model representation of mean ocean temperature and salinity (*medium confidence*).

3.6 Human Influence on the Biosphere

3.6.1 Terrestrial Carbon Cycle

The AR5 did not make attribution statements on changes in global carbon sinks. The IPCC SRCCL reported *medium evidence* but *high agreement* that global vegetation photosynthetic activity has increased since the 1980s (Jia et al., 2019). That increase is attributed to CO_2 fertilisation, nitrogen deposition, and climate change. The AR5 assessed with *high confidence* that CMIP5 ESMs simulate the global mean land and ocean carbon sinks within the range of observation-based estimates (Flato et al., 2013). The IPCC SRCCL, however, notes the remaining shortcomings of carbon cycle schemes in ESMs, which for example do not properly incorporate thermal responses of respiration and photosynthesis (Jia et al., 2019). Other routine omissions from terrestrial carbon cycle models of components expected to interact with climate change forcings are representations of permafrost thaw (Comyn-Platt et al., 2018), the nitrogen cycle (Thomas et al., 2015b) and its impact on vegetation dynamics (Jeffers et al., 2015), the phosphorus cycle (Fleischer et al., 2019), and accurate implications of carbon store changes for a range of land use options (Harper et al., 2018).

This section considers three main large-scale indicators of climate change relevant to the terrestrial carbon cycle: atmospheric CO_2 concentration, atmosphere-land CO_2 fluxes, and leaf area index. CMIP5 and CMIP6 ESMs generally provide century-timescale climate simulations and diagnose CO_2 emissions consistent with these. Such calculations require that the models simulate realistic changes in the terrestrial carbon cycle over the historical period, as changes to land carbon stores will influence the size of consistent CO_2 emissions. Such testing of existing models is needed while also recognising there are process representations still requiring inclusion.

Since the AR5, atmospheric inversion studies have helped test or constrain models, while new datasets have been used to constrain specific parts of the terrestrial carbon cycle such as plant respiration (Huntingford et al., 2017). Figure 3.30: shows historical emissions-driven CMIP6 simulations to compare the simulated global mean atmospheric CO_2 concentration, ocean and land carbon sinks to observational estimates provided by the Global Carbon Project (Le Quéré et al., 2016). The CMIP6 models simulate a range of current CO_2 values centred around the observed value of 380 ppmv in 2010, with a range of approximately 360 to 400 ppmv. Most models simulate a realistic temporal evolution of the global ocean carbon sink (Figure 3.30:b, see also Section 3.6.2). Models without nutrient limitations on plant growth generally overestimate the contemporary land carbon sink (Figure 3.30:c), predominantly because they do not include a modelled terrestrial nitrogen cycle (Peng and Dan, 2015), but also because of uncertainties in the photosynthetic response to CO_2 at global scales, shifts in carbon allocation and turnover, and land-use change (Hoffman et al., 2014). When considered globally, these simulated sinks fall within the range of observation-based estimates with *high confidence*, but only when the land models include representation of nutrient limitation (Thomas et al. (2015b) and Figure 3.30:).

All models and the observational estimates agree that interannual variability in net CO_2 uptake is much larger over land than over the ocean. Differences in the simulated interannual variability of the land carbon sink reveal differences in the simulated sensitivity of land carbon storage to climate fluctuations, and comparison of this variability with observations can be used to derive an emergent constraint on this sensitivity to long-term climate change (Section 5.4.6). Data-led studies demonstrate that regional variations in both the trends and the yearly strength of the terrestrial carbon sink are considerable. Datasets of the leaf

area index (LAI) and atmospheric inversions from point CO_2 concentration measurements, as well as land simulations, imply that the majority of current terrestrial carbon accumulation is in the tropics (Sitch et al., 2015). Extrapolation of eddy-covariance point measurements of land-atmosphere CO_2 exchanges suggests that for local to regional scales, the dominant control of yearly sink strength is water availability, while at continent to global scale, the main driver is whether it is an anomalously hot or cold year (Jung et al., 2017). The major role of levels of water stored in the ground in influencing land-atmosphere CO_2 exchange is reconfirmed through simultaneous analysis of satellite gravimetry and atmospheric CO_2 levels (Humphrey et al., 2018). New CMIP6 simulations reconfirm that Earth system models estimate overall mean land and ocean carbon sinks to be an on-going substantial fraction of emissions. When considered globally, these simulated sinks fall within the range of observation-based estimates with *high confidence*, but only when the land models include representation of nutrient limitation (Figure 3.30:).

[START FIGURE 3.30 HERE]

Figure 3.30: Evaluation of historical emissions-driven CMIP6 simulations for 1860-2014, against observational estimates of global mean (a) atmospheric CO_2 concentration (ppmv) (observational constraints are not yet included; red dot: 2005 Global CO_2 value) Models: BCC-CSM2-MR, CNRM-ESM2-1, (b) ocean carbon uptake (PgC yr^{-1}) Models: CanESM5, CNRM-ESM2-1, NorESM2-LM, GFDL-ESM4, (c) land carbon uptake (PgC yr^{-1}). Models: CanESM5, CNRM-ESM2-1, UKESM1-0-LL, NorESM2-LM. F_L represents the atmosphere-land CO_2 flux and can be compared with the models. F_{LN} is the residual land sink, excluding the effects of land-use change. (Figure produced with ESMValTool v2.0.0b3.)

[END FIGURE 3.30 HERE]

The seasonal cycle in atmospheric CO_2 in remote locations across the Northern Hemisphere, which is driven by the drawdown of carbon by photosynthesis on the land during the summer and release by respiration during the winter, has increased its amplitude since the start of systematic monitoring (Figure 3.31:, see also Section 2.3.4.6). This trend, which is larger at higher latitudes, was first reported by Keeling et al. (1996) and has continued. Proposed causes of this trend, and its amplification at higher latitudes, include increases in the summer productivity and/or increases in the magnitude of winter respiration of northern ecosystems (Barichivich et al., 2013; Graven et al., 2013; Forkel et al., 2016; Wenzel et al., 2016), increases in productivity throughout the Northern Hemisphere by CO_2 fertilisation, and increases in the productivity of agricultural crops in northern mid-latitudes (Gray et al., 2014; Zeng et al., 2014). Changes have been observed in both vegetation productivity as well as longer growing seasons (Park et al., 2016). However, a slowdown of the increasing trend has been noted, linked to a slowdown of both vegetation greening and growing-season length increases (Li et al., 2018). Terrestrial carbon cycle models partially capture the increasing amplitude observed at Mauna Loa Observatory, Hawaii, and suggest that the dominant driver is CO_2 fertilisation, with substantial uncertainty in the contributions from climate change and land use change (Zhao et al., 2016). However, many of these global models do not include nitrogen fertilization, changes to crop cultivars or irrigation effects, with the latter associated with deficiencies in simulated terrestrial water cycling (Yang et al., 2018). All these missing factors may influence the response. Attribution of the drivers at Barrow, Alaska, suggests a more even contribution of CO_2 fertilisation and warming in the high northern latitudes (Piao et al., 2017), although here too, models differ and are believed to underestimate current levels of carbon fixation (Winkler et al., 2019). Deficiencies in phenological representation of greenness levels in land models, and particularly for Autumn, are suggested as an explanation for remaining seasonal discrepancies between expected and measured CO_2 levels at Barrow (Li et al., 2018). Based on these studies and noting the uncertainty in the processes ultimately driving changes in atmospheric CO_2 seasonal cycles (Section 5.2.2.4.3), we assess as *likely*, with *medium confidence*, that anthropogenic increases in CO_2 have resulted in an increase in the amplitude of its atmospheric seasonal cycle.

Detection and attribution methods have been applied to Leaf Area Index (LAI), which represents "greenness" and general photosynthetic productivity (see Section 2.3.4.5). Nitrogen deposition and land cover change trends remain small compared to variability, so attributing changes in LAI to those processes is difficult. Using three satellite products and ten land models, Zhu et al. (2016) find increases in LAI

(greening) over 25-50% of global vegetated areas, which they attribute mostly to increasing atmospheric CO_2 concentrations. This observed greening supports findings of Mao et al. (2016), although Mao et al. (2013) note the faster warming rates in the Southern Hemisphere lessen this fertilisation effect compared to the Northern Hemisphere. These conclusions remain in Zhu et al. (2017), where land models are additionally first weighted by performance, but have been challenged by Chen et al. (submitted) who show that greening in India and China is driven by land-use change. LAI increases attributed to CO_2 fertilisation is due to a direct raised physiological response. However, for drylands, CO_2-induced stomatal closure may operate to conserve soil moisture and higher water use efficiency can offset closure impacts on photosynthesis (Lu et al., 2016). The recent merging of terrestrial ecosystem models with CO_2-enrichment experiments has better constrained the fertilisation effect (Liu et al., 2019). For models with nitrogen deposition, there is attributable evidence that this simulated effect is observable as influencing LAI trends. However, because only a very small number of large-scale land simulations include both nutrient limitation and crop intensification, and even fewer factorial simulations exist with these effects modelled as "on" or "off", it is not yet possible to make an attribution statement about their individual roles in LAI changes.

In summary, there is *medium confidence* that Earth system models simulate the magnitude and large interannual variability of the land carbon sink well if they account for nutrient limitation on plant growth. Based on new studies that attribute changes in atmospheric CO_2 seasonal cycle mostly to CO_2 fertilisation, combined with the *medium confidence* that models represent the processes driving changes in the seasonal cycle, we assess that anthropogenic increases in CO_2 have *likely* resulted in an increase in the amplitude of its atmospheric seasonal cycle. Based on new studies that attribute increases in LAI to CO_2 fertilisation, but noting the low number of models that represent the whole suite of processes involved, especially nutrient limitation and crop intensification, we assess with *low confidence* that CO_2 fertilisation due to the increase in atmospheric CO_2 has contributed to observed increases in LAI.

[START FIGURE 3.31 HERE]

Figure 3.31: Changes to the amplitude of the seasonal cycle of global land-carbon uptake in the historical simulations from 1961-2014. (a) Net biosphere production (nbp) estimates from CMIP6 models (CanESM5, MIROC-ES2L, UKESM1-0-LL, CNRM-ESM2-1, IPSL-CM6A-LR, GISS-E2-1-G, GISS-E2-1-G-CC, GISS-E2-1-H, CESM2, CESM2-WACCM, SAM0-UNICON, in black) and atmospheric CO_2 seasonal cycle amplitude changes from observations (global in blue, Mauna Loa Observatory (MLO) in grey). Seasonal Cycle Amplitude calculated using the curve fit algorithm package (https://www.esrl.noaa.gov/gmd/ccgg/mbl/crvfit/crvfit.html) from the National Oceanic and Atmospheric Administration Earth System Research Laboratory (NOAA ESRL). Trends are relative to the 1961-1970 mean and for short time series adjusted to have the same mean as the model ensemble in the last 10 years. Interannual variation was removed with a 9-year Gaussian smoothing. Shaded areas show the 1 sigma model spread (grey) and the 1 sigma standard deviation (light-grey) for the CMIP6 ensemble and the CO_2 MLO observations respectively. Inset: average seasonal cycle of ensemble mean for 1961-1970 and its 1 sigma model spread (dashed line, light grey shading) and 2005-2014 (solid line, darker grey shading). (b) Attribution of causes of increasing amplitude from CMIP6 models using historical, hist-bgc (fixed climate in biogeochemistry) and hist-noLu (no land-use change) simulations and calculated from the amplitude trend following panel a (similar to Zhao et al., 2016, their Figures 4 and 5), Models: CNRM-ESM2-1, UKESM1-0-LL. (Figure produced with ESMValTool v2.0.0b3.)

[END FIGURE 3.31 HERE]

3.6.2 Ocean Biogeochemical Variables

Since CMIP5, there has been a general increase in ocean horizontal grid resolution and vertical grid parametrization and resolution in ocean model components (Arora et al., submitted; Séférian et al., submitted). The latter of these developments is particularly significant for projections of ocean stressors as it directly affects the representation of stratification. Updates in the representation of ocean biogeochemical processes between CMIP5 and CMIP6 have typically involved an increase in model complexity. Specific

developments have been the more widespread inclusion of micronutrients, such as iron, variable stoichiometric ratios, more detailed representation of lower trophic levels including bacteria and the cycling and sinking of organic matter. CMIP6 biogeochemical model performance is generally an improvement on that of the parent CMIP5 generation of models (Séférian et al., submitted). The global representation of present-day air-sea carbon fluxes and surface chlorophyll concentrations show moderate improvements between CMIP5 and CMIP6. Similar improvements are seen in the representation of subsurface oxygen concentrations in most ocean basins, while the representation of surface macronutrient concentrations in CMIP6 is shown to have improved with respect to silicic acid but declined slightly with respect to nitrate. Model representation of micronutrient iron has not improved substantially since CMIP5, but many more models are capable of representing iron. In addition, a comparison of the feedbacks in carbon concentration and carbon climate shows no significant change between CMIP5 and CMIP6 (Arora et al., submitted).

Since AR5 research has also focused on the detection and attribution of regional patterns in ocean biogeochemical change relating to interior deoxygenation, air-sea CO_2 flux, and ocean carbon uptake and associated acidification. Characterization of flux variability requires understanding of the suite of physical and biological processes including transport, heat fluxes, interior ventilation, biological production and gas exchange which can have very different controls on seasonal versus interannual timescales in both the North Pacific (Ayers and Lozier, 2012) and North Atlantic (Breeden and McKinley, 2016). In the Southern Ocean, models have difficulty reproducing the observed seasonal cycle and interannual variability, making attribution particularly challenging (Lovenduski et al., 2016; Mongwe et al., 2016, 2018).

The AR5 concluded that oxygen concentrations have decreased in the open ocean since 1960 and such decreases can be attributed in part to human influences with *medium confidence*. The decrease in ocean oxygen content in the upper 1000m, between 1970-2010, is further confirmed in SROCC (*medium confidence*), with the oxygen minimum zone expanding in volume. Observed oxygen declines over the last several decades (Stendardo and Gruber, 2012; Stramma et al., 2012; Schmidtko et al., 2017) match model estimates in the surface ocean (Oschlies et al., 2017) but are much larger than model derived estimates in the interior (Bopp et al., 2013; Cocco et al., 2013). Some of this difference has been interpreted as a lack of representation of coastal eutrophication in these models (Breitburg et al., 2018), but much of it remains unexplained. This disparity is particularly true in the Eastern Pacific oxygen minimum zone, where some CMIP5 models showed increasing trends whereas observations show a strong decrease (Cabré et al., 2015). However, proxy reconstructions suggest that the last century may have in fact undergone increases in oxygen in the most oxygen poor regions (Deutsch et al., 2014). The global upper ocean O_2 inventory (0–1000 m) changed at the rate of -243 ± 124 T mol O_2 per decade and is negatively correlated with ocean heat content ($r = -0.86$; 0–1000 m) with a regression coefficient of -8.2 ± 0.66 nmol O_2 J^{-1}, on the same order of magnitude as the simulated O_2-heat relationship typically found in ocean climate models (Ito et al., 2017). Variability and trends in the observed upper ocean O_2 concentration are dominated by the apparent oxygen utilization component with relatively small contributions from O_2 solubility. While not providing a direct biogeochemical process, this consistency between the correlations suggests that changing ocean circulation, mixing, and/or biochemical processes, rather than the direct thermally induced solubility effects may be the explanation.

As one of the most commonly observed surface parameters, the partial pressure of CO_2 (pCO_2, an estimate of ocean CO_2 sink), has been the topic of considerable detection and attribution work. In North Atlantic subtropical and equatorial biomes, warming has been shown to be a significant and persistent contributor to the observed increase in pCO_2 since the mid-2000s with long-term warming leading to a reduction in ocean carbon uptake (Fay and McKinley, 2013), and with both pCO_2 and associated carbon uptake demonstrating strong predictability as a function of interannual to decadal climate state (Li et al., 2016a; Li and Ilyina, 2018). In the Southern Ocean however, detection and attribution of surface pCO_2 trends has proven more elusive and dependent on methodology, with some suggestion that Southern Ocean carbon uptake slowed from about 1990 to 2006 and subsequently strengthened from 2007 to 2010 (Lovenduski et al., 2008; Fay et al., 2014; Ritter et al., 2017). Other methods have suggested that representation of the seasonal cycle may confound models' ability to represent these signals (Nevison et al., 2016; Mongwe et al., 2018).

Based on pCO_2, the global net flux of CO_2 into the ocean is estimated to have weakened during the 1990s to

-0.8 ± 0.5 PgC yr^{-1} in 2000, and thereafter to have strengthened considerably to rates of -2.0 ± 0.5 PgC yr^{-1}, associated with changes in SST, the surface concentration of dissolved inorganic carbon and alkalinity, and decadal variations in atmospheric forcing (Landschützer et al., 2016, see also Section 5.2).

Ocean acidification is also one of the most detectible and attributable metrics of environmental change and was well covered in the AR5. The AR5 assessed with *high confidence* that the uptake of anthropogenic CO_2 has resulted in ocean acidification. Since then, observations and synthesis of multidecadal trends in surface carbon chemistry have increased in robustness, suggesting a detectable surface pH decrease of 0.018 ± 0.004 $decade^{-1}$ for the period of 1991-2011 (Lauvset et al., 2015) with an observed range of 0.013 - 0.026 $decade^{-1}$ (Bates et al., 2014). The evidence on ocean pH decline is further strengthened in SROCC (*virtually certain*) with a good agreement between CMIP5 models and observations. The ocean acidification occurs not only in the surface layer but also in the interior of the ocean (Section 5.3.3). Rates have been observed to be nearly as high (between −0.015 and −0.020 $decade^{-1}$) in mode and intermediate waters of the North Atlantic through the combination of increased anthropogenic and remineralized carbon (Ríos et al., 2015) and down to 3000 m in the deep water formation regions (Perez et al., 2018). There has also been considerable improvement in detection and attribution of anthropogenic CO_2 versus eutrophication based acidification in coastal waters (Wallace et al., 2014).

In summary, increased evidence in recent studies supports an assessment that it is *virtually certain* that the uptake of anthropogenic CO_2 has substantially contributed to the acidification of the global ocean. The observed increase in acidity over the North Atlantic subtropical and equatorial regions since mid-2000 is *likely* in part associated with an increase in ocean temperature, a response which corresponds to the expected weakening of the ocean carbon sink with warming. Due to strong internal climate variability, systematic changes in carbon uptake in response to climate warming have not been observed in most other ocean basins at present. We further assess, consistent with AR5 and SROCC, that deoxygenation in the surface ocean is due in part to anthropogenic forcing, with *medium* confidence. There is *high confidence* that Earth system models simulate a realistic time evolution of the global mean ocean carbon sink.

3.7 Human Influence on Modes of Climate Variability and their Teleconnections

3.7.1 North Atlantic Oscillation and Northern Annular Mode

The Northern Annular Mode (NAM; also known as Arctic Oscillation) is an oscillation of atmospheric mass between the Arctic and northern mid-latitudes, analogous to the Southern Annular Mode (SAM; Section 3.7.2). It is the leading mode of variability of sea-level pressure in the northern extratropics but also has a clear fingerprint through the troposphere up to the lower stratosphere, with maximum expression in boreal winter (Kidston et al., 2015). The North Atlantic Oscillation (NAO) can be interpreted as the regional expression of the NAM and captures most of the related variance in the troposphere over a broad North Atlantic/Europe domain. Indices measuring the state of the NAO correlate highly with those of the NAM, and teleconnection patterns for both modes are rather similar (Feldstein and Franzke, 2006). A detailed description of the NAM and the NAO is given in Technical Annex AVI.1.

AR5 found that while models simulated some general aspects of the NAM, substantial inter-model differences remained regarding the details of the associated teleconnection patterns. Also, models did not reproduce short-term (daily to subseasonal) variability of the NAO/NAM index and generally produced too few persistent episodes. AR5 reported that most models did not reproduce the observed positive trend of the NAO/NAM during the late 20th century; it was unclear to what extent this failure reflected model shortcomings and/or if the observed trend could be simply related to pronounced internal climate variability. AR5 accordingly did not comment on any anthropogenic influence on the NAO/NAM.

CMIP5 and newer models reproduce the structure and magnitude of the NAM reasonably well (Lee and Black, 2013; Zuo et al., 2013; Davini and Cagnazzo, 2014; Ying et al., 2014; Ning and Bradley, 2016; Deser et al., 2017b; Gong et al., 2017). But any progress from CMIP3 to CMIP5 models remains unclear (Davini and Cagnazzo, 2014). North Pacific SLP anomalies remain generally too strong (Zuo et al., 2013; Gong et

al., 2017) while the subtropical North Atlantic lobe of SLP anomalies is too weak (Ning and Bradley, 2016) in many models. Such overall biases persist in CMIP6 historical simulations, even if the multi-model multi-member ensemble mean spatial correlation between modelled and observed NAM is slightly better (Figure 3.32:a,d,g). Regarding the NAO, the majority of CMIP5 models successfully simulate its spatial structure (Lee et al., 2018) and its associations with jet, storm track and blocking variations over a broad North-Atlantic/Europe domain (Davini and Cagnazzo, 2014). The good performance of the models is confirmed in CMIP6 even showing a marginal improvement of the averaged observation-model spatial correlation (Figure 3.32:b,e,h) and better skill based on other evaluation metrics (Fasullo et al., submitted). The slight underestimation of the SLP anomalies related to the NAO centers of actions over the Azores and Greenland-Iceland-Norwegian Seas remain unchanged compared to CMIP5.

Low-top CMIP5 models (with model top within the stratosphere) seriously underestimate the variability of the wintertime NAM in the stratosphere, in contrast to high-top models (extending above the stratopause) (Lee and Black, 2015). However, even in the latter models, the stratospheric NAM events are insufficiently persistent (Lee and Black, 2015) and so are their downward influences on the troposphere (Charlton-Perez et al., 2013). Increased vertical resolution does not show any significant added value in reproducing the structure and magnitude of the tropospheric NAM (Lee and Black, 2013) nor in the NAO predictability as assessed in a seasonal prediction context from a multimodel approach (Butler et al., 2016). On the other hand, there is more evidence that a correct representation of the Quasi Biennal Oscillation and the extratropical stratospheric dynamics (polar vortex and sudden stratospheric warming) as well as their interplay with ENSO, are important for NAO/NAM temporality (Scaife et al., 2016; Karpechko et al., 2017; Domeisen, 2019; Domeisen et al., 2019), in spite of underestimated troposphere-stratosphere coupling found in models compared to observations (O'Reilly et al., 2019a).

The observed trend of the NAM and NAO over 1958-2014 is overall positive in winter (Chapter 2 Section 2.4.5.1; Technical Annex VI.1) while including large multidecadal variability, which means that the trend is not statistically significant (Gillett et al., 2013b). Dedicated SST-forced stand-alone atmospheric model experiments suggest that ocean forcing appears to play a role in decadal variability of the NAO and associated fluctuations in the strength of the jet (Woollings et al., 2015). In particular, Atlantic and Indian Ocean SST anomalies (Fletcher and Cassou, 2015; Baker et al., 2019; Douville et al., 2019) may have contributed to the long-term positive trend of the winter NAO/NAM over the 20th century, but there is only *low confidence* in such a causal relationship because of the limitation of imposed SST approach, the uncertainties in observed SST trends among datasets used as forcing and sampling issues due to limited ensemble size. There is also a tendency of the CMIP5 models to systematically underestimate the level of multidecadal versus interannual variability of the winter NAO and jet stream compared to observations (Bracegirdle et al., 2018; Simpson et al., 2018). This is further confirmed in CMIP6. Even if one cannot rule out that it was an exceptional period of variability, the observational estimates of 1958-2014 wintertime NAO trends lay outside of the 2.5-97.5th percentile range of the model distribution drawn from CMIP6 historical simulations, and multi-model multi-member ensemble means of the trends are equal to zero in both CMIP5 and CMIP6 (Figure 3.32:j,k). This has strong implications in the interpretation of climate seasonal trends over the Northern Hemisphere continents affected by NAM/NAO through teleconnections (Iles and Hegerl, 2017).

Focusing on the most recent two decades, the wintertime NAO/NAM trends are mostly negative since the mid-1990s, albeit very weak due to increased variability leading to record breaking in both phases (Hanna et al., 2015). Evidence is provided from observations (Gastineau and Frankignoul, 2015) and dedicated modeling experiments (Davini et al., 2015; Peings and Magnusdottir, 2016) that the recent dominance of negative NAM/NAO could be partly related to the latest shift of the Atlantic Multidecadal Variability (AMV) in a warm phase (Chapter 2 Section 2.4.3 and Section 3.7.7). Some recent modelling studies also find that the Arctic sea ice decline might be partly responsible for more recurrent negative NAM/NAO (Peings and Magnusdottir, 2013; Kim et al., 2014a; Nakamura et al., 2015), while other studies do not robustly identify such responses in models (Screen et al., 2013, 2018; Sun et al., 2016a; Boland et al., 2017; Blackport et al., 2019). These contradictory results may arise from nonlinearity in the NAO/NAM response to sea ice perturbations (Semenov and Latif, 2015; Chen et al., 2016b) and sensitivity to background state (Smith et al., 2017) in the atmospheric response to sea ice changes, lack of atmosphere-ice-ocean coupling in

many model experiments (Deser et al., 2016), and strong wintertime internal variability in the extratropics (Screen et al., 2014; Boland et al., 2017) (see also Cross-chapter Box 10.1).

As opposed to winter, the observed trend of the NAO over 1958-2014 is overall negative in summer associated with more recurrent blocking conditions over Greenland, in particular since the mid-1990s, thus contributing to accelerated ice melting (Fettweis et al., 2013; Hanna et al., 2015; Ding et al., 2017). The origin of the negative trend of the summer NAO is not clearly identified, and is hypothesized to be the result of combined influences (Lim et al., 2019). The recent observed negative NAO prevalence and related blocking over Greenland is not present in any of the CMIP5 models (Hanna et al., 2018) nor in the most recent CMIP6 historical simulations, which tends to produce opposite sign with decreased summertime blocking activity over Greenland and despite a clear reduction of the mean biases in the latest generation of models (Davini and D'Andrea, submitted).

Regarding the direct effects of external forcings, Gillett and Fyfe (2013) find a significant strengthening of the NAM in the CMIP5 historical ensemble, strongest in boreal autumn and winter. A single-model study suggests that aerosol changes may also have driven significant climate change in the Arctic in recent decades (Navarro et al., 2016) which would have been reflected in the NAO/NAM. However, a multi-model assessment of eight CMIP5 models finds no robust influence of aerosol changes onto the NAM (Gillett et al., 2013b). Ozone depletion does not have a robust detectable influence on long-term trends of the NAO/NAM (Maycock et al., 2018b) in contrast to the SAM (Section 3.7.2), but there are indications that extreme Arctic ozone depletion events and their surface expression are linked to an anomalously strong NAM (Calvo et al., 2015; Ivy et al., 2017). However, the direction of causality here is not clear.

These conclusions are supported by CMIP6 results based on single forcing ensembles (Figure 3.33:a). There is a slight tendency for positive trends of the winter NAM in historical simulations over 1958-2014 driven mainly by GHG increases. No contributions are found from the other external forcings, except for an apparent small negative trend due to natural forcing. Albeit weak, such a signal is consistent with the observed slow reduction of solar activity since the 1980s (Chapter 2 Section 2.1.1) whose influence would favor negative phases of NAM/NAO based on the fingerprint of the 11-year solar cycle extracted from models (Scaife et al., 2013; Andrews et al., 2015) or observations (Gray et al., 2016) in the Northern Hemisphere wintertime circulation. In winter, results are not sensitive to the metrics chosen for NAM throughout the report (Figure 3.33:a; also see Tech. Annex. AVI.1), by contrast to summertime. Fixed zonal indices (Jianping and Wang, 2003) do not exhibit any significant trends in summer NAM whatever the type of simulations of CMIP6, whereas positive trends are found in historical runs based on pattern indices (EOF, Lee et al., 2019). The sign of the trend, which is opposite to observational estimates, is associated with GHG forcing and is consistent with Davini and D'Andrea (submitted).

In summary, despite some model suggestions that anthropogenic forcings influence the NAM/NAO, the weakness of the model signals in the presence of pronounced internal variability indicates that there is little evidence for a significant role for anthropogenic forcings in driving the observed multidecadal variations of the NAM/NAO over the instrumental period. There is however *very high confidence* that the associated teleconnections have contributed to a significant fraction of observed multidecadal variability over the Northern Hemisphere continents and have modulated human-induced changes at regional scale. The difficulty in detecting and attributing NAM/NAO changes is mostly related to the larger role of internal variability relative to any human imprint over the historical period. However, although CMIP5 and CMIP6 models have medium to high performance in simulating the spatial features and the variance of the NAM/NAO and teleconnectivity (*high confidence*), there is an apparent signal-to-noise problem referred to as "paradox" as evident in seasonal hindcasts (Scaife and Smith, 2018). Whilst skillful NAO hindcast is demonstrated, it appears to have a relatively weak predictable signal and this may have possible implications in that the NAO response to external forcing could be too weak in models. The weakness of the signal has been related to chronic model biases in the persistence of the NAO/NAM regimes, which is critically underestimated in coupled models (Strommen and Palmer, 2019), and to the troposphere-stratosphere coupling which is too intermittent (O'Reilly et al., 2019a). Nonetheless, large ensembles and related new statistical techniques such as dynamical adjustment (Deser et al., 2016; Saffioti et al., 2016) allow us to better quantify the contributions of human-forced and internal components in observed changes in

temperature and precipitation over land affected by NAO/NAM teleconnectivity.

[START FIGURE 3.32 HERE]

Figure 3.32: Regression of Mean Sea Level Pressure (MSLP) anomalies (in hPa) onto the normalized principal component (PC) of the leading mode of variability obtained from empirical orthogonal decomposition (EOF) of the boreal winter (Dec.-Feb) MSLP poleward of 20ºN for the Northern Annular Mode (NAM, a) over 20-80°N, 90°W-40°E for the North Atlantic Oscillation (NAO, b), and poleward of 20ºS for the Southern Annular Mode (SAM, c) for the JRA-55 reanalysis. The selected period for NAO/NAM is 1958-2014 but 1979-2014 for SAM. (d-f) Same but for multi-model multi-member ensemble mean from CMIP6 historical simulations. Models are weighted in compositing to account for differences in their respective ensemble size. (g-i) Taylor diagram summarizing the representation of the modes in models and observations following Lee et al. (2019) for CMIP5 (light blue) and CMIP6 (red). The reference pattern is taken from JRA-55 (a-c). Ratio of standard deviation (radial distance), spatial correlation (radial angle) and resulting root-mean-squared-errors (solid isolines) are given from individual members and models and for other observational products (ERA-20C combined with ERA-Interim, NOAA-20CR atmospheric reanalyses, black dots). (j-l) Histogram of the trends built from all members and all the models PCs (light pink bars). Vertical lines in black stand for all the observational estimates. The red and light blue lines indicate the multi-model multi-member ensemble mean of CMIP6 and CMIP5, respectively. A total of 293 CMIP6 historical simulations from 35 models and 152 CMIP5 historical simulation from 39 models have been used for the computation.

[END FIGURE 3.32 HERE]

[START FIGURE 3.33 HERE]

Figure 3.33: Simulated and observed trends (hPa decade^{-1}) in NAM indices over 1958-2014 (a) and in SAM indices over 1979-2014 (b) for boreal winter (December-February average; DJF) and summer (June-August average; JJA). Ensemble mean, interquartile ranges and 5th and 95th percentiles are shown by boxes and whiskers based on CMIP6 DAMIP ensembles forced by individual forcings. The number of simulations used for computing the distribution is given in brackets with the colour code of the DAMIP ensemble. For grey shading (observations) and filled boxes, the indices are based on latitudinal difference of the zonally averaged mean sea level pressure (between 35ºN and 65ºN for the NAM and between 40ºS and 65ºS for the SAM as defined in Jianping and Wang (2003) and Gong and Wang (1999), respectively). For open boxes, the indices are defined as projection coefficients onto the EOF pattern as in Figure 3.32: but applied to the corresponding piControl simulations following Lee et al. (2019). Grey shading shows the range of observed trend among JRA-55, ERA-20C combined with ERA-Interim and NOAA-20CR.

[END FIGURE 3.33 HERE]

3.7.2 Southern Annular Mode

The Southern Annular Mode (SAM) consists of a meridional redistribution of atmospheric mass around Antarctica (Figure 3.32:e), associated with a meridional shift of the jet and surface westerlies over the Southern Ocean. SAM indices are variously defined as the difference in zonal-mean SLP between middle and high latitudes or via a principal-component analysis (Technical Annex AVI.2).

AR5 summarized that CMIP5 models have medium performance in reproducing the SAM with biases in shape and associated surface anomalies. It also concluded that the strengthening trend of the SAM in austral summer since the mid-20th century is *likely* to be due in part to stratospheric ozone depletion, and there was *medium confidence* that GHGs have also played a role. Based on proxy reconstructions, AR5 found with *medium confidence* that the SAM trend since 1950 was anomalous compared to the last 400 years.

Additional research has shown that CMIP5 models reproduce the spatial structure of SAM well, but tend to

overestimate its variability in austral summer at interannual time scales, albeit within the observational uncertainty (Zheng et al. 2013; Schenzinger and Osprey 2015; Figure 3.32:c,f,i). This is related to the models' tendency to simulate a slightly more persistent SAM circulation in summer than is found in the ERA-Interim reanalyses (Schenzinger and Osprey, 2015) due in part to too weak a negative feedback from tropospheric planetary waves (Simpson et al., 2013). CMIP6 models show improved performance in reproducing the spatial structure and interannual variance of the SAM in summer based on Lee et al. (2018) diagnostics (Figure 3.32:i), with a better match of its trend with reanalyses over 1979-2014 (Figure 3.32:), more realistic timescales of variability and improved positioning of the westerly jet which in CMIP5 models on average is located too far equatorward (Bracegirdle et al., submitted).

CMIP6 historical simulations capture the observed positive trend of summertime SAM since the 1970s (Figure 3.33:b). The chance for the observed 1980-2004 trend to occur only due to internal variability is less than 10% in many of the CMIP5 models according to Thomas et al. (2015), and with CMIP6 models the chance for the 1979-2014 trend is even lower (less than 5%; Figure 3.33:b). Although paleo-reconstructions of the SAM index are uncertain and vary in terms of long-term trends (Hessl et al., 2017), new reconstructions show that the summertime SAM trend since the mid-20th century is outside the 5-95% range of its pre-industrial variability, which well matches the trend range of CMIP5 pre-industrual control simulations (Dätwyler et al., 2018).

New research since AR5 continues to indicate that both stratospheric ozone depletion and increasing GHGs have contributed to the strengthening trend of the SAM during austral summer in recent decades (Solomon and Polvani, 2016), with ozone depletion dominating, in general agreement with AR5 (Gerber and Son, 2014; Son et al., 2018). The influences of ozone changes and GHG increases are confirmed based on CMIP6 single forcing historical simulations. For the period 1979-2014, the ozone and GHG contributions are nearly equal in summer while the ozone influence is much weaker in winter, and the results are not sensitive to the metrics chosen for SAM throughout the report (Figure 3.33:b). Since ~1997, the effective abundance of ozone-depleting halogen compounds has been decreasing in the stratosphere (WMO, 2018), leading to a stabilization or even a reversal of the influence of stratospheric ozone depletion. Accordingly, its impact on summertime SAM trends is more dominant during earlier periods dominated by declining ozone (such as 1979-2005) than in the last decade. Ozone recovery since ~2000 has even caused a pause in the strengthening of the summertime SAM (Banerjee et al., submitted), although one cannot rule out some influence from internal variability. Based on CMIP5, it is also found that high-top models (extending above the stratopause, typically 1hPa) tend to simulate stronger summertime trends in the late 20th century than their low-top counterparts (model top within the stratosphere, typically 10hPa) despite large inter-model diversity (Rea et al., 2018; Son et al., 2018). It is however unclear to what extent the increased vertical resolution is causing this behaviour, versus other differences between high-top and low-top configurations, such as additional physical processes operating in the stratosphere or interactive ozone chemistry (Gillett et al., 2003; Sigmond et al., 2008; Rea et al., 2018). At the surface, Ogawa et al. (2015) demonstrate with an AGCM the importance of sharp midlatitude SST gradients for stratospheric ozone depletion to induce a strengthening of the SAM in summer, suggesting a need for improved ocean horizontal simulation. While some studies find anthropogenic aerosol influence on the summertime SAM (Gillett et al., 2013b; Rotstayn, 2013), recent studies with a larger multi-model ensemble find that this effect is not robust (Steptoe et al., 2016; Choi et al., 2019), consistent with CMIP6 single forcing ensembles (Figure 3.33:). In the CMIP5 simulations, volcanic stratospheric aerosol has a significant weakening effect on the SAM in autumn and winter (Gillett and Fyfe, 2013), but there is no evidence that this effect leads to a significant multidecadal trend since the late 20th century. Beyond external forcing, Fogt et al. (2017) show a significant association of tropical Pacific variability with the summertime SAM trend since the mid-20th century, but this is based on a single AGCM experiment.

On longer time scales, last Millennium experiments by CMIP5 models fail to capture multicentennial variability seen in the reconstructions for the pre-industrial era (Abram et al., 2014; Dätwyler et al., 2018; Figure 3.34:), although there is large uncertainty among reconstructions (Hessl et al., 2017). This model failure suggests that either the variations in the imposed insolation may be too weak, models are insufficiently sensitive to such variations, or internal variability including that associated with tropical Pacific variability is underrepresented (Abram et al., 2014), or a combinaison of all these factors. However,

notwithstanding the aforementioned limitations of the reconstructions, the present anomalously positive state of the SAM is unprecedented since about the year 1400 in all reconstrutions. CMIP5 last-millennium simulations only capture this anomalous state during the final decades of the simulations dominated by human influence; this state is outside the range of variability characteristic of pre-industrial times.

In summary, there is *high confidence* that stratospheric ozone depletion and GHG increases have contributed to the strengthening trend of the summer SAM during the late 20th century. This assessment is supported by further model evidence of the influence of ozone depletion and GHG increases on the SAM with improved models since AR5. While ozone depletion was the dominant driver of the trend over 1980-2000 (*high confidence*), its influence is reduced after ~2000 because stratospheric ozone no longer declined, resulting in comparable contributions from long-lived GHG and ozone changes to trends over the 1979-2014 period as diagnosed from CMIP6 simulations. CMIP5 models reproduce the spatial structure of the summertime SAM well, despite biases in its magnitude and persistence and a large spread in the intensity of the SAM response to ozone and GHG changes (*high confidence*). CMIP6 models reproduce the spatiotemporal features and recent multidecadal trend of the summertime SAM better than CMIP5 models (*medium confidence*). CMIP5 models do not capture multicentennial variability of the SAM found in proxy reconstructions. It is however unclear whether this reflects a model or an observational shortcoming.

[START FIGURE 3.34 HERE]

Figure 3.34: SAM indices in the last millennium. SAM reconstructions (top: annual mean, middle: December-January-February) by Abram et al. (2014), Villalba et al. (2012) and Dätwyler et al. (2018). 7-year (thin lines) and 70-year (thick lines) moving averages. (bottom) CMIP5 Last Millennium simulations extended by historical simulations. 7-year (grey lines) and 70-year (thin black lines) moving averages for individual simulations and the MME mean of the 70-year running means (thick black line). Normalized with AD 1961-1990 means and standard deviations.

[END FIGURE 3.34 HERE]

3.7.3 El Niño-Southern Oscillation

The El Niño-Southern Oscillation (ENSO), which is generated via seasonally modulated interactions between the tropical Pacific ocean and atmosphere, influences severe weather, rainfall, river flow and agricultural production over large parts of the world (McPhaden et al. 2006). In fact, the impacts of ENSO are so large that knowledge of its current phase and forecasts of its future phase largely underpin many seasonal rainfall and temperature forecasts worldwide (Technical Annex AVI.3).

AR5 noted that there have been clear improvements in simulation of ENSO through previous generations of CMIP models (Flato et al., 2013), such that many CMIP5 models displayed behaviour that was qualitatively similar to that of the observed ENSO (e.g., Guilyardi et al., 2012). However, systematic errors were identified in the models' representation of the Tropical Pacific mean state and aspects of their interannual variability that impact quantitative comparisons. The AR5 assessment of ENSO concluded that considerable observed inter-decadal modulations in ENSO amplitude and spatial pattern were largely consistent with unforced model simulations. Thus, there was *low confidence* in the role of a human-induced influence in these changes.

Observed ENSO amplitude, which is measured by the standard deviation of central Pacific SST anomalies, and the lifecycle of events are both reasonably well reproduced by most CMIP5 and CMIP6 models (Figure 3.35:; Bellenger et al., 2014; Planton et al., submitted). The average CMIP5 model ENSO amplitude is slightly lower than that observed, while the average CMIP6 model ENSO amplitude displays slightly more variability than observed (Figure 3.35:). The modeled ENSO amplitude, however, is highly variable with many CMIP5 and CMIP6 models displaying more or less variability than observed (Grose et al., submitted; Planton et al., submitted; Stevenson, 2012).

[START FIGURE 3.35 HERE]

Figure 3.35: Life cycle of (left) El Niño and (right) La Niña events in observations (black) and historical simulations in CMIP5 (blue; extended with RCP4.5) and CMIP6 (red). An event is detected when December Niño 3.4 SST anomaly in year zero exceeds 0.5 times its standard deviation for 1950-2010. The horizontal axis represents month relative to the reference December, with numbers in parentheses indicating relative years. (a, b) Composites of Niño 3.4 SST anomalies (ºC). Shading and lines represent 5th-95th percentiles and ensemble means, respectively. (c, d) Mean durations (months) of El Niño and La Niña events defined as number of months in individual events for which Niño 3.4 SST anomaly exceeds 0.25 times its December standard deviation. The horizontal axis indicates modelling centres. The boxes and whiskers represent multi-model ensemble median, interquartile ranges and 5th and 95th percentiles of CMIP5 and CMIP6. All based on 5-month running mean SST anomalies with triangular-weights after linear detrending. Produced with 257 members from 38 CMIP6 models and 115 members from 35 CMIP5 models.

[END FIGURE 3.35 HERE]

ENSO events are often synchronized to the seasonal cycle in the observations, as the associated SST anomalies tend to peak in boreal winter (November-January) and be at their weakest in the boreal spring (March-April) (Harrison and Larkin, 1998; Larkin and Harrison, 2002). The majority of CMIP5 and CMIP6 models broadly reproduce the timing of ENSOs SST variability in the central equatorial Pacific (Abellán et al., 2017; Grose et al., submitted; Planton et al., submitted; Taschetto et al., 2014; Figure 3.36:). However, CMIP5 models, while displaying an improvement on CMIP3 models, appear to underrepresent the magnitude of the seasonal variance modulation (Bellenger et al. 2014;). This under-representation of seasonal variance modulation continues in CMIP6 models (Planton et al., submitted; Figure 3.36:).

[START FIGURE 3.36 HERE]

Figure 3.36: ENSO seasonality diagnosed from Niño 3.4 SST anomalies in observations (black) and historical simulations in CMIP5 (blue; extended with RCP4.5) and CMIP6 (red). (a) Climatological standard deviation of monthly Niño 3.4 SST (°C). Shading and lines represent 5th-95th percentiles and ensemble means, respectively. (b) Seasonality metric defined as the ratio of climatological standard deviation of Niño 3.4 SST between November-January (NDJ) and March-May (MAM). The boxes and whiskers represent multi-model ensemble median, interquartile ranges and 5th and 95th percentiles of CMIP5 and CMIP6 individually. Produced with 257 members from 38 CMIP6 models and 115 members from 35 CMIP5 models.

[END FIGURE 3.36 HERE]

Observations show strong multi-decadal modulation of ENSO variability throughout the 20th century, with the most recent period displaying larger variability while the mid-century displays relatively low ENSO variability. As reported in Chapter 2 Section 2.4.1.1, analysis of many paleo reconstructions of ENSO over the past 500-1000 years suggests that recent ENSO variability appears to be higher than during the 1400-1850 period (Chapter 2 Figure 2.40; Hope et al., 2017; Li et al., 2013; McGregor et al., 2013). Contrary to this evidence, however, coral records from within the tropical Pacific suggest that ENSO had higher variability than present during the mid 17th century. The former suggests that external forcing plays a role in the ENSO variance changes (Hope et al., 2017), while the latter suggests a prominent role for internal climate variability (Cobb et al., 2013). Large ensembles of single model or multiple model simulations do not find strong trends in ENSO variability over the historical period, which suggests that external forcing has not yet modulated ENSO variability with a magnitude that exceeds the range of internal variability (Hope et al., 2017; Stevenson et al., 2017; Maher et al., 2018b).

Most CMIP5 and CMIP6 models are found to realistically represent the intensity and location of maximum SST anomalies during ENSO events (Grose et al., submitted; Kim and Yu, 2012; Taschetto et al., 2014).

However, systematic biases exist in the representation of ENSO in CMIP5 that are related to SST anomalies as the majority of models display anomalies that: i) extend too far to the west (Capotondi et al., 2014; Taschetto et al., 2014); and ii) have meridional widths that are too narrow (Zhang and Jin, 2012) compared to the observations. CMIP6 models display a significant improvement in the longitudinal representation of ENSO SST anomalies relative to CMIP5 models, however the models still display systematic biases in the zonal extent and meridional width (Fasullo et al., submitted; Planton et al., submitted). The ENSO phase asymmetry, where observed strong El Niño events are larger and have a shorter duration than strong La Niña events (Ohba and Ueda, 2009; Frauen and Dommenget, 2010), is also underrepresented in both CMIP5 and CMIP6 models (Fasullo et al., submitted; Planton et al., submitted; Zhang and Sun, 2014). In this instance, both CMIP model phases display El Niño events that are longer than those observed, La Niña events which are shorter than those observed, and there is very little asymertry in the magnitude and duration of simulated El Niño and La Niña phases (Figure 3.35:). Roberts et al. (2018) find an improvement in amplitude asymmetry in a HighResMIP model, but the underrepresentation remains.

The continuum of El Niño events are typically stratified into two types (or flavours), Central Pacific (CP) and East Pacific (EP), where the name denotes the location of the events' largest SST anomalies (Technical Annex AVI.3). As discussed in Chapter 2, Section 2.4.1.2, the different types of events tend to produce different teleconnections and climatic impacts. For most of the CMIP5 models, the characteristics of El Niño events of these two flavours are comparable to the observations (Taschetto et al., 2014). The short observational record displays an increase in the number of the CP type events in recent decades (Ashok et al., 2007; McPhaden et al., 2011), which has also been identified as unusual in the context of the last 500-yrs by a recent paleo-climatic reconstruction (Section 2.4.1.3; Freund et al., 2019). However, the short observational record, observational (L'Heureux et al., 2013) and paleo-climatic reconstruction uncertainties preclude firm conclusions being made about the long-term changes in the occurrence of different El Niño event types. Initial analysis with a select number of CMIP3 models suggested that there may be a forced component to this recent prominence of CP type events (Yeh et al., 2009), but analysis since then suggests that this behavior is i) consistent with that expected from internal climate variability (Newman et al., 2011); and ii) not apparent across the full CMIP5 ensemble of historical simulations (Taschetto et al., 2014). Analysis of single models large ensemble of simulations suggests that changes to ENSO event type in response to historical radiative forcing is not significant (Stevenson et al., 2017). These same results, however, also suggest multiple forcings can have significant impacts on ENSO type and that the net response will depend on the accurate representation of the balance of these forcings (Stevenson et al., 2017).

The impacts of ENSO outside of the tropical Pacific largely arise through atmospheric teleconnections that are driven by changes in deep convection and atmospheric heating (Yeh et al., 2018). The teleconnections to higher latitudes are forced by waves that propagate into the extratropics (Hoskins and Karoly, 1981) and respectively excite a Pacific-North American (PNA) pattern (Horel and Wallace, 1981) and Pacific-South American (PSA) pattern (Karoly, 1989; Irving and Simmonds, 2016) in the Northern and Southern Hemispheres. Given the impact of these teleconnections on climate and extremes around the globe, it is important to understand how well they are reproduced in CMIP models. What has also become clear is that spatial correlations of ENSO's teleconnections over relatively short periods may not be the most effective way to assess these relationships (Langenbrunner and Neelin, 2013; Perry et al., 2017). This is because the spatial patterns are significantly impacted by internal atmospheric variability on relatively short time scales (<100 years) (Batehup et al., 2015; Perry et al., 2017). However, looking at simplified metrics like the agreement in the sign of the teleconnections (Langenbrunner and Neelin, 2013), regional average teleconnection strength over land (Perry et al., 2019), or a combination of both (Power and Delage, 2018) provides a more robust depiction of the teleconnection representation. Examining sign agreement for the teleconnection patterns, ensembles of CMIP5 AMIP simulations display broad spatial regions with high sign agreement with the observations, suggesting that the model ensemble is producing useful information regarding the teleconnected precipitation signal (Langenbrunner and Neelin, 2013; Figure 3.37:). Looking at regional averages of CMIP5 historical simulations, Power and Delage (2018) show that the average coupled model teleconnection pattern reproduces the sign of the observed teleconnections in the majority of the 25 SREX defined regions. The sign agreement between the observed teleconnection and the MMM teleconnection remains strong in CMIP6 (18 out of 20 displayed regions) (Figure 3.37:), and the observed DJF teleconnection strength falls within the modelled range in all of the displayed regions for temperature

and precipitation. It is noted, however, that while there is broad agreement in ENSO teleconnections between CMIP6 models and observations during DJF, there are regions and seasons where the modelled teleconnection strength is outside of the observed range (Chen et al., submitted).

[START FIGURE 3.37 HERE]

Figure 3.37: Observed and simulated ENSO teleconnections for 2m-temperature and precipitation during December-January-February. Teleconnections are identified by linear regression with the Niño 3.4 SST index based on ERSSTv5 during the period 1958-2014. Maps show observed patterns for temperature from the Berkeley Earth dataset over land and from ERSSTv5 over ocean (top) and for precipitation from GPCC over land and GPCP over ocean (contour, period: 1979-2014). Distributions of regression coefficients for regional means drawn from 261 historical simulations from 30 CMIP6 models are provided for a subset of pre-defined AR6 regions in the Atlas for temperature (light pink, top) and precipitation (green, bottom). Multi-model multi-member ensemble means are indicated by thick vertical coloured lines (red for temperature, blue for precipitation). Black vertical lines stand for observational estimates based on Berkeley Earth and GISTEMP datasets for temperature and from GPCC and GPCP datasets for precipitation.

[END FIGURE 3.37 HERE]

Most CMIP5 and CMIP6 models exhibit ENSO behavior that, to first order, is qualitatively similar to that of the observed ENSO. Many studies are now delving deeper into the models to understand if they are accurately producing the dynamics driving ENSO and its initiation (Bayr et al., 2019; Bellenger et al., 2014; Jin et al., 2006; Planton et al., submitted; Vijayeta and Dommenget, 2017). For both CMIP3 and CMIP5, diagnostics of ENSO event growth appear to show that the models, while producing ENSO variability that is qualitatively similar to that observed, do not represent the balance of the underlying dynamics well. The first look at ENSO in CMIP6 models provided by Planton et al. (submitted) suggests that these issues remain.The atmospheric Bjerknes feedback is too weak in the majority of models, while fluxes of heat at the surface are also too weak in the majority of models. The former restricts event growth, while the latter restricts event damping, which when combined allow most models to produce variability in a range that is consistent with the observations (Bellenger et al., 2014; Kim et al., 2014b; Vijayeta and Dommenget, 2017; Bayr et al., 2019).

To conclude, the instrumental record, paleo proxy evidence through the Holocene and coupled models all suggest that ENSO can display considerable modulations in amplitude, pattern and period (see also Section 2.4.1). Further to this, paleo-proxy evidence indicates (*medium confidence*) that ENSO activity in the late 20th and early 21st century was greater than at any time between 1400 and 1850 (Section 2.4.1). ENSO representation in CMIP5 models displayed a significant improvement from the representation of ENSO variability in CMIP3 models, which displayed much more intermodel spread in standard deviation, and stronger biennial tendencies (Guilyardi et al., 2012; Flato et al., 2013). In general there has been no large step changes in the representation of ENSO between CMIP5 and CMIP6, however, CMIP6 models appear to better represent some key ENSO charactoristics (Planton et al., submitted). Coupled models display large changes of ENSO behaviour in the absence of external forcing changes, and little-to-no variance sensitivity to anthropogenic forcing. Thus, we have *low confidence* that anthropogenic forcing has led to the observed changes of ENSO activity.

Chapter 2 reported *low confidence* that the apparent change from eastern Pacific to central Pacific type El Niño events that occurred in the last 20-30 years was representative of a long term change. While some coupled models do suggest external forcing may impact El Niño event type, model simulations also suggest that what has been observed is well within the range of natural variability. Thus, there is *low confidence* that anthropogenic forcing has had an impact on observed changes in El Niño event type.

3.7.4 Indian Ocean Basin and Dipole Modes

The Indian Ocean Basin (IOB) and Dipole (IOD) modes are the two leading modes of interannual SST variability over the tropical Indian Ocean, featuring basin-wide warming/cooling and an east-west dipole of SST anomalies, respectively (Technical Annex AVI.4). The IOD mode is anchored to boreal summer to autumn by the air-sea feedback, and develops often in concert with ENSO. Driven by matured ENSO, the IOB mode peaks in boreal spring and often persists into the subsequent summer. Similar patterns of Indian Ocean SST variability also dominate its decadal and longer time scale variability (Han et al., 2014b).

AR5 concluded that models show high and medium performance in reproducing IOB and IOD, respectively (*medium confidence*), with difficulty in reproducing persistence of the IOB and pattern and magnitude of IOD. There was *low confidence* that changes in the IOD were detectable or attributable to human influence. GHG-induced warming projects onto the IOB, and its 20th century trend is captured by CMIP3 20th century simulations.

Since the AR5, CMIP5 models have been analysed in detail, finding that most of the models qualitatively reproduce the spatial and seasonal features of the IOB and IOD modes (Chu et al., 2014; Liu et al., 2014; Tao et al., 2016b). Improvements in simulating the IOB mode since CMIP3 have been identified in reduced multi-model mean bias and inter-model spread (Tao et al., 2016b). CMIP5 models overall capture the transition from the IOD to IOB modes during an ENSO event (Tao et al., 2016b). The IOB mode is forced through the cross-equatorial wind-evaporation-SST feedback triggered by ENSO-forced anomalous ocean Rossby waves that propagate to the shallow climatological thermocline dome in the tropical southwestern Indian Ocean (Du et al., 2009). Consistently, models with a deeper climatological thermocline dome produce a weaker and less persistent IOB mode (Li et al., 2015b; Zheng et al., 2016). The deep thermocline bias remains in the ensemble mean of CMIP5 models due to a common surface easterly wind bias over the equatorial Indian Ocean (Lee et al., 2013) associated with a weaker South Asian summer monsoon (Li et al., 2015c). However, the influence of this systematic bias is compensated by other biases, resulting in a realistic IOB magnitude (Tao et al., 2016b). By contrast, the IOD magnitude is overestimated by CMIP5 models on average, with noticeable improvements from CMIP3 models (Liu et al., 2014). Both a shallower climatological thermocline off Sumatra and Java and biases in ENSO contribute to this IOD magnitude bias (Liu et al., 2014). Improvement in CMIP6 models is unknown due to lack of literature.

The observed Indian Ocean basin-average SST increase on multidecadal and centennial time scales is well represented by CMIP5 historical simulations, and attributed to compensating effects by GHGs and anthropogenic aerosols mainly through aerosol-cloud interactions (Dong and Zhou, 2014; Dong et al., 2014b). The observed SST trend is larger in the western than eastern tropical Indian Ocean, which leads to an apparent upward trend of the IOD index, but this trend is statistically insignificant (Chapter 2 Section 2.4.3). CMIP5 models capture this warming pattern, which may be associated with Walker circulation weakening over the Indian Ocean due to GHG forcing (Dong and Zhou, 2014). However, strong internal decadal IOD-like variability and observational uncertainty preclude validation of the simulated modulations and attribution (Cai et al., 2013; Gopika et al., submitted; Han et al., 2014b). Such a positive IOD-like change in equatorial zonal SST gradient suggests an increase in the frequency of extreme positive events (Cai et al., 2014) and skewness (Cowan et al., 2015) of the IOD mode. While proxy reconstructions indeed show IOD intensification and increase of extreme positive events in the 20th century (Chapter 2 Section 2.4.3), this trend still remains in the range of internal variablity simulated by CMIP5 models (Abram et al., submitted). Likewise, while a strengthening tendency of the ENSO-IOB mode correlation and resultant intensification of the IOB mode are found in historical or future simulations in selected CMIP5 models (Hu et al., 2014; Tao et al., 2015), such a change has not been detected in observational records.

After linear detrending, Pacific decadal variability (PDV) has been identified as the major driver of the decadal-to-multidecadal IOB mode (Dong et al., 2016). However, correlation between the PDV and a decadal IOB index, defined from linearly detrended SST, changed from positive to negative during the 1980s (Han et al., 2014a). The accelerating anthropogenic Indian Ocean warming and recovery from the eruptions of El Chichón in 1982 and Pinatubo in 1991, may have overwhelmed the PDV influence, and explain this change (Dong and McPhaden, 2017; Zhang et al., 2018a). However, the low number of statistical degrees of

freedom hampers clear detection of human influence in this correlation change.

To summarize, evidence is *limited* that anthropogenic forcing has changed the interannual IOB and IOD. On decadal-to-multidecadal time scales, there is *low confidence* that human influence has caused a reversal of the correlation between PDV and the decadal IOB mode. The low level of confidence in the latter assessment is due to the short observational record, limited number of models used for the attribution, lack of model evaluation on reproducibility of the decadal IOB mode, and uncertainty in the contribution from volcanic aerosols. Nevertheless, models have medium overall performance in reproducing both the interannual IOB and IOD modes, with an apparently good skill in reproducing the IOB magnitude arising from compensation of biases in the formation process (*high confidence*).

3.7.5 Atlantic Meridional and Zonal Modes

The Atlantic Equatorial Mode, often referred to as the Atlantic Niño, and Atlantic Meridional Mode (AMM) are the two leading basin wide patterns of interannual-to-decadal variability in the tropical Atlantic (Technical Annex AVI.5). Akin to ENSO in the Pacific, the term Atlantic Niño is broadly used to refer to years when the SSTs in the tropical eastern Atlantic basin along the cold tongue are significantly warmer than the climatological average. The AMM is characterized by anomalous cross-equatorial gradients in SST. Both modes are associated with altered strength of the ITCZ and/or latitudinal shifts in the ITCZ, which locally affect African and American monsoon systems and remotely affect Tropical Pacific and Indian Ocean variability through inter-basins teleconnections.

AR5 mentioned considerable difficulty simulating both Atlantic Niño and AMM despite some improvements in CMIP5 for some models. Severe biases in mean state and variance for both SST and atmospheric dynamics including rainfall (e.g. double ITCZ) as well as teleconnections were reported. AR5 highlighted the complexity of the Tropical Atlantic biases, which were explained by multiple sources both in the ocean and atmosphere.

Since AR5, further understanding of the major persistent biases in models has been reported (Xu et al., 2014; Jouanno et al., 2017; Yang et al., 2017b; Dippe et al., 2018; Lübbecke et al., 2018; Voldoire et al., 2019a). Critical errors in equatorial and basin wide trade winds, cloud cover and ocean vertical mixing and dynamics both locally and in remote subtropical upwelling regions, key thermodynamic ocean-atmosphere feedbacks, tropical land-atmosphere interaction, have been shown to be detrimental to the representation of both Atlantic Niño and AMM leading to poor teleconnectivity over land (Rodríguez-Fonseca et al., 2015) and between tropical basins (Ott et al., 2015).

Despite some improvements (Richter et al., 2014; Nnamchi et al., 2015) mean biases are so large that the mean east-west tridimensional temperature gradient at the equator remains opposite to observed in two thirds of the CMIP5 models (Section 3.5.1.1) which clearly affect the simulation of the Atlantic Niño and associated dynamics (Muñoz et al., 2012; Ding et al., 2015; Deppenmeier et al., 2016). The interhemispheric SST gradient is also systematically underestimated in models with erroneously too cold mean state in the northern part of the Tropical Atlantic ocean and too warm conditions in the Southern Atlantic basin. The seasonality is poorly reproduced and the wind-SST coupling is weaker than observed so that altogether, and despite AMM-like variability in 20th century climate simulations, AMM is not the dominant Atlantic mode in all CMIP5 models (Liu et al., 2013; Amaya et al., 2017). These biases translate into biases in modelling the ITCZ (Flato et al., 2013). Similar biases were found in experiments using CMIP5 models but with different mean background state, such as Last Glacial Maximum, Mid-Holocene and future scenario simulations (Brierley and Wainer, 2017). First analyses from CMIP6 show encouraging results in the representation of Atlantic Niño and AMM modes of variability in terms of amplitude and seasonality. Some models now display very small biases but persistent errors still remain on average in the timing of the modes and in the coupled nature of the modes, i.e. the strength of the link between ocean (SST, mixed layer depth) and atmospheric (wind) anomalies (Richter and Tokinaga, submitted).

There are some recent indications that increasing model resolution both vertically and horizontally, in the

ocean and atmospheric component (Richter, 2015; Small et al., 2015; Harlaß et al., 2018), could partly alleviate tropical Atlantic biases in mean state, seasonality, interannual-to-decadal variability and associated teleconnectivity over land (West African monsoon, Steinig et al., 2018) and the represenation of tropical cyclones (Roberts et al., 2015b), though this result appears to be model dependent (Goubanova et al., 2019). Preliminary results from CMIP6 tend to confirm such a statement which indicates that increasing resolution is not the unique way to address the biases in the Tropical Atlantic (Richter and Tokinaga, submitted).

In summary, based on CMIP5 and CMIP6 results, there is no robust evidence that observed changes in either Atlantic Niño or AMM modes and associated teleconnections are detectable and attributable to anthropogenic forcing. Considering the physical processes responsible for model biases in these modes, it is probable that increasing resolution in both ocean and atmosphere components may be an opportunity for progress as evidenced for some individual models (Roberts et al., 2018) but needs confirmation from a multi-model perspective.

The lack of confidence on possible human influence on the Atlantic Modes and associated teleconnections is dictated by the poor fidelity of CMIP5 and CMIP6 models in reproducing the mean tropical Atlantic climate, its seasonality and variability, despite hint for some improvement in CMIP6, as well as other sources of uncertainties related to limited process understanding in the observations (Foltz et al., 2019), the response of the tropical Atlantic climate to anthropogenic aerorol forcing (Booth et al., 2012; Zhang et al., 2013a) and the presence of strong multidecadal fluctuations related to AMV (Section 3.7.7) and cross-tropical basins interactions (Martín-Rey et al., 2018; Cai et al., 2019). For instance, there has been an observed decrease in the variability of the Atlantic Niño since the 1960s (Tokinaga and Xie, 2011). The fact that most models poorly represent the climatology and variability of the tropical Atlantic combined with the short observational record makes it difficult to place the recent observed changes in the context of natural internal multi-annual variability versus anthropogenic forcing.

3.7.6 Pacific Decadal Variability

Pacific decadal variability (PDV) is the generic term for the modes of variability in the Pacific Ocean that vary on decadal to interdecadal timescales. PDV and its related teleconnection encompasses the Pacific Decadal Oscillation (PDO; Mantua et al. 1997; Mantua and Hare 2002; Zhang et al. 1997), an anomalous SST pattern in the North Pacific, as well as a broader structure associated with Pacific-wide SSTs termed the Interdecadal Pacific Oscillation (IPO; Power et al. 1999; Folland et al. 2002; Henley et al. 2015). Since the PDO and IPO indices are highly correlated, this section assesses them together as the PDV (Technical Annex AVI.6).

AR5 mentioned an overall *limited* level of evidence for both CMIP3 and CMIP5 evaluation of the Pacific modes at interdecadal timescale leading to *low confidence* statements about the models' performance in reproducing PDV and similarly *low confidence* in the attribution of the observed PDV changes to human influence.

The implication of PDV in the observed slowdown of the GMST warming rate in the early 2000s (Cross-Chapter Box 3.1:) has triggered considerable research on decadal climate variability and predictability since the AR5 (Meehl et al., 2013, 2016b; England et al., 2014; Dai et al., 2015; Kosaka and Xie, 2016; Cassou et al., 2018). Many studies find that the broad spatial characteristics of PDV are reasonably well represented in unforced climate models (Henley 2017; Newman et al. 2016) and in historical simulations in CMIP5 and CMIP6 (Figure 3.38:), although sensitivity to methodology used to remove the externally-forced component of the SST exists (Bonfils and Santer, 2011; Xu and Hu, 2018). Compared with CMIP3, CMIP5 models exhibit overall slightly better performance in reproducing PDV and associated teleconnections (Polade et al., 2013; Joshi and Kucharski, 2017), and also smaller inter-model spread (Lyu et al., 2016). CMIP6 models on average show slightly improved reproduction of the PDV spatial structure than CMIP5 (Figure 3.38:a-c; Fasullo et al., submitted). SST anomalies in the subtropical South Pacific lobe remain however too weak relative to the equatorial and North Pacific lobes in both CMIP control and historical simulations (Henley et al., 2017).

Biases in the PDV temporal properties and amplitude are present in CMIP5 (Cheung et al., 2017; Henley, 2017). While model evaluation is severely hampered by short observational records, the duration of PDV phases appears to be shorter in coupled models than in observations, and correspondingly the ratio of decadal to interannual variance is underestimated (Henley et al. 2017; Figure 3.38:e,f). This apparent bias may be associated with overly biennial behaviour of Pacific trade wind variability and related ENSO activity (Kociuba and Power, 2015), although basin-scale ENSO influence in the extratropics at decadal timescales is very diverse among both CMIP3 and CMIP5 models, being controlled by multiple factors (Nidheesh et al., 2017). In terms of amplitude, the variance of the PDV index after decadal filtering is significantly weaker in the concatenated CMIP5 ensemble than the observational counterpart ($p < 0.05$ with F test). The observed fluctuations of PDV over the historical period often lay in the tails of the model distributions (Figure 3.38:e,f). Even if one cannot rule out that the observed PDV over the instrumental era represents an exceptional period of variability, the tendency of the CMIP5 models to systematically underestimate the low frequency variance is likely due to an incomplete representation of decadal-scale mechanisms in climate models. This situation is slightly improved in CMIP6 historical simulations but remains a concern (Fasullo et al., submitted). The results of McGregor et al. (2018) suggest that the underrepresentation of the magnitude stems from Atlantic mean SST bias through inter-basin coupling.

While PDV is primarily understood as an internal mode of variability (Si and Hu, 2017), there are some indications that anthropogenic forcing has partly contributed to past PDV evolution (Dong et al., 2014a). However, the level of evidence is *limited* because of the difficulty in correctly separating internal versus externally forced components in the observed SST. Part of the anthropogenically-induced warming signal might project onto the PDV (Bonfils and Santer, 2011; Xu and Hu, 2018). Over the last two to three decades, anthropogenic aerosols are suggested to have driven part of the PDV especially in the North Pacific (Yeh et al., 2013; Boo et al., 2015; Smith et al., 2016), while influence from both anthropogenic and volcanic aerosols are suggested on the tropial PDV (Maher et al., 2015; Takahashi and Watanabe, 2016). However, the mechanism is unclear and such a response is not robustly identified across CMIP5 models (Hua et al., 2018; Oudar et al., 2018). Alternatively, inter-basin teleconnections associated with the warming of the North Atlantic Ocean related to the mid-1990s phase shift of the AMV (McGregor et al., 2014; Li et al., 2015d; Chikamoto et al., 2016; Kucharski et al., 2016; Ruprich-Robert et al., 2017), and also in the Indian Ocean (Luo et al., 2012), could have favoured a delayed PDV transition to its negative phase in the 2000s. Considering the potential role of external forcing on the Indian Ocean decadal varability (Section 3.7.4) and AMV (Section 3.7.7), human influence on PDV would be indirect through changes in these ocean basins, being then imported to the Pacific via inter-basin coupling. However, this human influence on AMV, and how consistently the inter-basin processes affect PDV phase shifts, are uncertain. Lastly, the multimodel ensemble mean computed from CMIP6 historical simulations shows slightly stronger variation than the CMIP5 counterpart, suggesting a greater influence from anthropogenic and natural forcings. However, the magnitude of the forced signal relative to the ensemble spread is very low and not in phase with the observed PDV evolution (Figure 3.38:), in contrast to AMV (Section 3.7.7).

In CMIP5 last millennium simulations, there is no consistency in temporal variations of PDV across the ensemble (Fleming and Anchukaitis, 2016). This supports the notion that PDV is internal in nature. This issue remains difficult to firmly conclude because of short instrumental observations and the fact that paleoclimate recontructions of PDV have too poor a level of agreement for a rigorous model evaluation of PDV in past millennia (Henley, 2017).

To conclude, there is *low confidence* on whether human influence has induced any detectable changes in the PDV. This assessment is due to inconsistent results amongst models on anthropogenic influence, still limited understanding of physical mechanisms affecting the PDV and difficulties in clearly separating the externally forced versus internally generated components of Pacific variability at decadal timescales. Moreover, model evaluation is severely hampered by short observational records and poor agreement among paleoclimate reconstructions. Despite the limitations of these model-observation comparisons, CMIP5 models, on average, are *very likely* to underestimate PDV magnitude, while the simulated spatial structure is broadly realistic, but with a clear bias in the South Pacific (*medium confidence*). CMIP6 models tend to show better overall performance in spatial structure and magnitude of PDV, but there is *low confidence* in such a statement due to the lack of literature.

[START FIGURE 3.38 HERE]

Figure 3.38: PDV spatio-temporal properties in observations and models. (a, b) SST anomalies (ºC) regressed onto the Tripole Index (TPI; Henley et al., 2015) for 1900-2014 in (a) ERSSTv5 and (b) CMIP6 historical simulations (MME composite). A 10-year low-pass filter has been applied beforehand. (c) A Taylor diagram summarizing the representation of the PDV pattern in models and observations over [40ºS-60ºN, 110ºE-70ºW] for CMIP5 (light blue) and CMIP6 (red). The reference pattern is taken from ERSSTv5. Black dots indicate other observational products (ERSSTv3b and HadISSTv1). (d) Autocorrelation of unfiltered monthly TPI at lag 1 year ("unsmoothed") and 10-year low-pass filtered TPI at lag 10 years ("Low-Pass") for observations (grey shading) and 115-year chunks of piControl simulations (open boxes) and historical ensemble simulations (filled boxes) over 1900-2014 from CMIP5 and CMIP6. (e) As in (d), but standard deviation of unfiltered and filtered TPI (ºC). Boxes and whiskers show mean, interquartile ranges and 5th and 95th percentiles. (f) Time series of 10-year low-pass filtered TPI (ºC) in ERSSTv5 (black) and CMIP5 and CMIP6 historical simulations. The thick red and light blue lines are the MME mean for the historical simulations in CMIP5 and CMIP6, respectively, and the envelopes represent the ±2 standard deviation range across ensemble members. 39 models and 149 historical members have been used for evaluation in CMIP5; 29 models and 250 historical members for CMIP6.

[END FIGURE 3.38 HERE]

3.7.7 Atlantic Multidecadal Variability

Atlantic Multidecadal Variability (AMV) refers to a climate mode representing basin-wide multidecadal fluctuations in surface temperatures in the North Atlantic (Figure 3.39:a,f), with teleconnections particularly pronounced over the adjacent continents and the Arctic (Technical Annex AVI.8). Fingerprints of AMV exist in the subsurface ocean in AMOC fluctuations, gyre adjustments and salt and heat transport in the entire North Atlantic and subarctic basins.

In AR5, climate models suggested that the AMV was primarily internally-driven alongside some contribution from external forcings (mainly anthropogenic aerosols) over the late 20th century. But AR5 also concluded that models show medium performance in reproducing the observed AMV (*low confidence*), with difficulties in simulating the timescale and spatial structure.

Climate models analyzed since AR5 continue to simulate AMV-like variability as part of their internal variability. This statement is mostly based on CMIP5 piControl and historical simulations (Wouters et al., 2012; Schmith et al., 2014; Menary et al., 2015; Ruprich-Robert and Cassou, 2015; Brown et al., 2016b; Chen et al., 2016a) and is confirmed by the most recent CMIP6 versions (Menary et al., 2018; Voldoire et al., 2019b). Models also continue to support links to a wide array of climate impacts through teleconnections (Martin et al., 2013; Ruprich-Robert et al., 2017; Monerie et al., 2019). Even if debate remains (Clement et al., 2015; Cane et al., 2017), there is now stronger evidence for a crucial role of oceanic dynamics in internal AMV that is primarily linked to the AMOC and its interplay with the NAO (Zhang et al., 2013a; O'Reilly et al., 2016, 2019b; Delworth et al., 2017; Zhang, 2017; Kim et al., 2019; Sun et al., 2019). However, considerable diversity in the spatio-temporal properties of the simulated AMV is found in both piControl and historical CMIP5 experiments (Zhang and Wang, 2013; Wills et al., 2019). Such model diversity is presumably associated with the wide range of coupled processes associated with AMV (Baker et al., 2017; Woollings et al., 2018a) including atmospheric teleconnection and regional feedbacks (cloud and composition changes, etc.), whose relative importance and interactions across timescales are specific to each model (Brown et al., 2016; Martin et al, 2014).

Additional studies since the AR5 corroborate that CMIP5-era models tend to underestimate many aspects of observed AMV overall (Figure 3.39:). The duration of the modelled AMV is too short, its magnitude is too weak and its basin-wide spatial structure is limited by the poor representation of the link between the tropical North Atlantic and the subpolar North Atlantic/Nordic seas (Martin et al., 2013; Qasmi et al., 2017). Such mismatches between observed and simulated AMV has been associated with intrinsic model biases in both mean state (Menary et al., 2015; Drews and Greatbatch, 2016) and variability in the ocean and overlying

atmosphere. For instance, CMIP5 models appear to underestimate decadal versus interannual timescale of variability of the AMOC, NAO and related North Atlantic jet (Bracegirdle et al., 2018; Kim et al., 2018; Simpson et al., 2018; Yan et al., 2018), which has strong implications for the drivers of AMV, AMV-induced teleconnections (Ault et al., 2012; Menary et al., 2015) and AMV predictability.

These general statements for AMV are tempered in CMIP6. The modelled AMV in CMIP6 has a stronger magnitude and longer duration of the modelled AMV in historical simulations than in CMIP5 (Figure 3.39:). In particular, the increase of variance is mostly explained by the enhanced variability in the subpolar North Atlantic SST (Figure 3.39:b), which could be particularly pronounced in some models, associated with greater variability in the AMOC (Boucher et al., submitted; Voldoire et al., 2019a; Section 3.5.4) and greater GMST multidecadal variability (Parsons et al., submitted; Ribes et al., submitted, Section 3.3.1). The SST decadal variance in the subpolar North Atlantic is slightly overestimated in CMIP6 compared to observational estimates, while the AMV-related tropical SST anomalies remains weaker in line with CMIP5 (Figure 3.39:b,c). The mechanisms producing the tropical-extratropical relationship at decadal timescales remain poorly understood despite stronger evidence since AR5 for the importance of the subpolar gyre SST anomalies in generating tropical changes through atmospheric teleconnection (Caron et al., 2015; Ruprich-Robert et al., 2017; Kim et al., 2019).

The increase of temporal variance and persistence of the AMV in CMIP6 is present in historical simulations and marginally in piControl ones (Figure 3.39:d-f) providing additional evidence since AR5 that external forcing have played an important role in shaping the observed AMV temporality and intensity. The competition between GHG warming and anthropogenic sulphate aerosol cooling has been proposed to be particularly important over the latter half of the 20th century (Booth et al., 2012; Steinman et al., 2015; Murphy et al., 2017; Undorf et al., 2018a; Haustein et al., 2019). Volcanic forcing has been also shown to contribute in part to the cold phases of the AMV observed in the 20th century (Terray, 2012; Bellucci et al., 2017; Swingedouw et al., 2017; Birkel et al., 2018). Consistently, the timing of phase changes, and the magnitude and timescale of AMV, tend to be better reproduced in historical simulations compared to piControl simulations (Andrews et al., submitted; Bellomo et al., 2018), and in CMIP6 versus CMIP5 (Figure 3.39:). However, observations still lie in the extreme bounds of the model ensemble spread, even if the total AMV variance is enhanced in CMIP6 due essentially to a greater forced component (Figure 3.39:f), and there remain significant discrepancies in simulated AMV when compared to multivariate observations (Yan et al., 2018). Model biases may be related to deficiencies in the represenation of the atmosphere-ocean coupling in some models (Kim et al., 2018) as well as in their representation of internal variability or forced response associated with climate sensitivity and aerosol-cloud interactions, or both. Meanwhile, the latest observed AMV shift from the cold to the warm phase in the mid-1990s is well captured in the CMIP6 forced component and may be associated with the lagged response to increased AMOC due to strong anthropogenic aerosol forcing over 1955-1985 (Menary et al., submitted) in combination with the rapid response through surface fluxes processes to declining aerosol forcing since then. Over the last millennium, natural forcings including major volcanic eruptions and fluctuations in solar activity may however have driven a larger fraction of the multidecadal variations in the AMV, with some interplay with internal processes (Otterå et al., 2010; Wang et al., 2017b).

Model evaluation of the AMV remains difficult however because of the short observational records and a lack of stationarity in AMV variance, spatial patterns, frequency (Qasmi et al., 2017), the difficulties in estimating the forced signals in both historical simulations and observations (Tandon and Kushner, 2015), and because of probable interplay between internally and externally-driven processes (Watanabe and Tatebe, 2019). For example, the different response to external forcing in the tropical versus extratropical North Atlantic could explain the model-observations discrepancy in AMV spatial structure (Andrews et al., submitted). Related methodological and epistemological uncertainties also question the relevance of the traditional basin mean metrics to assessing AMV (Zanchettin et al., 2014; Frajka-Williams et al., 2017; Haustein et al., 2019; Wills et al., 2019).

To summarize, results from CMIP5 and CMIP6 models together with new statistical techniques to evaluate the forced component in modelled and observed AMV, provide robust evidence that natural climate processes and feedbacks (including internal mechanisms and response to natural, mostly volcanic, forcings)

are important in generating AMV (*high confidence*). There is also increased evidence that anthropogenic aerosols have played a role in the timing and intensity of the negative (cold) phase of AMV recorded from the mid-1960s to mid-1990s and subsequent warming (*medium confidence*), but there is *low confidence* in the estimated magnitude of the human influence. The limited level of confidence is primarily explained by the difficulties in accurately evaluating model performance in simulating realistic AMV phenomena. The evaluation is severely hampered by short instrumental records but also, equally importantly, by the lack of detailed and coherent long-term process-based observations (for example of the AMOC, aerosol optical depth, surface fluxes and cloud changes), which limit our process understanding. In addition, studies often rely solely on simplistic SST indices that may be hard to interpret (Zhang et al., 2016) and may mask critical physical inconsistency in simulations of AMV compared to observational estimates and processes (Zhang, 2017). Therefore, the relative importance of anthropogenic forcing on AMV and associated teleconnections in the historical period compared to natural (forced or internal) variability remains poorly understood and difficult to assess.

[START FIGURE 3.39 HERE]

Figure 3.39: AMV spatio-temporal properties in observations and models. (a, b) SST anomalies (ºC) regressed onto the AMV index defined as the 10-year low-pass filtered North Atlantic (0º-60°N, 80°W-0°E) area-weighted SST* anomalies over 1900-2014 in (a) ERSSTv5 and (b) CMIP6 historical simulations (MME composite). Asterisk denotes that the global mean SST anomaly has been removed at each time step of the computation. (c) A Taylor diagram summarizing the representation of the AMV pattern in models and observations over [0º-60°N, 80°W-0°E] for CMIP5 (light blue) and CMIP6 (red). The reference pattern is taken from ERSSTv5. Black dots indicate other observational products (ERSSTv3b and HadISSTv1). (d) Autocorrelation of unfiltered AMV index at lag 1 year ("Unsmoothed") and 10-year low-pass filtered AMV at lag 10 years ("Low-Pass") for observations (grey shading) and 115-year chunks of piControl simulations (open boxes) and historical ensemble simulations (filled boxes) over 1900-2014 from CMIP5 and CMIP6. (e) As in (d), but standard deviation of unfiltered and filtered AMV (ºC). Boxes and whiskers show mean, interquartile ranges and 5th and 95th percentiles. (f) Time series of the AMV index (ºC) in ERSSTv5 (black) and CMIP5 and CMIP6 historical simulations. The thick red and light blue line are the MME mean for the historical simulations in CMIP5 and CMIP6, respectively, and the envelopes represent the ±2 standard deviation range across ensemble members. 39 models and 149 historical members have been used for evaluation in CMIP5; 29 models and 262 historical members for CMIP6.

[END FIGURE 3.39 HERE]

3.8 Synthesis across Earth system components

3.8.1 Multivariate Attribution of Climate Change

Evidence has grown since AR5 that observed changes since the 1950s in many parts of the climate system are attributable to anthropogenic influences. So far, this chapter has mostly focused on examining individual aspects of the climate system in separate sections. The results presented in Sections 3.3 to 3.7 strengthen the conclusion that human influence on climate has played the dominant role in observed warming since the 1950s. In this section we look across the whole climate system to assess whether and to what extent a physically consistent picture of human induced change emerges across the climate system (Figure 3.40:).

The assessed likelihood of a detectable and quantifiable, human contribution ranges from *likely* to *extremely likely* for temperatures from the depths of the ocean on up through the surface of the Earth to the troposphere and stratosphere (Sections 3.3.1 and 3.5.1.3). The observed warming trends in the atmosphere, ocean and at the surface over the past 65 years are only explained when contributions from both anthropogenic and natural forcings are included. As might be expected from a warming atmosphere, moisture in the troposphere has increased and precipitation patterns have changed. Anthropogenic factors have *likely* contributed to the observed changes in humidity and precipitation. Sea ice in the Arctic continues to decline; this is *very likely*

due to increases in greenhouse gases. There is *medium confidence* that reductions in snow cover over the Northern Hemisphere are associated with warming of near surface air, and that anthropogenic climate change has changed streamflow in many parts of the world. There continues to be *low confidence* in the scientific understanding of the changes in Antarctic sea ice.

Combining the evidence from across the climate system increases the level of confidence in the attribution of observed climate change to human influence and reduces the uncertainties associated with assessments based on a single variable. From this combined evidence, it is *virtually certain* that human influence has warmed the global climate system.

Further, AR5 concluded that human influence on the climate system is clear (IPCC, 2013). This assessment was based on observed increasing greenhouse gas concentrations in the atmosphere, positive radiative forcing, observed warming, and physical understanding of the climate system. Further observed increases in greenhouse gas concentrations and global temperatures (Chapter 2), as well as stronger and better-constrained estimates of anthropogenic radiative forcing (Chapter 7), and improved physical understanding of these changes as reflected in stronger attribution assessments (Sections 3.3 to 3.7) demonstrate that this evidence has strengthened.

[START FIGURE 3.40 HERE]

Figure 3.40: Summary figure showing simulated and observed changes in key large-scale indicators of climate change across the climate system, for continental, ocean basin and larger scales. Black lines show observations, red lines and shading show the multi-model mean and 5-95th percentile ranges for CMIP6 historical simulations including anthropogenic and natural forcing, and blue lines and shading show corresponding ensemble means and 5-95th percentile ranges for CMIP6 natural-only simulations. Temperature timeseries are as in Figure 3.8, but with smoothing by a 2-years running mean. Precipitation timeseries are as in Figure 3.12. Additional variables shown will be added in the final draft. Figure produced with ESMValTool v2.0.0b2.

[END FIGURE 3.40 HERE]

3.8.2 Multivariate Model Evaluation

Similar to the assessment of multivariate attribution of climate change in the previous section, this section covers the performance of the models across different variables (Sections 3.8.2.1) and different classes of models (Section 3.8.2.2). Here the focus is on a system-wide assessment using integrative measures of model performance that characterize model performance using multiple diagnostic fields derived from multi-model ensembles.

3.8.2.1 Integrative Measures of Model Performance

For every diagnostic field considered, model performance is compared to one or multiple observational references, and the quality of the simulation is expressed as a single number, e.g. a correlation coefficient or a root mean square difference versus the observational reference. By simultaneously assessing different performance indices, model improvements can be quantified, similarities in behaviour between different models become apparent, and dependencies between various indices become evident (Gleckler et al., 2008; Waugh and Eyring, 2008).

AR5 found significant variations in skill across the CMIP5 ensemble when measured against meteorological reanalyses and observations (Flato et al., 2013). AR5 determined that for the diagnostic fields analysed, the models usually compared similarly against two different reference datasets, suggesting that model errors were generally larger than observational uncertainties or other differences between the observational references. In agreement with previous assessments, the CMIP5 multi-model mean generally performed

better than individual models (Annan and Hargreaves, 2011; Rougier, 2016). AR5 considered 13 atmospheric fields in its assessment for the instrumental period but did not assess multi-variate model performance in other climate domains (e.g., ocean, land, and sea ice). AR5 found only modest improvement regarding the simulation of climate for two periods of the Earth' history (the Last Glacial Maximum and the mid-Holocene) between CMIP5 and previous paleoclimate simulations. Similarly, for the modern period only incremental progress was found between CMIP3 and CMIP5 regarding the simulation of precipitation and radiation. The representation of clouds remained a leading problem in climate modelling.

The multi-variate analysis of CMIP5 models presented in AR5 is expanded to the previous-generation CMIP3 and present-generation CMIP6 models and also to more variables and more climate domains, covering land and ocean as well as sea ice. The multi-variate evaluation of these three generations of models is performed relative to the datasets listed in the Technical Annex on observations. For many of the observational datasets, a rigorous characterization of the observational uncertainty is not available, see discussion in Chapter 2. Here, as much as possible, multiple independent observational datasets are used. Disagreements amongst them would cause differences in model scoring, indicating that observational uncertainties may be substantial compared to model errors. Conversely, similar scores against different observational datasets would suggest model issues may be more important than the observational uncertainty.

An analysis of a basket of 17 atmospheric metrics (Figure 3.41:a), assessed across CMIP3, CMIP5, and CMIP6 models but excluding high-resolution models used in HighResMIP, reveals the progress made between these three generations of models (Bock et al., submitted). This is evidenced by the increasing prevalence of blue colours (indicating a performance better than the median) for the more recent model versions. As a consequence, a few CMIP6 models outperform the best-performing CMIP5 models. Progress is evident across all 17 metrics, meaning that the three particular metrics chosen in FAQ3.2 to illustrate progress are not critical. One model (HadCM3) has participated both in CMIP3 and CMIP5 and scores very similarly in both, suggesting that the changes in forcings between these two experiments are not the leading cause for this general improvement in model behaviour. However, a more in-depth analysis of the role of the forcings would be required to confirm this finding. The models typically score similarly against both observational reference datasets, indicating that indeed uncertainties in these references are smaller than model biases. Several models and model families perform better compared to observational references than the median, across a majority of the climate variables assessed, and conversely some other models or model families compare more poorly against these reference datasets. Such a good correspondence across a range of metrics enhances confidence that it is not achieved via a cancellation of errors which would likely cause mismatches in some metrics (although some such mismatches -- red colours -- are still evident in the CMIP6 generation of models). Family relationships between the models are apparent, for example, the GISS, GFDL, CESM, CNRM, and HadGEM/UKESM1/ACCESS families score similarly across all atmosphere variables, both for the CMIP5 and CMIP6 generations. In the cases of CESM2 / CESM2(WACCM) and HadGEM3 / UKESM1, both the low- and high-complexity members of these families score similarly, indicating that increasing complexity by adding "Earth System" features does not necessarily degrade a model's performance. In accordance with AR5 and earlier assessments, the multi-model mean, with some notable exceptions, is better than any individual model (Annan and Hargreaves, 2011; Rougier, 2016). Bock et al. (submitted) discuss Figure 3.41:a in more detail.

Regarding performance with regards to the ocean and the cryosphere (Figure 3.41:b), it is apparent that for many models there are substantial differences between the scores for Arctic and Antarctic sea ice concentration. This might suggest that it is not sea ice physics directly that is driving such differences in performance but rather other influences, such as differences in geography or large-scale ocean dynamics. As for atmospheric variables, progress is evident also across all 4 ocean and 10 land metrics from CMIP5 to CMIP6.

[START FIGURE 3.41 HERE]

Figure 3.41: Relative space-time root-mean-square deviation (RMSD) calculated from the climatological seasonal

cycle of the CMIP simulations (1980-1999) compared to observational datasets (Table 1 of the Technical Annex on Observations): (a) CMIP3, CMIP5, and CMIP6 for 17 atmospheric variables (SWCRE, LWCRE, RSUT, RLUT, CLT, PR, TS, TAS, HUS400, PSL ZG500, VA200, VA850, UA200, UA850, TA200, TA850), (b) CMIP5 and CMIP6 for 10 land variables (RLUS, RSDS, RSUS, RSDS, ET, FGCO2, GPP, LAI, NBP, SM) and four ocean/sea-ice variables (TOS, SICONC Antarctic, SICONC Arctic, HFDS). A relative performance is displayed, with blue shading indicating better and red shading indicating worse performance than the median of all model results. A diagonal split of a grid square shows the relative error with respect to the reference data set (lower right triangle) and the alternative data set (upper left triangle). White boxes are used when data are not available for a given model and variable. Updated and expanded from Figure 9.7 of Flato et al. (2013). (Figure from Bock et al. (submitted), their Figure 5, produced with ESMValTool v2.0.0b3.)

[END FIGURE 3.41 HERE]

Using centred pattern correlations for selected fields, the AR5 had documented improvements between CMIP3 and CMIP5 in surface air temperature (tas), outgoing longwave radiation (rlut), and precipitation (pr). Little progress was found for fields that were already quite well simulated in CMIP3 and CMIP5 (such as tas and rlut). For precipitation, the spread reduced because the worst-performing models improved. The short-wave cloud radiative effect remained relatively poorly simulated with significant inter-model spread. This comparison is designed to help determine the quality of simulation of different diagnostics relative to each other, and also to demonstrate progress between generations of models. Figure 3.42: shows the centered pattern correlations for an enhanced number of variables for CMIP3, CMIP5 and CMIP6 models. In the ensemble averages, CMIP6 performs better than CMIP5 and CMIP3 for near-surface temperature, precipitation, and mean sea-level pressure, but also for several other variables (Figure 3.42:).

[START FIGURE 3.42 HERE]

Figure 3.42: Centred pattern correlations between models and observations for the annual mean climatology over the period 1980–1999. Results are shown for individual CMIP3 (black), CMIP5 (blue) and CMIP6 (brown) models as short lines, along with the corresponding ensemble averages (long lines). The correlations are shown between the models and the reference observational data set listed in Table 5. In addition, the correlation between the reference and alternate observational data sets are shown (solid grey circles). To ensure a fair comparison across a range of model resolutions, the pattern correlations are computed after regridding all datasets to a resolution of 2.5º in longitude and 2.5º in latitude. Only one realization is used from each model from the CMIP3, CMIP5 and CMIP6 historical simulations. (Figure from Bock et al. (submitted), their Figure 6, produced with ESMValTool v2.0.0b3.)

[END FIGURE 3.42 HERE]

Simulations of selected periods of the Earth's past can additionally help benchmark climate models by exposing them to climate forcings that are more radically different from the present and recent past (Harrison et al., 2015, 2016; Kageyama et al., 2018). These time periods provide an out-of-sample test of models because they are not in general used in the process of model development. The two periods of the mid-Holocene (MH) and the Last Glacial Maximum (LGM) are considered below; details on both are given in Cross-Chapter Box 2.1. Two other periods, the Last Interglacial (LIG) and the mid-Pliocene Warm Period (mPWP) are also covered by the 4th Paleoclimate Model Intercomparison Project (PMIP4) but are not discussed here.

AR5 found that there was only a slight improvement in CMIP5/PMIP3 models compared with earlier model versions (PMIP2), when evaluating the MH and LGM simulations of a range of variables, including annual mean temperatures, mean temperature of the coldest and warmest month, growing degree days above a threshold of 5°C, mean annual precipitation, and the ratio of actual to equilibrium evapotranspiration. For several regional signals, the magnitude of change seen in the proxies relative to pre-industrial (for example the north-south temperature gradient in Europe, and regional precipitation changes) was underestimated by the models. For the LIG, it was noted that the magnitude of observed annual mean warming in the Northern Hemisphere was only reached in summer in the models. For the mPWP, it was noted that both proxies and

models showed polar amplification of temperature compared with pre-industrial, but a formal model evaluation was not carried out.

Since AR5, modelling protocols for evaluation of climate models as well as understanding of their differences with respect to today have been developed in the framework of PMIP4 (Kageyama et al. (2018) for an overview, Otto-Bliesner et al. (2017) for the mid-Holocene, and Kageyama et al. (2018) for the LGM). Both the mid-Holocene and the LGM climates have been continuously modeled with AMIP to CMIP models and serve as references to quantify model-data agreement from one IPCC assessment to another.

The results of 12 PMIP4-CMIP6 models have been used for the mid-Holocene in comparison to the PMIP3-CMIP5 models (Brierley et al., submitted). CMIP6 models show patterns of temperature changes similar to the CMIP5 ensemble, albeit with weaker cooling for Northern Hemisphere winters. The model spread is also similar in both ensembles. Therefore, there is no major improvement in the model's ability to represent the mid-Holocene temperature, this conclusion being reinforced by the fact that it is based on larger data sets, covering more sites (Figure 3.43:). All models show an expansion of the monsoon areas from the pre-industrial to the mid-Holocene simulations, but this expansion in some cases is just large enough to cancel out the low bias in the pre-industrial control simulations. However, there is a slight improvement in representing the northward expansion of the West African monsoon region, with one model reaching the reconstructed precipitation change.

The results of 8 new climate simulations run with 7 models for the LGM differ from the PMIP3-CMIP5 results in several aspects (Figure 3.43:). With a lower climate sensitvity of the models that have so far completed the PMIP4-CMIP6 simulations (i.e., not covering those models with a climate sensitivity at the upper end of the CMIP6 range, see Chapter 7) and lower ice sheet height in the updated boundary conditions used for those runs, the PMIP4-CMIP6 simulations tend to simulate a weaker cooling than the PMIP3-CMIP5 ones. This difference in ice sheet height also impacts atmospheric circulation, and the hydrological cycle is affected by both the difference in temperature and in atmospheric circulation. Changes in the AMOC tend to be less strong than in the PMIP3-CMIP5 simulations, although the PMIP4-CMIP6 models still simulate an increased North Atlantic Deep Water circulation (Kageyama and PMIP4, submitted). The PMIP4-CMIP6 models do not show a systematic improvement in their comparison with reconstructions, except for western Europe with several models showing much improved ability to represent winter temperatures and annual precipitation. These preliminary results show that biases are similar for both sets of models, and this analysis of biases is strengthened because it is based on larger and improved reconstructions (Cleator et al., 2019, for terrestrial reconstructions; Tierney et al., submitted, for SST reconstructions).

The MH and the LGM comparison over the same regions and for the same variables show that the biases are not the same for both periods. The reasons for this remain to be investigated.

[START FIGURE 3.43 HERE]

Figure 3.43: Data-model comparisons for the mid-Holocene (top line) and LGM (bottom line) periods, for PMIP3-CMIP5 and PMIP4-CMIP6 models. The figure shows the mid-Holocene - piControl (top) and LGM - piControl (bottom) averages and ranges computed for pollen-based reconstructions and model output taken over the grid points for which there are reconstructions, for the following regions: North America (20-50°N, 140-60°W), Western Europe (35-70°N, 10°W-30°E) and West Africa (0°-30°N, 10°W-30°E). MTCO: Mean Temperature of the Coldest Month (°C), MTWA: Mean Temperature of the Warmest Month (°C), MAP: Mean Annual Precipitation (mm/year). The ranges shown for the reconstructions are based on the standard error given at each site: the average and associated standard deviation over each area is obtained by computing 10000 times the average of randomly drawn values from the Gaussian distributions defined at each site by the reconstruction mean and standard error. The ranges for the model results are based on the interannual variability of the average over the area: the mean ± one standard deviation is plotted for each model. The reconstructions are from Bartlein et al. (2011) and Cleator et al. (2019). (Figure from Brierley et al. (submitted), their Figure S3 for the mid-Holocene and from Kageyama and PMIP4 (submitted), their Figure 12 for the LGM.)

[END FIGURE 3.43 HERE]

In summary, there is *high confidence* that across a large range of metrics chosen to capture large-scale aspects of mean climate across different domains, CMIP6 models as a group compare better against available observational references covering the recent instrumental period than their CMIP5 and CMIP3 predecessors. Subsets of the CMIP6 models have also been evaluated for the MH and the LGM. For the MH, little substantial progress is evident, with model spread for several diagnostics remaining about as large as for PMIP3-CMIP5 and biases remaining essentially unchanged. For the LGM, there is reduced inter-model spread and better agreement with a new reconstruction for some diagnostics, but no improvement from PMIP3-CMIP5 for others. There are no regions/variables for which the simulations compare favourably with reconstructions for both periods. There is therefore *low confidence* in the ability of the CMIP6 models to simulate the climates of the MH and the LGM at the regional scale.

3.8.2.2 Process Representation in Different Classes of Models

Based on new physical insights and newly available observations, many improvements have been made to models from CMIP5 to CMIP6, including changes in the representation of physics of the atmosphere, ocean, sea-ice, and land surface. In many cases, changes in the detailed representation of cloud and aerosol processes have been implemented. This new generation of climate models also features increases in spatial resolution, as well as inclusion of additional Earth system processes and new components (see further details in Chapter 1).

A key advance in CMIP6 compared to CMIP5 is the presence of several high-resolution models that have participated in the High-Resolution Model Intercomparison Project (HighResMIP, Haarsma et al., 2016). Resolution alone can significantly affect a model's performance, with some effects propagating to the global scale. For example, the equilibrium climate sensitivity (ECS) and the total climate response (TCR), both measures of the climate's response to anthropogenic forcings, can display a significant dependence on model resolution in experiments where resolution is the only difference between two model versions, although such findings are model dependent (Kiehl et al., 2006; Senior et al., 2016). Recent studies have shown that enhancing the horizontal resolution of models is seen to significantly affect aspects of large-scale circulation as well as improve the simulation of small-scale processes and extremes when compared to CMIP3 and CMIP5 models (Haarsma et al., 2016).

As discussed in Section 3.3, CMIP6 models reproduce observed large-scale mean surface temperature patterns as well as their CMIP5 predecessors, but biases in surface temperature in the mean HighResMIP model are smaller than those in the mean of the corresponding lower-resolution version of the same models (Figure 3.2:). The extent and causes of improvements due to increased horizontal resolution depend on model (Sidorenko et al.; Kuhlbrodt et al., 2018; Roberts et al., 2018, 2019a), although they typically involve improved biases in top of atmosphere radiation and cloudiness, and generally require increased horizontal resolutions of both the atmosphere and ocean models. Precipitation has likewise improved in CMIP6 versus CMIP5 models, but biases remain. The high resolution (< 25 km) class of models participating in HighResMIP compares regionally better against observations than low resolution models (Figure 3.10:), partly because of an improved representation of orographic (mountain-induced) precipitation which constitutes a major fraction of precipitation on land, but other processes also play an important role (Vannière et al., 2019). However, there are also large parts of the tropical ocean where precipitation in high-resolution models is not improved compared to low-resolution (Vannière et al., 2019).

Additionally, the representation of surface and deeper ocean mean temperature is improved in models with higher horizontal resolution (Sections 3.5.1.1 and 3.5.1.2) with systematic improvements in coupled tropical Atlantic sea surface temperature and precipitation biases at higher resolutions (Roberts et al., 2019a, single model; Vannière et al., 2019), the North Atlantic cold bias (Bock et al., submitted, multi-model; Caldwell et al., 2019; Roberts et al., 2018, 2019a, all single models) as well as deep ocean biases (Caldwell et al., 2019; Gutjahr et al., 2019; Roberts et al., 2019a; in addition to earlier work e.g. Griffies et al., 2015; Small et al.,

2014, all single model studies). Atlantic ocean transports (heat and volume) are also generally improved compared to observations (Caldwell et al., 2019; Docquier et al., 2019; Grist et al., 2018; Roberts et al., 2019a, submitted, b), as well as some aspects of air-sea interactions (Wu et al., 2019a, single model). However, warm-biased sea-surface temperatures in the Southern Ocean get worse in comparison to low-resolution models (Bock et al., submitted). AR5 noted problems with the simulation of clouds in this region which were later attributed to a lack of supercooled liquid clouds in this region (Bodas-Salcedo et al., 2016). Mesoscale ocean processes are critical to maintain the Southern Ocean stratification and response to wind forcing (Marshall and Radko, 2003; Hallberg and Gnanadesikan, 2006), and their explicit representation requires even higher ocean resolution (Hallberg, 2013). There is also evidence of improvements in the frequency, distribution and interannual variability of tropical cyclones (Roberts et al., 2019b, submitted, a), particularly in the Northern Hemisphere (see further discussion in Section 3.7.5), moisture budget (Vannière et al., 2019), and interaction with the ocean (Scoccimarro et al., 2017, single model). The track density of tropical cyclones is increased practically everywhere where tropical cyclones occur. Modelling of some climate extremes is shown to be improved in explosively developing extra-tropical cyclones (Gao et al.; Vries et al., 2019), blocking (Schiemann et al., submitted) and European extreme precipitation due to a better representation of the North Atlantic storm track (Van Haren et al., 2015) and orographic boundary conditions (Schiemann et al., 2018).

In addition to increased horizontal resolution, other factors can be equally important for model improvements. These include dynamical core type (spectral vs finite difference / finite volume), physics parameters and parameterisations, structural uncertainty – many of the coupled HighResMIP models available so far use the NEMO ocean model – and the range and degree of process realism (e.g. for aerosols, atmospheric chemistry and other Earth System components).

In CMIP6 a number of Earth system models have increased the realism by which key biogeochemical aspects of the coupled Earth system are represented (e.g. Danabasoglu et al., submitted; Séférian et al., 2019; Sellar et al., 2019). In addition to increased process realism, the level of coupling between the physical climate and biogeochemical components of the Earth system has also been enhanced in some models (Mulcahy et al., submitted), as well as across different biogeochemical components. The majority of these developments are intended to support investigation of potential future feedbacks in the coupled Earth system or to allow investigation of climate mitigation options (e.g. through managed land use change and terrestrial carbon uptake (Mahowald et al. (2017)) or interactions between differerent facets of the managed Earth system (e.g. interactions between mitigation efforts targeting climate warming and air quality (West et al., 2013). A number of developments also explicitly target improved simulation of the past.

Such developments include (i) Extending terrestrial carbon cycle models to simulate interactions between the carbon cycle and other nutrient cycles, such as nitrogen and phosphorous that are known to play an important role in limiting future plant uptake of CO_2 (Zaehle et al., 2015). (ii) Introducing explicit coupling between interactive atmospheric chemistry and aerosol schemes (Gettelman et al., 2019; Sellar et al., 2019), which has been shown to impact estimates of historical aerosol radiative forcing (Karset et al., 2018). Furthermore, interactive treatment of atmospheric chemistry in a full ESM supports investigation of interactions between climate and air quality mitigation efforts, such as planned in AerchemMIP (Collins et al., 2017) as well as potential interactions between stratospheric ozone recovery and global warming (Morgenstern et al., 2018). (iii) Couplings between components of Earth system models have been extended to increase their utility for studying future interactions across the full Earth system, such as between; ocean biogeochemistry and cloud-aerosol processes (Mulcahy et al., submitted), vegetation and impacts on dust production (Kok et al., 2018), production of secondary organic aerosols (SOA, Zhao et al., 2017) and even Effective Climate Sensitivity (ECS) via changes in regional surface albedo (Andrews et al., 2019). Increased coupling between physical climate and biogeochemical processes in a single ESM, along with an increased number of interactively represented processes, such as permafrost, vegetation, wildfires and continental ice sheets increases our ability to investigate the risk of abrupt and interactive changes in the Earth system (Lenton et al., 2019).

In summary, both high-resolution and high-complexity models have been evaluated as part of CMIP6. Higher resolution improves aspects of the simulation of climate (particularly concerning sea surface temperature) but discrepancies remain and there are some regions where currently attainable resolution

produces inferior performance (*high confidence*). Such model behaviour can indicate deficiencies in model physics that are not simply associated with resolution. In several cases, ESMs perform as well as their low-complexity counterparts, illustrating that interactively simulating these Earth System components as part of the climate system is now well established.

3.9 Limits to the Assessment

Physical understanding of the climate system and multiple lines of evidence of consistent changes across all climate components allowed us to provide a robust assessment of the human influence on the climate system, but observational and modelling uncertainties place upper limits on the level of confidence in our assessement. Firstly, despite longer observational records compared to AR5, the limied length of the observational record as well as observational uncertainty place upper limits on the confidence assessments of some variables assessed in this chapter. While instrumental observations of surface temperature extend back to the quasi-preindustrial base period, and therefore capture most of the anthropogenically-forced change, comprehensive direct instrumental observations of many important variables assessed in this chapter, such as the very short and geographically limited observational records of ocean circulation or the short observational record of Antarctic sea ice extent lower our confidence in the attribution of observed changes. In the case of the Antarctic sea ice extent, for example, the short period of comprehensive satellite observations, beginning in 1979, makes it challenging to set the observed increase between 1979 and 2015, or the subsequent decrease, in a long-term context, and to assess whether the difference in trend between observations and models, which all simulate long-term decreases, is systematic or a rare expression of internal variability. Moreover, for other variables, such as precipitation or atmospheric temperature, remaining observational uncertainty limits the confidence in our attribution and model evaluation assessments.

The short observational record, as well as less than perfect knowledge of the forced response, also limit our ability to accurately estimate internal variability, especially on decadal to multi-decadal timescales. This challenge is particularly acute in the case of the decadal to multidecadal modes of varibility, PDV and AMV, for which the observational record samples only a small number of phase transitions. The latest-generation CMIP6 multi-model ensemble includes some models with substantially higher multi-decadal internal variability in global mean temperature than the previous generation CMIP5 models, which may be in part related to stronger AMV and AMOC. Based on the currently available literature, the short observational record limits our ability to assess to what extent this high multi-decadal internal variability is realistic. Paleoclimate data can provide a distinct line of evidence to evaluate the models' forced and unforced internal variablity in the pre-industrial climate, but observational uncertainties and the inhomogeneous distribution of paleorecords limit the extent to which this can inform our assessment. Further, some lack in process understanding of the AMV and PDV, including their links to changes in ocean circulation and their teleconnections, as well as remaining uncertainty over the extent to which observed AMV has been forced by aerosol changes, constrains our ability to assess to what extent these modes are realistically represented in models.

Moving beyond detection and quantification of the overall anthropogenic response, uncertainties in forcing datasets (including greenhouse gas concentrations, land use changes, aerosol precursor emissions, solar irradiance variations and volcanic aerosols) limit the confidence with which we can separately quantify the contributions of individual forcings to observed changes. In particular, uncertainties in the simulated indirect aerosol effect are still large, resulting in differences in historical global mean temperature evolution and in diagnosed aerosol-attributable cooling between different models. Moreover, like previous generations of coupled model simulations, historical and single forcing CMIP6 simulations follow a common experimental design and are thus all driven by the same common set of forcings, even though these forcings are uncertain. While this limitation can to some extent be addressed by comparing with previous generation multi-model ensembles or individual model studies using different sets of forcings, forcing uncertainty is not directly accounted in most of the attribution and model evaluation studies assessed in this chapter. This is one reason, for example, why reported 5-95% uncertainty ranges in attributable warming from individual studies, are bracketed and assessed as *likely* rather than *very likely* in this chapter. Finally, although systematic biases

remain in many aspects of climate, CMIP6 models have improved over CMIP5 in many aspects.

Despite these remaining sources of uncertainty, observations, models and physical understanding of the role of human influence on climate system have evolved substantially since the time of AR5. And accounting for these limitations, it is still possible to make robust assessments on human influence across many parts of the climate system. Looking forward, we expect further improvements in models and physical understanding, along with a lengthening observational record and the availability of new measurements monitoring key aspects of the climate system, in order to support even better quantification of the role of human influence on the past and also future climate.

[START CROSS-CHAPTER BOX 3.1 HERE]

Cross-Chapter Box 3.1: Slower Surface Global Warming over the Early 21st Century

Contributors: Christophe Cassou (France), John Fyfe (Canada), Nathan Gillett (Canada), Edward Hawkins (UK), Yu Kosaka (Japan), Blair Trewin (Australia)

The observed rate of global mean surface temperature (GMST) increase was lower from the late 1990s to early 2010s compared to the preceding few decades and to the ensemble mean of historical simulations produced by process-based climate models from both CMIP5 (extended by RCP scenarios beyond 2005) and CMIP6 (Cross-Chapter Box 3.1, Figure 1a). This apparent slowdown of surface global warming from the preceding decades, often called the "hiatus", was assessed with *medium confidence* to have been caused in roughly equal measure by a cooling contribution from internal variability and a reduced trend in external forcing (particularly associated with solar and volcanic forcing) in the AR5 based on expert judgement (Flato et al., 2013). In the AR5 it was assessed that almost all CMIP5 simulations did not reproduce the observed slower warming, and that there was *medium confidence* that the difference in trends was to a substantial degree caused by internal variability with possible contributions from forcing error and model response uncertainty. This Cross-Chapter Box assesses new findings from observational products and statistical and process-based models on trends over the 1998-2012 period considered in AR5, for which the observed GMST trend was at or near its lowest when computed for running 15-year periods starting in 1981.

Updated observational data sets and reanalyses and comparison with model simulations

Since the AR5, there have been version updates and new releases of most observational GMST data sets (Chapter 2 Section 2.3.1.1). All the updated products now available consistently find stronger positive trends for 1998-2012 than those assessed in AR5 (Cowtan and Way, 2014; Karl et al., 2015; Hausfather et al., 2017; Medhaug et al., 2017; Simmons et al., 2017; Risbey et al., 2018), a result which is also supported by satellite data (Hausfather et al., 2017). Simmons et al. (2017) report that the 1998-2012 GMST trends in the updated observational and reanalysis data sets range from 0.06 °C to 0.14 °C per decade, compared with the 0.05 °C per decade on average as reported in AR5. The lowest value in Simmons et al. (2017) is from HadCRUT4, whose latest version, HadCRUT5, show 0.12 ºC per decade. The upward revision is mainly due to improved sea surface temperature (SST) data sets that account for an increased amount of buoy data (which has a cold bias relative to ship observations), improved information on ship observations over time (bucket measurements versus engine room intake measurements or hull-mounted sensors, which all require different calibration; Karl et al., 2015), and infilling of surface temperature on locations with missing records in observational products, mainly in the Arctic, where warming since the 1990s has been faster than the global average (Cowtan and Way, 2014; Huang et al., 2017). Low frequency daily sampling of land surface air temperature is found as another source of trend biases in observational products, but this impact is much smaller when averaged globally (Zhou and Wang, 2016).

Another artificial source of apparent model-observation discrepancy has been identified among the different methods of global temperature calculation used to evaluate models. Namely, global mean near-surface air temperature (GSAT), a field widely used for model outputs including by Flato et al. (2013), tends to show stronger warming trends than GMST, a blend of surface air temperature over land and sea ice and SST over open ocean, which currently available observational data sets operationally use (see Cross-Chapter Box 2.3 for details). In CMIP6, the ensemble mean difference of the 1998-2012 trend between globally complete GSAT

and spatially masked GMST based on the five observational data sets assessed in Cross-Chapter Box 3.1, Figure 1 is 0.02-0.03 ºC per decade.

Using updated observational data sets and blending and masking of simulated near-surface air temperature and SSTs (Cowtan et al., 2015) of CMIP6 data available at present, all the observed trends assessed in this Box lie within the 5th-95th percentile range of the simulated trends in CMIP6 (Cross-Chapter Box 3.1, Figure 1a). Most of those observed trends lie also within the same percentile range of CMIP5, with the exception of NOAAGlobalTemp with a narrow margin. The slightly different results between CMIP5 and CMIP6 arises from larger ensemble spread in the latter, related to higher internal variability in some models (Section 3.3.1.1) (Cross-Chapter Box 3.1, Figure 1a). Lin and Huybers (2016) take a continuous piecewise linear fitting approach and find no significant difference in 15-year GMST trends between HadCRUT4 and the CMIP5 ensemble since 1970. Therefore the observed 1998-2012 trend is not inconsistent with either the CMIP5 or CMIP6 multi-model ensemble of trends over the same period (*high confidence*).

Internal variability

The blending and spatial masking explains 14-20% of the trend difference between the observed GMST and CMIP6 ensemble mean GSAT. The residual, which is still dominant in the trend difference, suggests a possible cooling contribution from internal variability during this period. This is supported by initialized decadal hindcasts, which account for the phase of the multidecadal modes of variability (Sections 3.7.6 and 3.7.7), and which better reproduce observed global mean SST and GSAT trends than uninitialized historical simulations (Guemas et al., 2013; Meehl et al., 2014). Since trend difference between GMST and GSAT is small, the following argument on GSAT trends also applies to GMST trends.

On interannual timescales, the El Niño-Southern Oscillation (ENSO) is the leading internal driver of GSAT (Pan and Oort, 1983; Trenberth et al., 2002). Pacific Decadal Variability (PDV), which encompasses decadal modulations of ENSO, transitioned from positive (El Niño-like) to negative (La Niña-like) phases during the slow warming period (Cross-Chapter Box 3.1, Figure 1c). Statistical models based on the observed ENSO-GSAT relationship, which are expected to also capture the relationship between PDV and GSAT, and the simulated PDV-GSAT relationship in a climate model (Meehl et al., 2016b), yield a slower GSAT increase over the slowdown period and a better match with observations (Schmidt et al., 2014; Hu and Fedorov, 2017). Moreover, studies identify PDV as the leading mode of variability associated with unforced decadal GSAT fluctuations in observations and a majority of CMIP5 and CMIP6 models (Brown et al., 2015; Dai et al., 2015; Parsons et al., submitted), with a secondary influence from AMV (Dai et al., 2015; Steinman et al., 2015). Model ensemble members and time segments of model simulations that capture the observed slower warming under transient forcing and that show substantial GSAT decrease under fixed forcing feature negative PDV trends (Maher et al., 2014; Meehl et al., 2011, 2013, 2014; Middlemas and Clement, 2016; Cross-Chapter Box 3.1, Figure 1d). Alternatively, selecting ensemble members and time segments from model simulations where PDV by chance evolves in phase with observations over the slowdown period yields considerably better agreement with the observed GSAT increase (Huber and Knutti, 2014; Risbey et al., 2014). Coupled model experiments in which PDV evolution is constrained to follow the observations, simulate a slower GSAT increases than the ensemble mean of the historical simulations, and match the observations better (Kosaka and Xie, 2013, 2016; England et al., 2014; Watanabe et al., 2014; Delworth et al., 2015), despite uncertainties related to model and protocol sensitivity (Douville et al., 2015; Xu and Hu, 2018). It is noteworthy that part of the PDV trend may be driven by anthropogenic aerosols; however, this result is model-dependent (see Section 3.7.6).

New observational and modelling studies have improved understanding of how PDV affects GSAT. Stronger Pacific trade winds associated with the negative phase of PDV bring ocean subsurface cold water to the tropical eastern Pacific sea surface and subsiding warm water to the subsurface Indo-western Pacific Oceans (about 100-300m; England et al., 2014; Gastineau et al., 2019; Lee et al., 2015; Maher et al., 2018; Nieves et al., 2015). The tropical eastern Pacific SST anomalies affect global air temperature through teleconnections (Trenberth et al., 2014; Wang et al., 2017a). However, it is noteworthy that there is large model-to-model difference in remote influence of PDV (Wang et al., 2017a), introducing uncertainty in quantifying the PDV contribution to observed GSAT trends.

The reduced GMST trend over 1998-2012 is most pronounced in boreal winter, which accounts for the largest fraction of GMST variance at interannual timescales. This seasonality results from additional contributions from wintertime Northern Hemisphere atmospheric internal variability to GSAT changes, particularly associated with a trend towards the negative phase of the Northern Annular Mode/North Atlantic Oscillation (Section 3.7.1; Guan et al., 2015; Iles and Hegerl, 2017) or the Cold Ocean-Warm Land pattern (Molteni et al., 2017; Yang et al., submitted) leading to regional continental cooling over a large part of Eurasia and North America (Deser et al., 2017; Li et al., 2015; Cross-Chapter Box 3.1, Figure 1c).

The contribution of internal variability to surface temperature changes over the 1998-2012 period is regionally- and seasonally-varying (Trenberth et al., 2014; Zang et al., 2019; Cross-Chapter Box 3.1, Figure 1c). In the southern U.S., the negative PDV contributed to faster warming and droughts (Burgman and Jang, 2015; Delworth et al., 2015; Meehl et al., 2015). Also of note is that there was no slowdown in increasing occurrence of hot extremes over land (Seneviratne et al., 2014). Kamae et al. (2014) and Johnson et al. (2018) find contributions from PDV and AMV to the increase in summer warm extremes over Northern Hemisphere lands. Thus, the internally-driven slowdown of GMST increase does not correspond to slowdown of warming everywhere on the Earth's surface.

Updated forcing

CMIP5 historical simulations driven by observed forcing variations ended in 2005 and have been extended with RCP scenario simulations for model-observation comparisons beyond that date. Post AR5 studies based on updated external forcing show that while no net effect of updated anthropogenic aerosols is found (Murphy, 2013; Oudar et al., 2018), natural forcing by moderate volcanic eruptions in the 21st century (Ridley et al., 2014; Santer et al., 2014) and a prolonged solar irradiance minimum around 2009 compared to the normal 11-year cycle (Lean, 2018) yields a negative contribution to radiative forcing, which was missing in CMIP5. This explains part of the difference between observed trend deviations and CMIP5 trends, as shown based on EMIC simulations (Huber and Knutti, 2014; Ridley et al., 2014), statistical and mathematical models (Schmidt et al., 2014; Lean, 2018), and process-based climate models (Santer et al., 2014). However, in a single model study, updating all forcings (GHG concentrations, solar irradiance, and volcanic and anthropogenic aerosols) does not make a significant difference in 1998-2012 GMST trend from that obtained with original CMIP5 forcing (Thorne et al., 2015). Besides, CMIP6 historical simulations, in which observation-based forcing extends to 2014, show a slightly higher GMST trend in the ensemble mean than the CMIP5 historical ensemble mean extended by RCP4.5 (Cross-Chapter Box 3.1, Figure 1a), though based on different model sets. Uncertainty therefore remains in the contribution to the difference in observed and ensemble mean GMST trends over the slower warming period from net forcing. New datasets suggest an overestimation of the decrease in lower stratospheric water vapour (Hegglin et al., 2014), which was considered as a contributor to the warming slowdown (Solomon et al., 2010), whereas other studies suggest that internal variability affects the lower stratospheric water vapour (Chapter 2 Section 2.2.5.1). Thus, while there is *medium confidence* that natural forcing that was missing in CMIP5 and contributed to the difference of observed and simulated GMST trends, *confidence* remains *low* on the net forcing contribution.

Energy budget and heat redistribution

The early 21st century warming slowdown was observed in atmospheric temperatures, but the heat capacity of the atmosphere is very small compared to that of the ocean. Although there is noticeable uncertainty among observational products (Su et al., 2017a) and observation quality changes through time, global ocean heat content and sea level rise continued to increase during the slower surface warming period at a pace similar to before and similar to that in CMIP5 and CMIP6 historical simulations (Chapter 2 Sections 2.3.3.1 and 2.3.3.3 and Section 3.5.1.3). Internal decadal variability is mainly associated with redistribution of heat within the climate system (Yan et al., 2016c; Drijfhout, 2018) while associated top of the atmosphere radiation anomalies are weak (Palmer and McNeall, 2014). In the top 350 m of the ocean, heat redistribution in the Indian and Pacific Oceans has been the main contributor to reduced warming during the slower surface warming period (Lee et al., 2015; Nieves et al., 2015; Liu et al., 2016b), consistent with the simulated signature of PDV (England et al., 2014; Maher et al., 2018a; Gastineau et al., 2019). Below 700 m, enhanced heat uptake over the slower surface warming period is observed mainly in the North Atlantic and Southern Ocean (Chen and Tung, 2014), though whether this is a response to forcing or a unique signature of the slow GMST warming is questioned (Liu et al., 2016b).

Summary and implications for post-slow warming period

With updated observation-based GMST data sets and forcing, improved analysis methods, new modelling evidence and deeper understanding of mechanisms, there is *high confidence* that the observed slower GMST and GSAT increase in the 1998-2012 period was a temporary event induced by internal and naturally-forced variability that partly offset the anthropogenic warming tendency over this period. Global ocean heat content continued to increase throughout this period, and the slowdown was only evident in the atmosphere and at the surface (*very high confidence*). Considering all the sources of uncertainties, it is impossible to robustly identify a single cause of the early 2000s slowdown (Hedemann et al., 2017); rather, it should be interpreted as a combination of several factors (Huber and Knutti, 2014; Schmidt et al., 2014; Medhaug et al., 2017).

A major El Niño event in 2014-2016 led to three consecutive years of record annual GMST with unusually strong heat release from the Northwestern Pacific Ocean (Yin et al., 2018), which marked the end of the slower warming period (Hu and Fedorov, 2017; Su et al., 2017b; Cha et al., 2018). The past 5-year period (2014-2018) is the hottest 5-year period in the instrumental record up to 2018 (*high confidence*). This rapid warming was accompanied by a PDV shift toward its positive phase. Consistent with the important role of internal variability, ensemble members with a slower GMST increase for 1998-2012 in the CMIP6 historical ensemble simulate faster warming for 2012-2024 in currently available SSP2-4.5 simulations (Cross-Chapter Box 3.1, Figure 1b), but with no clear relationship to changes in PDV (Cross-Chapter Box 3.1, Figure 1e). This is consistent with the predictions in AR5 Box 9.2 (Flato et al., 2013) and with a statistical prediction system (Sévellec and Drijfhout, 2018). The latest initialized decadal predictions show higher GMST trends in the early 2020s compared to uninitialized simulations (Thoma et al., 2015; Meehl et al., 2016c). Internally-driven decadal slowdown and accelation of GSAT increase are commonly found in climate model simulations under transient forcing (Chapter 1 Section 1.4.1.1). Periods can be also found where the observed trend is larger than the ensemble mean of historical simulations (e.g. 1974-1988). In CMIP5, models with higher climate sensitivity tend to have stronger internal GMST and GSAT variability on decadal timescales (Colman and Power, 2018; Nijsse et al., 2019), although it is questioned whether this tendency is strong enough to increase the chance of slowdown by compensating the stronger forced warming (Modak and Mauritsen, submitted). While Brown et al. (2017) find that internal decadal to centennial GSAT variability becomes weaker under warmer equilibrium climate at 3% per ºC in CMIP5 models on average, the weakening is small under a realistic range of warming, the change under transient warming is unknown. Thus, there is *very high confidence* that events of reduced and increased GMST and GSAT trends at decadal timescales will continue to occur in the 21st century (Meehl et al., 2013; Roberts et al., 2015a). However, such internal decadal variations in GSAT trend do not affect the centennial warming (England et al., 2015).

[START CROSS-CHAPTER BOX 3.1, FIGURE 1 HERE]

Cross-Chapter Box 3.1, Figure 1: (a, b) GMST trends for 1998-2012 (a) and 2012-2026 (b). Histograms (scaled so that the area under the curve sums to one) based on historical simulations of CMIP6 (red shading, extended by SSP2-4.5) and CMIP5 (blue outlines; extended by RCP4.5). Hatching shows histograms of HadCRUT5.0.0.0 and (Cowtan and Way, 2014). Triangles at the top of (a) represent GISTEMP, NOAAGlobalTemp and Berkeley Earth estimates. Selected CMIP6 members whose 1998-2012 trends are lower than the HadCRUT5.0.0.0 mean trend are indicated by darker shading (a) and vertical lines (b) in the histograms. Model GMST is based on a blend of SST and SAT masked to match HadCRUT data coverage, following Cowtan et al. (2015). (c-e) Trend maps of annual near-surface temperature. (c, d) 1998-2012 trends based on HadCRUT5.0.0.0 mean (c) and composited trends of subsampled CMIP6 simulations included in darker shading area in (a). (e) Corresponding composited trends but for 2012-2026 indicated by dark red lines in (b). Ensemble size used for each of the histograms and trend composites is indicated at the top right of each of panels (a,b,d,e).

[END CROSS-CHAPTER BOX 3.1, FIGURE 1 HERE]

[END CROSS-CHAPTER BOX 3.1 HERE]

[START CROSS-CHAPTER BOX 3.2 HERE]

Cross-Chapter Box 3.2: Human Influence on Large-scale Changes in Temperature and Precipitation Extremes

Contributors: Nathan Gillett (Canada), Seung-Ki Min (Republic of Korea), Ying Sun (China), Xuebin Zhang (Canada)

Understanding how temperature and precipitation extremes have changed at large-scale and their possible causes are important for evaluating models' performance as well as future projections. Chapter 11 assesses changes in extremes and their causes, while this Cross-Chapter Box summarizes relevant assessments and supporting evidence in Chapter 11 and relates changes in extremes to mean changes on global and continental scales.

Attribution of extreme temperatures

One important aspect of various indicators of temperature extremes is their connections to mean temperature at local, regional and global scales. For example, the highest daily temperature in a summer is often highly correlated with the summer mean temperature. Model projections show that changes in temperature extremes are often the manifestation of shifts in mean temperature. It is thus no surprise that changes in temperature extremes are consistent with warming mean temperature, with warming leading to more hot extremes and fewer cold extremes. Given that it is *virtually certain* that human influence has warmed the global climate system, and the connection between changes in mean and extreme temperatures, it is to be expected that anthropogenic forcing has also influenced temperature extremes.

Chapter 11 shows widespread evidence of human influence on various aspects of temperature extremes, at global, continental, and regional scales. This includes attribution of observed changes to human influence on changes in intensity, frequency, and duration and other relevant characteristics at the global and continental scales. The left panel of Cross-Chapter Box 3.2 Figure 1 clearly shows that long-term changes in the global mean annual maximum daily maximum temperature can be reproduced by both CMIP5 and CMIP6 models forced with the combined effect of natural and anthropogenic forcings, but cannot be reproduced by simulations under natural forcing alone.

It is *virtually certain* that anthropogenic increases in greenhouse gases have caused increases in the likelihood and/or magnitude of observed hot extremes (annual, seasonal, daily, heatwaves) and decreases in the frequency and/or severity of cold extremes across nearly land areas (Chapter 11).

Attribution of precipitation extremes

An important piece of evidence that supports the SREX and AR5 assessment that there is *medium confidence* that anthropogenic forcing has contributed to a global scale intensification of heavy precipitation during the second half of the 20th century is the anthropogenic influence on global hydrological cycle. The most significant aspect of that is the increase in atmospheric moisture content associated with warming and that higher availability of moisture should, in general, lead to enhanced extreme precipitation. Such a connection is supported by the fact that annual maximum one-day precipitation increases with global mean temperature at a rate similar to the increase in the mositure holding capacity in response to warming, both in observations and in model simulations. Additionally, models project an increase in extreme precipitation across global land regions even in areas in which total precipitation is projected to decrease.

Evidence of human influence on extreme precipitation has become stronger since AR5, based on multiple lines of evidence. These include attribution of intensification of annual maximum 1-day and 5-day precipitation amounts to human influence and consistency between expected changes in record-breaking extreme precipitation in the observations and model simulations. The right panel of Cross-Chapter Box 3.2 Figure 1 demonstrates the consistency in global average annual maximum daily precipitation in the observations and model simulations under combined anthropogenic and natural forcing, and inconsistency with natural forcing alone.

It is *likely* that anthropogenic influence is the main cause of the observed intensification of heavy precipitation in global land regions (Chapter 11).

[START CROSS-CHAPTER BOX 3.2, FIGURE 1 HERE]

Cross-Chapter Box 3.2, Figure 1: Time series of global averaged 5-year mean anomalies of TXx (°C) and Rx1day (standardized probability index, %) during 1953-2017 from the HadEX3 observations and the CMIP5 and CMIP6 multi-models with natural and human forcing (upper) and natural forcing only (lower). For CMIP5, historical simulations for 1953-2005 are combined with corresponding RCP4.5 scenario runs for 2006-2017. For CMIP6, historical simulations for 1953-2014 are combined with SSP2-45 scenario runs for 2015-2017. Number in bracket represents the number of models used. The time-fixed observational mask has been applied to model data throughout the whole period. For TXx, grids with more than 70% data availability during 1953-2017 plus having data for at least 3 years during 2013-2017 are used. For Rx1day, grids with more than 70% data availability during 1953-2011 plus having data for at least 2 years during 2008-2011 are used. Thick coloured lines indicate multi-model means (with equal weighting given for each model). Shading represents the range of CMIP5 individual model (ensemble means) and thin lines display CMIP6 individual model ensemble means. Anomalies are relative to 1961-1990 means.

[END CROSS-CHAPTER BOX 3.2, FIGURE 1 HERE]

[END CROSS-CHAPTER BOX 3.2 HERE]

Frequently Asked Questions

FAQ 3.1: How much of recent Climate Change is Actually Natural Variability?

Natural variability refers to variations in climate which are caused by processes other than human influence. It includes variability that is internally generated within the climate system, for example via modes of variability like the El Niño-Southern Oscillation, as well as externally driven climate variations driven by changes in solar brightness and by aerosols released from volcanic eruptions. Internally-driven natural variability corresponds to a redistribution of energy within the climate system that is most clearly observed as regional-scale fluctuations in climate. Externally driven natural variability is driven by changes to Earth's energy balance, and its impacts are most clearly observed in large scale climate indices like global mean surface temperature. While both forms of natural climate variability can cause large-scale climate changes, their influence on multidecadal trends is relatively small. This means that natural variability may play a prominent role in changes observed over one or two decades. However, as the observational period becomes longer, human-induced forcing changes become the dominant contributor to the observed climate changes, such that the large scale warming observed since 1900 is almost entirely driven by human influence.

Paleoclimatic records (indirect measurements that span back thousands of years) and computer models all show that global temperatures have, and are always changing – and that these changes can occur for many reasons. One of these reasons is natural variability, which refers to variations in climate that are either internally generated within the climate system or externally driven by natural forcing changes. As well as variations in solar brightness and volcanoes, changes in Earth's orbital characteristics can also create natural radiative forcing changes and have been related to large climate changes of the past. However, the orbital changes operate on very long time scales, meaning that they have had very little influence on the changes observed over the past century.

To understand which aspects of observed climate change have been caused by natural variability, scientists use climate model simulations. When only natural climate drivers are used to force climate models, which implicitly generate their own natural internal variability, the resulting simulations are generally called naturally-forced similations. These simulations show small variations in climate in response to volcanic eruptions, variations in solar brightness, and internal models of climate variability, but they do not show long-term warming trends comparable to that observed. Only when human influences, particularly greenhouse gases, are included do the models simulate warming comparable to that observed.

In reality, what both of these pieces of information combine to mean, is that on short time scales of a decade or less natural climate variability can dominate the human-induced warming trend, leading to periods with little warming. However, over periods longer than about twenty years, the impact of natural forcing is smaller than the human-induced warming-trend. Thus, warming will always be experienced. Another way to think of this is, although humans are causing recent increases in global temperatures, natural variability plays a role in how fast or slow temperatures rise. Much like riding a bike over hilly terrain, the bike is always going forward but the presence of the hills will either reduce or increase the speed.

[START FAQ 3.1, FIGURE 1 HERE]

FAQ 3.1, Figure 1: (Upper left) Climate model estimate of human-induced change in global average temperature. (Lower left) Representation of natural global average temperature variability from a climate model. (Right) The combined signal, which is similar to that observed. Overlying blue lines represent temperature changes during a period with strong naturally driven cooling, while red lines represent temperature changes during a period with strong naturally driven warming.

[END FAQ 3.1, FIGURE 1 HERE]

FAQ 3.2: Are Climate Models Improving?

Yes, climate models have improved and continue to do so. Models are now more suitable for capturing the complexities and small-scale processes of the climate system and compare better with observations for key climate variables. For decades, models have shown that changes to the climate come from man-made greenhouse gas emissions, but now our understanding of the impacts of these changes, and of the changes yet to come, are better than ever before.

Since the 1950s, scientists have used computer models to understand the Earth's climate. Fundamentally, models have improved due to advances in technology that allow for greater sophistication and more complex computer simulations, resulting in models that compare more closely with real-world observations of climate change. However, even the models used in the First Assessment Report of 1990 had skill at reproducing many aspects of climate, and their projections have since been generally validated by the actual evolution of climate.

Fundamentally, climate models generally solve equations based on the laws of physics (fluid mechanics, thermodynamics, light and infrared radiation, to name a few), usually by representing atmosphere, ocean, and land with discrete grid points distributed around the globe. The quantity and spacing of grid points defines the resolution – more grid points with less space between them result in higher-resolution simulations of Earth's climate system. Scientists also use more complex models called Earth System models that complement climate physics with representations of land and ocean biology (which are important for simulating carbon dioxide), atmospheric and oceanic chemistry, and sometimes more components, such as ice sheets.

The internal make-up of models continues to evolve, making them more suitable for simulating a variety of climate processes. This evolution is driven by improvements in our understanding of the climate system, our ability to represent that understanding of processes in terms of computer code, and the availability of increasingly powerful computers needed to run such code. The most recent generation of models often has improved resolutions in the atmosphere, ocean, and land domains. Higher resolution means, for example, that the ocean components of some climate models now explicitly simulate the 100 km-scale eddies that are responsible for much of oceanic heat transport. Unlike the previous generation of models, many of the latest-generation models now simulate higher levels of the atmosphere (above 50 km in altitude), meaning that coupling processes between the upper and lower atmosphere are now more realistic.

Earth system models that simulate changes in greenhouse gas and aerosol concentrations in response to changes in emissions (rather than having these changes prescribed) are becoming more common. For carbon dioxide concentrations, this means that these models include interactive representations of the absorption of carbon dioxide by plants on land and by the ocean and how these systems respond to climate and environmental change, including for example the impacts of ocean warming and acidification on ocean biology.

Progress in climate modelling is gradual, and more remains to be achieved. For example, it is still impossible to explicitly simulate atmospheric convection globally for multidecadal timescales. However, key aspects of climate are now better simulated than in previous model evaluations. We know this through comparisons against observational estimates, often using multiple climate variables. For example, model simulations of near-surface temperature, precipitation, and sea-level pressure compare better against their observational references for recent decades (for which these references are most reliable; FAQ 3.1, Figure 1), although in most cases the improvement is only gradual. A prime example is surface temperature, which was already well simulated in previous intercomparisons, so simulations of surface temperature only improved marginally in the current generation of models. Precipitation, a key aspect of climate which was problematic in previous evaluations, is now better captured than in the previous generation of models (see also FAQ 7.1). However, climate models still do not operate at the resolution of about 1 km needed to realistically represent clouds. An evaluation of the simulations informing the last three Assessment Reports of IPCC shows that for most atmospheric metrics (three of which are shown in Figure 1), the models of each generation as a group outperform those of the previous generation regarding the simulation of mean climate. Such improvements

in comparison with observations illustrate the increasing skill of models at simulating current climate.

[START FAQ 3.2, FIGURE 1 HERE]

FAQ 3.2, Figure 1: Centred pattern correlations between models and observations for the annual mean climatology over the period 1980–1999 for three different variables: surface air temperature, precipitation and sea level pressure. Results are shown for individual CMIP3 (black), CMIP5 (blue) and CMIP6 (brown) models as short lines, along with the corresponding ensemble average (long line). The correlations are shown between the models and the reference observational data set. In addition, the correlation between the reference and alternate observational data sets are shown (solid grey circles). To ensure a fair comparison across a range of model resolutions, the pattern correlations are computed at a resolution of 2.5º in longitude and 2.5º in latitude. Only one realization is used from each model from the CMIP3, CMIP5 and CMIP6 historical simulations. (Figure produced with ESMValTool v2.0.0b2.)

[END FAQ 3.2, FIGURE 1 HERE]

FAQ 3.3: How do we Know Humans are Responsible for Climate Change?

Synthesizing information from observations of climate change, from paleoclimate records that can show changes over the past thousands of years, and from computer models that can simulate past climate change based on physical principles, allows us to clearly identify the dominant role of humans in driving recent climate change.

Climate is influenced by a range of factors. The main natural drivers of climate change on timescales of decades to centuries are variations in the sun's brightness, and large volcanic eruptions which cause an increase in the number of small particles (aerosols) in the upper atmosphere for several years, which reflect sunlight and cool the surface. The main human drivers of climate change are increases in the concentration of greenhouse gases, which trap infrared radiation near the surface and warm the climate, and of aerosols from burning fossil fuels and other sources, which, like those produced naturally by volcanoes, on average have a cooling influence by increasing the reflection of sunlight. Multiple lines of evidence demonstrate that human drivers are the main cause of recent climate change.

Firstly, the current rates of increase of the concentration of the major greenhouse gases (carbon dioxide, methane and nitrous oxide) are unprecedented over at least the last 22,000 years. Multiple lines of evidence show that these increases are the results of human activities. The basic physics underlying the warming effect of greenhouse gases on the climate has been understood for more than a century, and our latest understanding is encapsulated in the latest generation climate models. Like weather forecasting models, climate models represent the state of the atmosphere on a grid, and simulate its evolution over time based on physical principles. They include a representation of the ocean, sea ice and the main processes important in driving climate and climate change. Results consistently show that such climate models can only reproduce the observed warming (black line in FAQ 3.3, Figure 1) when including the effects of human activities (orange band in FAQ 3.3, Figure 1), in particular the increasing concentrations of greenhouse gases. These climate models show a dominant warming effect of greenhouse gas increases (grey band, which shows the warming effects of greenhouse gases by themselves), which has been partly offset by the cooling effect of increases in atmospheric aerosols (blue band). By contrast, simulations that include only natural processes, including internal climate variability related to El Niño and other similar variations, as well as variations in solar brightness and emissions from large volcanoes (green band in FAQ 3.3, Figure 1), are not able to reproduce the observed warming – they simulate much smaller temperature trends, indicating that these natural factors cannot explain the strong warming rate observed.

An additional line of evidence for the role of humans in driving climate change comes from comparing the rate of warming observed over recent decades with that which occurred prior to human influence on climate. Evidence from tree rings and other paleoclimate records shows that the rate of increase of global mean surface temperature observed over the past fifty years far exceeded that which occurred in any previous 50-year period over the past 2000 years. Taken together this evidence shows that humans are the dominant cause of observed global warming over recent decades.

[START FAQ 3.3, FIGURE 1 HERE]

FAQ 3.3, Figure 1: Global average changes in surface air temperature in observations (HadCRUT4), compared to climate model simulations of the response to all human and natural forcings (grey band), greenhouse gases only (red band), aerosols only (blue band) and natural forcings only (green band). Solid coloured lines show the multi-model mean, and coloured bands show the 5–95% range of individual simulations.

[END FAQ 3.3, FIGURE 1 HERE]

References

(WMO), W. M. I. (2018). Executive Summary: Scientific Assessment of Ozone Depletion: 2018. Geneva, Switzerland Available at: https://www.esrl.noaa.gov/csd/assessments/ozone/2018/executivesummary.pdf.

Abellán, E., McGregor, S., and England, M. H. (2017). Analysis of the southward wind shift of ENSO in CMIP5 models. *J. Clim.* 30, 2415–2435. doi:10.1175/JCLI-D-16-0326.1.

Abram, N. J., Hargreaves, J. A., Wright, N. M., Thirumalai, K., Ummenhofer, C. C., and England, M. H. (submitted). Palaeoclimate perspectives on the Indian Ocean Dipole. *Quarternary Sci. Rev.* (submitted).

Abram, N. J., McGregor, H. V., Tierney, J. E., Evans, M. N., McKay, N. P., Kaufman, D. S., et al. (2016). Early onset of industrial-era warming across the oceans and continents. *Nature* 536, 411–418. doi:10.1038/nature19082.

Abram, N. J., Mulvaney, R., Vimeux, F., Phipps, S. J., Turner, J., and England, M. H. (2014). Evolution of the Southern Annular Mode during the past millennium. *Nat. Clim. Chang.* 4, 564–569. doi:10.1038/nclimate2235.

Abram, N. J., Wolff, E. W., and Curran, M. A. J. (2013). A review of sea ice proxy information from polar ice cores. *Quat. Sci. Rev.* 79, 168–183. doi:https://doi.org/10.1016/j.quascirev.2013.01.011.

Ackerley, D., Reeves, J., Barr, C., Bostock, H., Fitzsimmons, K., Fletcher, M.-S., et al. (2017). Evaluation of PMIP2 and PMIP3 simulations of mid-Holocene climate in the Indo-Pacific, Australasian and\hack{\newline} Southern Ocean regions. *Clim. Past* 13, 1661–1684. doi:10.5194/cp-13-1661-2017.

Adler, R. F., Gu, G., Sapiano, M., Wang, J.-J., and Huffman, G. J. (2017). Global precipitation: means, variations and trends during the satellite era (1979-2014). *Surv. Geophys.* 38, 679–699.

Adler, R. F., Huffman, G. J., Chang, A., Ferraro, R., Xie, P. P., Janowiak, J., et al. (2003). The version-2 global precipitation climatology project (GPCP) monthly precipitation analysis (1979-present). *J. Hydrometeorol.* 4, 1147–1167. doi:10.1175/1525-7541(2003)004<1147:TVGPCP>2.0.CO;2.

Alkama, R., Marchand, L., Ribes, A., and Decharme, B. (2013). Detection of global runoff changes: results from observations and CMIP5 experiments. *Hydrol. Earth Syst. Sci.* 17, 2967–2979. doi:10.5194/hess-17-2967-2013.

Allan, R. P. (2014). Dichotomy of drought and deluge. *Nat. Geosci.* 7, 700–701. doi:10.1038/ngeo2243.

Allen, M. R., Dube, O. P., Solecki, W., Aragón-Durand, F., Cramer, W., Humphreys, S., et al. (2018). "Framing and Context," in *Global Warming of 1.5°C. An IPCC Special Report on the impacts of global warming of 1.5°C above pre-industrial levels and related global greenhouse gas emission pathways, in the context of strengthening the global response to the threat of climate change*, eds. V. Masson-Delmotte, P. Zhai, H.-O. Pörtner, D. Roberts, J. Skea, P. R. Shukla, et al. (In Press).

Allen, M. R., and Stott, P. A. (2003). Estimating signal amplitudes in optimal fingerprinting, part I: theory. *Clim. Dyn.* 21, 477–491. doi:10.1007/s00382-003-0313-9.

Allen, M. R., and Tett, S. F. B. (1999). Checking for model consistency in optimal fingerprinting. *Clim. Dyn.* 15, 419–434. doi:10.1007/s003820050291.

Allen, R. J., and Kovilakam, M. (2017). The role of natural climate variability in recent tropical expansion. *J. Clim.* 30, 6329–6350. doi:10.1175/JCLI-D-16-0735.1.

Allen, R. J., Norris, J. R., and Kovilakam, M. (2014). Influence of anthropogenic aerosols and the Pacific Decadal Oscillation on tropical belt width. *Nat. Geosci.* 7, 270–274. doi:10.1038/ngeo2091.

Amaya, D. J., DeFlorio, M. J., Miller, A. J., and Xie, S.-P. (2017). WES feedback and the Atlantic Meridional Mode: observations and CMIP5 comparisons. *Clim. Dyn.* 49, 1665–1679. doi:10.1007/s00382-016-3411-1.

Amaya, D. J., Siler, N., Xie, S.-P., and Miller, A. J. (2018). The interplay of internal and forced modes of Hadley Cell expansion: lessons from the global warming hiatus. *Clim. Dyn.* 51, 305–319. doi:10.1007/s00382-017-3921-5.

Amiri-Farahani, A., Allen, R. J., Li, K. F., and Chu, J. E. (2019). The Semidirect Effect of Combined Dust and Sea Salt Aerosols in a Multimodel Analysis. *Geophys. Res. Lett.* 46, 10512–10521. doi:10.1029/2019GL084590.

Andrews, M. B., Knight, J. R., and Gray, L. J. (2015). A simulated lagged response of the North Atlantic Oscillation to the solar cycle over the period 1960–2009. *Environ. Res. Lett.* 10, 054022. doi:10.1088/1748-9326/10/5/054022.

Andrews, M. B., Ridley, J. K., Wood, R. A., Andrews, T., Blockley, E., Booth, B. B. B., et al. (submitted). Historical simulations with HadGEM3-GC3.1 for CMIP6. (submitted).

Andrews, T., Andrews, M. B., Bodas-Salcedo, A., Jones, G. S., Kulhbrodt, T., Manners, J., et al. (2019). Forcings, feedbacks and climate sensitivity in HadGEM3-GC3. 1 and UKESM1. *J. Adv. Model. Earth Syst.* 11.

Annan, J. D., and Hargreaves, J. C. (2011). Understanding the CMIP3 Multimodel Ensemble. *J. Clim.* 24, 4529–4538. doi:10.1175/2011JCLI3873.1.

Annan, J. D., and Hargreaves, J. C. (2015). A perspective on model-data surface temperature comparison at the Last Glacial Maximum. *Quat. Sci. Rev.* 107, 1–10. doi:https://doi.org/10.1016/j.quascirev.2014.09.019.

Aquila, V., Swartz, W. H., Waugh, D. W., Colarco, P. R., Pawson, S., Polvani, L. M., et al. (2016). Isolating the roles of different forcing agents in global stratospheric temperature changes using model integrations with incrementally added single forcings. *J. Geophys. Res.* 121, 8067–8082. doi:10.1002/2015JD023841.

Arora, V. K., Katavouta, A., Williams, R. G., Jones, C. D., Brovkin, V., Friedlingstein, P., et al. (submitted). Carbon-concentration and carbon-climate feedbacks in CMIP6 models, and their comparison to CMIP5 models. *Biogeosciences Discuss.* (submitted).

Ashok, K., Behera, S. K., Rao, S. A., Weng, H., and Yamagata, T. (2007). El Niño Modoki and its possible teleconnection. *J. Geophys. Res. Ocean.* 112, 1–27. doi:10.1029/2006JC003798.

Ault, T. R., Cole, J. E., and St. George, S. (2012). The amplitude of decadal to multidecadal variability in precipitation simulated by state-of-the-art climate models. *Geophys. Res. Lett.* 39, n/a-n/a. doi:10.1029/2012GL053424.

Ayarzagüena, B., Polvani, L. M., Langematz, U., Akiyoshi, H., Bekki, S., Butchart, N., et al. (2018). No Robust Evidence of Future Changes in Major Stratospheric Sudden Warmings: A Multi-model Assessment from CCMI. *Atmos. Chem. Phys. Discuss.* 2018, 1–17. doi:10.5194/acp-2018-296.

Ayash, T., Gong, S., and Jia, C. Q. (2008). Direct and Indirect Shortwave Radiative Effects of Sea Salt Aerosols. *J. Clim.* 21, 3207–3220. doi:10.1175/2007JCLI2063.1.

Ayers, J. M., and Lozier, M. S. (2012). Unraveling dynamical controls on the North Pacific carbon sink. *J. Geophys. Res. Ocean.* 117. doi:10.1029/2011JC007368.

Baker, H. S., Woollings, T., Forest, C. E., and Allen, M. R. (2019). The Linear Sensitivity of the North Atlantic Oscillation and Eddy-Driven Jet to SSTs. *J. Clim.* 32, 6491–6511. doi:10.1175/JCLI-D-19-0038.1.

Baker, H. S., Woollings, T., and Mbengue, C. (2017). Eddy-Driven Jet Sensitivity to Diabatic Heating in an Idealized GCM. *J. Clim.* 30, 6413–6431. doi:10.1175/JCLI-D-16-0864.1.

Balaguru, K., Chang, P., Saravanan, R., Leung, L. R., Xu, Z., Li, M., et al. (2012). Ocean barrier layers' effect on tropical cyclone intensification. *Proc. Natl. Acad. Sci. U. S. A.* 109, 14343–14347. doi:10.1073/pnas.1201364109.

Balaguru, K., Foltz, G. R., Leung, L. R., and Emanuel, K. A. (2016). Global warming-induced upper-ocean freshening and the intensification of super typhoons. *Nat. Commun.* 7. doi:10.1038/ncomms13670.

Balmaseda, M. A., Trenberth, K. E., and Källén, E. (2013). Distinctive climate signals in reanalysis of global ocean heat content. *Geophys. Res. Lett.* 40, 1754–1759. doi:10.1002/grl.50382.

Balsamo, G., Albergel, C., Beljaars, A., Boussetta, S., Brun, E., Cloke, H., et al. (2015). ERA-Interim/Land: A global land surface reanalysis data set. *Hydrol. Earth Syst. Sci.* 19, 389–407. doi:10.5194/hess-19-389-2015.

Bamber, J. L., Westaway, R. M., Marzeion, B., and Wouters, B. (2018). The land ice contribution to sea level during the satellite era. *Environ. Res. Lett.* 13. doi:10.1088/1748-9326/aac2f0.

Banerjee, A., Fyfe, J. C., Polvani, L. M., Waugh, D., and Chang, K.-L. (submitted). A pause in Southern Hemisphere circulation trends due to the Montreal Protocol. *Nature* (submitted).

Barichivich, J., Briffa, K. R., Myneni, R. B., Osborn, T. J., Melvin, T. M., Ciais, P., et al. (2013). Large-scale variations in the vegetation growing season and annual cycle of atmospheric CO2 at high northern latitudes from 1950 to 2011. *Glob. Chang. Biol.* 19, 3167–3183. doi:doi:10.1111/gcb.12283.

Barkhordarian, A., von Storch, H., Behrangi, A., Loikith, P., Mechoso, C. R., and Detzer, J. (2018). Simultaneous regional detection of land-use changes and elevated GHG levels: the case of spring precipitation in tropical South America. *Geophys. Res. Lett.* 45.

Bartlein, P. J., Harrison, S. P., Brewer, S., Connor, S., Davis, B. A. S., Gajewski, K., et al. (2011). Pollen-based continental climate reconstructions at 6 and 21 ka: A global synthesis. *Clim. Dyn.* 37, 775–802. doi:10.1007/s00382-010-0904-1.

Bartlein, P. J., Harrison, S. P., and Izumi, K. (2017). Underlying causes of Eurasian midcontinental aridity in simulations of mid-Holocene climate. *Geophys. Res. Lett.* 44, 9020–9028.

Batehup, R., McGregor, S., and Gallant, A. J. E. (2015). The influence of non-stationary teleconnections on palaeoclimate reconstructions of ENSO variance using a pseudoproxy framework. *Clim. Past* 11, 1733–1749. doi:10.5194/cp-11-1733-2015.

Bates, N., Astor, Y., Church, M., Currie, K., Dore, J., Gonaález-Dávila, M., et al. (2014). A Time-Series View of Changing Ocean Chemistry Due to Ocean Uptake of Anthropogenic CO2 and Ocean Acidification. *Oceanography* 27, 126–141. doi:10.5670/oceanog.2014.16.

Bayr, T., Wengel, C., Latif, M., Dommenget, D., Lübbecke, J., and Park, W. (2019). Error compensation of ENSO atmospheric feedbacks in climate models and its influence on simulated ENSO dynamics. *Clim. Dyn.* 53, 155–172. doi:10.1007/s00382-018-4575-7.

Beadling, R. L., Russell, J. L., Stouffer, R. J., Mazloff, M., Talley, L, D., Goodman, P. J., et al. (submitted). Representation of Southern Ocean properties across Coupled Model Intercomparison Project generations: CMIP3 to CMIP6. *J. Clim.* (submitted).

Becker, M., Karpytchev, M., and Lennartz-Sassinek, S. (2014). Long-term sea level trends: Natural or anthropogenic? *Geophys. Res. Lett.* 41, 5571–5580. doi:10.1002/2014GL061027.

Bellenger, H., Drushka, K., Asher, W., Reverdin, G., Katsumata, M., and Watanabe, M. (2017). Extension of the prognostic model of sea surface temperature to rain-induced cool and fresh lenses. *J. Geophys. Res. Ocean.* 122, 484–507. doi:10.1002/2016JC012429.

Bellenger, H., Guilyardi, E., Leloup, J., Lengaigne, M., and Vialard, J. (2014). ENSO representation in climate models: From CMIP3 to CMIP5. *Clim. Dyn.* 42, 1999–2018. doi:10.1007/s00382-013-1783-z.

Bellomo, K., and Clement, A. C. (2015). Evidence for weakening of the Walker circulation from cloud observations. *Geophys. Res. Lett.* 42, 7758–7766. doi:10.1002/2015GL065463.

Bellomo, K., Murphy, L. N., Cane, M. A., Clement, A. C., and Polvani, L. M. (2018). Historical forcings as main drivers of the Atlantic multidecadal variability in the CESM large ensemble. *Clim. Dyn.* 50, 3687–3698.

doi:10.1007/s00382-017-3834-3.
Bellucci, A., Mariotti, A., and Gualdi, S. (2017). The Role of Forcings in the Twentieth-Century North Atlantic Multidecadal Variability: The 1940–75 North Atlantic Cooling Case Study. *J. Clim.* 30, 7317–7337. doi:10.1175/JCLI-D-16-0301.1.
Berger, M., Camps, A., Font, J., Kerr, Y., Miller, J., Johannessen, J. A., et al. (2002). Measuring Ocean Salinity with ESA's SMOS Mission – Advancing the Science. in (ESA Publications Division), 113–121. Available at: http://bora.uib.no/handle/1956/867 [Accessed September 16, 2018].
Bernie, D. J., Guilyardi, E., Madec, G., Slingo, J. M., and Woolnough, S. J. (2007). Impact of resolving the diurnal cycle in an ocean-atmosphere GCM. Part 1: A diurnally forced OGCM. *Clim. Dyn.* 29, 575–590. doi:10.1007/s00382-007-0249-6.
Bernie, D. J., Guilyardi, E., Madec, G., Slingo, J. M., Woolnough, S. J., and Cole, J. (2008). Impact of resolving the diurnal cycle in an ocean-atmosphere GCM. Part 2: A diurnally coupled CGCM. *Clim. Dyn.* 31, 909–925. doi:10.1007/s00382-008-0429-z.
Bernie, D. J., Woolnough, S. J., Slingo, J. M., and Guilyardi, E. (2005). Modeling diurnal and intraseasonal variability of the ocean mixed layer. *J. Clim.* 18, 1190–1202. doi:10.1175/JCLI3319.1.
Biasutti, M., Voigt, A., Boos, W. R., Braconnot, P., Hargreaves, J. C., Harrison, S. P., et al. (2018). Global energetics and local physics as drivers of past, present and future monsoons. *Nat. Geosci.* 11, 392–400. doi:10.1038/s41561-018-0137-1.
Bilbao, R. A. F., Gregory, J. M., Bouttes, N., Palmer, M. D., and Stott, P. (2019). Attribution of ocean temperature change to anthropogenic and natural forcings using the temporal, vertical and geographical structure. *Clim. Dyn.* 53, 5389–5413. doi:10.1007/s00382-019-04910-1.
Bindoff, N. L., Cheung, W. W. L., Kairo, J. G., Aristegui, J., Guinder, V. A., Hallberg, R., et al. (2019). "Changing Ocean, Marine Ecosystems, and Dependent Communities," in *IPCC Special Report on the Ocean and Cryosphere in a Changing Climate*, eds. H.-O. Pörtner, D. C. Roberts, V. Masson-Delmotte, P. Zhai, M. Tignor, E. Poloczanska, et al. (Cambridge University Press), tba. Available at: https://www.ipcc.ch/srocc.
Bindoff, N. L., Stott, P. A., AchutaRao, K. M., Allen, M. R., Gillett, N. P., Gutzler, D., et al. (2013). "Detection and attribution of climate change: From global to regional," in *Climate Change 2013 the Physical Science Basis: Working Group I Contribution to the Fifth Assessment Report of the Intergovernmental Panel on Climate Change*, ed. Intergovernmental Panel on Climate Change (Cambridge: Cambridge University Press), 867–952. doi:10.1017/CBO9781107415324.022.
Bindoff, N. L., Willebrand, J., Artale, V., Cazenave, A., Gregory, J. M., Gulev, S., et al. (2007). "Observations: oceanic climate change and sea level," in *Intergovernmental Panel on Climate Change Fourth Assessment Report Climate Change 2007: The Physical Science Basis*, ed. Intergovernmental Panel on Climate Change (Cambridge: Cambridge University Press), 385–432. Available at: http://nora.nerc.ac.uk/id/eprint/15400.
Bindschadler, R. A., Nowicki, S., Abe-OUCHI, A., Aschwanden, A., Choi, H., Fastook, J., et al. (2013). Ice-sheet model sensitivities to environmental forcing and their use in projecting future sea level (the SeaRISE project). *J. Glaciol.* 59, 195–224. doi:10.3189/2013JoG12J125.
Bintanja, R., van Oldenborgh, G. J., Drijfhout, S. S., Wouters, B., and Katsman, C. A. (2013). Important role for ocean warming and increased ice-shelf melt in Antarctic sea-ice expansion. *Nat. Geosci.* 6, 376. Available at: http://dx.doi.org/10.1038/ngeo1767.
Bintanja, R., van Oldenborgh, G. J., and Katsman, C. A. (2015). The effect of increased fresh water from Antarctic ice shelves on future trends in Antarctic sea ice. *Ann. Glaciol.* 56, 120–126. doi:DOI: 10.3189/2015AoG69A001.
Birkel, S. D., Mayewski, P. A., Maasch, K. A., Kurbatov, A. V., and Lyon, B. (2018). Evidence for a volcanic underpinning of the Atlantic multidecadal oscillation. *npj Clim. Atmos. Sci.* 1, 24. doi:10.1038/s41612-018-0036-6.
Bitz, C. M. (2008). Some aspects of uncertainty in predicting sea ice thinning.
Blackport, R., Screen, J. A., van der Wiel, K., and Bintanja, R. (2019). Minimal influence of reduced Arctic sea ice on coincident cold winters in mid-latitudes. *Nat. Clim. Chang.* 9, 697–704. doi:10.1038/s41558-019-0551-4.
Blazquez, J., and Solman, S. (2017). Fronts and precipitation in CMIP5 models for the austral winter of the Southern Hemisphere. *Clim. Dyn.* 50, 2705–2717. doi:10.1007/s00382-017-3765-z.
Bock, L., Lauer, A., Eyring, V., Schlundt, M., Barreiro, M., Bellouin, N., et al. (submitted). Quantifying progress across different CMIP phases with the ESMValTool. *J. Geophys. Res. Atmos.* (submitted).
Bodas-Salcedo, A., Hill, P. G., Furtado, K., Williams, K. D., Field, P. R., Manners, J. C., et al. (2016). Large Contribution of Supercooled Liquid Clouds to the Solar Radiation Budget of the Southern Ocean. *J. Clim.* 29, 4213–4228. doi:10.1175/JCLI-D-15-0564.1.
Boisséson, E., Balmaseda, M. A., Abdalla, S., Källén, E., and Janssen, P. A. E. M. (2014). How robust is the recent strengthening of the Tropical Pacific trade winds? *Geophys. Res. Lett.* 41, 4398–4405. doi:10.1002/2014GL060257.
Boland, E. J. D., Bracegirdle, T. J., and Shuckburgh, E. F. (2017). Assessment of sea ice-atmosphere links in CMIP5 models. *Clim. Dyn.* 49, 683–702. doi:10.1007/s00382-016-3367-1.
Bonfils, C. J. W., Santer, B. D., Fyfe, J. C., Marvel, K., Phillips, T. J., and Zimmerman, S. R. H. (submitted). Human

influence on joint changes in temperature, rainfall and continental aridity. (submitted).
Bonfils, C., and Santer, B. D. (2011). Investigating the possibility of a human component in various pacific decadal oscillation indices. *Clim. Dyn.* 37, 1457–1468. doi:10.1007/s00382-010-0920-1.
Bonjean, F., and Lagerloef, G. S. E. (2002). Diagnostic Model and Analysis of the Surface Currents in the Tropical Pacific Ocean. *J. Phys. Oceanogr.* 32, 2938–2954. doi:10.1175/1520-0485(2002)032<2938:DMAAOT>2.0.CO;2.
Boo, K.-O., Booth, B. B. B., Byun, Y.-H., Lee, J., Cho, C., Shim, S., et al. (2015). Influence of aerosols in multidecadal SST variability simulations over the North Pacific. *J. Geophys. Res. Atmos.* 120, 517–531. doi:10.1002/2014JD021933.
Boone, A., Samuelsson, P., Gollvik, S., Napoly, A., Jarlan, L., Brun, E., et al. (2017). The interactions between soil-biosphere-atmosphere land surface model with a multi-energy balance (ISBA-MEB) option in SURFEXv8-Part 1: Model description. *Geosci. Model Dev.* 10, 843–872. doi:10.5194/gmd-10-843-2017.
Boos, W. R., and Hurley, J. V (2012). Thermodynamic Bias in the Multimodel Mean Boreal Summer Monsoon. *J. Clim.* 26, 2279–2287. doi:10.1175/JCLI-D-12-00493.1.
Booth, B. B. B., Dunstone, N. J., Halloran, P. R., Andrews, T., and Bellouin, N. (2012). Aerosols implicated as a prime driver of twentieth-century North Atlantic climate variability. *Nature* 484, 228–232. doi:10.1038/nature10946.
Bopp, L., Resplandy, L., Orr, J. C., Doney, S. C., Dunne, J. P., Gehlen, M., et al. (2013). Multiple stressors of ocean ecosystems in the 21st century: projections with CMIP5 models. *Biogeosciences* 10, 6225–6245. doi:10.5194/bg-10-6225-2013.
Bordbar, M. H., Martin, T., Latif, M., and Park, W. (2017). Role of internal variability in recent decadal to multidecadal tropical Pacific climate changes. *Geophys. Res. Lett.* 44, 4246–4255. doi:10.1002/2016GL072355.
Boucher, O., Servonnat, J., Albright, A. L., Aumont, O., Balkanski, Y., Bastrikov, V., et al. (submitted). Presentation and evaluation of the IPSL-CM6A-LR climate model. *J. Adv. Model. Earth Syst.* (submitted).
Bracegirdle, T. J., Holmes, C. R., Hosking, J. S., Marshall, G. J., Osman, M., Patterson, M., et al. (submitted). Improvements in Circumpolar Southern Hemisphere Extratropical Atmospheric Circulation in CMIP6 Compared to CMIP5. *Earth Sp. Sci.* (submitted).
Bracegirdle, T. J., Lu, H., Eade, R., and Woollings, T. (2018). Do CMIP5 Models Reproduce Observed Low-Frequency North Atlantic Jet Variability? *Geophys. Res. Lett.* 45, 7204–7212. doi:10.1029/2018GL078965.
Braconnot, P., Harrison, S. P., Kageyama, M., and et al. (2012). Evaluation of climate models using palaeoclimatic data. *Nat. Clim. Chang.* 2, 417–424. doi:10.1038/nclimate1456.
Breeden, M. L., and McKinley, G. A. (2016). Climate impacts on multidecadal pCO2 variability in the North Atlantic: 1948–2009. *Biogeosciences* 13, 3387–3396. doi:10.5194/bg-13-3387-2016.
Breitburg, D., Levin, L. A., Oschlies, A., Grégoire, M., Chavez, F. P., Conley, D. J., et al. (2018). Declining oxygen in the global ocean and coastal waters. *Science* 359, eaam7240. doi:10.1126/science.aam7240.
Brierley, Chris M, Fedorov, A. V., Liu, Z., Herbert, T., Lawrence, K., and LaRiviere, J. (2009). Greatly expanded tropical warm pool and weakened Hadley circulation in the early Pliocene. *Science* 323, 1714–1718.
Brierley, C. M., Zhao, A., Harrison, S. P., Braconnot, P., Williams, C. J. R., Thornalley, D. J. R., et al. (submitted). Large-scale features and evaluation of the CMIP6/PMIP4 midHolocene simulations. (submitted).
Brierley, C., and Wainer, I. (2017). Interannual Variability in the Tropical Atlantic from the Last Glacial Maximum into Future Climate Projections simulated by CMIP5/PMIP3. *Clim. Past Discuss.* doi:10.5194/cp-2017-145.
Brown, R., Vikhamar-Schuler, D., Bulygina, O., Derksen, C., Loujus, K., Mudryk, L., … Yang, D. (2017). "Arctic terrestrial snow cover," in (Oslo: Arctic Monitoring and Assessment Programme (AMAP).), 25–64.
Brown, P. T., Li, W., Jiang, J. H., and Su, H. (2016a). Spread in the magnitude of climate model interdecadal global temperature variability traced to disagreements over high-latitude oceans. *Geophys. Res. Lett.* 43, 12,543-12,549. doi:10.1002/2016GL071442.
Brown, P. T., Li, W., and Xie, S.-P. (2015). Regions of significant influence on unforced global mean surface air temperature variability in climate models. *J. Geophys. Res. Atmos.* 120, 480–494. doi:10.1002/2014JD022576.
Brown, P. T., Lozier, M. S., Zhang, R., and Li, W. (2016b). The necessity of cloud feedback for a basin-scale Atlantic Multidecadal Oscillation. *Geophys. Res. Lett.* 43, 3955–3963. doi:10.1002/2016GL068303.
Brown, P. T., Ming, Y., Li, W., and Hill, S. A. (2017). Change in the magnitude and mechanisms of global temperature variability with warming. *Nat. Clim. Chang.* 7, 743–748. doi:10.1038/nclimate3381.
Brown, R. D., and Robinson, D. A. (2011). Northern Hemisphere spring snow cover variability and change over 1922-2010 including an assessment of uncertainty. *Cryosphere* 5, 219–229. doi:10.5194/tc-5-219-2011.
Brutel-Vuilmet, C., Menegoz, M., and Krinner, G. (2013). An analysis of present and future seasonal Northern Hemisphere land snow cover simulated by CMIP5 coupled climate models. *CRYOSPHERE* 7, 67–80. doi:10.5194/tc-7-67-2013.
Bryan, F., and Bachman, S. (2015). Isohaline Salinity Budget of the North Atlantic Salinity Maximum. *J. Phys. Oceanogr.* 45, 724–736. doi:10.1175/JPO-D-14-0172.1.
Bryden, H. L., Longworth, H. R., and Cunningham, S. A. (2005). Slowing of the Atlantic meridional overturning circulation at 25° N. *Nature* 438, 655–657. doi:10.1038/nature04385.
Buckley, M. W., and Marshall, J. (2016). Observations, inferences, and mechanisms of the Atlantic Meridional

Overturning Circulation: A review. *Rev. Geophys.* 54, 5–63. doi:10.1002/2015RG000493.
Bueler, E., and Brown, J. (2009). Shallow shelf approximation as a "sliding law" in a thermomechanically coupled ice sheet model. *J. Geophys. Res. Solid Earth* 114, F03008. doi:10.1029/2008JF001179.
Burgman, R. J., and Jang, Y. (2015). Simulated U.S. drought response to interannual and decadal pacific SST variability. *J. Clim.* 28, 4688–4705. doi:10.1175/JCLI-D-14-00247.1.
Burls, N., and Fedorov, A. V. (2014). What controls the mean east-west surface temperature gradient in the equatorial Pacific. *J. Clim.* 27, 2757–2778.
Burls, N., and Fedorov, A. V. (2017). Wetter subtropics in a warmer world: Contrasting past and future hydrological cycles. *Proc. Natl. Acad. Sci.* 114, 12888–12893.
Butler, A. H., Arribas, A., Athanassiadou, M., Baehr, J., Calvo, N., Charlton-Perez, A., et al. (2016). The Climate-system Historical Forecast Project: do stratosphere-resolving models make better seasonal climate predictions in boreal winter? *Q. J. R. Meteorol. Soc.* 142, 1413–1427. doi:10.1002/qj.2743.
Cabré, A., Marinov, I., Bernardello, R., and Bianchi, D. (2015). Oxygen minimum zones in the tropical Pacific across CMIP5 models: mean state differences and climate change trends. *Biogeosciences* 12, 5429–5454. doi:10.5194/bg-12-5429-2015.
Caesar, L., Rahmstorf, S., Robinson, A., Feulner, G., and Saba, V. (2018). Observed fingerprint of a weakening Atlantic Ocean overturning circulation. *Nature* 556, 191–196. doi:10.1038/s41586-018-0006-5.
Cai, W., Santoso, A., Wang, G., Weller, E., Wu, L., Ashok, K., et al. (2014). Increased frequency of extreme Indian Ocean Dipole events due to greenhouse warming. *Nature* 510, 254–258. doi:10.1038/nature13327.
Cai, W., Wu, L., Lengaigne, M., Li, T., McGregor, S., Kug, J.-S., et al. (2019). Pantropical climate interactions. *Science* 363, eaav4236. doi:10.1126/science.aav4236.
Cai, W., Zheng, X.-T., Weller, E., Collins, M., Cowan, T., Lengaigne, M., et al. (2013). Projected response of the Indian Ocean Dipole to greenhouse warming. *Nat. Geosci.* 6, 999. Available at: http://dx.doi.org/10.1038/ngeo2009.
Caldwell, P. M., Mametjanov, A., Tang, Q., Van Roekel, L. P., Golaz, J.-C., Lin, W., et al. (2019). The DOE E3SM Coupled Model Version 1: Description and Results at High Resolution. *J. Adv. Model. Earth Syst.* doi:10.1029/2019MS001870.
Calvo, N., Polvani, L. M., and Solomon, S. (2015). On the surface impact of Arctic stratospheric ozone extremes. *Environ. Res. Lett.* 10. doi:10.1088/1748-9326/10/9/094003.
Cane, M. A., Clement, A. C., Murphy, L. N., and Bellomo, K. (2017). Low-Pass Filtering, Heat Flux, and Atlantic Multidecadal Variability. *J. Clim.* 30, 7529–7553. doi:10.1175/JCLI-D-16-0810.1.
Capotondi, A., Wittenberg, A. T., Newman, M., Di Lorenzo, E., Yu, J.-Y., Braconnot, P., et al. (2014). Understanding ENSO Diversity. *Bull. Am. Meteorol. Soc.* 96, 921–938. doi:10.1175/BAMS-D-13-00117.1.
Capron, E., Govin, A., Feng, R., Otto-Bliesner, B. L., and Wolff, E. W. (2017). Critical evaluation of climate syntheses to benchmark CMIP6/PMIP4 127 ka Last Interglacial simulations in the high-latitude regions. *Quat. Sci. Rev.* 168, 137–150. doi:https://doi.org/10.1016/j.quascirev.2017.04.019.
Caron, L.-P., Hermanson, L., and Doblas-Reyes, F. J. (2015). Multiannual forecasts of Atlantic U.S. tropical cyclone wind damage potential. *Geophys. Res. Lett.* 42, 2417–2425. doi:10.1002/2015GL063303.
Cassou, C., Kushnir, Y., Hawkins, E., Pirani, A., Kucharski, F., Kang, I.-S., et al. (2018). Decadal Climate Variability and Predictability: Challenges and Opportunities. *Bull. Am. Meteorol. Soc.* 99, 479–490. doi:10.1175/BAMS-D-16-0286.1.
Cazenave, A., Meyssignac, B., Ablain, M., Balmaseda, M., Bamber, J., Barletta, V., et al. (2018). Global sea-level budget 1993-present. *Earth Syst. Sci. Data* 10, 1551–1590. doi:10.5194/essd-10-1551-2018.
Cha, S.-C., Moon, J.-H., and Song, Y. T. (2018). A Recent Shift Toward an El Niño-Like Ocean State in the Tropical Pacific and the Resumption of Ocean Warming. *Geophys. Res. Lett.* 45, 11,885-11,894. doi:10.1029/2018GL080651.
Chai, J., Liu, F., Liu, J., and Shen, X. (2018). Enhanced Global Monsoon in Present Warm Period Due to Natural and Anthropogenic Forcings. *Atmosphere (Basel).* 9, 136. doi:10.3390/atmos9040136.
Chang, E. K. M., Ma, C.-G., Zheng, C., and Yau, A. M. W. (2016). Observed and projected decrease in Northern Hemisphere extratropical cyclone activity in summer and its impacts on maximum temperature. *Geophys. Res. Lett.* 43, 2200–2208. doi:10.1002/2016GL068172.
Charlton-Perez, A. J., Baldwin, M. P., Birner, T., Black, R. X., Butler, A. H., Calvo, N., et al. (2013). On the lack of stratospheric dynamical variability in low-top versions of the CMIP5 models. *J. Geophys. Res. Atmos.* 118, 2494–2505. doi:10.1002/jgrd.50125.
Chassignet, E. P., Yeager, S., Fox-Kemper, B., Bozec, A., Castruccio, F., Danabasoglu, G., et al. (submitted). Impact of horizontal resolution on global ocean-sea-ice model simulations based on the experimental protocols of the Ocean Model Intercomparison Project phase 2 (OMIP-2). *Geosci. Model Dev.* (submitted).
Chen, H., Schneider, E. K., and Wu, Z. (2016a). Mechanisms of internally generated decadal-to-multidecadal variability of SST in the Atlantic Ocean in a coupled GCM. *Clim. Dyn.* 46, 1517–1546. doi:10.1007/s00382-015-2660-8.
Chen, H. W., Zhang, F., and Alley, R. B. (2016b). The Robustness of Midlatitude Weather Pattern Changes due to Arctic Sea Ice Loss. *J. Clim.* 29, 7831–7849. doi:10.1175/JCLI-D-16-0167.1.

Chen, R., Simpson, I. R., Deser, C., and Wang, B. (submitted). Model biases in the simulation of the springtime North Pacific ENSO teleconnection. *J. Clim.* (submitted).
Chen, X., and Tung, K.-K. (2014). Varying planetary heat sink led to global-warming slowdown and acceleration. *Science* 345, 897–903. doi:10.1126/science.1254937.
Cheng, L., Abraham, J., Hausfather, Z., and Trenberth, K. E. (2019). How fast are the oceans warming? *Science* 363, 128–129. doi:10.1126/science.aav7619.
Cheng, L., Trenberth, K. E., Fasullo, J., Boyer, T., Abraham, J., and Zhu, J. (2017). Improved estimates of ocean heat content from 1960 to 2015. *Sci. Adv.* 3, e1601545. doi:10.1126/sciadv.1601545.
Cheng, L., Trenberth, K. E., Palmer, M. D., Zhu, J., and Abraham, J. P. (2016). Observed and simulated full-depth ocean heat-content changes for 1970-2005. *Ocean Sci.* 12, 925–935. doi:10.5194/os-12-925-2016.
Cheng, W., Chiang, J. C. H., and Zhang, D. (2013). Atlantic meridional overturning circulation (AMOC) in CMIP5 Models: RCP and historical simulations. *J. Clim.* 26, 7187–7197. doi:10.1175/JCLI-D-12-00496.1.
Chenoli, S. N., Mazuki, M. Y. A., Turner, J., and Abu Samah, A. (2017). Historical and projected changes in the Southern Hemisphere Sub-tropical Jet during winter from the CMIP5 models. *Clim. Dyn.* 48, 661–681. doi:10.1007/s00382-016-3102-y.
Cheung, A. H., Mann, M. E., Steinman, B. A., Frankcombe, L. M., England, M. H., and Miller, S. K. (2017). Comparison of low-frequency internal climate variability in CMIP5 models and observations. *J. Clim.* 30, 4763–4776. doi:10.1175/JCLI-D-16-0712.1.
Chiang, J., Lan, C.-W., Chung, C.-H., Liao, Y.-C., and Lee, C.-J. (2013). Increase in the range between wet and dry season precipitation. *Nat. Geosci.* 6, 263–267.
Chikamoto, Y., Mochizuki, T., Timmermann, A., Kimoto, M., and Watanabe, M. (2016). Potential tropical Atlantic impacts on Pacific decadal climate trends. *Geophys. Res. Lett.* 43, 7143–7151. doi:10.1002/2016GL069544.
Choi, J., Son, S.-W., and Park, R. J. (2019). Aerosol versus greenhouse gas impacts on Southern Hemisphere general circulation changes. *Clim. Dyn.* 52, 4127–4142. doi:10.1007/s00382-018-4370-5.
Chu, J.-E., Ha, K.-J., Lee, J.-Y., Wang, B., Kim, B.-H., and Chung, C. E. (2014). Future change of the Indian Ocean basin-wide and dipole modes in the CMIP5. *Clim. Dyn.* 43, 535–551. doi:10.1007/s00382-013-2002-7.
Chung, E.-S., Soden, B. J., Sohn, B. J., and Shi, L. (2014). Upper-tropospheric moistening in response to anthropogenic warming. *Proc. Natl. Acad. Sci. U. S. A.* doi:10.1073/pnas.1409659111.
Chung, E.-S., Timmermann, A., Soden, B. J., Ha, K.-J., Shi, L., and John, V. O. (2019). Reconciling opposing Walker circulation trends in observations and model projections. *Nat. Clim. Chang.* 9, 405–412. doi:10.1038/s41558-019-0446-4.
Church, J. A., Clark, P. U., Cazenave, A., Gregory, J. M., Jevrejeva, S., Levermann, A., et al. (2013a). "Sea Level Change," in *Climate Change 2013 - The Physical Science Basis*, ed. Intergovernmental Panel on Climate Change (Cambridge: Cambridge University Press), 1137–1216. doi:10.1017/CBO9781107415324.026.
Church, J. A., Monselesan, D., Gregory, J. M., and Marzeion, B. (2013b). Evaluating the ability of process based models to project sea-level change. *Environ. Res. Lett.* 8, 014051. doi:10.1088/1748-9326/8/1/014051.
Cleator, S. F., Harrison, S. P., Nichols, N. K., Prentice, I. C., and Roulstone, I. (2019). A new multi-variable benchmark for Last Glacial Maximum climate simulations. *Clim. Past Discuss.* 2019, 1–22. doi:10.5194/cp-2019-55.
Clem, K. R., Renwick, J. A., and McGregor, J. (2017). Relationship between eastern tropical Pacific cooling and recent trends in the Southern Hemisphere zonal-mean circulation. *Clim. Dyn.* 49, 113–129. doi:10.1007/s00382-016-3329-7.
Clement, A., Bellomo, K., Murphy, L. N., Cane, M. A., Mauritsen, T., Rädel, G., et al. (2015). The Atlantic Multidecadal Oscillation without a role for ocean circulation. *Science* 350, 320–324. doi:10.1126/science.aab3980.
Coats, S., and Karnauskas, K. B. (2017). Are Simulated and Observed Twentieth Century Tropical Pacific Sea Surface Temperature Trends Significant Relative to Internal Variability? *Geophys. Res. Lett.* 44, 9928–9937. doi:10.1002/2017GL074622.
Coats, S., Smerdon, J. E., Cook, B. I., Seager, R., Cook, E. R., and Anchukaitis, K. J. (2016). Internal ocean-atmosphere variability drives megadroughts in Western North America. *Geophys. Res. Lett.* 43, 9886–9894. doi:10.1002/2016GL070105.
Cobb, K. M., Westphal, N., Sayani, H. R., Watson, J. T., Di Lorenzo, E., Cheng, H., et al. (2013). Highly variable El Niño-Southern Oscillation throughout the Holocene. *Science* 339, 67–70. doi:10.1126/science.1228246.
Cocco, V., Joos, F., Steinacher, M., Frölicher, T. L., Bopp, L., Dunne, J., et al. (2013). Oxygen and indicators of stress for marine life in multi-model global warming projections. *Biogeosciences* 10, 1849–1868. doi:10.5194/bg-10-1849-2013.
Collins, M., An, S.-I., Cai, W., Ganachaud, A., Guilyardi, E., Jin, F.-F., et al. (2010). The impact of global warming on the tropical Pacific Ocean and El Niño. *Nat. Geosci.* 3, 391. Available at: https://doi.org/10.1038/ngeo868.
Collins, W. J., Lamarque, J.-F., Schulz, M., Boucher, O., Eyring, V., Hegglin, M. I., et al. (2017). AerChemMIP: quantifying the effects of chemistry and aerosols in CMIP6.
Colman, R., and Power, S. B. (2018). What can decadal variability tell us about climate feedbacks and sensitivity? *Clim. Dyn.* 51, 3815–3828. doi:10.1007/s00382-018-4113-7.

Comyn-Platt, E., Hayman, G., Huntingford, C., Chadburn, S. E., Burke, E. J., Harper, A. B., et al. (2018). Carbon budgets for 1.5 and 2 °C targets lowered by natural wetland and permafrost feedbacks. *Nat. Geosci.* 11, 568–573. doi:10.1038/s41561-018-0174-9.

Cook, B. I., Anchukaitis, K. J., Touchan, R., Meko, D. M., and Cook, E. R. (2016a). Spatiotemporal drought variability in the mediterranean over the last 900 years. *J. Geophys. Res.* doi:10.1002/2015JD023929.

Cook, B. I., Cook, E. R., Smerdon, J. E., Seager, R., Williams, A. P., Coats, S., et al. (2016b). North American megadroughts in the Common Era: reconstructions and simulations. *Wiley Interdiscip. Rev. Clim. Chang.* 7, 411–432. doi:10.1002/wcc.394.

Cook, E. R., Anchukaitis, K. J., Buckley, B. M., D'Arrigo, R. D., Jacoby, G. C., and Wright, W. E. (2010). Asian monsoon failure and megadrought during the last millennium. *Science* doi:10.1126/science.1185188.

Cook, E. R., Seager, R., Kushnir, Y., Briffa, K. R., Büntgen, U., Frank, D., et al. (2015). Old World megadroughts and pluvials during the Common Era. *Sci. Adv.* doi:10.1126/sciadv.1500561.

Cook, E. R., Woodhouse, C. A., Eakin, C. M., Meko, D. H., and Stahle, D. W. (2004). Long-term aridity changes in the western United States. *Science* doi:10.1126/science.1102586.

Corvec, S., and Fletcher, C. G. (2017). Changes to the tropical circulation in the mid-Pliocene and their implications for future climate. *Clim. Past* 13, 135–147. doi:10.5194/cp-13-135-2017.

Cowan, T., Cai, W., Ng, B., and England, M. (2015). The Response of the Indian Ocean Dipole Asymmetry to Anthropogenic Aerosols and Greenhouse Gases. *J. Clim.* 28, 2564–2583. doi:10.1175/JCLI-D-14-00661.1.

Cowtan, K., Hausfather, Z., Hawkins, E., Jacobs, P., Mann, M. E., Miller, S. K., et al. (2015). Robust comparison of climate models with observations using blended land air and ocean sea surface temperatures. 42, 6526–6535. doi:10.1002/2015GL064888.Abstract.

Cowtan, K., and Way, R. G. (2014). Coverage bias in the HadCRUT4 temperature series and its impact on recent temperature trends. *Q. J. R. Meteorol. Soc.* 140, 1935–1944. doi:10.1002/qj.2297.

Crueger, T., Giorgetta, M. A., Brokopf, R., Esch, M., Fiedler, S., Hohenegger, C., et al. (2018). ICON-A, The Atmosphere Component of the ICON Earth System Model: II. Model Evaluation. *J. Adv. Model. Earth Syst.* doi:10.1029/2017MS001233.

D'Andrea, F., Tibaldi, S., Blackburn, M., Boer, G., Déqué, M., Dix, M. R., et al. (1998). Northern Hemisphere atmospheric blocking as simulated by 15 atmospheric general circulation models in the period 1979--1988. *Clim. Dyn.* 14, 385–407. doi:10.1007/s003820050230.

Dai, A., and Bloecker, C. E. (2018). Impacts of internal variability on temperature and precipitation trends in large ensemble simulations by two climate models. *Clim. Dyn.*, 1–18. doi:10.1007/s00382-018-4132-4.

Dai, A., Fyfe, J. C., Xie, S. P., and Dai, X. (2015). Decadal modulation of global surface temperature by internal climate variability. *Nat. Clim. Chang.* 5. doi:10.1038/nclimate2605.

Daley, R. (1993). Estimating observation error statistics for atmospheric data assimilation. *Ann. Geophys. Eur. Geophys. Soc.* 11, 634–634.

Danabasoglu, G., Lamarque, J.-F., Bacmeister, J., Bailey, D. A., DuVivier, A., Edwards, J., et al. (submitted). The Community Earth System Model version 2 (CESM2). *J. Adv. Model. Earth Syst.* (submitted).

Danabasoglu, G., Yeager, S., Bailey, D., Behrens, E., Bentsen, M., Bi, D., et al. (2014). North Atlantic Simulations in Coordinated Ocean-ice Reference Experiments phase 2 (CORE-II). Part 1: Mean States. *Ocean Model.* 73, 76–107. doi:10.1016/j.ocemod.2013.10.005.

Danabasoglu, G., Yeager, S. G., Kim, W. M., Behrens, E., Bentsen, M., Bi, D., et al. (2016). North Atlantic simulations in Coordinated Ocean-ice Reference Experiments phase II (CORE-II). Part II: Inter-annual to decadal variability. *Ocean Model.* 97, 65–90. doi:10.1016/j.ocemod.2015.11.007.

Dangendorf, S., Marcos, M., Müller, A., Zorita, E., Riva, R., Berk, K., et al. (2015). Detecting anthropogenic footprints in sea level rise. *Nat. Commun.* 6, 7849. doi:10.1038/ncomms8849.

Dätwyler, C., Neukom, R., Abram, N. J., Gallant, A. J. E., Grosjean, M., Jacques-Coper, M., et al. (2018). Teleconnection stationarity, variability and trends of the Southern Annular Mode (SAM) during the last millennium. *Clim. Dyn.* 51, 2321–2339. doi:10.1007/s00382-017-4015-0.

Davini, P., and Cagnazzo, C. (2014). On the misinterpretation of the North Atlantic Oscillation in CMIP5 models. *Clim. Dyn.* 43, 1497–1511. doi:10.1007/s00382-013-1970-y.

Davini, P., Corti, S., D'Andrea, F., Rivière, G., and von Hardenberg, J. (2017). Improved Winter European Atmospheric Blocking Frequencies in High-Resolution Global Climate Simulations. *J. Adv. Model. Earth Syst.* 9, 2615–2634. doi:10.1002/2017MS001082.

Davini, P., and D'Andrea, F. (2016). Northern Hemisphere Atmospheric Blocking Representation in Global Climate Models: Twenty Years of Improvements? *J. Clim.* 29, 8823–8840. doi:10.1175/JCLI-D-16-0242.1.

Davini, P., and D'Andrea, F. (submitted). From CMIP-3 to CMIP-6: Northern Hemisphere atmospheric blocking simulation in present and future climate. *J. Clim.* (submitted).

Davini, P., von Hardenberg, J., and Corti, S. (2015). Environmental Research Letters Related content Tropical origin for the impacts of the Atlantic Multidecadal Variability on the Euro-Atlantic climate. *Environ. Res. Lett.* 10, 94010. Available at: http://iopscience.iop.org/article/10.1088/1748-9326/8/3/034037/pdf.

Davis, N., and Birner, T. (2017). On the Discrepancies in Tropical Belt Expansion between Reanalyses and Climate

Models and among Tropical Belt Width Metrics. *J. Clim.* 30, 1211–1231. doi:10.1175/JCLI-D-16-0371.1.
DelSole, T., Trenary, L., Yan, X., and Tippett, M. K. (2019). Confidence intervals in optimal fingerprinting. *Clim. Dyn.* 52, 4111–4126. doi:10.1007/s00382-018-4356-3.
Delworth, T. L., and Dixon, K. W. (2006). Have anthropogenic aerosols delayed a greenhouse gas-induced weakening of the North Atlantic thermohaline circulation? *Geophys. Res. Lett.* 33. doi:10.1029/2005GL024980.
Delworth, T. L., Zeng, F., Rosati, A., Vecchi, G. A., and Wittenberg, A. T. (2015). A Link between the Hiatus in Global Warming and North American Drought. *J. Clim.* 28, 3834–3845. doi:10.1175/JCLI-D-14-00616.1.
Delworth, T. L., Zeng, F., Zhang, L., Zhang, R., Vecchi, G. A., and Yang, X. (2017). The Central Role of Ocean Dynamics in Connecting the North Atlantic Oscillation to the Extratropical Component of the Atlantic Multidecadal Oscillation. *J. Clim.* 30, 3789–3805. doi:10.1175/JCLI-D-16-0358.1.
Dennison, F. W., McDonald, A. J., and Morgenstern, O. (2015). The effect of ozone depletion on the Southern Annular Mode and stratosphere-troposphere coupling. *J. Geophys. Res. Atmos.* 120, 6305–6312. doi:10.1002/2014JD023009.
Dennison, F. W., McDonald, A., and Morgenstern, O. (2016). The influence of ozone forcing on blocking in the Southern Hemisphere. *J. Geophys. Res. Atmos.* 121, 14,358-14,371. doi:10.1002/2016JD025033.
Deppenmeier, A.-L., Haarsma, R. J., and Hazeleger, W. (2016). The Bjerknes feedback in the tropical Atlantic in CMIP5 models. *Clim. Dyn.* 47, 2691–2707. doi:10.1007/s00382-016-2992-z.
Deser, C., Guo, R., and Lehner, F. (2017a). The relative contributions of tropical Pacific sea surface temperatures and atmospheric internal variability to the recent global warming hiatus. *Geophys. Res. Lett.* 44, 7945–7954. doi:10.1002/2017GL074273.
Deser, C., Hurrell, J. W., and Phillips, A. S. (2017b). The role of the North Atlantic Oscillation in European climate projections. *Clim. Dyn.* 49, 3141–3157. doi:10.1007/s00382-016-3502-z.
Deser, C., Phillips, A. S., and Alexander, M. A. (2010). Twentieth century tropical sea surface temperature trends revisited. *Geophys. Res. Lett.* 37, n/a-n/a. doi:10.1029/2010GL043321.
Deser, C., Sun, L., Tomas, R. A., and Screen, J. (2016). Does ocean coupling matter for the northern extratropical response to projected Arctic sea ice loss? *Geophys. Res. Lett.* 43, 2149–2157. doi:10.1002/2016GL067792.
Deutsch, C., Berelson, W., Thunell, R., Weber, T., Tems, C., McManus, J., et al. (2014). Oceanography. Centennial changes in North Pacific anoxia linked to tropical trade winds. *Science* 345, 665–8. doi:10.1126/science.1252332.
DiNezio, P. N., Clement, A., Vecchi, G. A., Soden, B., Broccoli, A. J., Otto-Bliesner, B. L., et al. (2011). The response of the Walker circulation to Last Glacial Maximum forcing: Implications for detection in proxies. *Paleoceanography* 26. doi:10.1029/2010PA002083.
DiNezio, P. N., and Tierney, J. E. (2013). The effect of sea level on glacial Indo-Pacific climate. *Nat. Geosci.* 6, 485–491. doi:10.1038/ngeo1823.
DiNezio, P. N., Tierney, J. E., Otto-Bliesner, B. L., Timmermann, A., Bhattacharya, T., Rosenbloom, N., et al. (2018). Glacial changes in tropical climate amplified by the Indian Ocean. *Sci. Adv.* 4, eaat9658.
DiNezio, P. N., Vecchi, G. A., and Clement, A. C. (2013). Detectability of Changes in the Walker Circulation in Response to Global Warming. *J. Clim.* 26, 4038–4048. doi:10.1175/JCLI-D-12-00531.1.
Ding, H., Greatbatch, R. J., Latif, M., and Park, W. (2015). The impact of sea surface temperature bias on equatorial Atlantic interannual variability in partially coupled model experiments. *Geophys. Res. Lett.* 42, 5540–5546. doi:10.1002/2015GL064799.
Ding, Q., Schweiger, A., L'Heureux, M., Battisti, D. S., Po-Chedley, S., Johnson, N. C., et al. (2017). Influence of high-latitude atmospheric circulation changes on summertime Arctic sea ice. *Nat. Clim. Chang.* 7, 289–295. doi:10.1038/nclimate3241.
Ding, Q., Schweiger, A., L'Heureux, M., Steig, E. J., Battisti, D. S., Johnson, N. C., et al. (2019). Fingerprints of internal drivers of Arctic sea ice loss in observations and model simulations. *Nat. Geosci.* 12, 28–33. doi:10.1038/s41561-018-0256-8.
Dippe, T., Greatbatch, R. J., and Ding, H. (2018). On the relationship between Atlantic Niño variability and ocean dynamics. *Clim. Dyn.* 51, 597–612. doi:10.1007/s00382-017-3943-z.
Dittus, A. J., Hawkins, E., Wilcox, L. J., Sutton, R. T., Smith, C. J., Andrews, M., et al. (submitted). Sensitivity of historical climate simulations to uncertain aerosol forcing. *Geophys. Res. Lett.* (submitted).
Docquier, D., Grist, J. P., Roberts, M. J., Roberts, C. D., Semmler, T., Ponsoni, L., et al. (2019). Impact of model resolution on Arctic sea ice and North Atlantic Ocean heat transport. *Clim. Dyn.* 53, 4989–5017. doi:10.1007/s00382-019-04840-y.
Domeisen, D. I. V., Garfinkel, C. I., and Butler, A. H. (2019). The Teleconnection of El Niño Southern Oscillation to the Stratosphere. *Rev. Geophys.* 57, 5–47. doi:10.1029/2018RG000596.
Domeisen, D. I. V (2019). Estimating the Frequency of Sudden Stratospheric Warming Events From Surface Observations of the North Atlantic Oscillation. *J. Geophys. Res. Atmos.* 124, 3180–3194. doi:10.1029/2018JD030077.
Domingues, C. M., Church, J. A., White, N. J., Gleckler, P. J., Wijffels, S. E., Barker, P. M., et al. (2008). Improved estimates of upper-ocean warming and multi-decadal sea-level rise. *Nature* 453, 1090–1093. doi:10.1038/nature07080.

Dong, L., and McPhaden, M. J. (2017). Why has the relationship between Indian and Pacific Ocean decadal variability changed in recent decades? *J. Clim.* 30, 1971–1983. doi:10.1175/JCLI-D-16-0313.1.

Dong, L., and Zhou, T. (2014). The Indian Ocean Sea Surface Temperature Warming Simulated by CMIP5 Models during the Twentieth Century: Competing Forcing Roles of GHGs and Anthropogenic Aerosols. *J. Clim.* 27, 3348–3362. doi:10.1175/JCLI-D-13-00396.1.

Dong, L., Zhou, T., and Chen, X. (2014a). Changes of Pacific decadal variability in the twentieth century driven by internal variability, greenhouse gases, and aerosols. *Geophys. Res. Lett.* 41, 8570–8577. doi:10.1002/2014GL062269.

Dong, L., Zhou, T., Dai, A., Song, F., Wu, B., and Chen, X. (2016). The Footprint of the Inter-decadal Pacific Oscillation in Indian Ocean Sea Surface Temperatures. *Sci. Rep.* 6, 21251. Available at: http://dx.doi.org/10.1038/srep21251.

Dong, L., Zhou, T., and Wu, B. (2014b). Indian Ocean warming during 1958-2004 simulated by a climate system model and its mechanism. *Clim. Dyn.* 42, 203–217. doi:10.1007/s00382-013-1722-z.

Douville, H., and Plazzotta, M. (2017). Midlatitude summer drying: and underestimated threat in CMIP5 models? *Geophys. Res. Lett.* 44. doi:10.1002/2017GL075353.

Douville, H., Ribes, A., and Tyteca, S. (2019). Breakdown of NAO reproducibility into internal versus externally-forced components: a two-tier pilot study. *Clim. Dyn.* 52, 29–48. doi:10.1007/s00382-018-4141-3.

Douville, H., Voldoire, A., and Geoffroy, O. (2015). The recent global warming hiatus: What is the role of Pacific variability? *Geophys. Res. Lett.* 42, 880–888. doi:10.1002/2014GL062775.

Downes, S. M., Farneti, R., Uotila, P., Griffies, S. M., Marsland, S. J., Bailey, D., et al. (2015). An assessment of Southern Ocean water masses and sea ice during 1988-2007 in a suite of interannual CORE-II simulations. *Ocean Model.* 94, 67–94. doi:10.1016/j.ocemod.2015.07.022.

Downes, S. M., and Hogg, A. M. (2013). Southern Ocean Circulation and Eddy Compensation in CMIP5 Models. *J. Clim.* 26, 7198–7220. doi:10.1175/JCLI-D-12-00504.1.

Downes, S. M., Spence, P., and Hogg, A. M. (2018). Understanding variability of the Southern Ocean overturning circulation in CORE-II models. *Ocean Model.* 123, 98–109. doi:https://doi.org/10.1016/j.ocemod.2018.01.005.

Drews, A., and Greatbatch, R. J. (2016). Atlantic Multidecadal Variability in a model with an improved North Atlantic Current. *Geophys. Res. Lett.* 43, 8199–8206. doi:10.1002/2016GL069815.

Drijfhout, S. (2018). The relation between natural variations in ocean heat uptake and global mean surface temperature anomalies in CMIP5. *Sci. Rep.* 8, 7402. doi:10.1038/s41598-018-25342-7.

Du, Y., Xie, S.-P., Huang, G., and Hu, K. (2009). Role of Air–Sea Interaction in the Long Persistence of El Niño–Induced North Indian Ocean Warming. *J. Clim.* 22, 2023–2038. doi:10.1175/2008JCLI2590.1.

Dunn-Sigouin, E., and Son, S.-W. (2013). Northern Hemisphere blocking frequency and duration in the CMIP5 models. *J. Geophys. Res.* 118, 1179–1188. doi:10.1002/jgrd.50143.

Dunn, R. J. H., Willett, K. M., Ciavarella, A., and Stott, P. A. (2017). Comparison of land surface humidity between observations and CMIP5 models. *Earth Syst. Dyn.* 8, 719–747. doi:10.5194/esd-8-719-2017.

Dunne, J. P., Horowitz, L. W., Adcroft, A. J., Ginoux, P., Held, I. M., John, J. G., et al. (submitted). The GFDL Earth System Model version 4.1 (GFDL-ESM4.1): Model description and simulation characteristics. *J. Adv. Model. Earth Syst.* (submitted).

Durack, P., Gleckler, P., Purkey, S., Johnson, G., Lyman, J., and Boywe, T. (2018). Ocean Warming: From the Surface to the Deep in Observations and Models. *Oceanography* 31, 41–51. doi:10.5670/oceanog.2018.227.

Durack, P. J. (2015). Ocean salinity and the global water cycle. *Oceanography* 28, 20–31. doi:10.5670/oceanog.2015.03.

Durack, P. J., Gleckler, P. J., Landerer, F. W., and Taylor, K. E. (2014a). Quantifying underestimates of long-term upper-ocean warming. *Nat. Clim. Chang.* 4, 999–1005. doi:10.1038/nclimate2389.

Durack, P. J., and Wijffels, S. E. (2010). Fifty-Year trends in global ocean salinities and their relationship to broad-scale warming. *J. Clim.* 23, 4342–4362. doi:10.1175/2010JCLI3377.1.

Durack, P. J., Wijffels, S. E., and Boyer, T. P. (2013). Long-term salinity changes and implications for the global water cycle. *Int. Geophys.* 103, 727–757. doi:10.1016/B978-0-12-391851-2.00028-3.

Durack, P. J., Wijffels, S. E., and Gleckler, P. J. (2014b). Long-term sea-level change revisited: The role of salinity. *Environ. Res. Lett.* 9. doi:10.1088/1748-9326/9/11/114017.

Durack, P. J., Wijffels, S. E., and Matear, R. J. (2012). Ocean salinities reveal strong global water cycle intensification during 1950 to 2000. *Science* 336, 455–458. doi:10.1126/science.1212222.

Dwyer, J. G., Biasutti, M., and Sobel, A. H. (2014). The effect of greenhouse gas-induced changes in SST on the annual cycle of zonal mea tropical precipitation. *J. Clim.* 27, 4544–4565.

England, M. H., Kajtar, J. B., and Maher, N. (2015). Robust warming projections despite the recent hiatus. *Nat. Clim. Chang.* 5, 394. Available at: http://dx.doi.org/10.1038/nclimate2575.

England, M. H., Mcgregor, S., Spence, P., Meehl, G. A., Timmermann, A., Cai, W., et al. (2014). Recent intensification of wind-driven circulation in the Pacific and the ongoing warming hiatus. *Nat. Clim. Chang.* 4, 222–227. doi:10.1038/nclimate2106.

Eyring, V., Arblaster, J. M., Cionni, I., Sedláček, J., Perlwitz, J., Young, P. J., et al. (2013). Long-term ozone changes

and associated climate impacts in CMIP5 simulations. *J. Geophys. Res. Atmos.* 118, 5029–5060. doi:10.1002/jgrd.50316.

Eyring, V., Bock, L., Lauer, A., Righi, M., Schlund, M., Andela, B., et al. (2019a). ESMValTool v2.0 -- Extended set of large-scale diagnostics for quasi-operational and comprehensive evaluation of Earth system models in CMIP. *Geosci. Model Dev. Discuss.* 2019, 1–81. doi:10.5194/gmd-2019-291.

Eyring, V., Bony, S., Meehl, G. A., Senior, C. A., Stevens, B., Stouffer, R. J., et al. (2016). Overview of the Coupled Model Intercomparison Project Phase 6 (CMIP6) experimental design and organization. *Geosci. Model Dev.* 9, 1937–1958. doi:10.5194/gmd-9-1937-2016.

Eyring, V., Cox, P. M., Flato, G. M., Gleckler, P. J., Abramowitz, G., Caldwell, P., et al. (2019b). Taking climate model evaluation to the next level. *Nat. Clim. Chang.* 9, 102–110. doi:10.1038/s41558-018-0355-y.

Ezer, T., Atkinson, L. P., Corlett, W. B., and Blanco, J. L. (2013). Gulf Stream's induced sea level rise and variability along the U.S. mid-Atlantic coast. *J. Geophys. Res. Ocean.* 118, 685–697. doi:10.1002/jgrc.20091.

Farinotti, D., Huss, M., Fürst, J. J., Landmann, J., Machguth, H., Maussion, F., et al. (2019). A consensus estimate for the ice thickness distribution of all glaciers on Earth. *Nat. Geosci.*, 1. doi:10.1038/s41561-019-0300-3.

Farneti, R., Downes, S. M., Griffies, S. M., Marsland, S. J., Behrens, E., Bentsen, M., et al. (2015). An assessment of Antarctic Circumpolar Current and Southern Ocean meridional overturning circulation during 1958-2007 in a suite of interannual CORE-II simulations. *Ocean Model.* 93, 84–120. doi:10.1016/j.ocemod.2015.07.009.

Fasullo, J. T., Phillips, A. S., and Deser, C. (submitted). Evaluation of Leading Modes of Climate Variability in the CMIP Archives. *J Clim.* (submitted).

Fathrio, I., Iizuka, S., Manda, A., Kodama, Y. M., Ishida, S., Moteki, Q., et al. (2017a). Assessment of western Indian Ocean SST bias of CMIP5 models. *J. Geophys. Res. Ocean.* 122, 3123–3140. doi:10.1002/2016JC012443.

Fathrio, I., Manda, A., Iizuka, S., Kodama, Y. M., and Ishida, S. (2017b). Evaluation of CMIP5 models on sea surface salinity in the Indian Ocean. *IOP Conf. Ser. Earth Environ. Sci.* 54, 012039. doi:10.1088/1755-1315/54/1/012039.

Fay, A. R., and McKinley, G. A. (2013). Global trends in surface ocean $p\,CO_2$ from in situ data. *Global Biogeochem. Cycles* 27, 541–557. doi:10.1002/gbc.20051.

Fay, A. R., McKinley, G. A., and Lovenduski, N. S. (2014). Southern Ocean carbon trends: Sensitivity to methods. *Geophys. Res. Lett.* 41, 6833–6840. doi:10.1002/2014GL061324.

Fedorov, A. V., Dekens, P., McCarthy, M., Ravelo, A., deMenocal, P. B., Barreiro, M., et al. (2006). The Pliocene paradox (Mechanisms for a permanent El Niño). *Science* 312, 1485–1489.

Feldstein, S. B., and Franzke, C. (2006). Are the North Atlantic Oscillation and the Northern Annular Mode Distinguishable? *J. Atmos. Sci.* 63, 2915–2930. doi:10.1175/JAS3798.1.

Ferreira, D., and Marshall, J. (2015). Freshwater transport in the coupled ocean-atmosphere system: a passive ocean. *Ocean Dyn.* 65, 1029–1036. doi:10.1007/s10236-015-0846-6.

Ferreira, D., Marshall, J., Bitz, C. M., Solomon, S., and Plumb, A. (2014). Antarctic Ocean and Sea Ice Response to Ozone Depletion: A Two-Time-Scale Problem. *J. Clim.* 28, 1206–1226. doi:10.1175/JCLI-D-14-00313.1.

Fettweis, X., Hanna, E., Lang, C., Belleflamme, A., Erpicum, M., and Gallée, H. (2013). Brief communication "Important role of the mid-tropospheric atmospheric circulation in the recent surface melt increase over the Greenland ice sheet." *Cryosph.* 7, 241–248. doi:10.5194/tc-7-241-2013.

Fine, E. C., Bryan, F. O., Large, W. G., and Bailey, D. A. (2015). An initial estimate of the global distribution of diurnal variation in sea surface salinity. *J. Geophys. Res. Ocean.* 120, 3211–3228. doi:10.1002/2014JC010483.

Flato, G., Marotzke, J., Abiodun, B., Braconnot, P., Chou, S. C. C., Collins, W., et al. (2013). "Evaluation of climate models," in *Climate Change 2013 the Physical Science Basis: Working Group I Contribution to the Fifth Assessment Report of the Intergovernmental Panel on Climate Change*, eds. T. F. Stocker, D. Qin, G.-K. Plattner, M. Tignor, S. K. Allen, J. Boschung, et al. (Cambridge, United Kingdom and New York, NY, USA: Cambridge University Press), 741–866. doi:10.1017/CBO9781107415324.020.

Fleischer, K., Rammig, A., De Kauwe, M. G., Walker, A. P., Domingues, T. F., Fuchslueger, L., et al. (2019). Amazon forest response to CO2 fertilization dependent on plant phosphorus acquisition. *Nat. Geosci.* doi:10.1038/s41561-019-0404-9.

Fleming, L. E., and Anchukaitis, K. J. (2016). North Pacific decadal variability in the CMIP5 last millennium simulations. *Clim. Dyn.* 47, 3783–3801. doi:10.1007/s00382-016-3041-7.

Fletcher, C. G., and Cassou, C. (2015). The Dynamical Influence of Separate Teleconnections from the Pacific and Indian Oceans on the Northern Annular Mode. *J. Clim.* 28, 7985–8002. doi:10.1175/JCLI-D-14-00839.1.

Flynn, C. M., and Mauritsen, T. (submitted). On the Climate Sensitivity and HistoricalWarming Evolution in Recent Coupled Model Ensembles. *Atmos. Chem. Phys.* (submitted).

Fogt, R. L., Goergens, C. A., Jones, J. M., Schneider, D. P., Nicolas, J. P., Bromwich, D. H., et al. (2017). A twentieth century perspective on summer Antarctic pressure change and variability and contributions from tropical SSTs and ozone depletion. *Geophys. Res. Lett.* 44, 9918–9927. doi:10.1002/2017GL075079.

Folland, C. K., Renwick, J. A., Salinger, M. J., and Mullan, A. B. (2002). Relative influences of the Interdecadal Pacific Oscillation and ENSO on the South Pacific Convergence Zone. *Geophys. Res. Lett.* 29, 2–5. doi:10.1029/2001GL014201.

Foltz, G. R., Brandt, P., Richter, I., Rodríguez-Fonseca, B., Hernandez, F., Dengler, M., et al. (2019). The Tropical

Atlantic Observing System. *Front. Mar. Sci.* 6. doi:10.3389/fmars.2019.00206.
Forkel, M., Carvalhais, N., Rödenbeck, C., Keeling, R., Heimann, M., Thonicke, K., et al. (2016). Enhanced seasonal CO2 exchange caused by amplified plant productivity in northern ecosystems. *Science* 351, 696–699. doi:10.1126/science.aac4971.
Frajka-Williams, E., Beaulieu, C., and Duchez, A. (2017). Emerging negative Atlantic Multidecadal Oscillation index in spite of warm subtropics. *Sci. Rep.* 7, 11224. doi:10.1038/s41598-017-11046-x.
Frauen, C., and Dommenget, D. (2010). El Niño and La Niña amplitude asymmetry caused by atmospheric feedbacks. *Geophys. Res. Lett.* 37. doi:10.1029/2010GL044444.
Freund, M. B., Henley, B. J., Karoly, D. J., McGregor, H. V, Abram, N. J., and Dommenget, D. (2019). Higher frequency of Central Pacific El Niño events in recent decades relative to past centuries. *Nat. Geosci.* 12, 450–455. doi:10.1038/s41561-019-0353-3.
Friedman, A. R., Hegerl, G. C., Schurer, A., Lee, S.-Y., Kong, W., and Chiang, J. C. H. (submitted). Forced and unforced behavior of the interhemispheric SST contrast during the instrumental period. (submitted).
Friedman, A. R., Reverdin, G., Khodri, M., and Gastineau, G. (2017). A new record of Atlantic sea surface salinity from 1896 to 2013 reveals the signatures of climate variability and long-term trends. *Geophys. Res. Lett.* 44, 1866–1876. doi:10.1002/2017GL072582.
Fučkar, N. S., Massonnet, F., Guemas, V., García-Serrano, J., Bellprat, O., Acosta, M., et al. (2016). Record Low Northern Hemisphere Sea Ice Extent in March 2015. *Bull. Am. Meteorol. Soc.* 97, S136–S140. doi:10.1175/BAMS-D-16-0153.1.
Fyke, J., Sergienko, O., Löfverström, M., Price, S., and Lenaerts, J. T. M. (2018). An Overview of Interactions and Feedbacks Between Ice Sheets and the Earth System. *Rev. Geophys.* 56, 361–408. doi:10.1029/2018RG000600.
Gagné, M.-È., Fyfe, J. C., Gillett, N. P., Polyakov, I. V, and Flato, G. M. (2017a). Aerosol-driven increase in Arctic sea ice over the middle of the twentieth century. *Geophys. Res. Lett.* 44, 7338–7346. doi:10.1002/2016GL071941.
Gagné, M.-È., Gillett, N. P., and Fyfe, J. C. (2015). Observed and simulated changes in Antarctic sea ice extent over the past 50 years. *Geophys. Res. Lett.* 42, 90–95. doi:10.1002/2014GL062231.
Gagné, M.-È., Kirchmeier-Young, M. C., Gillett, N. P., and Fyfe, J. C. (2017b). Arctic sea ice response to the eruptions of Agung, El Chichón, and Pinatubo. *J. Geophys. Res. Atmos.* 122, 8071–8078. doi:10.1002/2017JD027038.
Gao, J., Minobe, S., Roberts, M. J., Haarsma, R., Putrasahan, D., Roberts, C. D., et al. (submitted). Influence of Model Resolution on Bomb Cyclones Revealed by HighResMIP-PRIMAVERA Simulations. *Environ. Res. Lett.* (submitted).
Garreaud, R. D., Alvarez-Garreton, C., Barichivich, J., Boisier, J. P., Christie, D., Galleguillos, M., et al. (2017). The 2010–2015 megadrought in central Chile: impacts on regional hydroclimate and vegetation. *Hydrol. Earth Syst. Sci.* 21, 6307–6327. doi:10.5194/hess-21-6307-2017.
Garry, F. K., Roberts, C. D., Blaker, A. T., McDonagh, E. L., Frajka-Williams, E., and King, B. A. (submitted). Increasing importance of deep ocean heat storage in 21st century climate projections. *Nat. Sci. Reports* (submitted).
Gastineau, G., and Frankignoul, C. (2015). Influence of the North Atlantic SST variability on the atmospheric circulation during the twentieth century. *J. Clim.* 28, 1396–1416. doi:10.1175/JCLI-D-14-00424.1.
Gastineau, G., Friedman, A. R., Khodri, M., and Vialard, J. (2019). Global ocean heat content redistribution during the 1998–2012 Interdecadal Pacific Oscillation negative phase. *Clim. Dyn.* 53, 1187–1208. doi:10.1007/s00382-018-4387-9.
Gebbie, G., and Huybers, P. (2019). The Little Ice Age and 20th-century deep Pacific cooling. *Science* 363, 70–74. doi:10.1126/science.aar8413.
Gedney, N., Huntingford, C., Weedon, G. P., Bellouin, N., Boucher, O., and Cox, P. M. (2014). *Detection of solar dimming and brightening effects on Northern Hemisphere river flow*. Nature Geoscience doi:10.1038/ngeo2263.
Gent, P. R. (2016). Effects of Southern Hemisphere Wind Changes on the Meridional Overturning Circulation in Ocean Models. *Ann. Rev. Mar. Sci.* 8, 79–94. doi:10.1146/annurev-marine-122414-033929.
Gerber, E. P., and Son, S.-W. (2014). Quantifying the Summertime Response of the Austral Jet Stream and Hadley Cell to Stratospheric Ozone and Greenhouse Gases. *J. Clim.* 27, 5538–5559. doi:10.1175/JCLI-D-13-00539.1.
Gettelman, A., Mills, M. J., Kinnison, D. E., Garcia, R. R., Smith, A. K., Marsh, D. R., et al. (2019). The Whole Atmosphere Community Climate Model Version 6 (WACCM6). *J. Geophys. Res. Atmos.* doi:10.1029/2019JD030943.
Gierz, P., Werner, M., and Lohmann, G. (2017). Simulating climate and stable water isotopes during the Last Interglacial using a coupled climate-isotope model. *J. Adv. Model. Earth Syst.* 9, 2027–2045. doi:10.1002/2017MS001056.
Gillett, N. P., Allen, M. R., and Williams, K. D. (2003). Modelling the atmospheric response to doubled CO2 and depleted stratospheric ozone using a stratosphere-resolving coupled GCM. *Q. J. R. Meteorol. Soc.* 129, 947–966. doi:10.1256/qj.02.102.
Gillett, N. P., Arora, V. K., Matthews, D., and Allen, M. R. (2013a). Constraining the ratio of global warming to cumulative CO2emissions using CMIP5 simulations. *J. Clim.* doi:10.1175/JCLI-D-12-00476.1.
Gillett, N. P., and Fyfe, J. C. (2013). Annular mode changes in the CMIP5 simulations. *Geophys. Res. Lett.* 40, 1189–

1193. doi:10.1002/grl.50249.
Gillett, N. P., Fyfe, J. C., and Parker, D. E. (2013b). Attribution of observed sea level pressure trends to greenhouse gas, aerosol, and ozone changes. *Geophys. Res. Lett.* 40, 2302–2306. doi:10.1002/grl.50500.
Gillett, N. P., Kirchmeier-Young, M. C., Ribes, A., Shiogama, H., Hegerl, G. C., Knutti, R., et al. (submitted). Constraining human contributions to observed warming since preindustrial. *Nat. Clim. Chang.* (submitted).
Gillett, N. P., Shiogama, H., Funke, B., Hegerl, G., Knutti, R., Matthes, K., et al. (2016). The Detection and Attribution Model Intercomparison Project (DAMIP v1.0) contribution to CMIP6. *Geosci. Model Dev.* 9, 3685–3697. doi:10.5194/gmd-9-3685-2016.
Gleckler, P. J., Durack, P. J., Stouffer, R. J., Johnson, G. C., and Forest, C. E. (2016). Industrial-era global ocean heat uptake doubles in recent decades. *Nat. Clim. Chang.* 6, 394–398. doi:10.1038/nclimate2915.
Gleckler, P. J., Santer, B. D., Domingues, C. M., Pierce, D. W., Barnett, T. P., Church, J. A., et al. (2012). Human-induced global ocean warming on multidecadal timescales. *Nat. Clim. Chang.* 2, 524–529. doi:10.1038/nclimate1553.
Gleckler, P. J., Taylor, K. E., and Doutriaux, C. (2008). Performance metrics for climate models. *J. Geophys. Res.* 113, D06104. doi:10.1029/2007JD008972.
Goelzer, H., Nowicki, S., Edwards, T., Beckley, M., Abe-Ouchi, A., Aschwanden, A., et al. (2018). Design and results of the ice sheet model initialisation initMIP-Greenland: An ISMIP6 intercomparison. *Cryosphere* 12, 1433–1460. doi:10.5194/tc-12-1433-2018.
Goelzer, H., Robinson, A., Seroussi, H., and van de Wal, R. S. W. (2017). Recent Progress in Greenland Ice Sheet Modelling. *Curr. Clim. Chang. Reports* 3, 291–302. doi:10.1007/s40641-017-0073-y.
Golaz, J. C., Caldwell, P. M., Van Roekel, L. P., Petersen, M. R., Tang, Q., Wolfe, J. D., et al. (2019). The DOE E3SM Coupled Model Version 1: Overview and Evaluation at Standard Resolution. *J. Adv. Model. Earth Syst.* doi:10.1029/2018MS001603.
Gong, D., and Wang, S. (1999). Definition of Antarctic Oscillation index. *Geophys. Res. Lett.* 26, 459–462. doi:10.1029/1999GL900003.
Gong, H., Wang, L., Chen, W., Chen, X., and Nath, D. (2017). Biases of the wintertime Arctic Oscillation in CMIP5 models. *Environ. Res. Lett.* 12, 14001. Available at: http://stacks.iop.org/1748-9326/12/i=1/a=014001.
Gonzalez, P. L. M., Polvani, L. M., Seager, R., and Correa, G. J. P. (2014). Stratospheric ozone depletion: a key driver of recent precipitation trends in Southeastern South America. *Clim. Dyn.* 42, 1775–1792.
Good, P., Chadwick, R., Holloway, C., Kennedy, J., Lowe, J., Roehrig, R., et al. (submitted). High sensitivity of seasonal tropical precipitation to local sea-surface temperature. *Nature* (submitted).
Goosse, H., Arzel, O., Bitz, C. M., de Montety, A., and Vancoppenolle, M. (2009). Increased variability of the Arctic summer ice extent in a warmer climate. *Geophys. Res. Lett.* 36, L23702. doi:10.1029/2009GL040546.
Gopika, S., Izumo, T., Vialard, J., Lengaigne, M., Suresh, I., and Ramesh Kumar, M. R. (submitted). Aliasing of the Indian Ocean anthropogenic warming spatial pattern by natural climate variability. *Clim. Dyn.* (submitted).
Goubanova, K., Sanchez-Gomez, E., Frauen, C., and Voldoire, A. (2019). Respective roles of remote and local wind stress forcings in the development of warm SST errors in the South-Eastern Tropical Atlantic in a coupled high-resolution model. *Clim. Dyn.* 52, 1359–1382. doi:10.1007/s00382-018-4197-0.
Govin, A., Varma, V., and Prange, M. (2014). Astronomically forced variations in western African rainfall (21°N-20°S) during the Last Interglacial period. *Geophys. Res. Lett.* 41, 2117–2125. doi:10.1002/2013GL058999.
Graven, H. D., Keeling, R. F., Piper, S. C., Patra, P. K., Stephens, B. B., Wofsy, S. C., et al. (2013). Enhanced Seasonal Exchange of CO2 by Northern Ecosystems Since 1960. *Science* doi:10.1126/science.1239207.
Gray, J. M., Frolking, S., Kort, E. A., Ray, D. K., Kucharik, C. J., Ramankutty, N., et al. (2014). Direct human influence on atmospheric CO2 seasonality from increased cropland productivity. *Nature* 515, 398.
Gray, L. J., Woollings, T. J., Andrews, M., and Knight, J. (2016). Eleven-year solar cycle signal in the NAO and Atlantic/European blocking. *Q. J. R. Meteorol. Soc.* 142, 1890–1903. doi:10.1002/qj.2782.
Gregory, J. M., Stott, P. A., Cresswell, D. J., Rayner, N. A., Gordon, C., and Sexton, D. M. H. (2002). Recent and future changes in Arctic sea ice simulated by the HadCM3 AOGCM. *Geophys. Res. Lett.* 29, 24–28. doi:10.1029/2001GL014575.
Greve, P., Orlowsky, B., Mueller, B., Sheffield, J., Reichstein, M., and Seneviratne, S. I. (2014). Global assessment of trends in wetting and drying over land. *Nat. Geosci.* 7, 716–721. doi:10.1038/ngeo2247.
Griffies, S. M., Biastoch, A., Böning, C., Bryan, F., Danabasoglu, G., Chassignet, E. P., et al. (2009). Coordinated Ocean-ice Reference Experiments (COREs). *Ocean Model.* 26, 1–46. doi:10.1016/j.ocemod.2008.08.007.
Griffies, S. M., Danabasoglu, G., Durack, P. J., Adcroft, A. J., Balaji, V., Böning, C. W., et al. (2016). OMIP contribution to CMIP6: Experimental and diagnostic protocol for the physical component of the Ocean Model Intercomparison Project. *Geosci. Model Dev.* 9, 3231–3296. doi:10.5194/gmd-9-3231-2016.
Griffies, S. M., Winton, M., Anderson, W. G., Benson, R., Delworth, T. L., Dufour, C. O., et al. (2015). Impacts on ocean heat from transient mesoscale eddies in a hierarchy of climate models. *J. Clim.* 28, 952–977. doi:10.1175/JCLI-D-14-00353.1.
Griffies, S. M., Yin, J., Durack, P. J., Goddard, P., Bates, S. C., Behrens, E., et al. (2014). An assessment of global and regional sea level for years 1993-2007 in a suite of interannual core-II simulations. *Ocean Model.* 78, 35–89.

doi:10.1016/j.ocemod.2014.03.004.
Griffin, D., and Anchukaitis, K. J. (2014). How unusual is the 2012-2014 California drought? *Geophys. Res. Lett.* doi:10.1002/2014GL062433.
Grise, K. M., Davis, S. M., Simpson, I. R., Waugh, D. W., Fu, Q., Allen, R. J., et al. (2019). Recent Tropical Expansion: Natural Variability or Forced Response? *J. Clim.* 32, 1551–1571. doi:10.1175/JCLI-D-18-0444.1.
Grise, K. M., Davis, S. M., Staten, P. W., and Adam, O. (2018). Regional and Seasonal Characteristics of the Recent Expansion of the Tropics. *J. Clim.* 31, 6839–6856. doi:10.1175/JCLI-D-18-0060.1.
Grist, J. P., Josey, S. A., New, A. L., Roberts, M., Koenigk, T., and Iovino, D. (2018). Increasing Atlantic Ocean Heat Transport in the Latest Generation Coupled Ocean-Atmosphere Models: The Role of Air-Sea Interaction. *J. Geophys. Res. Ocean.* 123, 8624–8637. doi:10.1029/2018JC014387.
Grist, J. P., Josey, S. A., Zika, J. D., Evans, D. G., and Skliris, N. (2016). Assessing recent air-sea freshwater flux changes using a surface temperature-salinity space framework. *J. Geophys. Res. Ocean.* 121, 8787–8806. doi:10.1002/2016JC012091.
Grodsky, S. A., Reul, N., Lagerloef, G., Reverdin, G., Carton, J. A., Chapron, B., et al. (2012). Haline hurricane wake in the Amazon/Orinoco plume: AQUARIUS/SACD and SMOS observations. *Geophys. Res. Lett.* 39, 2012GL053335. doi:10.1029/2012GL053335.
Grose, M. R., Narsey, S., Delage, F. P., Dowdy, A. J., Bador, M., Boschat, G., et al. (submitted). Insights from CMIP6 for Australia's future climate. *EARTHS Futur.* (submitted).
Gu, G., and Adler, R. F. (2018). Precipitation Intensity Changes in the Tropics from Observations and Models. *J. Clim.* 31, 4775–4790. doi:10.1175/JCLI-D-17-0550.1.
Guan, X., Huang, J., Guo, R., and Lin, P. (2015). The role of dynamically induced variability in the recent warming trend slowdown over the Northern Hemisphere. *Sci. Rep.* 5, 12669. doi:10.1038/srep12669.
Gudmundsson, L., and et al. (2019). Globally observed trends in mean and extreme river flow attributed to man-made climate change. *Submitt. to Sci.*
Gudmundsson, L., and Seneviratne, S. I. (2016). Anthropogenic climate change affects meteorological drought risk in Europe. *Environ. Res. Lett.* doi:10.1088/1748-9326/11/4/044005.
Gudmundsson, L., Seneviratne, S. I., and Zhang, X. (2017). Anthropogenic climate change detected in European renewable freshwater resources. *Nat. Clim. Chang.* 7, 813. Available at: http://dx.doi.org/10.1038/nclimate3416.
Guemas, V., Doblas-Reyes, F. J., Andreu-Burillo, I., and Asif, M. (2013). Retrospective prediction of the global warming slowdown in the past decade. *Nat. Clim. Chang.* 3, 649. Available at: http://dx.doi.org/10.1038/nclimate1863.
Guilyardi, E., Bellenger, H., Collins, M., Ferrett, S., Cai, W., and Wittenberg, A. (2012). A first look at ENSO in CMIP5. *Clivar Exch.* 17.
Guo, L., Turner, A. G., and Highwood, E. J. (2015). Impacts of 20th century aerosol emissions on the South Asian monsoon in the CMIP5 models. *Atmos. Chem. Phys.* 15, 6367–6378. doi:10.5194/acp-15-6367-2015.
Gutjahr, O., Putrasahan, D., Lohmann, K., Jungclaus, J. H., von Storch, J.-S., Brüggemann, N., et al. (2019). Max Planck Institute Earth System Model (MPI-ESM1.2) for the High-Resolution Model Intercomparison Project (HighResMIP). *Geosci. Model Dev.* 12, 3241–3281. doi:10.5194/gmd-12-3241-2019.
Haarsma, R. J., Roberts, M. J., Vidale, P. L., Senior, C. A., Bellucci, A., Bao, Q., et al. (2016). High Resolution Model Intercomparison Project (HighResMIP~v1.0) for CMIP6. *Geosci. Model Dev.* 9, 4185–4208. doi:10.5194/gmd-9-4185-2016.
Hallberg, R. (2013). Using a resolution function to regulate parameterizations of oceanic mesoscale eddy effects. *Ocean Model.* 72, 92–103.
Hallberg, R., and Gnanadesikan, A. (2006). The role of eddies in determining the structure and response of the wind-driven Southern Hemisphere overturning: Results from the Modeling Eddies in the Southern Ocean (MESO) project. *J. Phys. Oceanogr.* 36, 2232–2252.
Han, W., Meehl, G. A., Hu, A., Alexander, M. A., Yamagata, T., Yuan, D., et al. (2014a). Intensification of decadal and multi-decadal sea level variability in the western tropical Pacific during recent decades. *Clim. Dyn.* 43, 1357–1379. doi:10.1007/s00382-013-1951-1.
Han, W., Vialard, J., McPhaden, M. J., Lee, T., Masumoto, Y., Feng, M., et al. (2014b). Indian ocean decadal variability: A review. *Bull. Am. Meteorol. Soc.* 95, 1679–1703. doi:10.1175/BAMS-D-13-00028.1.
Hanna, E., Cropper, T. E., Jones, P. D., Scaife, A. A., and Allan, R. (2015). Recent seasonal asymmetric changes in the NAO (a marked summer decline and increased winter variability) and associated changes in the AO and Greenland Blocking Index. *Int. J. Climatol.* 35, 2540–2554. doi:10.1002/joc.4157.
Hanna, E., Fettweis, X., and Hall, R. J. (2018). Brief communication: Recent changes in summer Greenland blocking captured by none of the CMIP5 models. *Cryosph.* 12, 3287–3292. doi:10.5194/tc-12-3287-2018.
Hannart, A. (2016). Integrated optimal fingerprinting: Method description and illustration. *J. Clim.* 29, 1977–1998. doi:10.1175/JCLI-D-14-00124.1.
Hannart, A., and Naveau, P. (2018). Probabilities of causation of climate changes. *J. Clim.* 31, 5507–5524. doi:10.1175/JCLI-D-17-0304.1.
Hannart, A., Ribes, A., and Naveau, P. (2014). Optimal fingerprinting under multiple sources of uncertainty. *Geophys.*

Res. Lett. 41, 1261–1268. doi:10.1002/2013GL058653.
Hargreaves, J. C., and Annan, J. (2014). Can we trust climate models? *WIREs Clim. Chang.* 5, 435–440. doi:10.1002/wcc.288.
Harlaß, J., Latif, M., and Park, W. (2018). Alleviating tropical Atlantic sector biases in the Kiel climate model by enhancing horizontal and vertical atmosphere model resolution: climatology and interannual variability. *Clim. Dyn.* 50, 2605–2635. doi:10.1007/s00382-017-3760-4.
Harper, A. B., Powell, T., Cox, P. M., House, J., Huntingford, C., Lenton, T. M., et al. (2018). Land-use emissions play a critical role in land-based mitigation for Paris climate targets. *Nat. Commun.* doi:10.1038/s41467-018-05340-z.
Harrison, D. E., and Larkin, N. K. (1998). El Nino-Southern Oscillation sea surface temperature and wind anomalies, 1946-1993. *Rev. Geophys.* 36, 353–399. doi:10.1029/98RG00715.
Harrison, S. P., Bartlein, P. J., Brewer, S., Prentice, I. C., Boyd, M., Hessler, I., et al. (2014). Climate model benchmarking with glacial and mid-Holocene climates. *Clim. Dyn.* 43, 671–688. doi:10.1007/s00382-013-1922-6.
Harrison, S. P., Bartlein, P. J., Izumi, K., Li, G., Annan, J., Hargreaves, J., et al. (2015). Evaluation of CMIP5 palaeo-simulations to improve climate projections. *Nat. Clim. Chang.* 5, 735–743. doi:10.1038/nclimate2649.
Harrison, S. P., Bartlein, P. J., and Prentice, I. C. (2016). What have we learnt from palaeoclimate simulations? *J. Quat. Sci.* 31, 363–385. doi:10.1002/jqs.2842.
Hasselmann, K. (1997). Multi-pattern fingerprint method for detection and attribution of climate change. *Clim. Dyn.* 13, 601–611. doi:10.1007/s003820050185.
Hausfather, Z., Cowtan, K., Clarke, D. C., Jacobs, P., Richardson, M., and Rohde, R. (2017). Assessing recent warming using instrumentally homogeneous sea surface temperature records. *Sci. Adv.* 3. doi:10.1126/sciadv.1601207.
Haustein, K., Allen, M. R., Forster, P. M., Otto, F. E. L., Mitchell, D. M., Matthews, H. D., et al. (2017). A real-time Global Warming Index. *Sci. Rep.* 7. doi:10.1038/s41598-017-14828-5.
Haustein, K., Otto, F. E. L., Venema, V., Jacobs, P., Cowtan, K., Hausfather, Z., et al. (2019). A Limited Role for Unforced Internal Variability in Twentieth-Century Warming. *J. Clim.* 32, 4893–4917. doi:10.1175/JCLI-D-18-0555.1.
Haywood, A. M., Dowsett, H. J., Dolan, A. M., Rowley, D., Abe-Ouchi, A., Otto-Bliesner, B., et al. (2016). The Pliocene Model Intercomparison Project (PlioMIP) Phase 2: scientific objectives and experimental design. *Clim. Past* 12, 663–675. doi:10.5194/cp-12-663-2016.
Haywood, A. M., Hill, D. J., Dolan, A. M., Otto-Bliesner, B. L., Bragg, F., Chan, W. L., et al. (2013). Large-scale features of Pliocene climate: Results from the Pliocene Model Intercomparison Project. *Clim. Past*. doi:10.5194/cp-9-191-2013.
Haywood, A. M., Tindall, J. C., Dowsett, H. J., Dolan, A. M., Foley, K. M., Hunter, S. J., et al. (submitted). A return to large-scale features of Pliocene climate: the Pliocene Model Intercomparison Project Phase 2. *Clim. Past Discuss.* (submitted). doi:10.5194/cp-2019-145.
Hedemann, C., Mauritsen, T., Jungclaus, J., and Marotzke, J. (2017). The subtle origins of surface-warming hiatuses. *Nat. Clim. Chang.* 7, 336. Available at: http://dx.doi.org/10.1038/nclimate3274.
Hegerl, G., Broennimann, S., Cowan, T., Friedman, A. R., Hawkins, E., Iles, C. E., et al. (2019). Causes of climate change over the historical record. *Environ. Res. Lett.* Available at: http://iopscience.iop.org/10.1088/1748-9326/ab4557.
Hegerl, G. C., Black, E., Allan, R. P., Ingram, W. J., Polson, D., Trenberth, K. E., et al. (2015). Challenges in quantifying changes in the global water cycle. *Bull. Am. Meteorol. Soc.* 96, 1097–1115. doi:10.1175/BAMS-D-13-00212.1.
Hegerl, G. C., Brönnimann, S., Schurer, A., and Cowan, T. (2018). The early 20th century warming: Anomalies, causes, and consequences. *Wiley Interdiscip. Rev. Clim. Chang.* 9, e522. doi:10.1002/wcc.522.
Hegerl, G. C., Storch, H. von, Hasselmann, K., Santer, B. D., Cubasch, U., and Jones, P. D. (1996). Detecting Greenhouse-Gas-Induced Climate Change with an Optimal Fingerprint Method. *J. Clim.* 9, 2281–2306. doi:10.2307/26201437.
Hegerl, G., and Zwiers, F. (2011). Use of models in detection and attribution of climate change. *Wiley Interdiscip. Rev. Clim. Chang.* 2, 570–591. doi:10.1002/wcc.121.
Hegglin, M. I., Plummer, D. A., Shepherd, T. G., Scinocca, J. F., Anderson, J., Froidevaux, L., et al. (2014). Vertical structure of stratospheric water vapour trends derived from merged satellite data. *Nat. Geosci.* 7, 768–776. doi:10.1038/NGEO2236.
Henley, B. J. (2017). Pacific decadal climate variability: Indices, patterns and tropical-extratropical interactions. *Glob. Planet. Change* 155, 42–55. doi:https://doi.org/10.1016/j.gloplacha.2017.06.004.
Henley, B. J., Gergis, J., Karoly, D. J., Power, S., Kennedy, J., and Folland, C. K. (2015). A Tripole Index for the Interdecadal Pacific Oscillation. *Clim. Dyn.* 45, 3077–3090. doi:10.1007/s00382-015-2525-1.
Henley, B. J., Meehl, G., Power, S. B., Folland, C. K., King, A. D., Brown, J. N., et al. (2017). Spatial and temporal agreement in climate model simulations of the Interdecadal Pacific Oscillation. *Environ. Res. Lett.* 12, 44011. Available at: http://stacks.iop.org/1748-9326/12/i=4/a=044011.
Hessl, A., Allen, K. J., Vance, T., Abram, N. J., and Saunders, K. M. (2017). Reconstructions of the southern annular mode (SAM) during the last millennium. *Prog. Phys. Geogr.* 41, 834–849. doi:10.1177/0309133317743165.

Heuzé, C., Heywood, K. J., Stevens, D. P., and Ridley, J. K. (2013). Southern Ocean bottom water characteristics in CMIP5 models. *Geophys. Res. Lett.* 40, 1409–1414. doi:10.1002/grl.50287.

Heuzé, C., Heywood, K. J., Stevens, D. P., and Ridley, J. K. (2015). Changes in Global Ocean Bottom Properties and Volume Transports in CMIP5 Models under Climate Change Scenarios. *J. Clim.* 28, 2917–2944. doi:10.1175/JCLI-D-14-00381.1.

Hewitt, H. T., Bell, M. J., Chassignet, E. P., Czaja, A., Ferreira, D., Griffies, S. M., et al. (2017). Will high-resolution global ocean models benefit coupled predictions on short-range to climate timescales? *Ocean Model.* 120, 120–136. doi:10.1016/j.ocemod.2017.11.002.

Hewitt, H. T., Roberts, M. J., Hyder, P., Graham, T., Rae, J., Belcher, S. E., et al. (2016). The impact of resolving the Rossby radius at mid-latitudes in the ocean: results from a high-resolution version of the Met Office GC2 coupled model. *Geosci. Model Dev.* 9, 3655–3670. doi:10.5194/gmd-9-3655-2016.

Hirabayashi, Y., Nakano, K., Zhang, Y., Watanabe, S., Tanoue, M., and Kanae, S. (2016). Contributions of natural and anthropogenic radiative forcing to mass loss of Northern Hemisphere mountain glaciers and quantifying their uncertainties. *Sci. Rep.* 6, 29723. doi:10.1038/srep29723.

Hobbs, W. R., Bindoff, N. L., and Raphael, M. N. (2015). New Perspectives on Observed and Simulated Antarctic Sea Ice Extent Trends Using Optimal Fingerprinting Techniques. *J. Clim.* 28, 1543–1560. doi:10.1175/JCLI-D-14-00367.1.

Hobbs, W. R., Massom, R., Stammerjohn, S., Reid, P., Williams, G., and Meier, W. (2016). A review of recent changes in Southern Ocean sea ice, their drivers and forcings. *Glob. Planet. Change* 143, 228–250. doi:https://doi.org/10.1016/j.gloplacha.2016.06.008.

Hock, R., Marzeion, B. E. N., Bliss, A., Giesen, R. H., Hirabayashi, Y., Huss, M., et al. (2019a). GlacierMIP-A model intercomparison of global-scale glacier mass-balance models and projections. *J. Glaciol.* 65, 453–467. doi:10.1017/jog.2019.22.

Hock, R., Rasul, G., Adler, C., Cáceres, B., Gruber, S., Hirabayashi, Y., et al. (2019b). "High Mountain Areas," in *IPCC Special Report on the Ocean and Cryosphere in a Changing Climate*, eds. H.-O. Pörtner, D. C. Roberts, V. Masson-Delmotte, P. Zhai, M. Tignor, E. Poloczanska, et al. (Cambridge University Press), tba. Available at: https://www.ipcc.ch/srocc.

Hoell, A., Hoerling, M., Eischeid, J., Quan, X.-W., and Liebmann, B. (2017). Reconciling Theories for Human and Natural Attribution of Recent East Africa Drying. *J. Clim.* 30, 1939–1957. doi:10.1175/JCLI-D-16-0558.1.

Hoffman, F. M., Randerson, J. T., Arora, V. K., Bao, Q., Cadule, P., Ji, D., et al. (2014). Causes and implications of persistent atmospheric carbon dioxide biases in Earth System Models. *J. Geophys. Res. Biogeosciences* 119, 141–162. doi:10.1002/2013JG002381.

Holland, M. M., Landrum, L., Kostov, Y., and Marshall, J. (2017). Sensitivity of Antarctic sea ice to the Southern Annular Mode in coupled climate models. *Clim. Dyn.* 49, 1813–1831. doi:10.1007/s00382-016-3424-9.

Hollis, C. J., Dunkley Jones, T., Anagnostou, E., Bijl, P. K., Cramwinckel, M. J., Cui, Y., et al. (2019). The DeepMIP contribution to PMIP4: methodologies for selection, compilation and analysis of latest Paleocene and early Eocene climate proxy data, incorporating version 0.1 of the DeepMIP database. *Geosci. Model Dev.* 12, 3149–3206. doi:10.5194/gmd-12-3149-2019.

Hopcroft, P. O., Valdes, P. J., Harper, A. B., and Beerling, D. J. (2017). Multi vegetation model evaluation of the Green Sahara climate regime. *Geophys. Res. Lett.* doi:10.1002/2017GL073740.

Hope, P., Henley, B. J., Gergis, J., Brown, J., and Ye, H. (2017). Time-varying spectral characteristics of ENSO over the Last Millennium. *Clim. Dyn.* 49, 1705–1727. doi:10.1007/s00382-016-3393-z.

Horel, J. D., and Wallace, J. M. (1981). Planetary-Scale Atmospheric Phenomena Associated with the Southern Oscillation. *Mon. Weather Rev.* 109, 813–829. doi:10.1175/1520-0493(1981)109<0813:PSAPAW>2.0.CO;2.

Hori, M., Sugiura, K., Kobayashi, K., Aoki, T., Tanikawa, T., Kuchiki, K., et al. (2017). A 38-year (1978-2015) Northern Hemisphere daily snow cover extent product derived using consistent objective criteria from satellite-borne optical sensors. *Remote Sens. Environ.* 191, 402–418. doi:10.1016/j.rse.2017.01.023.

Hoskins, B. J., and Karoly, D. J. (1981). The Steady Linear Response of a Spherical Atmosphere to Thermal and Orographic Forcing. *J. Atmos. Sci.* 38, 1179–1196. doi:10.1175/1520-0469(1981)038<1179:TSLROA>2.0.CO;2.

Hourdin, F., Găinusă-Bogdan, A., Braconnot, P., Dufresne, J.-L., Traore, A.-K., and Rio, C. (2015). Air moisture control on ocean surface temperature, hidden key to the warm bias enigma. *Geophys. Res. Lett.* 42, 10,885-10,893. doi:10.1002/2015GL066764.

Hourdin, F., Mauritsen, T., Gettelman, A., Golaz, J.-C., Balaji, V., Duan, Q., et al. (2017). The art and science of climate model tuning. *Bull. Am. Meteorol. Soc.* 98, 589–602. doi:10.1175/BAMS-D-15-00135.1.

Hu, K., Huang, G., Zheng, X.-T., Xie, S.-P., Qu, X., Du, Y., et al. (2014). Interdecadal Variations in ENSO Influences on Northwest Pacific–East Asian Early Summertime Climate Simulated in CMIP5 Models. *J. Clim.* 27, 5982–5998. doi:10.1175/JCLI-D-13-00268.1.

Hu, S., and Fedorov, A. V. (2017). The extreme El Niño of 2015-2016 and the end of global warming hiatus. *Geophys. Res. Lett.* 44, 3816–3824. doi:10.1002/2017GL072908.

Hua, W., Dai, A., and Qin, M. (2018). Contributions of Internal Variability and External Forcing to the Recent Pacific Decadal Variations. *Geophys. Res. Lett.* 45, 7084–7092. doi:10.1029/2018GL079033.

Huang, J., Zhang, X., Zhang, Q., Lin, Y., Hao, M., Luo, Y., et al. (2017). Recently amplified arctic warming has contributed to a continual global warming trend. *Nat. Clim. Chang.* 7, 875–879. doi:10.1038/s41558-017-0009-5.

Huber, M., and Knutti, R. (2014). Natural variability, radiative forcing and climate response in the recent hiatus reconciled. *Nat. Geosci.* 7, 651. Available at: http://dx.doi.org/10.1038/ngeo2228.

Humphrey, V., Zscheischler, J., Ciais, P., Gudmundsson, L., Sitch, S., and Seneviratne, S. I. (2018). Sensitivity of atmospheric CO 2 growth rate to observed changes in terrestrial water storage. *Nature*. doi:10.1038/s41586-018-0424-4.

Huntingford, C., Atkin, O. K., Martinez-de la Torre, A., Mercado, L. M., Heskel, M. A., Harper, A. B., et al. (2017). Implications of improved representations of plant respiration in a changing climate. *Nat. Commun.* 8, 1602. doi:10.1038/s41467-017-01774-z.

Huntingford, C., Stott, P. A., Allen, M. R., and Lambert, F. H. (2006). Incorporating model uncertainty into attribution of observed temperature change. *Geophys. Res. Lett.* 33. doi:10.1029/2005GL024831.

Huss, M., and Hock, R. (2015). A new model for global glacier change and sea-level rise. *Front. Earth Sci.* 3. doi:10.3389/feart.2015.00054.

Huybrechts, P., Payne, T., Abe-Ouchi, A., Calov, R., Fabre, A., Fastook, J. L., et al. (1996). The EISMINT benchmarks for testing ice-sheet models. *Ann. Glaciol.* 23, 1-X1. doi:10.1017/S0260305500013197.

Ibarra, D. E., Oster, J. L., Winnick, M. J., Rugenstein, J. K. C., Byrne, M. P., and Chamberlain, C. P. (2018). Warm and cold wet states in the western United States during the Pliocene-Pleistocene. *Geology*. doi:10.1130/G39962.1.

Iglesias-Suarez, F., Young, P. J., and Wild, O. (2016). Stratospheric ozone change and related climate impacts over 1850-2100 as modelled by the ACCMIP ensemble. *Atmos. Chem. Phys.* 16, 343–363. doi:10.5194/acp-16-343-2016.

Iles, C., and Hegerl, G. (2017). Role of the North Atlantic Oscillation in decadal temperature trends. *Environ. Res. Lett.* 12, 114010. doi:10.1088/1748-9326/aa9152.

Iles, C., and Hegerl, G. C. (2015). Systematic change in global patterns of streamflow following volcanic eruptions. *Nat. Geosci.* doi:10.1038/NGEO2545.

Ilicak, M., Drange, H., Wang, Q., Gerdes, R., Aksenov, Y., Bailey, D., et al. (2016). An assessment of the Arctic Ocean in a suite of interannual CORE-II simulations. Part III: Hydrography and fluxes. *Ocean Model.* 100, 141–161. doi:10.1016/j.ocemod.2016.02.004.

Imbers, J., Lopez, A., Huntingford, C., and Allen, M. (2014). Sensitivity of Climate Change Detection and Attribution to the Characterization of Internal Climate Variability. *J. Clim.* 27, 3477–3491. doi:10.1175/JCLI-D-12-00622.1.

Iovino, D., Masina, S., Storto, A., Cipollone, A., and Stepanov, V. N. (2016). A 1/16° eddying simulation of the global NEMO sea-ice–ocean system. *Geosci. Model Dev.* 9, 2665–2684. doi:10.5194/gmd-9-2665-2016.

IPCC (2013). "Summary for Policymakers," in *Climate Change 2013: The Physical Science Basis. Contribution of Working Group I to the Fifth Assessment Report of the Intergovernmental Panel on Climate Change*, eds. T. F. Stocker, D. Qin, G. K. Plattner, M. Tignor, S. K. Allen, J. Boschung, et al. (Cambridge, United Kingdom and New York, NY, USA: Cambridge University Press), 3–29.

IPCC (2018). Global Warming of 1.5°C. An IPCC Special Report on the impacts of global warming of 1.5°C above pre-industrial levels and related global greenhouse gas emission pathways, in the context of strengthening the global response to the threat of climate change,. , eds. V. Masson-Delmotte, P. Zhai, H.-O. Pörtner, D. Roberts, J. Skea, P. R. Shukla, et al. In Press.

IPCC (2019). IPCC Special Report on the Ocean and Cryosphere in a Changing Climate. , eds. H.-O. Pörtner, D. C. Roberts, V. Masson-Delmotte, P. Zhai, M. Tignor, E. Poloczanska, et al.

Irving, D., and Simmonds, I. (2016). A New Method for Identifying the Pacific–South American Pattern and Its Influence on Regional Climate Variability. *J. Clim.* 29, 6109–6125. doi:10.1175/JCLI-D-15-0843.1.

Ishii, M., and Kimoto, M. (2009). Reevaluation of historical ocean heat content variations with time-varying XBT and MBT depth bias corrections. *J. Oceanogr.* 65, 287–299. doi:10.1007/s10872-009-0027-7.

Ito, T., Minobe, S., Long, M. C., and Deutsch, C. (2017). Upper ocean O_2 trends: 1958-2015. *Geophys. Res. Lett.* 44, 4214–4223. doi:10.1002/2017GL073613.

Ivanova, D. P., Gleckler, P. J., Taylor, K. E., Durack, P. J., and Marvel, K. D. (2016). Moving beyond the total sea ice extent in gauging model biases. *J. Clim.* 29, 8965–8987. doi:10.1175/JCLI-D-16-0026.1.

Ivy, D. J., Solomon, S., Calvo, N., and Thompson, D. W. J. (2017). Observed connections of Arctic stratospheric ozone extremes to Northern Hemisphere surface climate. *Environ. Res. Lett.* 12. doi:10.1088/1748-9326/aa57a4.

Jackson, L. C., Dubois, C., Forget, G., Haines, K., Harrison, M., Iovino, D., et al. (2019). The Mean State and Variability of the North Atlantic Circulation: A Perspective From Ocean Reanalyses. *J. Geophys. Res. Ocean.* n/a. doi:10.1029/2019JC015210.

Jahn, A., Kay, J. E., Holland, M. M., and Hall, D. M. (2016). How predictable is the timing of a summer ice-free Arctic? *Geophys. Res. Lett.* 43, 9113–9120. doi:10.1002/2016GL070067.

Janjić, T., Bormann, N., Bocquet, M., Carton, J. A., Cohn, S. E., Dance, S. L., et al. (2018). On the representation error in data assimilation. *Q. J. R. Meteorol. Soc.* 144, 1257–1278. doi:10.1002/qj.3130.

Janjić, T., and Cohn, S. E. (2006). Treatment of Observation Error due to Unresolved Scales in Atmospheric Data Assimilation. *Mon. Weather Rev.* 134, 2900–2915. doi:10.1175/MWR3229.1.

Jeffers, E. S., Bonsall, M. B., Froyd, C. A., Brooks, S. J., and Willis, K. J. (2015). The relative importance of biotic and abiotic processes for structuring plant communities through time. *J. Ecol.* doi:10.1111/1365-2745.12365.

Jenkins, S., Cain, M., Friedlingstein, P., Gillett, N. P., and Allen, M. R. (submitted). Quantifying non-CO2 contributions to remaining carbon budgets. *Nat. Clim. Chang.* (submitted).

Jeong, D. Il, Sushama, L., and Naveed Khaliq, M. (2017). Attribution of spring snow water equivalent (SWE) changes over the northern hemisphere to anthropogenic effects. *Clim. Dyn.* 48, 3645–3658. doi:10.1007/s00382-016-3291-4.

Jia, G., E. Shevliakova, Artaxo, P., Noblet-Ducoudré, N. De, Houghton, R., House, J., et al. (2019). Land–climate interactions. In: Climate Change and Land: an IPCC special report on climate change, desertification, land degradation, sustainable land management, food security, and greenhouse gas fluxes in terrestrial ecosystems. , eds. P.R. Shukla, J. Skea, E. Calvo Buendia, V. Masson-Delmotte, H.-O. Pörtner, D. C. Roberts, et al.

Jia, L., and DelSole, T. (2012). Optimal Determination of Time-Varying Climate Change Signals. *J. Clim.* 25, 7122–7137. doi:10.1175/JCLI-D-11-00434.1.

Jiang, B., Wang, D., Shen, X., Chen, J., and Lin, W. (2019). Effects of sea salt aerosols on precipitation and upper troposphere/lower stratosphere water vapour in tropical cyclone systems. *Sci. Rep.* 9. doi:10.1038/s41598-019-51757-x.

Jiang, D., Tian, Z., and Lang, X. (2015). Mid-Holocene global monsoon area and precipitation from PMIP simulations. *Clim. Dyn.* 44, 2493–2512. doi:10.1007/s00382-014-2175-8.

Jiang, J. H., Su, H., and Zhai, C. (2012). Evaluation of cloud and water vapor simulations in CMIP5 climate models using NASA “A-Train” satellite observations. *J. Geophys. Res.* 118. doi:10.10 29/2011JD017237.

Jianping, L., and Wang, J. X. L. (2003). A new North Atlantic Oscillation index and its variability. *Adv. Atmos. Sci.* 20, 661–676. doi:10.1007/BF02915394.

Jin, F. F., Kim, S. T., and Bejarano, L. (2006). A coupled-stability index for ENSO. *Geophys. Res. Let.* 33, L23708.

Johnson, N. C., Xie, S.-P., Kosaka, Y., and Li, X. (2018). Increasing occurrence of cold and warm extremes during the recent global warming slowdown. *Nat. Commun.* 9, 1724. doi:10.1038/s41467-018-04040-y.

Johnson, S. J., Levine, R. C., Turner, A. G., Martin, G. M., Woolnough, S. J., Schiemann, R., et al. (2016). The resolution sensitivity of the South Asian monsoon and Indo-Pacific in a global 0.35° AGCM. *Clim. Dyn.* 46, 807–831. doi:10.1007/s00382-015-2614-1.

Jones, G. S., and Kennedy, J. J. (2017). Sensitivity of attribution of anthropogenic near-surface warming to observational uncertainty. *J. Clim.* 30, 4677–4691. doi:10.1175/JCLI-D-16-0628.1.

Jones, G. S., Stott, P. A., and Christidis, N. (2013). Attribution of observed historical near-surface temperature variations to anthropogenic and natural causes using CMIP5 simulations. *J. Geophys. Res. Atmos.* 118, 4001–4024. doi:10.1002/jgrd.50239.

Jones, G. S., Stott, P. A., and Mitchell, J. F. B. (2016a). Uncertainties in the attribution of greenhouse gas warming and implications for climate prediction. *J. Geophys. Res.* 121, 6969–6992. doi:10.1002/2015JD024337.

Jones, J. M., Gille, S. T., Goosse, H., Abram, N. J., Canziani, P. O., Charman, D. J., et al. (2016b). Assessing recent trends in high-latitude Southern Hemisphere surface climate. *Nat. Clim. Chang.* 6, 917.

Joshi, M. K., and Kucharski, F. (2017). Impact of Interdecadal Pacific Oscillation on Indian summer monsoon rainfall: an assessment from CMIP5 climate models. *Clim. Dyn.* 48, 2375–2391. doi:10.1007/s00382-016-3210-8.

Jouanno, J., Hernandez, O., and Sanchez-Gomez, E. (2017). Equatorial Atlantic interannual variability and its relation to dynamic and thermodynamic processes. *Earth Syst. Dyn.* 8, 1061–1069. doi:10.5194/esd-8-1061-2017.

Jung, M., Reichstein, M., Schwalm, C. R., Huntingford, C., Sitch, S., Ahlström, A., et al. (2017). Compensatory water effects link yearly global land CO 2 sink changes to temperature. *Nature*. doi:10.1038/nature20780.

Kageyama, M., Braconnot, P., Harrison, S. P., Haywood, A. M., Jungclaus, J. H., Otto-Bliesner, B. L., et al. (2018). The PMIP4 contribution to CMIP6 – Part 1: Overview and over-archinganalysis plan. *Geosci. Model Dev.* 11, 1033–1057. doi:10.5194/gmd-11-1033-2018.

Kageyama, M., and PMIP4 (submitted). The PMIP4-CMIP6 Last Glacial Maximum experiments: preliminary results and comparison with the PMIP3-CMIP5 simulations. (submitted).

Kam, J., Knutson, T. R., and Milly, P. C. D. (2018). Climate model assessment of changes in winter-spring streamflow timing over north America. *J. Clim.* doi:10.1175/JCLI-D-17-0813.1.

Kamae, Y., Li, X., Xie, S.-P., and Ueda, H. (2017). Atlantic effects on recent decadal trends in global monsoon. *Clim. Dyn.* 49, 3443–3455. doi:10.1007/s00382-017-3522-3.

Kamae, Y., Shiogama, H., Watanabe, M., Ishii, M., Ueda, H., and Kimoto, M. (2015). Recent slowdown of tropical upper tropospheric warming associated with Pacific climate variability. *Geophys. Res. Lett.* 42, 2995–3003. doi:10.1002/2015GL063608.

Kamae, Y., Shiogama, H., Watanabe, M., and Kimoto, M. (2014). Attributing the increase in Northern Hemisphere hot summers since the late 20th century. *Geophys. Res. Lett.* 41, 5192–5199. doi:10.1002/2014GL061062.

Kang, S. M., Polvani, L. M., Fyfe, J. C., and Sigmond, M. (2011). Impact of Polar Ozone Depletion on Subtropical Precipitation. *Science* 332, 951–954. doi:10.1126/science.1202131.

Karl, T. R., Arguez, A., Huang, B., Lawrimore, J. H., McMahon, J. R., Menne, M. J., et al. (2015). Possible artifacts of data biases in the recent global surface warming hiatus. *Science* 348, 1469–1472. doi:10.1126/science.aaa5632.

Karnauskas, K. B., Seager, R., Kaplan, A., Kushnir, Y., and Cane, M. A. (2009). Observed strengthening of the zonal sea surface temperature gradient across the equatorial Pacific Ocean. *J. Clim.* doi:10.1175/2009JCLI2936.1.

Karoly, D. J. (1989). Southern Hemisphere Circulation Features Associated with El Niño–Southern Oscillation Events. *J. Clim.* 2, 1239–1252.

Karpechko, A. Y., Hitchcock, P., Peters, D. H. W., and Schneidereit, A. (2017). Predictability of downward propagation of major sudden stratospheric warmings. *Q. J. R. Meteorol. Soc.* 143, 1459–1470. doi:10.1002/qj.3017.

Karpechko, A. Y., Maycock, A., and et al. (2018). Chapter 5 of Scientific Assessment of Ozone Depletion: 2018. Geneva.

Karset, I. H. H., Berntsen, T. K., Storelvmo, T., Alterskjær, K., Grini, A., Olivié, D., et al. (2018). Strong impacts on aerosol indirect effects from historical oxidant changes. *Atmos. Chem. Phys.* 18, 7669–7690.

Katzfuss, M., Hammerling, D., and Smith, R. L. (2017). A Bayesian hierarchical model for climate change detection and attribution. *Geophys. Res. Lett.* 44, 5720–5728. doi:10.1002/2017GL073688.

Kaufman, D. S., McKay, N. P., Routson, C. C., Erb, M. P., Datwyler, C., Sommer, P., et al. (submitted). Holocene global mean surface temperature: A multi-method reconstruction approach. *Sci. Data* (submitted).

Kay, J. E., Deser, C., Phillips, A., Mai, A., Hannay, C., Strand, G., et al. (2015). The community earth system model (CESM) large ensemble project : A community resource for studying climate change in the presence of internal climate variability. *Bull. Am. Meteorol. Soc.* 96, 1333–1349. doi:10.1175/BAMS-D-13-00255.1.

Kay, J. E., Holland, M. M., and Jahn, A. (2011). Inter-annual to multi-decadal Arctic sea ice extent trends in a warming world. *Geophys. Res. Lett.* 38. doi:10.1029/2011GL048008.

Keeling, C. D., Chin, J. F. S., and Whorf, T. P. (1996). Increased activity of northern vegetation inferred from atmospheric CO2 measurements. *Nature* 382, 146.

Kelley, C. P., Mohtadi, S., Cane, M. A., Seager, R., and Kushnir, Y. (2015). Climate change in the Fertile Crescent and implications of the recent Syrian drought. *Proc. Natl. Acad. Sci.* 112, 3241–3246.

Kidston, J., Scaife, A. A., Hardiman, S. C., Mitchell, D. M., Butchart, N., Baldwin, M. P., et al. (2015). Stratospheric influence on tropospheric jet streams, storm tracks and surface weather. *Nat. Geosci.* 8, 433–440. doi:10.1038/ngeo2424.

Kiehl, J. T., Shields, C. A., Hack, J. J., and Collins, W. D. (2006). The Climate Sensitivity of the Community Climate System Model Version 3 (CCSM3). *J. Clim.* 19, 2584–2596. doi:10.1175/JCLI3747.1.

Kim, B. M., Son, S. W., Min, S. K., Jeong, J. H., Kim, S. J., Zhang, X., et al. (2014a). Weakening of the stratospheric polar vortex by Arctic sea-ice loss. *Nat. Commun.* 5, 1–8. doi:10.1038/ncomms5646.

Kim, J., Son, S.-W., Gerber, E. P., and Park, H.-S. (2017a). Defining Sudden Stratospheric Warming in Climate Models: Accounting for Biases in Model Climatologies. *J. Clim.* 30, 5529–5546. doi:10.1175/JCLI-D-16-0465.1.

Kim, S. T., Cai, W., Jin, F. F., and Yu, J. Y. (2014b). ENSO stability in coupled climate models and its association with mean state. *Clim. Dyn.* 42, 3313–3321. doi:10.1007/s00382-013-1833-6.

Kim, S. T., and Yu, J. Y. (2012). The two types of ENSO in CMIP5 models. *Geophys. Res. Lett.* 39, 1–6. doi:10.1029/2012GL052006.

Kim, W. M., Yeager, S., Chang, P., and Danabasoglu, G. (2018). Low-Frequency North Atlantic Climate Variability in the Community Earth System Model Large Ensemble. *J. Clim.* 31, 787–813. doi:10.1175/JCLI-D-17-0193.1.

Kim, W. M., Yeager, S., and Danabasoglu, G. (2019). Atlantic Multidecadal Variability and Associated Climate Impacts Initiated by Ocean Thermohaline Dynamics. *J. Clim.*, JCLI-D-19-0530.1. doi:10.1175/JCLI-D-19-0530.1.

Kim, Y. H., Min, S. K., Son, S. W., and Choi, J. (2017b). Attribution of the local Hadley cell widening in the Southern Hemisphere. *Geophys. Res. Lett.* 44, 1015–1024. doi:10.1002/2016GL072353.

Kirchmeier-Young, M. C., Zwiers, F. W., and Gillett, N. P. (2017). Attribution of Extreme Events in Arctic Sea Ice Extent. *J. Clim.* 30, 553–571. doi:10.1175/JCLI-D-16-0412.1.

Kjeldsen, K. K. K., Korsgaard, N. J. J., Bjørk, A. A. A., Khan, S. A. A., Box, J. E. E., Funder, S., et al. (2015). Spatial and temporal distribution of mass loss from the Greenland Ice Sheet since AD 1900. *Nature* 528, 396–400. doi:10.1038/nature16183.

Knutson, T. R., and Zeng, F. (2018). Model Assessment of observed precipitation trends over land regions: Detectable human influences and possible low bias in model trends. *J. Clim.* 31, 4617–4637. doi:10.1175/JCLI-D-17-0672.1.

Knutti, R., Sedláček, J., Sanderson, B. M., Lorenz, R., Fischer, E. M., and Eyring, V. (2017). A climate model projection weighting scheme accounting for performance and interdependence. *Geophys. Res. Lett.* 44, 1909–1918. doi:10.1002/2016GL072012.

Kociuba, G., and Power, S. B. (2015). Inability of CMIP5 models to simulate recent strengthening of the walker circulation: Implications for projections. *J. Clim.* 28, 20–35. doi:10.1175/JCLI-D-13-00752.1.

Kok, J. F., Ward, D. S., Mahowald, N. M., and Evan, A. T. (2018). Global and regional importance of the direct dust-climate feedback. *Nat. Commun.* 9, 241.

Kopp, R., Kemp, A., Bittermann, K., Horton, B., Donnelly, J., Gehrels, R., et al. (2016). Temperature-driven global sea-level variability in the Common Era. *Proc. Natl. Acad. Sci.* 113, E1434–E1441. doi:doi: 10.1073/pnas.1517056113.

Kosaka, Y., and Xie, S.-P. (2013). Recent global-warming hiatus tied to equatorial Pacific surface cooling. *Nature* 501,

403–407. doi:10.1038/nature12534.
Kosaka, Y., and Xie, S.-P. (2016). The tropical Pacific as a key pacemaker of the variable rates of global warming. *Nat. Geosci.* 9. doi:10.1038/ngeo2770.
Kostov, Y., Marshall, J., Hausmann, U., Armour, K. C., Ferreira, D., and Holland, M. M. (2017). Fast and slow responses of Southern Ocean sea surface temperature to SAM in coupled climate models. *Clim. Dyn.* 48, 1595–1609. doi:10.1007/s00382-016-3162-z.
Kucharski, F., Ikram, F., Molteni, F., Farneti, R., Kang, I.-S., No, H.-H., et al. (2016). Atlantic forcing of Pacific decadal variability. *Clim. Dyn.* 46, 2337–2351. doi:10.1007/s00382-015-2705-z.
Kuhlbrodt, T., Jones, C. G., Sellar, A., Storkey, D., Blockley, E., Stringer, M., et al. (2018). The Low-Resolution Version of HadGEM3 GC3.1: Development and Evaluation for Global Climate. *J. Adv. Model. Earth Syst.* 10, 2865–2888. doi:10.1029/2018MS001370.
Kuhlbrodt, T., Smith, R. S., Wang, Z., and Gregory, J. M. (2012). The influence of eddy parameterizations on the transport of the Antarctic Circumpolar Current in coupled climate models. *Ocean Model.* 52–53, 1–8. doi:https://doi.org/10.1016/j.ocemod.2012.04.006.
Kumar, A., Jha, B., and Wang, H. (2014). Attribution of SST variability in global oceans and the role of ENSO. *Clim. Dyn.* 43, 209–220. doi:10.1007/s00382-013-1865-y.
Kumar, S., Allan, R. P., Zwiers, F. W., Lawrence, D. M., and Dirmeyer, P. A. (2015). Revisiting trends in wetness and dryness in the presence of internal climate variability and water limitations over land. *Geophys. Res. Lett.* 42, 10867–10875. doi:10.1002/2015GL066858.
L'Heureux, M. L., Lee, S., and Lyon, B. (2013). Recent multidecadal strengthening of the Walker circulation across the tropical Pacific. *Nat. Clim. Chang.* 3, 571–576. doi:10.1038/nclimate1840.
Laepple, T., and Huybers, P. (2014). Ocean surface temperature variability: Large modeldata differences at decadal and longer periods. *Proc. Natl. Acad. Sci.* 111, 16682–16687. doi:10.1073/pnas.1412077111.
Lagerloef, G., Colomb, F. R., Le Vine, D., Wentz, F., Yueh, S., Ruf, C., et al. (2008). The Aquarius/SAC-D Mission: Designed to Meet the Salinity Remote-Sensing Challenge. *Oceanography* 21, 68–81. doi:10.5670/oceanog.2008.68.
Lago, V., Wijffels, S. E., Durack, P. J., Church, J. A., Bindoff, N. L., and Marsland, S. J. (2015a). Simulating the Role of Surface Forcing on Observed Multidecadal Upper-Ocean Salinity Changes. *J. Clim.* 29, 5575–5588. doi:10.1175/JCLI-D-15-0519.1.
Lago, V., Wijffels, S. E., Durack, P. J., Church, J. A., Bindoff, N. L., and Marsland, S. J. (2015b). Simulating the Role of Surface Forcing on Observed Multidecadal Upper-Ocean Salinity Changes. *J. Clim.* 29, 5575–5588. doi:10.1175/JCLI-D-15-0519.1.
Landrum, L. L., Holland, M. M., Raphael, M. N., and Polvani, L. M. (2017). Stratospheric Ozone Depletion: An Unlikely Driver of the Regional Trends in Antarctic Sea Ice in Austral Fall in the Late Twentieth Century. *Geophys. Res. Lett.* 44, 11,11-62,70. doi:10.1002/2017GL075618.
Landschützer, P., Gruber, N., and Bakker, D. C. E. (2016). Decadal variations and trends of the global ocean carbon sink. *Global Biogeochem. Cycles* 30, 1396–1417. doi:10.1002/2015GB005359.
Langenbrunner, B., and Neelin, J. D. (2013). Analyzing enso teleconnections in cmip models as a measure of model fidelity in simulating precipitation. *J. Clim.* 26, 4431–4446. doi:10.1175/JCLI-D-12-00542.1.
Large, W. G., and Caron, J. M. (2015). Diurnal cycling of sea surface temperature, salinity, and current in the CESM coupled climate model. *J. Geophys. Res. Ocean.* 120, 3711–3729. doi:10.1002/2014JC010691.
Larkin, N. K., and Harrison, D. E. (2002). ENSO warm (El Niño) and cold (La Niña) event life cycles: Ocean surface anomaly patterns, their symmetries, asymmetries, and implications. *J. Clim.* 15, 1118–1140. doi:10.1175/1520-0442(2002)015<1118:EWENOA>2.0.CO;2.
Latif, M., Martin, T., and Park, W. (2013). Southern ocean sector centennial climate variability and recent decadal trends. *J. Clim.* 26, 7767–7782. doi:10.1175/JCLI-D-12-00281.1.
Lau, W. K. M., and Kim, K.-M. (2015). Robust Hadley Circulation changes and increasing global dryness due to CO2warming from CMIP5 model projections. *Proc. Natl. Acad. Sci. U. S. A.* 112, 3630–3635. doi:10.1073/pnas.1418682112.
Lauer, A., Eyring, V., Righi, M., Buchwitz, M., Defourny, P., Evaldsson, M., et al. (2017). Benchmarking CMIP5 models with a subset of ESA CCI Phase 2 data using the ESMValTool. *Remote Sens. Environ.* 203, 9–39. doi:10.1016/j.rse.2017.01.007.
Lauer, A., Jones, C., Eyring, V., Evaldsson, M., Hagemann, S., Mäkelä, J., et al. (2018). Process-level improvements in CMIP5 models and their impact on tropical variability, the Southern Ocean, and monsoons. *Earth Syst. Dyn.* 9, 33–67. doi:10.5194/esd-9-33-2018.
Lauvset, S. K., Gruber, N., Landschützer, P., Olsen, A., and Tjiputra, J. (2015). Trends and drivers in global surface ocean pH over the past 3 decades. *Biogeosciences* 12, 1285–1298. doi:10.5194/bg-12-1285-2015.
Le Quéré, C., Andrew, R. M., Canadell, J. G., Sitch, S., Ivar Korsbakken, J., Peters, G. P., et al. (2016). Global Carbon Budget 2016. *Earth Syst. Sci. Data*. doi:10.5194/essd-8-605-2016.
Lean, J. L. (2018). Observation-based detection and attribution of 21st century climate change. *Wiley Interdiscip. Rev. Clim. Chang.* 9. doi:10.1002/wcc.511.

Lee, J.-Y., and Wang, B. (2014). Future change of global monsoon in the CMIP5. *Clim. Dyn.* 42, 101–119. doi:10.1007/s00382-012-1564-0.

Lee, J., Sperber, K. R., Gleckler, P. J., Bonfils, C. J. W., and Taylor, K. E. (2018). Quantifying the agreement between observed and simulated extratropical modes of interannual variability. *Clim. Dyn.* doi:10.1007/s00382-018-4355-4.

Lee, S. K., Park, W., Baringer, M. O., Gordon, A. L., Huber, B., and Liu, Y. (2015). Pacific origin of the abrupt increase in Indian Ocean heat content during the warming hiatus. *Nat. Geosci.* 8, 445–449. doi:10.1038/NGEO2438.

Lee, T., Waliser, D. E., Li, J.-L. F., Landerer, F. W., and Gierach, M. M. (2013). Evaluation of CMIP3 and CMIP5 Wind Stress Climatology Using Satellite Measurements and Atmospheric Reanalysis Products. *J. Clim.* 26, 5810–5826. doi:10.1175/JCLI-D-12-00591.1.

Lee, Y.-Y., and Black, R. X. (2013). Boreal winter low-frequency variability in CMIP5 models. *J. Geophys. Res. Atmos.* 118, 6891–6904. doi:10.1002/jgrd.50493.

Lee, Y.-Y., and Black, R. X. (2015). The Structure and Dynamics of the Stratospheric Northern Annular Mode in CMIP5 Simulations. *J. Clim.* 28, 86–107. doi:10.1175/JCLI-D-13-00570.1.

Lehner, F., Schurer, A. P., Hegerl, G. C., Deser, C., and Frölicher, T. L. (2016). The importance of ENSO phase during volcanic eruptions for detection and attribution. *Geophys. Res. Lett.* 43, 2851–2858. doi:10.1002/2016GL067935.

Lenton, T. M., Rockström, J., Gaffney, O., Rahmstorf, S., Richardson, K., Steffen, W., et al. (2019). Climate tipping points—too risky to bet against.

Leroux, S., Penduff, T., Bessières, L., Molines, J.-M., Brankart, J.-M., Sérazin, G., et al. (2018). Intrinsic and Atmospherically Forced Variability of the AMOC: Insights from a Large-Ensemble Ocean Hindcast. *J. Clim.* 31, 1183–1203. doi:10.1175/JCLI-D-17-0168.1.

Levang, S. J., and Schmitt, R. W. (2015). Centennial changes of the global water cycle in CMIP5 models. *J. Clim.* 28, 6489–6502. doi:10.1175/JCLI-D-15-0143.1.

Li, C., Stevens, B., and Marotzke, J. (2015a). Eurasian winter cooling in the warming hiatus of 1998-2012. *Geophys. Res. Lett.* 42, 8131–8139. doi:10.1002/2015GL065327.

Li, G., Xie, S.-P., and Du, Y. (2015b). Climate Model Errors over the South Indian Ocean Thermocline Dome and Their Effect on the Basin Mode of Interannual Variability. *J. Clim.* 28, 3093–3098. doi:10.1175/JCLI-D-14-00810.1.

Li, G., Xie, S.-P., and Du, Y. (2015c). Monsoon-Induced Biases of Climate Models over the Tropical Indian Ocean. *J. Clim.* 28, 3058–3072. doi:10.1175/JCLI-D-14-00740.1.

Li, G., Xie, S.-P., Li, G., and Xie, S.-P. (2014). Tropical Biases in CMIP5 Multimodel Ensemble: The Excessive Equatorial Pacific Cold Tongue and Double ITCZ Problems*. *J. Clim.* 27, 1765–1780. doi:10.1175/JCLI-D-13-00337.1.

Li, H., and Ilyina, T. (2018). Current and Future Decadal Trends in the Oceanic Carbon Uptake Are Dominated by Internal Variability. *Geophys. Res. Lett.* 45, 916–925. doi:10.1002/2017GL075370.

Li, J., Xie, S. P., Cook, E. R., Morales, M. S., Christie, D. A., Johnson, N. C., et al. (2013). El Niño modulations over the past seven centuries. *Nat. Clim. Chang.* 3, 822–826. doi:10.1038/nclimate1936.

Li, L., Schmitt, R. W., Ummenhofer, C. C., and Karnauskas, K. B. (2016a). Implications of North Atlantic sea surface salinity for summer precipitation over the U.S. Midwest: Mechanisms and predictive value. *J. Clim.* 29, 3143–3159. doi:10.1175/JCLI-D-15-0520.1.

Li, X., Hu, Z. Z., Jiang, X., Li, Y., Gao, Z., Yang, S., et al. (2016b). Trend and seasonality of land precipitation in observations and CMIP5 model simulations. *Int. J. Climatol.* 36, 3781–3793. doi:10.1002/joc.4592.

Li, X., Xie, S.-P., Gille, S. T., and Yoo, C. (2015d). Atlantic-induced pan-tropical climate change over the past three decades. *Nat. Clim. Chang.* 6. doi:10.1038/nclimate2840.

Li, Y., Chen, K., Yan, J., and Zhang, X. (submitted). Uncertainty in Optimal Fingerprinting is Underestimated. *Nature* (submitted).

Li, Y., Wang, T., Zeng, Z., Peng, S., Lian, X., and Piao, S. (2016c). Evaluating biases in simulated land surface albedo from CMIP5 global climate models. *J. Geophys. Res.* 121, 6178–6190. doi:10.1002/2016JD024774.

Li, Z., Xia, J., Ahlström, A., Rinke, A., Koven, C., Hayes, D. J., et al. (2018). Non-uniform seasonal warming regulates vegetation greening and atmospheric CO2 amplification over northern lands. *Environ. Res. Lett.* 13, 124008. doi:10.1088/1748-9326/aae9ad.

Lim, Y.-K., Cullather, R. I., Nowicki, S. M. J., and Kim, K.-M. (2019). Inter-relationship between subtropical Pacific sea surface temperature, Arctic sea ice concentration, and North Atlantic Oscillation in recent summers. *Sci. Rep.* 9, 3481. doi:10.1038/s41598-019-39896-7.

Lin, M., and Huybers, P. (2016). Revisiting Whether Recent Surface Temperature Trends Agree with the CMIP5 Ensemble. *J. Clim.* 29, 8673–8687. doi:10.1175/JCLI-D-16-0123.1.

Lipscomb, W. H., Fyke, J. G., Vizcaíno, M., Sacks, W. J., Wolfe, J., Vertenstein, M., et al. (2013). Implementation and Initial Evaluation of the Glimmer Community Ice Sheet Model in the Community Earth System Model. *J. Clim.* 26, 7352–7371. doi:10.1175/JCLI-D-12-00557.1.

Liu, F., Chai, J., Wang, B., Liu, J., Zhang, X., and Wang, Z. (2016a). Global monsoon precipitation responses to large

volcanic eruptions. *Sci. Rep.* 6, 24331. doi:10.1038/srep24331.
Liu, H., Wang, C., Lee, S.-K., and Enfield, D. (2013). Atlantic Warm Pool Variability in the CMIP5 Simulations. *J. Clim.* 26, 5315–5336. doi:10.1175/JCLI-D-12-00556.1.
Liu, J., Wang, B., Yim, S.-Y., Lee, J.-Y., Jhun, J.-G., and Ha, K.-J. (2012). What drives the global summer monsoon over the past millennium? *Clim. Dyn.* 39, 1063–1072. doi:10.1007/s00382-012-1360-x.
Liu, L., Xie, S.-P., Zheng, X.-T., Li, T., Du, Y., Huang, G., et al. (2014). Indian Ocean variability in the CMIP5 multi-model ensemble: the zonal dipole mode. *Clim. Dyn.* 43, 1715–1730. doi:10.1007/s00382-013-2000-9.
Liu, S., Jiang, D., and Lang, X. (2018). A multi-model analysis of moisture changes during the last glacial maximum. *Quat. Sci. Rev.* 191, 363–377.
Liu, W., Xie, S.-P., Liu, Z., and Zhu, J. (2017). Overlooked possibility of a collapsed Atlantic Meridional Overturning Circulation in warming climate. *Sci. Adv.* 3. Available at: http://advances.sciencemag.org/content/3/1/e1601666.abstract.
Liu, W., Xie, S. P., and Lu, J. (2016b). Tracking ocean heat uptake during the surface warming hiatus. *Nat. Commun.* 7, 1–9. doi:10.1038/ncomms10926.
Liu, Y., Piao, S., Gasser, T., Ciais, P., Yang, H., Wang, H., et al. (2019). Field-experiment constraints on the enhancement of the terrestrial carbon sink by CO2 fertilization. *Nat. Geosci.* doi:10.1038/s41561-019-0436-1.
Lora, J. M. (2018). Components and mechanisms of hydrologic cycle changes over North America at the Last Glacial Maximum. *J. Clim.* 31, 7035–7051. doi:10.1175/JCLI-D-17-0544.1.
Lovenduski, N. S., Gruber, N., and Doney, S. C. (2008). Toward a mechanistic understanding of the decadal trends in the Southern Ocean carbon sink. *Global Biogeochem. Cycles* 22, n/a-n/a. doi:10.1029/2007GB003139.
Lovenduski, N. S., McKinley, G. A., Fay, A. R., Lindsay, K., and Long, M. C. (2016). Partitioning uncertainty in ocean carbon uptake projections: Internal variability, emission scenario, and model structure. *Global Biogeochem. Cycles* 30, 1276–1287. doi:10.1002/2016GB005426.
Lu, X., Wang, L., and McCabe, M. F. (2016). Elevated CO2 as a driver of global dryland greening. *Sci. Rep.* 6, 20716. Available at: http://dx.doi.org/10.1038/srep20716.
Lübbecke, J. F., Rodríguez-Fonseca, B., Richter, I., Martín-Rey, M., Losada, T., Polo, I., et al. (2018). Equatorial Atlantic variability—Modes, mechanisms, and global teleconnections. *Wiley Interdiscip. Rev. Clim. Chang.* 9, e527. doi:10.1002/wcc.527.
Lunt, D. J., Bragg, F., Chan, W.-L., Hutchinson, D. K., Ladant, J.-B., Niezgodzki, I., et al. (submitted). DeepMIP: Model intercomparison of early Eocene climatic optimum (EECO) large-scale climate features and comparison with proxy data. *Clim. Past Discuss.* (submitted), 1–27. doi:10.5194/cp-2019-149.
Lunt, D. J., Huber, M., Anagnostou, E., Baatsen, M. L. J., Caballero, R., DeConto, R., et al. (2017). The DeepMIP contribution to PMIP4: experimental designfor model simulations of the EECO, PETM, and pre-PETM (version 1.0). *Geosci. Model Dev.* 10, 889–901. doi:10.5194/gmd-10-889-2017.
Luo, J.-J., Sasaki, W., and Masumoto, Y. (2012). Indian Ocean warming modulates Pacific climate change. *Proc. Natl. Acad. Sci.* 109, 18701–18706. doi:10.1073/pnas.1210239109.
Lyu, K., Zhang, X., Church, J. A., and Hu, J. (2016). Evaluation of the interdecadal variability of sea surface temperature and sea level in the Pacific in CMIP3 and CMIP5 models. *Int. J. Climatol.* 36, 3723–3740. doi:10.1002/joc.4587.
Ma, S., and Zhou, T. (2016). Robust Strengthening and Westward Shift of the Tropical Pacific Walker Circulation during 1979–2012: A Comparison of 7 Sets of Reanalysis Data and 26 CMIP5 Models. *J. Clim.* 29, 3097–3118. doi:10.1175/JCLI-D-15-0398.1.
Maher, N., England, M. H., Gupta, A. Sen, and Spence, P. (2018a). Role of Pacific trade winds in driving ocean temperatures during the recent slowdown and projections under a wind trend reversal. *Clim. Dyn.* 51, 321–336. doi:10.1007/s00382-017-3923-3.
Maher, N., Gupta, A. Sen, and England, M. H. (2014). Drivers of decadal hiatus periods in the 20th and 21st centuries. *Geophys. Res. Lett.* 41, 5978–5986. doi:10.1002/2014GL060527.
Maher, N., Matei, D., Milinski, S., and Marotzke, J. (2018b). ENSO Change in Climate Projections: Forced Response or Internal Variability? *Geophys. Res. Lett.* 45. doi:10.1029/2018GL079764.
Maher, N., McGregor, S., England, M. H., and Gupta, A. Sen (2015). Effects of volcanism on tropical variability. *Geophys. Res. Lett.* 42, 6024–6033. doi:10.1002/2015GL064751.
Mahlstein, I., Gent, P. R., and Solomon, S. (2013). Historical Antarctic mean sea ice area, sea ice trends, and winds in CMIP5 simulations. *J. Geophys. Res. Atmos.* 118, 5105–5110. doi:10.1002/jgrd.50443.
Mahlstein, I., and Knutti, R. (2011). Ocean Heat Transport as a Cause for Model Uncertainty in Projected Arctic Warming. *J. Clim.* 24, 1451–1460. doi:10.1175/2010JCLI3713.1.
Mahlstein, I., and Knutti, R. (2012). September Arctic sea ice predicted to disappear near 2°C global warming above present. *J. Geophys. Res. Atmos.* 117. doi:10.1029/2011JD016709.
Mahowald, N. M., Randerson, J. T., Lindsay, K., Munoz, E., Doney, S. C., Lawrence, P., et al. (2017). Interactions between land use change and carbon cycle feedbacks. *Global Biogeochem. Cycles* 31, 96–113.
Mantsis, D. F., Sherwood, S., Allen, R., and Shi, L. (2017). Natural variations of tropical width and recent trends. *Geophys. Res. Lett.* 44, 3825–3832. doi:10.1002/2016GL072097.

Mantua, N. J., and Hare, S. R. (2002). The Pacific Decadal Oscillation. *J. Oceanogr.* 58, 35–44. doi:10.1023/A:1015820616384.

Mantua, N. J., Hare, S. R., Zhang, Y., Wallace, J. M., and Francis, R. C. (1997). A Pacific Interdecadal Climate Oscillation with Impacts on Salmon Production*. *Bull. Am. Meteorol. Soc.* 78, 1069–1080. doi:10.1175/1520-0477(1997)078<1069:APICOW>2.0.CO;2.

Mao, J., Ribes, A., Yan, B., Shi, X., Thornton, P. E., Séférian, R., et al. (2016). Human-induced greening of the northern extratropical land surface. *Nat. Clim. Chang.* 6, 959. Available at: https://doi.org/10.1038/nclimate3056.

Mao, J., Shi, X., Thornton, P. E., Hoffman, F. M., Zhu, Z., and Myneni, R. B. (2013). Global latitudinal-asymmetric vegetation growth trends and their driving mechanisms: 1982-2009. *Remote Sens.* doi:10.3390/rs5031484.

Marcos, M., and Amores, A. (2014). Quantifying anthropogenic and natural contributions to thermosteric sea level rise. *Geophys. Res. Lett.* 41, 2502–2507. doi:10.1002/2014GL059766.

Marshall, J., and Radko, T. (2003). Residual-mean solutions for the Antarctic Circumpolar Current and its associated overturning circulation. *J. Phys. Oceanogr.* 33, 2341–2354.

Martín-Rey, M., Polo, I., Rodríguez-Fonseca, B., Losada, T., and Lazar, A. (2018). Is There Evidence of Changes in Tropical Atlantic Variability Modes under AMO Phases in the Observational Record? *J. Clim.* 31, 515–536. doi:10.1175/JCLI-D-16-0459.1.

Martin, E. R., Thorncroft, C., and Booth, B. B. B. (2013). The Multidecadal Atlantic SST—Sahel Rainfall Teleconnection in CMIP5 Simulations. *J. Clim.* 27, 784–806. doi:10.1175/JCLI-D-13-00242.1.

Marvel, K., Biasutti, M., Bonfils, C., Taylor, K., Kushnir, Y., and Cook, B. (2017). Observed and projected changes to the precipitation annual cycle. *J Clim.* 30, 4983–4995.

Marvel, K., Cook, B. I., Bonfils, C. J. W., Durack, P. J., Smerdon, J. E., and Williams, A. P. (2019). Twentieth-century hydroclimate changes consistent with human influence. *Nature* 569, 59–65. doi:10.1038/s41586-019-1149-8.

Marvel, K., Schmidt, G. A., Shindell, D., Bonfils, C., Legrande, A. N., Nazarenko, L., et al. (2015). Do responses to different anthropogenic forcings add linearly in climate models? *Environ. Res. Lett.* 10. doi:10.1088/1748-9326/10/10/104010.

Marzeion, B., Cogley, J. G., Richter, K., and Parkes, D. (2014). Glaciers. Attribution of global glacier mass loss to anthropogenic and natural causes. *Science* 345, 919–921. doi:10.1126/science.1254702.

Marzeion, B., Hock, R., Anderson, B., Bliss, A., Champollion, N., Fujita, K., et al. (submitted). Partitioning the Uncertainty of Ensemble Projections of Global Glacier Mass Change. *Earth's Futur.* (submitted).

Masson-Delmotte, V., Schulz, M., Abe-Ouchi, A., Beer, J., Ganopolski, A., González Rouco, J. F., et al. (2013). Information from paleoclimate archives. *Clim. Chang.* 383464, 2013.

Massonnet, F., Fichefet, T., Goosse, H., Bitz, C. M., Philippon-Berthier, G., Holland, M. M., et al. (2012). Constraining projections of summer Arctic sea ice. *Cryosph.* 6, 1383–1394. doi:10.5194/tc-6-1383-2012.

Massonnet, F., Vancoppenolle, M., Goosse, H., Docquier, D., Fichefet, T., and Blanchard-Wrigglesworth, E. (2018). Arctic sea-ice change tied to its mean state through thermodynamic processes. *Nat. Clim. Chang.* 8, 599–603. doi:10.1038/s41558-018-0204-z.

Maussion, F., Butenko, A., Champollion, N., Dusch, M., Eis, J., Fourteau, K., et al. (2019). The Open Global Glacier Model (OGGM) v1.1. *Geosci. Model Dev.* 12, 909–931. doi:10.5194/gmd-12-909-2019.

Maussion, F., Butenko, A., Eis, J., Fourteau, K., Jarosch, A. H., Landmann, J., et al. (2018). The Open Global Glacier Model (OGGM) v1.0. *Geosci. Model Dev. Discuss.*, 1–33. doi:10.5194/gmd-2018-9.

Maycock, A. C., Randel, W. J., Steiner, A. K., Karpechko, A. Y., Cristy, J., Saunders, R., et al. (2018a). Revisiting the mystery of recent stratospheric temperature trends. *Geophys. Res. Lett.* doi:10.1029/2018GL078035.

Maycock, A., Karpechko, A. Y., and et al. (2018b). Chapter 5 of Scientific Assessment of Ozone Depletion: 2014. Geneva.

McGregor, H. V., Evans, M. N., Goosse, H., Leduc, G., Martrat, B., Addison, J. A., et al. (2015). Robust global ocean cooling trend for the pre-industrial Common Era. *Nat. Geosci.* 8, 671–677. doi:10.1038/ngeo2510.

McGregor, S., Stuecker, M. F., Kajtar, J. B., England, M. H., and Collins, M. (2018). Model tropical Atlantic biases underpin diminished Pacific decadal variability. *Nat. Clim. Chang.* 8, 493–498. doi:10.1038/s41558-018-0163-4.

McGregor, S., Timmermann, A., England, M. H., Elison Timm, O., and Wittenberg, A. T. (2013). Inferred changes in El Niño–Southern Oscillation variance over the past six centuries. *Clim. Past* 9, 2269–2284. doi:10.5194/cp-9-2269-2013.

McGregor, S., Timmermann, A., Stuecker, M. F., England, M. H., Merrifield, M., Jin, F. F., et al. (2014). Recent walker circulation strengthening and pacific cooling amplified by atlantic warming. *Nat. Clim. Chang.* 4. doi:10.1038/nclimate2330.

McKitrick, R., and Christy, J. (2018). A Test of the Tropical 200- to 300-hPa Warming Rate in Climate Models. *Earth Sp. Sci.* 5, 529–536. doi:10.1029/2018EA000401.

McPhaden, M. J., Lee, T., and McClurg, D. (2011). El Niño and its relationship to changing background conditions in the tropical Pacific Ocean. *Geophys. Res. Lett.* 38, 2–5. doi:10.1029/2011GL048275.

McPhaden, M. J., Zebiak, S. E., and Glantz, M. H. (2006). ENSO as an integrating concept in earth science. *Science* 314, 1740–1745. doi:10.1126/science.1132588.

Mecking, J. V, Drijfhout, S. S., Jackson, L. C., and Andrews, M. B. (2017). The effect of model bias on Atlantic

freshwater transport and implications for AMOC bi-stability. *Tellus A Dyn. Meteorol. Oceanogr.* 69, 1299910. doi:10.1080/16000870.2017.1299910.

Medhaug, I., Stolpe, M. B., Fischer, E. M., and Knutti, R. (2017). Reconciling controversies about the 'global warming hiatus.' *Nature* 545, 41. Available at: http://dx.doi.org/10.1038/nature22315.

Meehl, G. A., Arblaster, J. M., Bitz, C. M., Chung, C. T. Y., and Teng, H. (2016a). Antarctic sea-ice expansion between 2000 and 2014 driven by tropical Pacific decadal climate variability. *Nat. Geosci.* 9, 590–595. doi:10.1038/ngeo2751.

Meehl, G. A., Arblaster, J. M., and Chung, C. T. Y. (2015). Disappearance of the southeast U.S. "warming hole" with the late 1990s transition of the Interdecadal Pacific Oscillation. *Geophys. Res. Lett.* 42, 5564–5570. doi:10.1002/2015GL064586.

Meehl, G. A., Arblaster, J. M., Chung, C. T. Y., Holland, M. M., DuVivier, A., Thompson, L., et al. (2019). Sustained ocean changes contributed to sudden Antarctic sea ice retreat in late 2016. *Nat. Commun.* 10, 14. doi:10.1038/s41467-018-07865-9.

Meehl, G. A., Arblaster, J. M., Fasullo, J. T., Hu, A., and Trenberth, K. E. (2011). Model-based evidence of deep-ocean heat uptake during surface-temperature hiatus periods. *Nat. Clim. Chang.* 1, 360–364. doi:10.1038/nclimate1229.

Meehl, G. A., Chung, C. T. Y., Arblaster, J. M., Holland, M. M., and Bitz, C. M. (2018). Tropical Decadal Variability and the Rate of Arctic Sea Ice Decrease. *Geophys. Res. Lett.* 45, 11,311-326,333. doi:10.1029/2018GL079989.

Meehl, G. A., Covey, C., Delworth, T., Latif, M., McAvaney, B., Mitchell, J. F. B., et al. (2007). The WCRP CMIP3 multimodel dataset: A new era in climatic change research. *Bull. Am. Meteorol. Soc.* 88, 1383–1394. doi:10.1175/BAMS-88-9-1383.

Meehl, G. A., Hu, A., Arblaster, J. M., Fasullo, J., and Trenberth, K. E. (2013). Externally Forced and Internally Generated Decadal Climate Variability Associated with the Interdecadal Pacific Oscillation. *J. Clim.* 26, 7298–7310. doi:10.1175/JCLI-D-12-00548.1.

Meehl, G. A., Hu, A., Santer, B. D., and Xie, S. P. (2016b). Contribution of the Interdecadal Pacific Oscillation to twentieth-century global surface temperature trends. *Nat. Clim. Chang.* 6, 1005–1008. doi:10.1038/nclimate3107.

Meehl, G. A., Hu, A., and Teng, H. (2016c). Initialized decadal prediction for transition to positive phase of the Interdecadal Pacific Oscillation. *Nat. Commun.* 7, 1–7. doi:10.1038/ncomms11718.

Meehl, G. A., Teng, H., and Arblaster, J. M. (2014). Climate model simulations of the observed early-2000s hiatus of global warming. *Nat. Clim. Chang.* 4, 898–902. doi:10.1038/nclimate2357.

Meijers, A. J. S., Shuckburgh, E., Bruneau, N., Sallee, J. B., Bracegirdle, T. J., and Wang, Z. (2012). Representation of the Antarctic Circumpolar Current in the CMIP5 climate models and future changes under warming scenarios. *J. Geophys. Res. Ocean.* 117, n/a-n/a. doi:10.1029/2012JC008412.

Menary, M. B., Hodson, D. L. R., Robson, J. I., Sutton, R. T., Wood, R. A., and Hunt, J. A. (2015). Exploring the impact of CMIP5 model biases on the simulation of North Atlantic decadal variability. *Geophys. Res. Lett.* 42, 5926–5934. doi:10.1002/2015GL064360.

Menary, M. B., Kuhlbrodt, T., Ridley, J., Andrews, M. B., Dimdore-Miles, O. B., Deshayes, J., et al. (2018). Preindustrial Control Simulations With HadGEM3-GC3.1 for CMIP6. *J. Adv. Model. Earth Syst.*, 2018MS001495. doi:10.1029/2018MS001495.

Menary, M. B., Roberts, C. D., Palmer, M. D., Halloran, P. R., Jackson, L., Wood, R. A., et al. (2013). Mechanisms of aerosol-forced AMOC variability in a state of the art climate model. *J. Geophys. Res. Ocean.* 118, 2087–2096. doi:10.1002/jgrc.20178.

Menary, M. B., Robson, J., Allan, R., Booth, B. B., Cassou, C., Gastineau, G., et al. (submitted). Aerosol-forced AMOC changes in CMIP6 historical simulations. *Nat. Geosci.* (submitted).

Menary, M. B., and Scaife, A. A. (2014). Naturally forced multidecadal variability of the Atlantic meridional overturning circulation. *Clim. Dyn.* 42, 1347–1362. doi:10.1007/s00382-013-2028-x.

Meredith, M., Sommerkorn, M., Cassotta, S., Derksen, C., Ekaykin, A., Hollowed, A., et al. (2019). "Polar Regions," in *IPCC Special Report on the Ocean and Cryosphere in a Changing Climate*, eds. H.-O. Pörtner, D. C. Roberts, V. Masson-Delmotte, P. Zhai, M. Tignor, E. Poloczanska, et al. (Cambridge University Press), tba. Available at: https://www.ipcc.ch/srocc.

Meyssignac, B., Slangen, A. B. A., Melet, A., Church, J. A., Fettweis, X., Marzeion, B., et al. (2017). Evaluating model simulations of twentieth-century sea-level rise. Part II: Regional sea-level changes. *J. Clim.* 30, 8565–8593. doi:10.1175/JCLI-D-17-0112.1.

Middlemas, E. A., and Clement, A. C. (2016). Spatial Patterns and Frequency of Unforced Decadal-Scale Changes in Global Mean Surface Temperature in Climate Models. *J. Clim.* 29, 6245–6257. doi:10.1175/JCLI-D-15-0609.1.

Min, S.-K., Zhang, X., Zwiers, F. W., and Agnew, T. (2008). Human influence on Arctic sea ice detectable from early 1990s onwards. *Geophys. Res. Lett.* 35. doi:10.1029/2008GL035725.

Mitchell, D., Davini, P., Harvey, B., Massey, N., Haustein, K., Woollings, T., et al. (2017). Assessing mid-latitude dynamics in extreme event attribution systems. *Clim. Dyn.* 48, 3889–3901. doi:10.1007/s00382-016-3308-z.

Mitchell, D. M. (2016). Attributing the forced components of observed stratospheric temperature variability to external drivers. *Q. J. R. Meteorol. Soc.* 142, 1041–1047. doi:10.1002/qj.2707.

Mitchell, D. M., Lo, Y. T. E., Seviour, W. J. M., and Polvani, L. M. (submitted). The vertical profile of recent tropical

temperature trends: Persistent model biases in the context of internal variability. *Environ. Res. Lett.* (submitted).
Mitchell, D. M., Osprey, S. M., Gray, L. J., Butchart, N., Hardiman, S. C., Charlton-Perez, A. J., et al. (2012). The effect of climate change on the variability of the Northern Hemisphere stratospheric polar vortex. *J. Atmos. Sci.* 69, 2608–2618.
Mitchell, D. M., Thorne, P. W., Stott, P. A., and Gray, L. J. (2013). Revisiting the controversial issue of tropical tropospheric temperature trends. *Geophys. Res. Lett.* 40, 2801–2806. doi:10.1002/grl.50465.
Modak, A., and Mauritsen, T. (submitted). The 2000-2012 global warming hiatus more likely with a low climate sensitivity. *Geophys. Res. Lett.* (submitted).
Mohtadi, M., Prange, M., and Steinke, S. (2016). Palaeoclimatic insights into forcing and response of monsoon rainfall. *Nature* 533, 191–199. doi:10.1038/nature17450.
Molteni, F., Farneti, R., Kucharski, F., and Stockdale, T. N. (2017). Modulation of air-sea fluxes by extratropical planetary waves and its impact during the recent surface warming slowdown. *Geophys. Res. Lett.* 44, 1494–1502. doi:10.1002/2016GL072298.
Monerie, P.-A., Robson, J., Dong, B., Hodson, D. L. R., and Klingaman, N. P. (2019). Effect of the Atlantic Multidecadal Variability on the Global Monsoon. *Geophys. Res. Lett.* 46, 1765–1775. doi:10.1029/2018GL080903.
Mongwe, N. P., Vichi, M., and Monteiro, P. M. S. (2018). The seasonal cycle of pCO2 and CO2 fluxes in the Southern Ocean: diagnosing anomalies in CMIP5 Earth system models. *Biogeosciences* 15, 2851–2872. doi:10.5194/bg-15-2851-2018.
Monselesan, D. P., O'Kane, T. J., Risbey, J. S., and Church, J. (2015). Internal climate memory in observations and models. *Geophys. Res. Lett.* 42, 1232–1242. doi:10.1002/2014GL062765.
Morgenstern, O., Stone, K. A., Schofield, R., Akiyoshi, H., Yamashita, Y., Kinnison, D. E., et al. (2018). Ozone sensitivity to varying greenhouse gases and ozone-depleting substances in CCMI-1 simulations. *Atmos. Chem. Phys.* 18, 1091–1114. doi:10.5194/acp-18-1091-2018.
Morice, C. P., Kennedy, J. J., Rayner, N. A., and Jones, P. D. (2012). Quantifying uncertainties in global and regional temperature change using an ensemble of observational estimates: The HadCRUT4 data set. *J. Geophys. Res. Atmos.* 117.
Mouginot, J., Rignot, E., Bjørk, A. A., van den Broeke, M., Millan, R., Morlighem, M., et al. (2019). Forty-six years of Greenland Ice Sheet mass balance from 1972 to 2018. *Proc. Natl. Acad. Sci.* 116, 9239 LP – 9244. doi:10.1073/pnas.1904242116.
Mueller, B. L., Gillett, N. P., Monahan, A. H., and Zwiers, F. W. (2018). Attribution of Arctic Sea Ice Decline from 1953 to 2012 to Influences from Natural, Greenhouse Gas, and Anthropogenic Aerosol Forcing. *J. Clim.* 31, 7771–7787. doi:10.1175/JCLI-D-17-0552.1.
Muglia, J., and Schmittner, A. (2015). Glacial Atlantic overturning increased by wind stress in climate models. *Geophys. Res. Lett.* 42, 9862–9868. doi:10.1002/2015GL064583.
Mulcahy, J. P., Johnson, C., Jones, C. G., Povey, A. C., Scott, C. E., Sellar, A., et al. (submitted). Description and evaluation of aerosol in UKESM1 and HadGEM3-GC3.1 CMIP6 historical simulations. *Geosci. Model. Dev. Discuss.* (submitted).
Mulcahy, J. P., Jones, C., Sellar, A., Johnson, B., Boutle, I. A., Jones, A., et al. (2018). Improved Aerosol Processes and Effective Radiative Forcing in HadGEM3 and UKESM1. *J. Adv. Model. Earth Syst.* 10, 2786–2805. doi:10.1029/2018MS001464.
Muñoz, E., Weijer, W., Grodsky, S. A., Bates, S. C., and Wainer, I. (2012). Mean and variability of the tropical Atlantic Ocean in the CCSM4. *J. Clim.* 25, 4860–4882. doi:10.1175/JCLI-D-11-00294.1.
Murphy, D. M. (2013). Little net clear-sky radiative forcing from recent regional redistribution of aerosols. *Nat. Geosci.* 6, 258.
Murphy, L. N., Bellomo, K., Cane, M., and Clement, A. (2017). The role of historical forcings in simulating the observed Atlantic multidecadal oscillation. *Geophys. Res. Lett.* 44, 2472–2480. doi:10.1002/2016GL071337.
Najafi, M. R., Zwiers, F. W., and Gillett, N. P. (2016). Attribution of the spring snow cover extent decline in the Northern Hemisphere, Eurasia and North America to anthropogenic influence. *Clim. Change* 136, 571–586. doi:10.1007/s10584-016-1632-2.
Najafi, M. R., Zwiers, F. W., and Gillett, N. P. (2017). Attribution of observed streamflow changes in key British Columbia drainage basins. *Geophys. Res. Lett.* 44, 11–12.
Nakamura, T., Yamazaki, K., Iwamoto, K., Honda, M., Miyoshi, Y., Ogawa, Y., et al. (2015). A negative phase shift of the winter AO/NAO due to the recent Arctic sea-ice reduction in late autumn. *J. Geophys. Res. Atmos.* 120, 3209–3227. doi:10.1002/2014JD022848.
Napoly, A., Boone, A., Samuelsson, P., Gollvik, S., Martin, E., Seferian, R., et al. (2017). The interactions between soil–biosphere–atmosphere (ISBA) land surface model multi-energy balance (MEB) option in SURFEXv8 – Part 2: Introduction of a litter formulation and model evaluation for local-scale forest sites. *Geosci. Model Dev.* 10, 1621–1644. doi:10.5194/gmd-10-1621-2017.
Navarro, J. C. A., Varma, V., Riipinen, I., Seland, O., Kirkevag, A., Struthers, H., et al. (2016). Amplification of Arctic warming by past air pollution reductions in Europe (vol 9, pg 277, 2016). *Nat. Geosci.* 9, 470.

Neukom, R., Barboza, L. A., Erb, M. P., Shi, F., Emile-Geay, J., Evans, M. N., et al. (2019). Consistent multidecadal variability in global temperature reconstructions and simulations over the Common Era. *Nat. Geosci.* 12, 643–649. doi:10.1038/s41561-019-0400-0.

Neukom, R., Schurer, A. P., Steiger, N. J., and Hegerl, G. C. (2018). Possible causes of data model discrepancy in the temperature history of the last Millennium. *Sci. Rep.* 8, 7572. doi:10.1038/s41598-018-25862-2.

Nevison, C. D., Manizza, M., Keeling, R. F., Stephens, B. B., Bent, J. D., Dunne, J., et al. (2016). Evaluating CMIP5 ocean biogeochemistry and Southern Ocean carbon uptake using atmospheric potential oxygen: Present-day performance and future projection. *Geophys. Res. Lett.* 43, 2077–2085. doi:10.1002/2015GL067584.

Newman, M., Alexander, M. A., Ault, T. R., Cobb, K. M., Deser, C., Di Lorenzo, E., et al. (2016). The Pacific decadal oscillation, revisited. *J. Clim.* 29, 4399–4427. doi:10.1175/JCLI-D-15-0508.1.

Newman, M., Shin, S.-I., and Alexander, M. A. (2011). Natural variation in ENSO flavors. *Geophys. Res. Lett.* 38. doi:10.1029/2011GL047658.

Nguyen, H., Lucas, C., Evans, A., Timbal, B., and Hanson, L. (2015). Expansion of the Southern Hemisphere hadley cell in response to greenhouse gas forcing. *J. Clim.* 28, 8067–8077. doi:10.1175/JCLI-D-15-0139.1.

Ni, Y., and Hsu, P.-C. (2018). Inter-annual variability of global monsoon precipitation in present-day and future warming scenarios based on 33 Coupled Model Intercomparison Project Phase 5 models. *Int. J. Clim.* doi:10.1002/joc.5704.

Nidheesh, A. G., Lengaigne, M., Vialard, J., Izumo, T., Unnikrishnan, A. S., and Cassou, C. (2017). Influence of ENSO on the Pacific decadal oscillation in CMIP models. *Clim. Dyn.* 49, 3309–3326. doi:10.1007/s00382-016-3514-8.

Nieves, V., Willis, J. K., and Patzert, W. C. (2015). Recent hiatus caused by decadal shift in Indo-Pacific heating. *Science* 349, 532–535. doi:10.1126/science.aaa4521.

Nijsse, F. J. M. M., Cox, P. M., Huntingford, C., and Williamson, M. S. (2019). Decadal global temperature variability increases strongly with climate sensitivity. *Nat. Clim. Chang.* 9, 598–601. doi:10.1038/s41558-019-0527-4.

Nilsson, J., Langen, P. L., Ferreira, D., and Marshall, J. (2013). Ocean basin geometry and the salinification of the atlantic ocean. *J. Clim.* 26, 6163–6184. doi:10.1175/JCLI-D-12-00358.1.

Ning, L., and Bradley, R. S. (2016). NAO and PNA influences on winter temperature and precipitation over the eastern United States in CMIP5 GCMs. *Clim. Dyn.* 46, 1257–1276. doi:10.1007/s00382-015-2643-9.

Nnamchi, H. C., Li, J., Kucharski, F., Kang, I.-S., Keenlyside, N. S., Chang, P., et al. (2015). Thermodynamic controls of the Atlantic Niño. *Nat. Commun.* 6, 8895. doi:10.1038/ncomms9895.

Notz, D., Dörr, J., Bailey, D. A., Blockley, E., Bushuk, N., Debernard, J. B., et al. (submitted). Arctic Sea Ice in CMIP6. *Geophys. Res. Lett.* (submitted).

Notz, D., and Marotzke, J. (2012). Observations reveal external driver for Arctic sea-ice retreat. *Geophys. Res. Lett.* 39. doi:10.1029/2012GL051094.

Notz, D., and Stroeve, J. (2016). Observed Arctic sea-ice loss directly follows anthropogenic CO2 emission. *Science* 354, 747–750. doi:10.1126/science.aag2345.

Nowicki, S., Bindschadler, R. A., Abe-Ouchi, A., Aschwanden, A., Bueler, E., Choi, H., et al. (2013). Insights into spatial sensitivities of ice mass response to environmental change from the SeaRISE ice sheet modeling project II: Greenland. *J. Geophys. Res. Earth Surf.* 118, 1025–1044. doi:10.1002/jgrf.20076.

Nowicki, S. M. J., Payne, A., Larour, E., Seroussi, H., Goelzer, H., Lipscomb, W., et al. (2016). Ice Sheet Model Intercomparison Project (ISMIP6) contribution to CMIP6. *Geosci. Model Dev.* 9, 4521–4545. doi:10.5194/gmd-9-4521-2016.

Nowicki, S., and Seroussi, H. (2018). Projections of Future Sea Level Contributions from the Greenland and Antarctic Ice Sheets: Challenges Beyond Dynamical Ice Sheet Modeling. *Oceanography* 31. doi:10.5670/oceanog.2018.216.

O'Reilly, C. H., Huber, M., Woollings, T., and Zanna, L. (2016). The signature of low-frequency oceanic forcing in the Atlantic Multidecadal Oscillation. *Geophys. Res. Lett.* 43, 2810–2818. doi:10.1002/2016GL067925.

O'Reilly, C. H., Weisheimer, A., Woollings, T., Gray, L. J., and MacLeod, D. (2019a). The importance of stratospheric initial conditions for winter North Atlantic Oscillation predictability and implications for the signal-to-noise paradox. *Q. J. R. Meteorol. Soc.* 145, 131–146. doi:10.1002/qj.3413.

O'Reilly, C. H., Zanna, L., and Woollings, T. (2019b). Assessing External and Internal Sources of Atlantic Multidecadal Variability Using Models, Proxy Data, and Early Instrumental Indices. *J. Clim.* 32, 7727–7745. doi:10.1175/JCLI-D-19-0177.1.

Ogata, T., Johnson, S. J., Schiemann, R., Demory, M.-E., Mizuta, R., Yoshida, K., et al. (2017). The resolution sensitivity of the Asian summer monsoon and its inter-model comparison between MRI-AGCM and MetUM. *Clim. Dyn.* 49, 3345–3361. doi:10.1007/s00382-016-3517-5.

Ogawa, F., Omrani, N.-E., Nishii, K., Nakamura, H., and Keenlyside, N. (2015). Ozone-induced climate change propped up by the Southern Hemisphere oceanic front. *Geophys. Res. Lett.* 42, 10,056-10,063. doi:10.1002/2015GL066538.

Ohba, M., and Ueda, H. (2009). Role of Nonlinear Atmospheric Response to SST on the Asymmetric Transition Process of ENSO. *J. Clim.* 22, 177–192. doi:10.1175/2008JCLI2334.1.

Oke, P. R., and Sakov, P. (2008). Representation Error of Oceanic Observations for Data Assimilation. *J. Atmos.*

Ocean. Technol. 25, 1004–1017. doi:10.1175/2007JTECHO558.1.
Osborne, J., Lambert, F. H., Groenendijk, M., Harper, A., Koven, C., Poulter, B., et al. (2015). Reconciling precipitation with runoff: observed hydrological change in the midlatitudes. *J. Hydrometeorol.* 16, 2403–2420.
Oschlies, A., Duteil, O., Getzlaff, J., Koeve, W., Landolfi, A., and Schmidtko, S. (2017). Patterns of deoxygenation: sensitivity to natural and anthropogenic drivers. *Philos. Trans. R. Soc. A Math. Eng. Sci.* 375, 20160325. doi:10.1098/rsta.2016.0325.
Osprey, S. M., Gray, L. J., Hardiman, S. C., Butchart, N., and Hinton, T. J. (2013). Stratospheric Variability in Twentieth-Century CMIP5 Simulations of the Met Office Climate Model: High Top versus Low Top. *J. Clim.* 26, 1595–1606. doi:10.1175/JCLI-D-12-00147.1.
Oster, J. L., Ibarra, D. E., Winnick, M. J., and Maher, K. (2015). Steering of westerly storms over western North America at the Last Glacial Maximum. *Nat. Geosci.* doi:10.1038/ngeo2365.
Ott, I., Romberg, K., and Jacobeit, J. (2015). Teleconnections of the tropical Atlantic and Pacific Oceans in a CMIP5 model ensemble. *Clim. Dyn.* 44, 3043–3055. doi:10.1007/s00382-014-2394-z.
Otterå, O. H., Bentsen, M., Drange, H., and Suo, L. (2010). External forcing as a metronome for Atlantic multidecadal variability. *Nat. Geosci.* 3, 688–694. doi:10.1038/ngeo955.
Otto-Bliesner, B. L., Braconnot, P., Harrison, S. P., Lunt, D. J., Abe-Ouchi, A., Albani, S., et al. (2017). The PMIP4 contribution to CMIP6 -- Part 2: Two interglacials, scientific objective and experimental design for Holocene and \hack{\newline} Last Interglacial simulations. *Geosci. Model Dev.* 10, 3979–4003. doi:10.5194/gmd-10-3979-2017.
Otto-Bliesner, B. L., Brady, E. C., Fasullo, J., Jahn, A., Landrum, L., Stevenson, S., et al. (2016). Climate Variability and Change since 850 CE: An Ensemble Approach with the Community Earth System Model. *Bull. Am. Meteorol. Soc.* 97, 735–754. doi:10.1175/BAMS-D-14-00233.1.
Otto-Bliesner, B. L., Hewitt, C. D., Marchitto, T. M., Brady, E., Abe-Ouchi, A., Crucifix, M., et al. (2007). Last Glacial Maximum ocean thermohaline circulation: PMIP2 model intercomparisons and data constraints. *Geophys. Res. Lett.* 34.
Otto, F. E. L., Frame, D. J., Otto, A., and Allen, M. R. (2015). Embracing uncertainty in climate change policy. *Nat. Clim. Chang.* 5, 917–921. doi:10.1038/nclimate2716.
Oudar, T., Kushner, P. J., Fyfe, J. C., and Sigmond, M. (2018). No impact of anthropogenic aerosols on early 21st century global temperature trends in a large initial-condition ensemble. *Geophys. Res. Lett.* 45. doi:10.1029/2018GL078841.
Paeth, H., Pollinger, F., and Ring, C. (2017). Detection and Attribution of Multivariate Climate Change Signals Using Discriminant Analysis and Bayesian Theorem. *J. Clim.* 30, 7757–7776. doi:10.1175/JCLI-D-16-0850.1.
PAGES 2k-PMIP3 (2015). Continental-scale temperature variability in PMIP3 simulations and PAGES 2k regional temperature reconstructions over the past millennium. *Clim. Past* 11, 1673–1699. doi:10.5194/cp-11-1673-2015.
Paik, S.-M., and Min, S.-K. (submitted). Quantifying greenhouse gas contribution to the observed spring snow cover decline using the CMIP6 multi-model ensemble. *J. Clim.* (submitted).
Pallotta, G., and Santer, B. D. (submitted). Multi-frequency analysis of simulated versus observed variability in tropospheric temperature. *Proc. Natl. Acad. Sci.* (submitted).
Palmer, M. D., and McNeall, D. J. (2014). Internal variability of Earth's energy budget simulated by CMIP5 climate models. *Environ. Res. Lett.* 9, 34016. doi:10.1088/1748-9326/9/3/034016.
Pan, Y. H., and Oort, A. H. (1983). Global Climate Variations Connected with Sea Surface Temperature Anomalies in the Eastern Equatorial Pacific Ocean for the 1958–73 Period. *Mon. Weather Rev.* 111, 1244–1258. doi:10.1175/1520-0493(1983)111<1244:GCVCWS>2.0.CO;2.
Park, T., Ganguly, S., TØmmervik, H., Euskirchen, E. S., HØgda, K. A., Karlsen, S. R., et al. (2016). Changes in growing season duration and productivity of northern vegetation inferred from long-term remote sensing data. *Environ. Res. Lett.* doi:10.1088/1748-9326/11/8/084001.
Parsons, L. A., Brennan, M. K., and Proistosescu, C. (submitted). Magnitudes and spatial patterns of interdecadal temperature variability in CMIP6. *Geophys. Res. Lett.* (submitted).
Parsons, S., Renwick, J. A., and McDonald, A. J. (2016). An Assessment of Future Southern Hemisphere Blocking Using CMIP5 Projections from Four GCMs. *J. Clim.* 29, 7599–7611. doi:10.1175/JCLI-D-15-0754.1.
Passey, B. H., Ayliffe, L. K., Kaakinen, A., Zhang, Z., Eronen, J. T., Zhu, Y., et al. (2009). Strengthened East Asian summer monsoons during a period of high-latitude warmth? Isotopic evidence from Mio-Pliocene fossil mammals and soil carbonates from northern China. *Earth Planet. Sci. Lett.* doi:10.1016/j.epsl.2008.11.008.
Pattyn, F., Favier, L., Sun, S., and Durand, G. (2017). Progress in Numerical Modeling of Antarctic Ice-Sheet Dynamics. *Curr. Clim. Chang. Reports* 3, 174–184. doi:10.1007/s40641-017-0069-7.
Pattyn, F., Perichon, L., Aschwanden, A., Breuer, B., De Smedt, B., Gagliardini, O., et al. (2008). Benchmark experiments for higher-order and full-Stokes ice sheet models (ISMIP-HOM). *Cryosphere* 2, 95–108. doi:10.5194/tc-2-95-2008.
Pattyn, F., Schoof, C., Perichon, L., Hindmarsh, R. C. A., Bueler, E., de Fleurian, B., et al. (2012). Results of the Marine Ice Sheet Model Intercomparison Project, MISMIP. *Cryosph.* 6, 573–588. doi:10.5194/tc-6-573-2012.
Pauling, A. G., Bitz, C. M., Smith, I. J., and Langhorne, P. J. (2016). The Response of the Southern Ocean and

Antarctic Sea Ice to Freshwater from Ice Shelves in an Earth System Model. *J. Clim.* 29, 1655–1672. doi:10.1175/JCLI-D-15-0501.1.
Pausata, F. S. R., Messori, G., and Zhang, Q. (2016). Impacts of dust reduction on the northware expansion of the African monsoon during the Green Sahara period. *Earth Planet. Sci. Lett.* 434, 298–307.
Payne, A. J., Huybrechts, P., Abe-Ouchi, A., Calov, R., Fastook, J. L., Greve, R., et al. (2000). Results from the EISMINT model intercomparison: The effects of thermomechanical coupling. *J. Glaciol.* 46, 227–238. doi:10.3189/172756500781832891.
Pearl, J. (2009). *Causality*. Cambridge university press.
Pedersen, R. A., Langen, P. L., and Vinther, B. M. (2017). The last interglacial climate: comparing direct and indirect impacts of insolation changes. *Clim. Dyn.* 48, 3391–3407. doi:10.1007/s00382-016-3274-5.
Pederson, N., Hessl, A. E., Baatarbileg, N., Anchukaitis, K. J., and Di Cosmo, N. (2014). Pluvials, droughts, the Mongol Empire, and modern Mongolia. *Proc. Natl. Acad. Sci.* doi:10.1073/pnas.1318677111.
Peings, Y., and Magnusdottir, G. (2013). Response of the Wintertime Northern Hemisphere Atmospheric Circulation to Current and Projected Arctic Sea Ice Decline: A Numerical Study with CAM5. *J. Clim.* 27, 244–264. doi:10.1175/JCLI-D-13-00272.1.
Peings, Y., and Magnusdottir, G. (2016). Wintertime atmospheric response to Atlantic multidecadal variability: effect of stratospheric representation and ocean–atmosphere coupling. *Clim. Dyn.* 47, 1029–1047. doi:10.1007/s00382-015-2887-4.
Peng, J., and Dan, L. (2015). Impacts of CO2 concentration and climate change on the terrestrial carbon flux using six global climate--carbon coupled models. *Ecol. Modell.* 304, 69–83.
Perez-Sanz, A., Li, G., Gonzalez-Samperiz, P., and et al. (2014). Evaluation of modern and mid-Holocene seasonal precipitation of the Mediterranean and northern Africa in the CMIP5 simulations. *Clim Past* 10, 551–568. doi:10.5194/cp-10-551-2014.
Perez, F. F., Fontela, M., García-Ibáñez, M. I., Mercier, H., Velo, A., Lherminier, P., et al. (2018). Meridional overturning circulation conveys fast acidification to the deep Atlantic Ocean. *Nature* 554, 515–518. doi:10.1038/nature25493.
Perry, S. J., McGregor, S., Gupta, A. Sen, and England, M. H. (2017). Future Changes to El Niño–Southern Oscillation Temperature and Precipitation Teleconnections. *Geophys. Res. Lett.* 44, 10,608-10,616. doi:10.1002/2017GL074509.
Perry, S. J., McGregor, S., Gupta, A. Sen, England, M. H., and Maher, N. (2019). Projected late 21st century changes to the regional impacts of the El Niño-Southern Oscillation. *Clim. Dyn.*, 1–18.
Pfeffer, W. T., Arendt, A. A., Bliss, A., Bolch, T., Cogley, J. G., Gardner, A. S., et al. (2014). The Randolph Glacier Inventory: a globally complete inventory of glaciers. *J. Glaciol.* 60, 537–552. doi:10.3189/2014JoG13J176.
Philip, S., Kew, S. F., van Oldenborgh, G. J., Otto, F., O'Keefe, S., Haustein, K., et al. (2018). Attribution analysis of the Ethiopian drought of 2015. *J. Clim.* doi:10.1175/JCLI-D-17-0274.1.
Phillips, A. S., Deser, C., and Fasullo, J. (2014). Evaluating Modes of Variability in Climate Models. *Eos, Trans. Am. Geophys. Union* 95, 453–455. doi:10.1002/2014EO490002.
Piao, S., Liu, Z., Wang, Y., Ciais, P., Yao, Y., Peng, S., et al. (2017). On the causes of trends in the seasonal amplitude of atmospheric CO2. *Glob. Chang. Biol.* 24, 608–616. doi:doi:10.1111/gcb.13909.
Pierce, D. W., Gleckler, P. J., Barnett, T. P., Santer, B. D., and Durack, P. J. (2012). The fingerprint of human-induced changes in the ocean's salinity and temperature fields. *Geophys. Res. Lett.* 39, n/a-n/a. doi:10.1029/2012GL053389.
Planton, Y., Guilyardia, E., Wittenberg, A. T., Lee, J., Gleckler, P., Bayr, T., et al. (submitted). ENSO evaluation in climate models: The CLIVAR 2020 metrics package. *Bull. Am. Meteorol. Soc.* (submitted).
Polade, S. D., Gershunov, A., Cayan, D. R., Dettinger, M. D., and Pierce, D. W. (2013). Natural climate variability and teleconnections to precipitation over the Pacific-North American region in CMIP3 and CMIP5 models. *Geophys. Res. Lett.* 40, 2296–2301. doi:10.1002/grl.50491.
Polson, D., Bollasina, M., Hegerl, G. C., and Wilcox, L. J. (2014). Decreased monsoon precipitation in the northern hemisphere due to anthropogenic aerosols. *Geophys. Res. Lett.* 41, 6023–6029. doi:10.1002/2014GL060811.
Polson, D., and Hegerl, G. C. (2017). Strengthening contrast between precipitation in tropical wet and dry regions. *Geophys. Res. Lett.* 44, 365–373.
Polson, D., Hegerl, G. C., and Solomon, S. (2016). Precipitation sensitivity to warming estimated from long island records. *Environ. Res. Lett.* 11, 074024. doi:10.1088/1748-9326/11/7/074024.
Polvani, L. M., and Smith, K. L. (2013). Can natural variability explain observed Antarctic sea ice trends? New modeling evidence from CMIP5. *Geophys. Res. Lett.* 40, 3195–3199. doi:10.1002/grl.50578.
Poulsen, M. B., Jochum, M., and Nuterman, R. (2018). Parameterized and resolved Southern Ocean eddy compensation. *Ocean Model.* 124, 1–15. doi:https://doi.org/10.1016/j.ocemod.2018.01.008.
Power, S. B., and Delage, F. P. D. (2018). El Niño-Southern oscillation and associated climatic conditions around the world during the latter half of the twenty-first century. *J. Clim.* 31, 6189–6207. doi:10.1175/JCLI-D-18-0138.1.
Power, S., Casey, T., Folland, C., Colman, A., and Mehta, V. (1999). Inter-decadal modulation of the impact of ENSO on Australia. *Clim. Dyn.* 15, 319–324. doi:10.1007/s003820050284.

Priestley, M. D. K., Ackerley, D., Catto, J., Hodges, K. I., McDonald, R., and Lee, R. (submitted). An overview of the extratropical storm tracks in CMIP6. *J. Clim.* (submitted).
Purich, A., Cai, W., England, M. H., and Cowan, T. (2016). Evidence for link between modelled trends in Antarctic sea ice and underestimated westerly wind changes. *Nat. Commun.* 7, 10409. Available at: http://dx.doi.org/10.1038/ncomms10409.
Purich, A., and England, M. H. (2019). Tropical Teleconnections to Antarctic Sea Ice During Austral Spring 2016 in Coupled Pacemaker Experiments. *Geophys. Res. Lett.* 46, 6848–6858. doi:10.1029/2019GL082671.
Purkey, S. G., and Johnson, G. C. (2010). Warming of global abyssal and deep Southern Ocean waters between the 1990s and 2000s: Contributions to global heat and sea level rise budgets. *J. Clim.* 23, 6336–6351. doi:10.1175/2010JCLI3682.1.
Qasmi, S., Cassou, C., and Boé, J. (2017). Teleconnection Between Atlantic Multidecadal Variability and European Temperature: Diversity and Evaluation of the Coupled Model Intercomparison Project Phase 5 Models. *Geophys. Res. Lett.* doi:10.1002/2017GL074886.
Qian, C., and Zhang, X. (2015). Human Influences on Changes in the Temperature Seasonality in Mid- to High-Latitude Land Areas. *J. Clim.* 28, 5908–5921. doi:10.1175/JCLI-D-14-00821.1.
Qu, T., Gao, S., and Fukumori, I. (2011). What governs the North Atlantic salinity maximum in a global GCM? *Geophys. Res. Lett.* 38, n/a-n/a. doi:10.1029/2011GL046757.
Qu, T., Gao, S., and Fukumori, I. (2013). Formation of salinity maximum water and its contribution to the overturning circulation in the North Atlantic as revealed by a global general circulation model. *J. Geophys. Res. Ocean.* 118, 1982–1994. doi:10.1002/jgrc.20152.
Quan, X.-W., Hoerling, M. P., Perlwitz, J., and Diaz, H. F. (2018). On the Time of Emergence of Tropical Width Change. *J. Clim.* 31, 7225–7236. doi:10.1175/JCLI-D-18-0068.1.
Radić, V., and Hock, R. (2014). Glaciers in the Earth's Hydrological Cycle: Assessments of Glacier Mass and Runoff Changes on Global and Regional Scales. *Surv. Geophys.* 35, 813–837. doi:10.1007/s10712-013-9262-y.
Rahaman, H., Srinivasu, U., Panickal, S., Durgadoo, J. V., Griffies, S. M., Ravichandran, M., et al. (2020). An assessment of the Indian Ocean mean state and seasonal cycle in a suite of interannual CORE-II simulations. *Ocean Model.* 145. doi:10.1016/j.ocemod.2019.101503.
Rayner, N. A., Parker, D. E., Horton, E. B., Folland, C. K., Alexander, L. V, Rowell, D. P., et al. (2003). Global analyses of sea surface temperature, sea ice, and night marine air temperature since the late nineteenth century. *J. Geophys. Res. Atmos.* 108. doi:10.1029/2002JD002670.
Rea, G., Riccio, A., Fierli, F., Cairo, F., and Cagnazzo, C. (2018). Stratosphere-resolving CMIP5 models simulate different changes in the Southern Hemisphere. *Clim. Dyn.* 50, 2239–2255. doi:10.1007/s00382-017-3746-2.
Reintges, A., Martin, T., Latif, M., and Keenlyside, N. S. (2017). Uncertainty in twenty-first century projections of the Atlantic Meridional Overturning Circulation in CMIP3 and CMIP5 models. *Clim. Dyn.* 49, 1495–1511. doi:10.1007/s00382-016-3180-x.
Reul, N., Quilfen, Y., Chapron, B., Fournier, S., Kudryavtsev, V., and Sabia, R. (2014). Multisensor observations of the Amazon-Orinoco river plume interactions with hurricanes. *J. Geophys. Res. Ocean.* 119, 8271–8295. doi:10.1002/2014JC010107.
RGI Consortium (2017). Randolph Glacier Inventory 6.0. doi:10.7265/n5-rgi-60.
Rhein, M., Rintoul, S. R., Aoki, S., Campos, E., Chambers, D., Feely, R. A., et al. (2013). "Observations: Ocean," in *Climate Change 2013 the Physical Science Basis: Working Group I Contribution to the Fifth Assessment Report of the Intergovernmental Panel on Climate Change*, ed. Intergovernmental Panel on Climate Change (Cambridge: Cambridge University Press), 255–316. doi:10.1017/CBO9781107415324.010.
Ribes, A., Azaïs, J.-M., and Planton, S. (2009). Adaptation of the optimal fingerprint method for climate change detection using a well-conditioned covariance matrix estimate. *Clim. Dyn.* 33, 707–722. doi:10.1007/s00382-009-0561-4.
Ribes, A., Qasmi, S., and Gillett, N. P. (submitted). Kriging climate change to narrow uncertainty on past and future climate. *Nat. Clim. Chang.* (submitted).
Ribes, A., and Terray, L. (2013). Application of regularised optimal fingerprinting to attribution. Part II: Application to global near-surface temperature. *Clim. Dyn.* 41, 2837–2853. doi:10.1007/s00382-013-1736-6.
Ribes, A., Zwiers, F. W., Azaïs, J.-M., and Naveau, P. (2017). A new statistical approach to climate change detection and attribution. *Clim. Dyn.* 48, 367–386. doi:10.1007/s00382-016-3079-6.
Richardson, T., Forster, P., Andrews, T., Boucher, O., Faluvegi, G., Flaschner, D., et al. (2018). Drivers of precipitation change: an energetic understanding. *J. Clim.* doi:10.1175/JCLI-D-17-0240.1.
Richter, I. (2015). Climate model biases in the eastern tropical oceans: causes, impacts and ways forward. *Wiley Interdiscip. Rev. Clim. Chang.* 6, 345–358. doi:10.1002/wcc.338.
Richter, I., and Tokinaga, H. (submitted). An overview of the performance of CMIP6 models in the tropical Atlantic: mean state, variability, and remote impacts. *Clim. Dyn.* (submitted).
Richter, I., Xie, S. P., Behera, S. K., Doi, T., and Masumoto, Y. (2014). Equatorial Atlantic variability and its relation to mean state biases in CMIP5. *Clim. Dyn.* 42, 171–188. doi:10.1007/s00382-012-1624-5.
Ridley, D. A., Solomon, S., Barnes, J. E., Burlakov, V. D., Deshler, T., Dolgii, S. I., et al. (2014). Total volcanic

stratospheric aerosol optical depths and implications for global climate change. *Geophys. Res. Lett.* 41, 7763–7769. doi:10.1002/2014GL061541.

Righi, M., Andela, B., Eyring, V., Lauer, A., Predoi, V., Schlund, M., et al. (2019). ESMValTool v2.0 -- Technical overview. *Geosci. Model Dev. Discuss.* 2019, 1–28. doi:10.5194/gmd-2019-226.

Rignot, E., Mouginot, J., Scheuchl, B., van den Broeke, M. R., van Wessem, M. J., and Morlighem, M. (2019). Four decades of Antarctic Ice Sheet mass balance from 1979-2017. *Proc. Natl. Acad. Sci.* 116, 1–9. doi:10.1073/pnas.1812883116.

Rind, D., Orbe, C., Jonas, J., Nazarenko, L., Zhou, T., Kelley, M., et al. GISS Model E2.2: A Climate Model Optimized for the Middle Atmosphere. Part 1: Model Structure, Climatology, Variability and Climate Sensitivity. *J. Geophys. Res. Atmos.*

Ríos, A. F., Resplandy, L., García-Ibáñez, M. I., Fajar, N. M., Velo, A., Padin, X. A., et al. (2015). Decadal acidification in the water masses of the Atlantic Ocean. *Proc. Natl. Acad. Sci. U. S. A.* 112, 9950–5. doi:10.1073/pnas.1504613112.

Risbey, J. S., Lewandowsky, S., Cowtan, K., Oreskes, N., Rahmstorf, S., Jokimäki, A., et al. (2018). A fluctuation in surface temperature in historical context: reassessment and retrospective on the evidence. *Environ. Res. Lett.* 13, 123008. doi:10.1088/1748-9326/aaf342.

Risbey, J. S., Lewandowsky, S., Langlais, C., Monselesan, D. P., O'Kane, T. J., and Oreskes, N. (2014). Well-estimated global surface warming in climate projections selected for ENSO phase. *Nat. Clim. Chang.* 4, 835. Available at: http://dx.doi.org/10.1038/nclimate2310.

Riser, S. C., Freeland, H. J., Roemmich, D., Wijffels, S., Troisi, A., Belbéoch, M., et al. (2016). Fifteen years of ocean observations with the global Argo array. *Nat. Clim. Chang.* 6, 145–153. doi:10.1038/nclimate2872.

Ritter, R., Landschützer, P., Gruber, N., Fay, A. R., Iida, Y., Jones, S., et al. (2017). Observation-Based Trends of the Southern Ocean Carbon Sink. *Geophys. Res. Lett.* 44, 12,339-12,348. doi:10.1002/2017GL074837.

Roach, L. A., Dean, S. M., and Renwick, J. A. (2018). Consistent biases in Antarctic sea ice concentration simulated by climate models. *Cryosph.* 12, 365–383. doi:10.5194/tc-12-365-2018.

Roach, L. A., Dörr, J., Holmes, C. R., Massonnet, F., Blockley, E. W., Notz, D., et al. (submitted). Antarctic Sea Ice in CMIP6. *Geophys. Res. Lett.* (submitted).

Roberts, C. D., Jackson, L., and McNeall, D. (2014). Is the 2004–2012 reduction of the Atlantic meridional overturning circulation significant? *Geophys. Res. Lett.* 41, 3204–3210. doi:10.1002/2014GL059473.

Roberts, C. D., Palmer, M. D., McNeall, D., and Collins, M. (2015a). Quantifying the likelihood of a continued hiatus in global warming. *Nat. Clim. Chang.* 5, 337–342. doi:10.1038/nclimate2531.

Roberts, C. D., Senan, R., Molteni, F., Boussetta, S., Mayer, M., and Keeley, S. P. E. (2018). Climate model configurations of the ECMWF Integrated ForecastingSystem (ECMWF-IFS cycle 43r1) for HighResMIP. *Geosci. Model Dev.* 11, 3681–3712. doi:10.5194/gmd-11-3681-2018.

Roberts, M. J., Baker, A., Blockley, E. W., Calvert, D., Coward, A., Hewitt, H. T., et al. (2019a). Description of the resolution hierarchy of the global coupled HadGEM3-GC3.1 model as used in CMIP6 HighResMIP experiments. *Geosci. Model Dev. Discuss.* 12, 1–47. doi:10.5194/gmd-2019-148.

Roberts, M. J., Camp, J., Seddon, J., Vidale, P. L., Hodges, K., Vanniere, B., et al. (2019b). Impact of model resolution on tropical cyclone simulation using the HighResMIP-PRIMAVERA multi-model ensemble. *J. Clim.* accepted.

Roberts, M. J., Camp, J., Seddon, J., Vidale, P. L., Hodges, K., Vanniere, B., et al. (submitted, a). Projected Future Changes in Tropical Cyclones using the CMIP6 HighResMIP Multi-model Ensemble. *Geophys. Res. Lett.* (submitted).

Roberts, M. J., Jackson, L. C., Roberts, C. D., Meccia, V., Docquier, D., Koenigk, T., et al. (submitted, b). Sensitivity of the Atlantic Meridional Overturning Circulation to Model Resolution in CMIP6 HighResMIP Simulations and Implications for Future Changes. *J. Adv. Model. Earth Syst.* (submitted).

Roberts, M. J., Vidale, P. L., Mizielinski, M. S., Demory, M.-E., Schiemann, R., Strachan, J., et al. (2015b). Tropical Cyclones in the UPSCALE Ensemble of High-Resolution Global Climate Models*. *J. Clim.* 28, 574–596. doi:10.1175/JCLI-D-14-00131.1.

Robson, J., Sutton, R., Lohmann, K., Smith, D., and Palmer, M. D. (2012). Causes of the Rapid Warming of the North Atlantic Ocean in the Mid-1990s. *J. Clim.* 25, 4116–4134. doi:10.1175/JCLI-D-11-00443.1.

Rodríguez-Fonseca, B., Mohino, E., Mechoso, C. R., Caminade, C., Biasutti, M., Gaetani, M., et al. (2015). Variability and Predictability of West African Droughts: A Review on the Role of Sea Surface Temperature Anomalies. *J. Clim.* 28, 4034–4060. doi:10.1175/JCLI-D-14-00130.1.

Roe, G. H., Baker, M. B., and Herla, F. (2017). Centennial glacier retreat as categorical evidence of regional climate change. *Nat. Geosci.* 10, 95–99. doi:10.1038/ngeo2863.

Roemmich, D., Alford, M. H., Claustre, H., Johnson, K. S., King, B., Moum, J., et al. (2019). On the future of Argo: A global, full-depth, multi-disciplinary array. *Front. Mar. Sci.* 6. doi:10.3389/fmars.2019.00439.

Roemmich, D., Church, J., Gilson, J., Monselesan, D., Sutton, P., and Wijffels, S. (2015). Unabated planetary warming and its ocean structure since 2006. *Nat. Clim. Chang.* 5, 240–245. doi:10.1038/nclimate2513.

Roemmich, D., John Gould, W., and Gilson, J. (2012). 135 years of global ocean warming between the Challenger expedition and the Argo Programme. *Nat. Clim. Chang.* 2, 425–428. doi:10.1038/nclimate1461.

Rosenblum, E., and Eisenman, I. (2017). Sea Ice Trends in Climate Models Only Accurate in Runs with Biased Global Warming. *J. Clim.* 30, 6265–6278. doi:10.1175/JCLI-D-16-0455.1.

Rotstayn, L. D. (2013). Projected effects of declining anthropogenic aerosols on the southern annular mode. *Environ. Res. Lett.* 8, 044028. doi:10.1088/1748-9326/8/4/044028.

Rougier, J. (2016). Ensemble Averaging and Mean Squared Error. *J. Clim.* 29, 8865–8870. doi:10.1175/JCLI-D-16-0012.1.

Rupp, D. E., Mote, P. W., Bindoff, N. L., Stott, P. A., and Robinson, D. A. (2013). Detection and attribution of observed changes in northern hemisphere spring snow cover. *J. Clim.* doi:10.1175/JCLI-D-12-00563.1.

Ruprich-Robert, Y., and Cassou, C. (2015). Combined influences of seasonal East Atlantic Pattern and North Atlantic Oscillation to excite Atlantic multidecadal variability in a climate model. *Clim. Dyn.* 44, 229–253. doi:10.1007/s00382-014-2176-7.

Ruprich-Robert, Y., Msadek, R., Castruccio, F., Yeager, S., Delworth, T., and Danabasoglu, G. (2017). Assessing the climate impacts of the observed atlantic multidecadal variability using the GFDL CM2.1 and NCAR CESM1 global coupled models. *J. Clim.* 30, 2785–2810. doi:10.1175/JCLI-D-16-0127.1.

Russell, J. L., Kamenkovich, I., Bitz, C., Ferrari, R., Gille, S. T., Goodman, P. J., et al. (2018). Metrics for the Evaluation of the Southern Ocean in Coupled Climate Models and Earth System Models. *J. Geophys. Res. Ocean.* 123, 3120–3143. doi:10.1002/2017JC013461.

Saffioti, C., Fischer, E. M., Scherrer, S. C., and Knutti, R. (2016). Reconciling observed and modeled temperature and precipitation trends over Europe by adjusting for circulation variability. *Geophys. Res. Lett.* 43, 8189–8198. doi:10.1002/2016GL069802.

Saito, F., Abe-Ouchi, A., and Blatter, H. (2006). European Ice Sheet Modelling Initiative (EISMINT) model intercomparison experiments with first-order mechanics. *J. Geophys. Res. Earth Surf.* 111, F02012. doi:10.1029/2004JF000273.

Saji, N. H., Xie, S.-P., Yamagata, T., Saji, N. H., Xie, S.-P., and Yamagata, T. (2006). Tropical Indian Ocean Variability in the IPCC Twentieth-Century Climate Simulations*. *J. Clim.* 19, 4397–4417. doi:10.1175/JCLI3847.1.

Sallée, J.-B., Pellichero, V., Akhoudas, C., Pauthenet, E., Vignes, L., Schmidtko, S., et al. (submitted). Fifty-year changes of the world ocean's surface layer in response to climate change. *Nature* (submitted).

Sallée, J. B., Shuckburgh, E., Bruneau, N., Meijers, A. J. S., Bracegirdle, T. J., and Wang, Z. (2013a). Assessment of Southern Ocean mixed-layer depths in CMIP5 models: Historical bias and forcing response. *J. Geophys. Res. Ocean.* 118, 1845–1862. doi:10.1002/jgrc.20157.

Sallée, J. B., Shuckburgh, E., Bruneau, N., Meijers, A. J. S., Bracegirdle, T. J., Wang, Z., et al. (2013b). Assessment of Southern Ocean water mass circulation and characteristics in CMIP5 models: Historical bias and forcing response. *J. Geophys. Res. Ocean.* 118, 1830–1844. doi:10.1002/jgrc.20135.

Salzmann, M. (2016). Global warming without global mean precipitation increase? *Clim. Model.* doi:10.1126/sciadv.1501572.

Sandeep, S., Stordal, F., Sardeshmukh, P. D., and Compo, G. P. (2014). Pacific Walker Circulation variability in coupled and uncoupled climate models. *Clim. Dyn.* 43, 103–117. doi:10.1007/s00382-014-2135-3.

Santer, B. D., Bonfils, C., Painter, J. F., Zelinka, M. D., Mears, C., Solomon, S., et al. (2014). Volcanic contribution to decadal changes in tropospheric temperature. *Nat. Geosci.* 7, 185–189. doi:10.1038/ngeo2098.

Santer, B. D., Fyfe, J. C., Pallotta, G., Flato, G. M., Meehl, G. A., England, M. H., et al. (2017a). Causes of differences in model and satellite tropospheric warming rates. *Nat. Geosci.* 10, 478–485. doi:10.1038/ngeo2973.

Santer, B. D., Fyfe, J. C., Solomon, S., Painter, J. F., Bonfils, C., Pallotta, G., et al. (2019). Quantifying stochastic uncertainty in detection time of human-caused climate signals. *Proc. Natl. Acad. Sci.* 116, 19821–19827.

Santer, B. D., Painter, J. F., Bonfils, C., Mears, C. A., Solomon, S., Wigley, T. M. L., et al. (2013). Human and natural influences on the changing thermal structure of the atmosphere. *Proc. Natl. Acad. Sci. U. S. A.* 110, 17235–17240. doi:10.1073/pnas.1305332110.

Santer, B. D., Po-Chedley, S., Zelinka, M. D., Cvijanovic, I., Bonfils, C., Durack, P. J., et al. (2018). Human influence on the seasonal cycle of tropospheric temperature. *Science* 361. doi:10.1126/science.aas8806.

Santer, B. D., Solomon, S., Pallotta, G., Mears, C., Po-Chedley, S., Fu, Q., et al. (2017b). Comparing tropospheric warming in climate models and satellite data. *J. Clim.* 30, 373–392. doi:10.1175/JCLI-D-16-0333.1.

Santer, B. D., Solomon, S., Wentz, F. J., Fu, Q., Po-Chedley, S., Mears, C., et al. (2017c). Tropospheric Warming over the Past Two Decades. *Sci. Rep.* 7. doi:10.1038/s41598-017-02520-7.

Scaife, A. A., Ineson, S., Knight, J. R., Gray, L., Kodera, K., and Smith, D. M. (2013). A mechanism for lagged North Atlantic climate response to solar variability. *Geophys. Res. Lett.* 40, 434–439. doi:10.1002/grl.50099.

Scaife, A. A., Karpechko, A. Y., Baldwin, M. P., Brookshaw, A., Butler, A. H., Eade, R., et al. (2016). Seasonal winter forecasts and the stratosphere. *Atmos. Sci. Lett.* 17, 51–56. doi:10.1002/asl.598.

Scaife, A. A., and Smith, D. (2018). A signal-to-noise paradox in climate science. *npj Clim. Atmos. Sci.* 1, 28. doi:10.1038/s41612-018-0038-4.

Scheff, J., Seager, R., Liu, H., and Coats, S. (2017). Are glacials dry? Consequences for paleoclimatology and for greenhouse warming. *J. Clim.* 30, 6593–6609. doi:10.1175/JCLI-D-16-0854.1.

Schenzinger, V., and Osprey, S. M. (2015). Interpreting the nature of Northern and Southern Annular Mode variability in CMIP5 Models. *J. Geophys. Res. Atmos.* 120, 11203–11214. doi:10.1002/2014JD022989.
Schiemann, R., Athanasiadis, P., Barriopedro, D., Doblas-Reyes, F., Lohmann, K., Roberts, M. J., et al. (submitted). The representation of Northern Hemisphere blocking in current global climate models. (submitted).
Schiemann, R., Demory, M.-E., Shaffrey, L. C., Strachan, J., Vidale, P. L., Mizielinski, M. S., et al. (2017). The Resolution Sensitivity of Northern Hemisphere Blocking in Four 25-km Atmospheric Global Circulation Models. *J. Clim.* 30, 337–358. doi:10.1175/JCLI-D-16-0100.1.
Schiemann, R., Vidale, P. L., Shaffrey, L. C., Johnson, S. J., Roberts, M. J., Demory, M.-E., et al. (2018). Mean and extreme precipitation over European river basins better simulated in a 25km AGCM. *Hydrol. Earth Syst. Sci.* 22, 3933–3950.
Schimanke, S., Spangehl, T., Huebener, H., and Cubasch, U. (2013). Variability and trends of major stratospheric warmings in simulations under constant and increasing GHG concentrations. *Clim. Dyn.* 40, 1733–1747.
Schlosser, E., Haumann, F. A., and Raphael, M. N. (2018). Atmospheric influences on the anomalous 2016 Antarctic sea ice decay. *Cryosph.* 12, 1103–1119. doi:10.5194/tc-12-1103-2018.
Schmidt, G. A., Shindell, D. T., and Tsigaridis, K. (2014). Reconciling warming trends. *Nat. Geosci.* 7, 158.
Schmidtko, S., Stramma, L., and Visbeck, M. (2017). Decline in global oceanic oxygen content during the past five decades. *Nature* 542, 335–339. doi:10.1038/nature21399.
Schmith, T., Yang, S., Gleeson, E., and Semmler, T. (2014). How Much Have Variations in the Meridional Overturning Circulation Contributed to Sea Surface Temperature Trends since 1850? A Study with the EC-Earth Global Climate Model. *J. Clim.* 27, 6343–6357. doi:10.1175/JCLI-D-13-00651.1.
Schneider, D. P., and Deser, C. (2018). Tropically driven and externally forced patterns of Antarctic sea ice change: reconciling observed and modeled trends. *Clim. Dyn.* 50, 4599–4618. doi:10.1007/s00382-017-3893-5.
Schneider, D. P., Deser, C., and Fan, T. (2015). Comparing the Impacts of Tropical SST Variability and Polar Stratospheric Ozone Loss on the Southern Ocean Westerly Winds. *J. Clim.* 28, 9350–9372. doi:10.1175/JCLI-D-15-0090.1.
Schott, F. A., Xie, S.-P., and McCreary, J. P. (2009). Indian Ocean circulation and climate variability. *Rev. Geophys.* 47, RG1002. doi:10.1029/2007RG000245.
Schurer, A., Hegerl, G., Ribes, A., Polson, D., Morice, C., and Tett, S. (2018). Estimating the Transient Climate Response from Observed Warming. *J. Clim.* 31, 8645–8663. doi:10.1175/JCLI-D-17-0717.1.
Schurer, A. P., Hegerl, G. C., Ballinger, A., and Friedman, A. R. (submitted). Human influence strengthens the contrast between tropical wet and dry regions. *Environ. Res. Lett.* (submitted).
Schurer, A. P., Hegerl, G. C., Mann, M. E., Tett, S. F. B., and Phipps, S. J. (2013). Separating Forced from Chaotic Climate Variability over the Past Millennium. *J. Clim.* 26, 6954–6973. doi:10.1175/JCLI-D-12-00826.1.
Schurer, A. P., Hegerl, G. C., and Obrochta, S. P. (2015). Determining the likelihood of pauses and surges in global warming. *Geophys. Res. Lett.* 42, 5974–5982. doi:10.1002/2015GL064458.
Schurer, A. P., Tett, S. F. B., and Hegerl, G. C. (2014). Small influence of solar variability on climate over the past millennium. *Nat. Geosci.* 7, 104–108. doi:10.1038/ngeo2040.
Scoccimarro, E., Fogli, P. G., Reed, K. A., Gualdi, S., Masina, S., and Navarra, A. (2017). Tropical cyclone interaction with the ocean: The role of high-frequency (subdaily) coupled processes. *J. Clim.* 30, 145–162.
Screen, J. A. (2014). Arctic amplification decreases temperature variance in northern mid- to high-latitudes. *Nat. Clim. Chang.* 4, 577–582. doi:10.1038/nclimate2268.
Screen, J. A., Deser, C., Simmonds, I., and Tomas, R. (2014). Atmospheric impacts of Arctic sea-ice loss, 1979--2009: separating forced change from atmospheric internal variability. *Clim. Dyn.* 43, 333–344. doi:10.1007/s00382-013-1830-9.
Screen, J. A., Deser, C., Smith, D. M., Zhang, X., Blackport, R., Kushner, P. J., et al. (2018). Consistency and discrepancy in the atmospheric response to Arctic sea-ice loss across climate models. *Nat. Geosci.* 11, 155–163. doi:10.1038/s41561-018-0059-y.
Screen, J. A., Simmonds, I., Deser, C., and Tomas, R. (2013). The Atmospheric Response to Three Decades of Observed Arctic Sea Ice Loss. *J. Clim.* 26, 1230–1248. doi:10.1175/JCLI-D-12-00063.1.
Scussolini, P., Bakker, P., Guo, C., Stepanek, C., Zhang, Q., Braconnot, P., et al. (2019). Agreement between reconstructed and modeled boreal precipitation of the Last Interglacial. *Sci. Adv.* 5. doi:10.1126/sciadv.aax7047.
Seager, R., Cane, M., Henderson, N., Lee, D.-E., Abernathey, R., and Zhang, H. (2019). Strengthening tropical Pacific zonal sea surface temperature gradient consistent with rising greenhouse gases. *Nat. Clim. Chang.* 9, 517–522. doi:10.1038/s41558-019-0505-x.
Seager, R., Liu, H., Henderson, N., Simpson, I., Kelley, C., Shaw, T., et al. (2014a). Causes of increasing aridification of the mediterranean region in response to rising greenhouse gases. *J. Clim.* doi:10.1175/JCLI-D-13-00446.1.
Seager, R., Neelin, D., Simpson, I., Liu, H., Henderson, N., Shaw, T., et al. (2014b). Dynamical and Thermodynamical Causes of Large-Scale Changes in the Hydrological Cycle over North America in Response to Global Warming*. *J. Clim.* 27, 7921–7948. doi:10.1175/JCLI-D-14-00153.1.
Séférian, R., Berthet, S., Yool, A., Palmiéri, J., Bopp, L., Tagliabue, A., et al. (submitted). Tracking improvement in simulated marine biogeochemistry between CMIP5 and CMIP6. (submitted).

Séférian, R., Delire, C., Decharme, B., Voldoire, A., David Salas, Y. M., Chevallier, M., et al. (2016). Development and evaluation of CNRM Earth system model-CNRM-ESM1. *Geosci. Model Dev.* 9, 1423–1453. doi:10.5194/gmd-9-1423-2016.

Séférian, R., Nabat, P., Michou, M., Saint-Martin, D., Voldoire, A., Colin, J., et al. (2019). Evaluation of CNRM Earth System Model, CNRM-ESM2-1: Role of Earth System Processes in Present-Day and Future Climate. *J. Adv. Model. Earth Syst.* n/a. doi:10.1029/2019MS001791.

Sellar, A. A., Jones, C. G., Mulcahy, J., Tang, Y., Yool, A., Wiltshire, A., et al. (2019). UKESM1: Description and evaluation of the UK Earth System Model. *J. Adv. Model. Earth Syst.*

Semenov, V. A., and Latif, M. (2015). Nonlinear winter atmospheric circulation response to Arctic sea ice concentration anomalies fordifferent periods during 1966–2012. *Environ. Res. Lett.* 10, 054020. Available at: http://stacks.iop.org/1748-9326/10/i=5/a=054020.

Seneviratne, S. I., Donat, M. G., Mueller, B., and Alexander, L. V. (2014). No pause in the increase of hot temperature extremes. *Nat. Clim. Chang.* 4, 161–163. doi:10.1038/nclimate2145.

Senftleben, D., Lauer, A., and Karpechko, A. (2019). Constraining uncertainties in CMIP5 projections of September Arctic sea ice extent with observations. *J. Clim.*

Senior, C. A., Andrews, T., Burton, C., Chadwick, R., Copsey, D., Graham, T., et al. (2016). Idealized climate change simulations with a high-resolution physical model: HadGEM3-GC2. *J. Adv. Model. Earth Syst.* 8, 813–830. doi:10.1002/2015MS000614.

Seth, A., Giannini, A., Rojas, M., Rauscher, S. A., Bordoni, S., Singh, D., et al. (2019). Monsoon Responses to Climate Changes—Connecting Past, Present and Future. *Curr. Clim. Chang. Reports* 5, 63–79. doi:10.1007/s40641-019-00125-y.

Sévellec, F., and Drijfhout, S. S. (2018). A novel probabilistic forecast system predicting anomalously warm 2018-2022 reinforcing the long-term global warming trend. *Nat. Commun.* 9, 3024. doi:10.1038/s41467-018-05442-8.

Seviour, W. J. M., Gray, L. J., and Mitchell, D. M. (2016). Stratospheric polar vortex splits and displacements in the high-top CMIP5 climate models. *J. Geophys. Res. Atmos.* 121, 1400–1413. doi:10.1002/2015JD024178.

Shannon, S., Smith, R., Wiltshire, A., Payne, T., Huss, M., Betts, R., et al. (2019a). Global glacier volume projections under high-end climate change scenarios. *Cryosph.* 13, 325–350. doi:10.5194/tc-13-325-2019.

Shannon, S., Smith, R., Wiltshire, A., Payne, T., Huss, M., Betts, R., et al. (2019b). Global glacier volume projections under high-end climate change scenarios. *Cryosph.* 13, 325–350. doi:10.5194/tc-13-325-2019.

Sheffield, J., Barrett, A. P., Colle, B., Nelun Fernando, D., Fu, R., Geil, K. L., et al. (2013). North American Climate in CMIP5 Experiments. Part I: Evaluation of Historical Simulations of Continental and Regional Climatology. *J. Clim.* 26, 9209–9245. doi:10.1175/JCLI-D-12-00592.1.

Shepherd, A., Ivins, E. R., Geruo, A., Barletta, V. R., Bentley, M. J., Bettadpur, S., et al. (2012). A reconciled estimate of ice-sheet mass balance. *Science* 338, 1183–1189. doi:10.1126/science.1228102.

Shepherd, A., Ivins, E., Rignot, E., Smith, B., van den Broeke, M., Velicogna, I., et al. (2019a). Mass balance of the Greenland Ice Sheet from 1992 to 2018. *Nature*. doi:10.1038/s41586-019-1855-2.

Shepherd, A., Ivins, E., Rignot, E., Smith, B., van den Broeke, M., Velicogna, I., et al. (2019b). Mass balance of the Greenland Ice Sheet from 1992 to 2018. *Nature*. doi:10.1038/s41586-019-1855-2.

Shepherd, A., Ivins, E., Rignot, E., Smith, B., Van Den Broeke, M., Velicogna, I., et al. (2018). Mass balance of the Antarctic Ice Sheet from 1992 to 2017. *Nature* 558, 219–222. doi:10.1038/s41586-018-0179-y.

Shepherd, T. G. (2014). Atmospheric circulation as a source of uncertainty in climate change projections. *Nat. Geosci.* 7, 703–708. doi:10.1038/NGEO2253.

Sherwood, S. C., and Nishant, N. (2015). Atmospheric changes through 2012 as shown by iteratively homogenized radiosonde temperature and wind data (IUKv2). *Environ. Res. Lett.* 10. doi:10.1088/1748-9326/10/5/054007.

Shi, L., Alves, O., Wedd, R., Balmaseda, M. A., Chang, Y., Chepurin, G., et al. (2017). An assessment of upper ocean salinity content from the Ocean Reanalyses Inter-comparison Project (ORA-IP). *Clim. Dyn.* 49, 1009–1029. doi:10.1007/s00382-015-2868-7.

Shikha, S., and Valsala, V. (2018). Subsurface ocean biases in climate models and its implications in the simulated interannual variability: A case study for Indian Ocean. *Dyn. Atmos. Ocean.* 84, 55–74. doi:10.1016/J.DYNATMOCE.2018.10.001.

Si, D., and Hu, A. (2017). Internally Generated and Externally Forced Multidecadal Oceanic Modes and Their Influence on the Summer Rainfall over East Asia. *J. Clim.* 30, 8299–8316. doi:10.1175/JCLI-D-17-0065.1.

Sidorenko, D., Goessling, H. F., Koldunov, N. V, Scholz, P., Danilov, S., Barbi, D., et al. Evaluation of FESOM2.0 coupled to ECHAM6.3: Pre-industrial and HighResMIP simulations. *J. Adv. Model. Earth Syst.* n/a. doi:10.1029/2019MS001696.

Sigmond, M., Scinocca, J. F., and Kushner, P. J. (2008). Impact of the stratosphere on tropospheric climate change. *Geophys. Res. Lett.* 35. doi:10.1029/2008GL033573.

Simmons, A. J., Berrisford, P., Dee, D. P., Hersbach, H., Hirahara, S., and Thépaut, J.-N. (2017). A reassessment of temperature variations and trends from global reanalyses and monthly surface climatological datasets. *Q. J. R. Meteorol. Soc.* 143, 101–119. doi:10.1002/qj.2949.

Simpson, I. R., Deser, C., McKinnon, K. A., and Barnes, E. A. (2018). Modeled and Observed Multidecadal Variability

in the North Atlantic Jet Stream and Its Connection to Sea Surface Temperatures. *J. Clim.* 31, 8313–8338. doi:10.1175/JCLI-D-18-0168.1.

Simpson, I. R., Shepherd, T. G., Hitchcock, P., and Scinocca, J. F. (2013). Southern Annular Mode Dynamics in Observations and Models. Part II: Eddy Feedbacks. *J. Clim.* 26, 5220–5241. doi:10.1175/JCLI-D-12-00495.1.

Singh, H. A., Polvani, L. M., and Rasch, P. J. (2019). Antarctic Sea Ice Expansion, Driven by Internal Variability, in the Presence of Increasing Atmospheric CO2. *Geophys. Res. Lett.* 46. doi:10.1029/2019GL083758.

Sinha, B., Smeed, D. A., McCarthy, G., Moat, B. I., Josey, S. A., Hirschi, J. J.-M., et al. (2018). The accuracy of estimates of the overturning circulation from basin-wide mooring arrays. *Prog. Oceanogr.* 160, 101–123. doi:https://doi.org/10.1016/j.pocean.2017.12.001.

Sippel, S., Meinshausen, N., Fischer, E. M., Székely, E., and Knutti, R. (2020). Climate change now detectable from any single day of weather at global scale. *Nat. Clim. Chang.* 10, 35–41. doi:10.1038/s41558-019-0666-7.

Sippel, S., Meinshausen, N., Merrifield, A., Lehner, F., Pendergrass, A. G., Fischer, E., et al. (2019). Uncovering the Forced Climate Response from a Single Ensemble Member Using Statistical Learning. *J. Clim.* 32, 5677–5699. doi:10.1175/JCLI-D-18-0882.1.

Sitch, S., Friedlingstein, P., Gruber, N., Jones, S. D., Murray-Tortarolo, G., Ahlström, A., et al. (2015). Recent trends and drivers of regional sources and sinks of carbon dioxide. *Biogeosciences*. doi:10.5194/bg-12-653-2015.

Skliris, N., Marsh, R., Josey, S. A., Good, S. A., Liu, C., and Allan, R. P. (2014). Salinity changes in the World Ocean since 1950 in relation to changing surface freshwater fluxes. *Clim. Dyn.* 43, 709–736. doi:10.1007/s00382-014-2131-7.

Skliris, N., Zika, J. D., Nurser, G., Josey, S. A., and Marsh, R. (2016). Global water cycle amplifying at less than the Clausius-Clapeyron rate. *Sci. Rep.* 6, 38752. doi:10.1038/srep38752.

Slangen, A. B. A., Church, J. A., Agosta, C., Fettweis, X., Marzeion, B., and Richter, K. (2016). Anthropogenic forcing dominates global mean sea-level rise since 1970. *Nat. Clim. Chang.* 6, 701–705. doi:10.1038/nclimate2991.

Slangen, A. B. A., Church, J. A., Zhang, X., and Monselesan, D. (2014). Detection and attribution of global mean thermosteric sea level change. *Geophys. Res. Lett.* 41, 5951–5959. doi:10.1002/2014GL061356.

Slangen, A. B. A., Church, J. A., Zhang, X., and Monselesan, D. P. (2015). The sea level response to external forcings in historical simulations of CMIP5 climate models. *J. Clim.* 28, 8521–8539. doi:10.1175/JCLI-D-15-0376.1.

Slangen, A. B. A., Meyssignac, B., Agosta, C., Champollion, N., Church, J. A., Fettweis, X., et al. (2017). Evaluating Model Simulations of Twentieth-Century Sea Level Rise. Part I: Global Mean Sea Level Change. *J. Clim.* 30, 8539–8563. doi:10.1175/JCLI-D-17-0110.1.

Small, R. J., Bacmeister, J., Bailey, D., Baker, A., Bishop, S., Bryan, F., et al. (2014). A new synoptic scale resolving global climate simulation using the Community Earth System Model. *J. Adv. Model. Earth Syst.* 6, 1065–1094. doi:10.1002/2014MS000363.

Small, R. J., Curchitser, E., Hedstrom, K., Kauffman, B., and Large, W. G. (2015). The Benguela Upwelling System: Quantifying the Sensitivity to Resolution and Coastal Wind Representation in a Global Climate Model*. *J. Clim.* 28, 9409–9432. doi:10.1175/JCLI-D-15-0192.1.

Smeed, D. A., Josey, S. A., Beaulieu, C., Johns, W. E., Moat, B. I., Frajka-Williams, E., et al. (2018). The North Atlantic Ocean Is in a State of Reduced Overturning. *Geophys. Res. Lett.* 45, 1527–1533. doi:10.1002/2017GL076350.

Smeed, D. A., McCarthy, G. D., Cunningham, S. A., Frajka-Williams, E., Rayner, D., Johns, W. E., et al. (2014). Observed decline of the Atlantic meridional overturning circulation 2004–2012. *Ocean Sci.* 10, 29–38. doi:10.5194/os-10-29-2014.

Smith, D. M., Booth, B. B. B., Dunstone, N. J., Eade, R., Hermanson, L., Jones, G. S., et al. (2016). Role of volcanic and anthropogenic aerosols in the recent global surface warming slowdown. *Nat. Clim. Chang.* 6, 936–940. doi:10.1038/nclimate3058.

Smith, D. M., Dunstone, N. J., Scaife, A. A., Fiedler, E. K., Copsey, D., and Hardiman, S. C. (2017). Atmospheric Response to Arctic and Antarctic Sea Ice: The Importance of Ocean–Atmosphere Coupling and the Background State. *J. Clim.* 30, 4547–4565. doi:10.1175/JCLI-D-16-0564.1.

Solman, S., and Orlanski, I. (2016). Climate change over the extratropical southern hemisphere: the tale from an ensemble of reanalysis datasets. *J. Clim.* doi:10.1175/JCLI-D-15-0588.1.

Solomon, A., and Polvani, L. M. (2016). Highly Significant Responses to Anthropogenic Forcings of the Midlatitude Jet in the Southern Hemisphere. *J. Clim.* 29, 3463–3470. doi:10.1175/JCLI-D-16-0034.1.

Solomon, S., Rosenlof, K. H., Portmann, R. W., Daniel, J. S., Davis, S. M., Sanford, T. J., et al. (2010). Contributions of Stratospheric Water Vapor to Decadal Changes in the Rate of Global Warming. *Science* 327, 1219–1223. doi:10.1126/science.1182488.

Son, S.-W., Han, B.-R., Garfinkel, C. I., Kim, S.-Y., Park, R., Abraham, N. L., et al. (2018). Tropospheric jet response to Antarctic ozone depletion: An update with Chemistry-Climate Model Initiative (CCMI) models. *Environ. Res. Lett.* 13. doi:10.1088/1748-9326/aabf21.

Song, M., Wei, L., and Wang, Z. (2016). Quantifying the contribution of natural variability to September Arctic sea ice decline. *Acta Oceanol. Sin.* 35, 49–53. doi:10.1007/s13131-016-0854-5.

Song, Y. T., Lee, T., Moon, J. H., Qu, T., and Yueh, S. (2015). Modeling skin-layer salinity with an extended surface-

salinity layer. *J. Geophys. Res. Ocean.* 120, 1079–1095. doi:10.1002/2014JC010346.
Srivastava, A. K., and DelSole, T. (2014). Robust Forced Response in South Asian Summer Monsoon in a Future Climate. *J. Clim.* 27, 7849–7860. doi:10.1175/JCLI-D-13-00599.1.
Staten, P. W., Lu, J., Grise, K. M., Davis, S. M., and Birner, T. (2018). Re-examining tropical expansion. *Nat. Clim. Chang.* 8, 768–775. doi:10.1038/s41558-018-0246-2.
Steinig, S., Harlaß, J., Park, W., and Latif, M. (2018). Sahel rainfall strength and onset improvements due to more realistic Atlantic cold tongue development in a climate model. *Sci. Rep.* 8, 2569. doi:10.1038/s41598-018-20904-1.
Steinman, B. A., Mann, M. E., and Miller, S. K. (2015). Atlantic and Pacific multidecadal oscillations and Northern Hemisphere temperatures. *Science* 347, 988–991. doi:10.1126/science.1257856.
Stendardo, I., and Gruber, N. (2012). Oxygen trends over five decades in the North Atlantic. *J. Geophys. Res. Ocean.* 117, n/a-n/a. doi:10.1029/2012JC007909.
Steptoe, H., Wilcox, L. J., and Highwood, E. J. (2016). Is there a robust effect of anthropogenic aerosols on the Southern Annular Mode? *J. Geophys. Res. Atmos.* 121, 10,029-10,042. doi:10.1002/2015JD024218.
Stevenson, S., Capotondi, A., Fasullo, J., and Otto-Bliesner, B. (2017). Forced changes to twentieth century ENSO diversity in a last Millennium context. *Clim. Dyn.* doi:10.1007/s00382-017-3573-5.
Stevenson, S. L. (2012). Significant changes to ENSO strength and impacts in the twenty-first century: Results from CMIP5. *Geophys. Res. Lett.* 39, 1–5. doi:10.1029/2012GL052759.
Stone, D. A., and Hansen, G. (2016). Rapid systematic assessment of the detection and attribution of regional anthropogenic climate change. *Clim. Dyn.* 47, 1399–1415. doi:10.1007/s00382-015-2909-2.
Stone, E. J., Capron, E., Lunt, D. J., Payne, A. J., Singarayer, J. S., Valdes, P. J., et al. (2016). Impact of meltwater on high-latitude early Last Interglacial climate. *Clim. Past* 12, 1919–1932. doi:10.5194/cp-12-1919-2016.
Storto, A., and Masina, S. (2017). Objectively estimating the temporal evolution of accuracy and skill in a global ocean reanalysis. *Meteorol. Appl.* 24, 101–113. doi:10.1002/met.1609.
Stott, P. A., Sutton, R. T., and Smith, D. M. (2008). Detection and attribution of Atlantic salinity changes. *Geophys. Res. Lett.* 35, L21702. doi:10.1029/2008GL035874.
Stramma, L., Oschlies, A., and Schmidtko, S. (2012). Mismatch between observed and modeled trends in dissolved upper-ocean oxygen over the last 50 yr. *Biogeosciences* 9, 4045–4057. doi:10.5194/bg-9-4045-2012.
Stroeve, J. C., Kattsov, V., Barrett, A., Serreze, M., Pavlova, T., Holland, M., et al. (2012). Trends in Arctic sea ice extent from CMIP5, CMIP3 and observations. *Geophys. Res. Lett.* 39. doi:10.1029/2012GL052676.
Stroeve, J., and Notz, D. (2015). Insights on past and future sea-ice evolution from combining observations and models. *Glob. Planet. Change* 135, 119–132.
Strommen, K., and Palmer, T. N. (2019). Signal and noise in regime systems: A hypothesis on the predictability of the North Atlantic Oscillation. *Q. J. R. Meteorol. Soc.* 145, 147–163. doi:10.1002/qj.3414.
Stuecker, M. F., Bitz, C. M., and Armour, K. C. (2017). Conditions leading to the unprecedented low Antarctic sea ice extent during the 2016 austral spring season. *Geophys. Res. Lett.* 44, 9008–9019. doi:10.1002/2017GL074691.
Su, H., Wu, X., Lu, W., Zhang, W., and Yan, X. H. (2017a). Inconsistent Subsurface and Deeper Ocean Warming Signals During Recent Global Warming and Hiatus. *J. Geophys. Res. Ocean.* 122, 8182–8195. doi:10.1002/2016JC012481.
Su, J., Zhang, R., and Wang, H. (2017b). Consecutive record-breaking high temperatures marked the handover from hiatus to accelerated warming. *Sci. Rep.* 7, 43735. Available at: http://dx.doi.org/10.1038/srep43735.
Suárez-Gutiérrez, L., Li, C., Thorne, P. W., and Marotzke, J. (2017). Internal variability in simulated and observed tropical tropospheric temperature trends. *Geophys. Res. Lett.* 44, 5709–5719. doi:10.1002/2017GL073798.
Sun, C., Li, J., Kucharski, F., Xue, J., and Li, X. (2019). Contrasting spatial structures of Atlantic Multidecadal Oscillation between observations and slab ocean model simulations. *Clim. Dyn.* 52, 1395–1411. doi:10.1007/s00382-018-4201-8.
Sun, L., Perlwitz, J., and Hoerling, M. (2016a). What caused the recent “Warm Arctic, Cold Continents” trend pattern in winter temperatures? *Geophys. Res. Lett.* 43, 5345–5352. doi:10.1002/2016GL069024.
Sun, Y., Zhou, T., Ramstein, G., Contoux, C., and Zhang, Z. (2016b). Drivers and mechanisms for enhanced summer monsoon precipitation over East Asia during the mid-Pliocene in the IPSL-CM5A. *Clim. Dyn.* 46, 1437–1457. doi:10.1007/s00382-015-2656-4.
Swart, N. C., Cole, J. N. S., Kharin, V. V., Lazare, M., Scinocca, J. F., Gillett, N. P., et al. (2019). The Canadian Earth System Model version 5 (CanESM5.0.3). *Geosci. Model Dev. Discuss.* doi:10.5194/gmd-2019-177.
Swart, N. C., Fyfe, J. C., Hawkins, E., Kay, J. E., and Jahn, A. (2015). Influence of internal variability on Arctic sea-ice trends. *Nat. Clim. Chang.* 5, 86.
Swart, N. C., Gille, S. T., Fyfe, J. C., and Gillett, N. P. (2018). Recent Southern Ocean warming and freshening driven by greenhouse gas emissions and ozone depletion. *Nat. Geosci.*, 1. doi:10.1038/s41561-018-0226-1.
Swingedouw, D., Mignot, J., Ortega, P., Khodri, M., Menegoz, M., Cassou, C., et al. (2017). Impact of explosive volcanic eruptions on the main climate variability modes. *Glob. Planet. Change* 150, 24–45. doi:https://doi.org/10.1016/j.gloplacha.2017.01.006.
Takahashi, C., and Watanabe, M. (2016). Pacific trade winds accelerated by aerosol forcing over the past two decades.

Nat. Clim. Chang. 6, 768–772. doi:10.1038/nclimate2996.
Takahashi, H., Su, H., and Jiang, J. H. (2016). Error analysis of upper tropospheric water vapor in CMIP5 models using "A-Train" satellite observations and reanalysis data. *Clim. Dyn.* 46, 2787–2803.
Tandon, N. F., and Kushner, P. J. (2015). Does External Forcing Interfere with the AMOC's Influence on North Atlantic Sea Surface Temperature? *J. Clim.* 28, 6309–6323. doi:10.1175/JCLI-D-14-00664.1.
Tang, W., Fore, A., Yueh, S., Lee, T., Hayashi, A., Sanchez-Franks, A., et al. (2017). Validating SMAP SSS with in situ measurements. in *International Geoscience and Remote Sensing Symposium (IGARSS)* (Elsevier), 2561–2564. doi:10.1109/IGARSS.2017.8127518.
Tao, L., Hu, Y., and Liu, J. (2016a). Anthropogenic forcing on the Hadley circulation in CMIP5 simulations. *Clim. Dyn.* 46, 3337–3350. doi:10.1007/s00382-015-2772-1.
Tao, W., Huang, G., Hu, K., Gong, H., Wen, G., and Liu, L. (2016b). A study of biases in simulation of the Indian Ocean basin mode and its capacitor effect in CMIP3/CMIP5 models. *Clim. Dyn.* 46, 205–226. doi:10.1007/s00382-015-2579-0.
Tao, W., Huang, G., Hu, K., Qu, X., Wen, G., and Gong, H. (2015). Interdecadal modulation of ENSO teleconnections to the Indian Ocean Basin Mode and their relationship under global warming in CMIP5 models. *Int. J. Climatol.* 35, 391–407. doi:10.1002/joc.3987.
Taschetto, A. S., Gupta, A. Sen, Jourdain, N. C., Santoso, A., Ummenhofer, C. C., and England, M. H. (2014). Cold tongue and warm pool ENSO Events in CMIP5: Mean state and future projections. *J. Clim.* 27, 2861–2885. doi:10.1175/JCLI-D-13-00437.1.
Taylor, K. E., Stouffer, R. J., and Meehl, G. A. (2012). An overview of CMIP5 and the experiment design. *Bull. Am. Meteorol. Soc.* 93, 485–498. doi:10.1175/BAMS-D-11-00094.1.
Terray, L. (2012). Evidence for multiple drivers of North Atlantic multi-decadal climate variability. *Geophys. Res. Lett.* 39, n/a-n/a. doi:10.1029/2012GL053046.
Terray, L., Corre, L., Cravatte, S., Delcroix, T., Reverdin, G., and Ribes, A. (2012). Near-surface salinity as nature's rain gauge to detect human influence on the Tropical water cycle. *J. Clim.* 25, 958–977. doi:10.1175/JCLI-D-10-05025.1.
Thackeray, C. W., DeAngelis, A. M., Hall, A., Swain, D. L., and Qu, X. (2018). On the Connection Between Global Hydrologic Sensitivity and Regional Wet Extremes. *Geophys. Res. Lett.* 45, 11,343-11,351. doi:10.1029/2018GL079698.
Thackeray, C. W., Fletcher, C. G., and Derksen, C. (2015). Quantifying the skill of CMIP5 models in simulating seasonal albedo and snow cover evolution. *J. Geophys. Res.* 120, 5831–5849. doi:10.1002/2015JD023325.
Thackeray, C. W., Fletcher, C. G., Mudryk, L. R., and Derksen, C. (2016). Quantifying the Uncertainty in Historical and Future Simulations of Northern Hemisphere Spring Snow Cover. *J. Clim.* 29, 8647–8663. doi:10.1175/JCLI-D-16-0341.1.
Thoma, M., Greatbatch, R. J., Kadow, C., and Gerdes, R. (2015). Decadal hindcasts initialized using observed surface wind stress: Evaluation and prediction out to 2024. *Geophys. Res. Lett.* 42, 6454–6461. doi:10.1002/2015GL064833.
Thomas, J. L., Waugh, D. W., and Gnanadesikan, A. (2015a). Southern Hemisphere extratropical circulation: Recent trends and natural variability. *Geophys. Res. Lett.* 42, 5508–5515. doi:10.1002/2015GL064521.
Thomas, R. Q., Brookshire, E. N. J., and Gerber, S. (2015b). Nitrogen limitation on land: how can it occur in Earth system models? *Glob. Chang. Biol.* 21, 1777–1793. doi:10.1111/gcb.12813.
Thompson, D. M., Cole, J. E., Shen, G. T., Tudhope, A. W., and Meehl, G. A. (2014). Early twentieth-century warming linked to tropical Pacific wind strength. *Nat. Geosci.* 8, 117.
Thornalley, D. J. R., Oppo, D. W., Ortega, P., Robson, J. I., Brierley, C. M., Davis, R., et al. (2018). Anomalously weak Labrador Sea convection and Atlantic overturning during the past 150 years. *Nature* 556, 227–230. doi:10.1038/s41586-018-0007-4.
Thorne, P., Outten, S., Bethke, I., and Seland, Ø. (2015). Investigating the recent apparent hiatus in surface temperature increases: 2. Comparison of model ensembles to observational estimates. *J. Geophys. Res. Atmos.* 120, 8597–8620. doi:10.1002/2014JD022805.
Tian, B., Fetzer, E. J., Kahng, B., Teixiera, J., Manning, E., and Hearty, T. (2013). Evaluating CMIP5 models using AIRS tropospheric air temperature and specific humidity climatology. *J. Geophys. Res. Atmos.* 118, 114–134. doi:10.1029/2012JD018607.
Tierney, J. E., Haywood, A. M., Feng, R., Bhattacharya, T., and Otto-Bliesner, B. L. (2019). Pliocene warmth consistent with greenhouse gas forcing. *Geophys. Res. Lett.* 46, 9136–9144. doi:10.1029/2019gl083802.
Tierney, J. E., Pausata, F. S. R., and deMenocal, P. B. (2017). Rainfall regimes of the Green Sahara. *Sci. Adv.* 3. doi:10.1126/sciadv.1601503.
Tierney, J. E., Ummenhofer, C. C., and DeMenocal, P. B. (2015). Past and future rainfall in the Horn of Africa. *Sci. Adv.* 1, e1500682--e1500682. doi:10.1126/sciadv.1500682.
Tierney, J. E., Zhu, J., King, J., Malevich, S. B., Hakim, G. J., and Poulsen, C. J. (submitted). Glacial cooling and climate sensitivity revisited. (submitted).
Tokarska, K. B., Hegerl, G. C., Schurer, A. P., Ribes, A., and Fasullo, J. T. (2019). Quantifying human contributions to

past and future ocean warming and thermosteric sea level rise. *Environ. Res. Lett.* 14. doi:10.1088/1748-9326/ab23c1.

Tokarska, K. B., Stolpe, M. B., Sippel, S., Fischer, E. M., Smith, C. J., Lehner, F., et al. (submitted). Past warming trend constrains future warming in CMIP6 models. (submitted).

Tokinaga, H., and Xie, S.-P. (2011). Weakening of the equatorial Atlantic cold tongue over the past six decades. *Nat. Geosci.* 4, 222. Available at: http://dx.doi.org/10.1038/ngeo1078.

Tokinaga, H., Xie, S. P., Deser, C., Kosaka, Y., and Okumura, Y. M. (2012). Slowdown of the Walker circulation driven by tropical Indo-Pacific warming. *Nature* 491, 439–443. doi:10.1038/nature11576.

Trenberth, K. E., Caron, J. M., Stepaniak, D. P., and Worley, S. (2002). Evolution of El Niño–Southern Oscillation and global atmospheric surface temperatures. *J. Geophys. Res.* 107, 4065. doi:10.1029/2000JD000298.

Trenberth, K. E., Fasullo, J. T., Branstator, G., and Phillips, A. S. (2014). Seasonal aspects of the recent pause in surface warming. *Nat. Clim. Chang.* 4, 911–916. doi:10.1038/nclimate2341.

Triacca, U., Pasini, A., Attanasio, A., Giovannelli, A., and Lippi, M. (2014). Clarifying the roles of greenhouse gases and ENSO in recent global warming through their prediction performance. *J. Clim.* 27, 7903–7910. doi:10.1175/JCLI-D-13-00784.1.

Tseng, Y. heng, Lin, H., Chen, H. ching, Thompson, K., Bentsen, M., Böning, C. W., et al. (2016). North and equatorial Pacific Ocean circulation in the CORE-II hindcast simulations. *Ocean Model.* 104, 143–170. doi:10.1016/j.ocemod.2016.06.003.

Tsujino, H., Urakawa, L. S., Griffies, S. M., Danabasoglu, G., Adcroft, A. J., Amaral, A. E., et al. (submitted). Evaluation of global ocean–sea-ice model simulations based on the experimental protocols of the Ocean Model Intercomparison Project phase 2 (OMIP-2). *Geosci. Model Dev.* (submitted).

Tuel, A. (2019). Explaining Differences Between Recent Model and Satellite Tropospheric Warming Rates With Tropical SSTs. *Geophys. Res. Lett.* doi:10.1029/2019GL083994.

Turner, J., Bracegirdle, T. J., Phillips, T., Marshall, G. J., and Scott Hosking, J. (2013). An initial assessment of antarctic sea ice extent in the CMIP5 models. *J. Clim.* 26, 1473–1484. doi:10.1175/JCLI-D-12-00068.1.

Turner, J., Hosking, J. S., Marshall, G. J., Phillips, T., and Bracegirdle, T. J. (2016). Antarctic sea ice increase consistent with intrinsic variability of the Amundsen Sea Low. *Clim. Dyn.* 46, 2391–2402. doi:10.1007/s00382-015-2708-9.

Turner, J., Phillips, T., Marshall, G. J., Hosking, J. S., Pope, J. O., Bracegirdle, T. J., et al. (2017). Unprecedented springtime retreat of Antarctic sea ice in 2016. *Geophys. Res. Lett.* 44, 6868–6875. doi:10.1002/2017GL073656.

Undorf, S., Bollasina, M. A., Booth, B. B. B., and Hegerl, G. C. (2018a). Contrasting the Effects of the 1850–1975 Increase in Sulphate Aerosols from North America and Europe on the Atlantic in the CESM. *Geophys. Res. Lett.* 45, 11,911-930,940. doi:10.1029/2018GL079970.

Undorf, S., Polson, D., Bollasina, M. A., Ming, Y., Schurer, A., and Hegerl, G. C. (2018b). Detectable Impact of Local and Remote Anthropogenic Aerosols on the 20th Century Changes of West African and South Asian Monsoon Precipitation. *J. Geophys. Res. Atmos.* 123, 4871–4889. doi:10.1029/2017JD027711.

UNFCCC, S. (2015). Report of the Conference of the Parties on its twenty-first session, held in Paris from 30 November to 13 December 2015. Addendum. Part two: Action taken by the Conference of the Parties at its twenty-first session. in.

Uotila, P., Holland, P. R., Vihma, T., Marsland, S. J., and Kimura, N. (2014). Is realistic Antarctic sea-ice extent in climate models the result of excessive ice drift? *Ocean Model.* 79, 33–42. doi:https://doi.org/10.1016/j.ocemod.2014.04.004.

van den Hurk, B., Kim, H., Krinner, G., Seneviratne, S. I., Derksen, C., Oki, T., et al. (2016). LS3MIP (v1.0) contribution to CMIP6: the Land Surface, Snow and Soil moisture Model Intercomparison Project – aims, setup and expected outcome. *Geosci. Model Dev.* 9, 2809–2832. doi:10.5194/gmd-9-2809-2016.

Van Haren, R., Haarsma, R. J., Van Oldenborgh, G. J., and Hazeleger, W. (2015). Resolution dependence of European precipitation in a state-of-the-art atmospheric general circulation model. *J. Clim.* 28, 5134–5149.

Vannière, B., Demory, M.-E., Vidale, P. L., Schiemann, R., Roberts, M. J., Roberts, C. D., et al. (2019). Multi-model evaluation of the sensitivity of the global energy budget and hydrological cycle to resolution. *Clim. Dyn.* 52, 6817–6846. doi:10.1007/s00382-018-4547-y.

Vaughan, D. G., Comiso, J. C., Allison, I., Carrasco, J., Kaser, G., Kwok, R., et al. (2013). "Observations: Cryosphere," in *Climate Change 2013 - The Physical Science Basis*, ed. Intergovernmental Panel on Climate Change (Cambridge: Cambridge University Press), 317–382. doi:10.1017/CBO9781107415324.012.

Vecchi, G. A., and Soden, B. J. (2007). Global Warming and the Weakening of the Tropical Circulation. *J. Clim.* 20, 4316–4340. doi:10.1175/JCLI4258.1.

Vecchi, G. A., Soden, B. J., Wittenberg, A. T., Held, I. M., Leetmaa, A., and Harrison, M. J. (2006). Weakening of tropical Pacific atmospheric circulation due to anthropogenic forcing. *Nature* 441, 73–76. doi:10.1038/nature04744.

Vera, C. S., and Diaz, L. (2014). Anthropogenic influence on summer precipitation trends over South America in CMIP5 models. *Int. J. Clim.* doi:10.1002/joc.4153.

Vijayeta, A., and Dommenget, D. (2017). An evaluation of ENSO dynamics in CMIP simulations in the framework of

the recharge oscillator model. *Clim. Dyn.*, 1–19. doi:10.1007/s00382-017-3981-6.
Villalba, R., Lara, A., Masiokas, M. H., Urrutia, R., Luckman, B. H., Marshall, G. J., et al. (2012). Unusual Southern Hemisphere tree growth patterns induced by changes in the Southern Annular Mode. *Nat. Geosci.* 5, 793–798. doi:10.1038/ngeo1613.
Vizcaino, M., Mikolajewicz, U., Ziemen, F., Rodehacke, C. B., Greve, R., and Van Den Broeke, M. R. (2015). Coupled simulations of Greenland Ice Sheet and climate change up to A.D. 2300. *Geophys. Res. Lett.* 42, 3927–3935. doi:10.1002/2014GL061142.
Voigt, A., and Shaw, T. A. (2016). Impact of Regional Atmospheric Cloud Radiative Changes on Shifts of the Extratropical Jet Stream in Response to Global Warming. *J. Clim.* 29, 8399–8421. doi:10.1175/JCLI-D-16-0140.1.
Voldoire, A., Exarchou, E., Sanchez-Gomez, E., Demissie, T., Deppenmeier, A.-L., Frauen, C., et al. (2019a). Role of wind stress in driving SST biases in the Tropical Atlantic. *Clim. Dyn.* 53, 3481–3504. doi:10.1007/s00382-019-04717-0.
Voldoire, A., Saint-Martin, D., Sénési, S., Decharme, B., Alias, A., Chevallier, M., et al. (2019b). Evaluation of CMIP6 DECK Experiments With CNRM-CM6-1. *J. Adv. Model. Earth Syst.* 11, 2177–2213. doi:10.1029/2019MS001683.
von Schuckmann, K., Palmer, M. D., Trenberth, K. E., Cazenave, A., Chambers, D., Champollion, N., et al. (2016). An imperative to monitor Earth's energy imbalance. *Nat. Clim. Chang.* 6, 138–144. doi:doi: 10.1038/nclimate2876.
von Storch, J.-S., Haak, H., Hertwig, E., and Fast, I. (2016). Vertical heat and salt fluxes due to resolved and parameterized meso-scale Eddies. *Ocean Model.* 108, 1–19. doi:10.1016/J.OCEMOD.2016.10.001.
Vries, H. de, Scher, S., Haarsma, R., Drijfhout, S., and Delden, A. van (2019). How Gulf-Stream SST-fronts influence Atlantic winter storms. *Clim. Dyn.* 52, 5899–5909. doi:10.1007/s00382-018-4486-7.
Wahr, J. M., Jayne, S. R., and Bryan, F. O. (2002). A method of inferring changes in deep ocean currents from satellite measurements of time-variable gravity. *J. Geophys. Res. Ocean.* 107, 11–17. doi:10.1029/2001JC001274.
Wallace, R. B., Baumann, H., Grear, J. S., Aller, R. C., and Gobler, C. J. (2014). Coastal ocean acidification: The other eutrophication problem. *Estuar. Coast. Shelf Sci.* 148, 1–13. doi:10.1016/J.ECSS.2014.05.027.
Wan, H., Zhang, X., Zwiers, F., and Min, S.-K. (2015). Attributing northern high-latitude precipitation change over the period 1966--2005 to human influence. *Clim. Dyn.* 45, 1713–1726. doi:10.1007/s00382-014-2423-y.
Wang, B., Biasutti, M., Byrne, M., Castro, C., Chang, C.-P., Cook, K., et al. (submitted). Monsoon Climate Change Assessment. *Bull. Am. Meteorol. Soc.* (submitted).
Wang, B., and Ding, Q. (2008). Global monsoon: Dominant mode of annual variation in the tropics. *Dyn. Atmos. Ocean.* 44, 165–183. doi:10.1016/j.dynatmoce.2007.05.002.
Wang, B., Li, J., Cane, M. A., Liu, J., Webster, P. J., Xiang, B., et al. (2018). Toward Predicting Changes in the Land Monsoon Rainfall a Decade in Advance. *J. Clim.* 31, 2699–2714. doi:10.1175/JCLI-D-17-0521.1.
Wang, B., Liu, J., Kim, H.-J., Webster, P. J., Yim, S.-Y., and Xiang, B. (2013). Northern Hemisphere summer monsoon intensified by mega-El Nino/southern oscillation and Atlantic multidecadal oscillation. *Proc. Natl. Acad. Sci.* 110, 5347–5352. doi:10.1073/pnas.1219405110.
Wang, C.-Y., Xie, S.-P., Kosaka, Y., Liu, Q., and Zheng, X.-T. (2017a). Global influence of tropical Pacific variability with implications for global warming slowdown. *J. Clim.* 30. doi:10.1175/JCLI-D-15-0496.1.
Wang, C., Zhang, L., Lee, S.-K., Wu, L., and Mechoso, C. R. (2014). A global perspective on CMIP5 climate model biases. *Nat. Clim. Chang.* 4, 201. Available at: http://dx.doi.org/10.1038/nclimate2118.
Wang, G., Hendon, H. H., Arblaster, J. M., Lim, E.-P., Abhik, S., and van Rensch, P. (2019a). Compounding tropical and stratospheric forcing of the record low Antarctic sea-ice in 2016. *Nat. Commun.* 10, 13. doi:10.1038/s41467-018-07689-7.
Wang, J., Yang, B., Ljungqvist, F. C., Luterbacher, J., Osborn, T. J., Briffa, K. R., et al. (2017b). Internal and external forcing of multidecadal Atlantic climate variability over the past 1,200 years. *Nat. Geosci.* 10, 512–517. doi:10.1038/ngeo2962.
Wang, Q., Ilicak, M., Gerdes, R., Drange, H., Aksenov, Y., Bailey, D. A., et al. (2016a). An assessment of the Arctic Ocean in a suite of interannual CORE-II simulations. Part II: Liquid freshwater. *Ocean Model.* 99, 86–109. doi:10.1016/J.OCEMOD.2015.12.008.
Wang, Q., Ilicak, M., Samuels, B. L., Spence, P., Tsujino, H., Valcke, S., et al. (2016b). An assessment of the Arctic Ocean in a suite of interannual CORE-II simulations : Part I: Sea ice and freshwater. *Ocean Model.* 99, 110–132. doi:10.1016/j.ocemod.2015.12.009.
Wang, Z., Bi, L., Yi, B., and Zhang, X. (2019b). How the Inhomogeneity of Wet Sea Salt Aerosols Affects Direct Radiative Forcing. *Geophys. Res. Lett.* 46, 1805–1813. doi:10.1029/2018GL081193.
Watanabe, M., Dufresne, J.-L., Kosaka, Y., Mauritsen, T., and Tatebe, H. (submitted). Reconciling equatorial Pacific sea surface temperature pattern changes over the past six decades in observations and models. *Nat. Clim. Chang.* (submitted).
Watanabe, M., Shiogama, H., Tatebe, H., Hayashi, M., Ishii, M., and Kimoto, M. (2014). Contribution of natural decadal variability to global warming acceleration and hiatus. *Nat. Clim. Chang.* 4. doi:10.1038/nclimate2355.
Watanabe, M., and Tatebe, H. (2019). Reconciling roles of sulphate aerosol forcing and internal variability in Atlantic

multidecadal climate changes. *Clim. Dyn.* 53, 4651–4665. doi:10.1007/s00382-019-04811-3.
Waugh, D. W., and Eyring, V. (2008). Quantitative performance metrics for stratospheric-resolving chemistry-climate models. *Atmos. Chem. Phys.* 8, 5699–5713. doi:10.5194/acp-8-5699-2008.
Waugh, D. W., Grise, K. M., Seviour, W. J. M., Davis, S. M., Davis, N., Adam, O., et al. (2018). Revisiting the Relationship among Metrics of Tropical Expansion. *J. Clim.* 31, 7565–7581. doi:10.1175/JCLI-D-18-0108.1.
Weijer, W., Cheng, W., Garuba, O. A., Hu, A., and Nadiga, B. T. (submitted). CMIP6 Models Predict Significant 21st Century Decline of the Atlantic Meridional Overturning Circulation. *Geophys. Res. Lett* (submitted).
Weller, E., Min, S. K., Cai, W., Zwiers, F. W., Kim, Y. H., and Lee, D. (2016). Human-caused Indo-Pacific warm pool expansion. *Sci. Adv.* 2, e1501719–e1501719. doi:10.1126/sciadv.1501719.
Wenzel, S., Cox, P. M., Eyring, V., and Friedlingstein, P. (2016). Projected land photosynthesis constrained by changes in the seasonal cycle of atmospheric CO 2. *Nature*. doi:10.1038/nature19772.
West, J. J., Smith, S. J., Silva, R. A., Naik, V., Zhang, Y., Adelman, Z., et al. (2013). Co-benefits of mitigating global greenhouse gas emissions for future air quality and human health. *Nat. Clim. Chang.* 3, 885.
Williams, A. P., Seager, R., Abatzoglou, J. T., Cook, B. I., Smerdon, J. E., and Cook, E. R. (2015). Contribution of anthropogenic warming to California drought during 2012-2014. *Geophys. Res. Lett.* doi:10.1002/2015GL064924.
Wills, R. C. J., Armour, K. C., Battisti, D. S., and Hartmann, D. L. (2019). Ocean–Atmosphere Dynamical Coupling Fundamental to the Atlantic Multidecadal Oscillation. *J. Clim.* 32, 251–272. doi:10.1175/JCLI-D-18-0269.1.
Winkelmann, R., Martin, M. A., Haseloff, M., Albrecht, T., Bueler, E., Khroulev, C., et al. (2011). The Potsdam Parallel Ice Sheet Model (PISM-PIK) - Part 1: Model description. *Cryosphere* 5, 715–726. doi:10.5194/tc-5-715-2011.
Winkler, A. J., Myneni, R. B., Alexandrov, G. A., and Brovkin, V. (2019). Earth system models underestimate carbon fixation by plants in the high latitudes. *Nat. Commun.* doi:10.1038/s41467-019-08633-z.
Woollings, T., Barnes, E., Hoskins, B., Kwon, Y.-O., Lee, R. W., Li, C., et al. (2018a). Daily to Decadal Modulation of Jet Variability. *J. Clim.* 31, 1297–1314. doi:10.1175/JCLI-D-17-0286.1.
Woollings, T., Barriopedro, D., Methven, J., Son, S.-W., Martius, O., Harvey, B., et al. (2018b). Blocking and its Response to Climate Change. *Curr. Clim. Chang. Reports* 4, 287–300. doi:10.1007/s40641-018-0108-z.
Woollings, T., Franzke, C., Hodson, D. L. R., Dong, B., Barnes, E. A., Raible, C. C., et al. (2015). Contrasting interannual and multidecadal NAO variability. *Clim. Dyn.* 45, 539–556. doi:10.1007/s00382-014-2237-y.
Wouters, B., Drijfhout, S., and Hazeleger, W. (2012). Interdecadal North-Atlantic meridional overturning circulation variability in EC-EARTH. *Clim. Dyn.* 39, 2695–2712. doi:10.1007/s00382-012-1366-4.
Wouters, B., Gardner, A. S., and Moholdt, G. (2019). Global Glacier Mass Loss During the GRACE Satellite Mission (2002-2016). *Front. Earth Sci.* 7. doi:10.3389/feart.2019.00096.
Wu, P., Christidis, N., and Stott, P. (2013). Anthropogenic impact on Earth's hydrological cycle. *Nat. Clim. Chang.* 3. doi:10.1038/NCLIMATE1932.
Wu, P., Roberts, M., Martin, G., Chen, X., Zhou, T., and Vidale, P. L. (2019a). The impact of horizontal atmospheric resolution in modelling air–sea heat fluxes. *Q. J. R. Meteorol. Soc.* 145, 3271–3283. doi:10.1002/qj.3618.
Wu, T., Lu, Y., Fang, Y., Xin, X., Li, L., Li, W., et al. (2019b). The Beijing Climate Center Climate System Model (BCC-CSM): the main progress from CMIP5 to CMIP6. *Geosci. Model Dev.* 12, 1573–1600. doi:10.5194/gmd-12-1573-2019.
Xiao, L., Che, T., Chen, L., Xie, H., and Dai, L. (2017). Quantifying Snow Albedo Radiative Forcing and Its Feedback during 2003–2016. *Remote Sens.* 9.
Xu, Y., and Hu, A. (2018). How Would the Twenty-First-Century Warming Influence Pacific Decadal Variability and Its Connection to North American Rainfall: Assessment Based on a Revised Procedure for the IPO/PDO. *J. Clim.* 31, 1547–1563. doi:10.1175/JCLI-D-17-0319.1.
Xu, Z., Chang, P., Richter, I., Kim, W., and Tang, G. (2014). Diagnosing southeast tropical Atlantic SST and ocean circulation biases in the CMIP5 ensemble. *Clim. Dyn.* 43, 3123–3145. doi:10.1007/s00382-014-2247-9.
Yan, M., Wang, B., and Liu, J. (2016a). Global monsoon change during the Last Glacial Maximum: a multi-model study. *Clim. Dyn.* 47, 359–374. doi:10.1007/s00382-015-2841-5.
Yan, X., DelSole, T., and Tippett, M. K. (2016b). What Surface Observations Are Important for Separating the Influences of Anthropogenic Aerosols from Other Forcings? *J. Clim.* 29, 4165–4184. doi:10.1175/JCLI-D-15-0667.1.
Yan, X. H., Boyer, T., Trenberth, K., Karl, T. R., Xie, S. P., Nieves, V., et al. (2016c). The global warming hiatus: Slowdown or redistribution? *Earth's Futur.* 4, 472–482. doi:10.1002/2016EF000417.
Yan, X., Zhang, R., and Knutson, T. R. (2018). Underestimated AMOC Variability and Implications for AMV and Predictability in CMIP Models. *Geophys. Res. Lett.* 45, 4319–4328. doi:10.1029/2018GL077378.
Yang, H., Piao, S., Huntingford, C., Ciais, P., Li, Y., Wang, T., et al. (2018). Changing the retention properties of catchments and their influence on runoff under climate change. *Environ. Res. Lett.* doi:10.1088/1748-9326/aadd32.
Yang, H., Zhou, F., Piao, S., Huang, M., Chen, A., Ciais, P., et al. (2017a). Regional patterns of future runoff changes from Earth system models constrained by observation. *Geophys. Res. Lett.* 44, 5540–5549.

doi:10.1002/2017GL073454.
Yang, J.-C., Lin, X., Xie, S.-P., Zhang, Y., Kosaka, Y., and Li, Z. (submitted). Synchronized tropical Pacific and extratropical variability during the past three decades. *Nat. Clim. Chang.* (submitted).
Yang, Y., Xie, S.-P., Wu, L., Kosaka, Y., and Li, J. (2017b). Causes of Enhanced SST Variability over the Equatorial Atlantic and Its Relationship to the Atlantic Zonal Mode in CMIP5. *J. Clim.* 30, 6171–6182. doi:10.1175/JCLI-D-16-0866.1.
Yeh, S.-W., Cai, W., Min, S.-K., McPhaden, M. J., Dommenget, D., Dewitte, B., et al. (2018). ENSO Atmospheric Teleconnections and Their Response to Greenhouse Gas Forcing. *Rev. Geophys.*, 77–117. doi:110.1002/2017RG000568.
Yeh, S.-W., Kim, W.-M., Kim, Y. H., Moon, B.-K., Park, R. J., and Song, C.-K. (2013). Changes in the variability of the North Pacific sea surface temperature caused by direct sulfate aerosol forcing in China in a coupled general circulation model. *J. Geophys. Res. Atmos.* 118, 1261–1270. doi:10.1029/2012JD017947.
Yeh, S.-W., Kug, J.-S., Dewitte, B., Kwon, M.-H., Kirtman, B. P., and Jin, F.-F. (2009). El Niño in a changing climate. *Nature* 461, 511. Available at: https://doi.org/10.1038/nature08316.
Yin, J., Overpeck, J., Peyser, C., and Stouffer, R. (2018). Big Jump of Record Warm Global Mean Surface Temperature in 2014-2016 Related to Unusually Large Oceanic Heat Releases. *Geophys. Res. Lett.* 45, 1069–1078. doi:10.1002/2017GL076500.
Ying, K.-R., Zhao, T.-B., and Zheng, X.-G. (2014). Slow and Intraseasonal Modes of the Boreal Winter Atmospheric Circulation Simulated by CMIP5 Models. *Atmos. Ocean. Sci. Lett.* 7, 34–41. doi:10.3878/j.issn.1674-2834.13.0058.
Yoshimori, M., and Suzuki, M. (2019). The relevance of mid-Holocene Arctic warming to the future. *Clim. Past* 15, 1375–1394. doi:10.5194/cp-15-1375-2019.
Young, P. J., Butler, A. H., Calvo, N., Haimberger, L., Kushner, P. J., Marsh, D. R., et al. (2013). Agreement in late twentieth century southern hemisphere stratospheric temperature trends in observations and ccmval-2, CMIP3, and CMIP5 models. *J. Geophys. Res. Atmos.* 118, 605–613. doi:10.1002/jgrd.50126.
Zaehle, S., Jones, C. D., Houlton, B., Lamarque, J.-F., and Robertson, E. (2015). Nitrogen availability reduces CMIP5 projections of twenty-first-century land carbon uptake. *J. Clim.* 28, 2494–2511.
Zanchettin, D., Bothe, O., Müller, W., Bader, J., and Jungclaus, J. H. (2014). Different flavors of the Atlantic Multidecadal Variability. *Clim. Dyn.* 42, 381–399. doi:10.1007/s00382-013-1669-0.
Zang, C. S., Jochner-Oette, S., Cortés, J., Rammig, A., and Menzel, A. (2019). Regional trend changes in recent surface warming. *Clim. Dyn.* 52, 6463–6473. doi:10.1007/s00382-018-4524-5.
Zanna, L., Khatiwala, S., Gregory, J. M., Ison, J., and Heimbach, P. (2019). Global reconstruction of historical ocean heat storage and transport. *Proc. Natl. Acad. Sci.* 116, 1126–1131. doi:10.1073/pnas.1808838115.
Zappa, G., Masato, G., Shaffrey, L., Woollings, T., and Hodges, K. (2014). Linking Northern Hemisphere blocking and storm track biases in the CMIP5 climate models. *Geophys. Res. Lett.* 41, 135–139. doi:10.1002/2013GL058480.
Zappa, G., Shaffrey, L. C., and Hodges, K. I. (2013). The ability of CMIP5 models to simulate North Atlantic extratropical cyclones. *J. Clim.* 26, 5379–5396. doi:10.1175/JCLI-D-12-00501.1.
Zemp, M., Huss, M., Thibert, E., Eckert, N., McNabb, R., Huber, J., et al. (2019). Global glacier mass changes and their contributions to sea-level rise from 1961 to 2016. *Nature* 568, 382–386. doi:10.1038/s41586-019-1071-0.
Zeng, N., Zhao, F., Collatz, G. J., Kalnay, E., Salawitch, R. J., West, T. O., et al. (2014). Agricultural Green Revolution as a driver of increasing atmospheric CO 2 seasonal amplitude. *Nature* 515, 394–397. doi:10.1038/nature13893.
Zhang, L., Delworth, T. L., Cooke, W., and Yang, X. (2019). Natural variability of Southern Ocean convection as a driver of observed climate trends. *Nat. Clim. Chang.* 9, 59–65. doi:10.1038/s41558-018-0350-3.
Zhang, L., Delworth, T. L., Yang, X., Gudgel, R. G., Jia, L., Vecchi, G. A., et al. (2017). Estimating Decadal Predictability for the Southern Ocean Using the GFDL CM2.1 Model. *J. Clim.* 30, 5187–5203. doi:10.1175/JCLI-D-16-0840.1.
Zhang, L., Han, W., and Sienz, F. (2018a). Unraveling Causes for the Changing Behavior of the Tropical Indian Ocean in the Past Few Decades. *J. Clim.* 31, 2377–2388. doi:10.1175/JCLI-D-17-0445.1.
Zhang, L., and Wang, C. (2013). Multidecadal North Atlantic sea surface temperature and Atlantic meridional overturning circulation variability in CMIP5 historical simulations. *J. Geophys. Res. Ocean.* 118, 5772–5791. doi:10.1002/jgrc.20390.
Zhang, L., Zhou, T., Klingaman, N. P., Wu, P., and Roberts, M. (2018b). Effect of Horizontal Resolution on the Representation of the Global Monsoon Annual Cycle in AGCMs. *Adv. Atmos. Sci.* 35, 1003–1020. doi:10.1007/s00376-018-7273-9.
Zhang, R. (2017). On the persistence and coherence of subpolar sea surface temperature and salinity anomalies associated with the Atlantic multidecadal variability. *Geophys. Res. Lett.* 44, 7865–7875. doi:10.1002/2017GL074342.
Zhang, R., Delworth, T. L., Sutton, R., Hodson, D. L. R., Dixon, K. W., Held, I. M., et al. (2013a). Have Aerosols Caused the Observed Atlantic Multidecadal Variability? *J. Atmos. Sci.* 70, 1135–1144. doi:10.1175/JAS-D-12-0331.1.
Zhang, R., Jiang, D., and Zhang, Z. (2015). Causes of mid-Pliocene strengthened summer and weakened winter

monsoons over East Asia. *Adv. Atmos. Sci.* 32, 1016–1026. doi:10.1007/s00376-014-4183-3.
Zhang, R., and Knutson, T. R. (2013). The role of global climate change in the extreme low summer Arctic sea ice extent in 2012. *Bull. Am. Meteorol. Soc.* 94, S23.
Zhang, R., Sutton, R., Danabasoglu, G., Delworth, T. L., Kim, W. M., Robson, J., et al. (2016). Comment on "The Atlantic Multidecadal Oscillation without a role for ocean circulation." *Science* 352, 1527–1527. doi:10.1126/science.aaf1660.
Zhang, R., Yan, Q., Zhang, Z. S., Jiang, D., Otto-Bliesner, B. L., Haywood, A. M., et al. (2013b). Mid-Pliocene East Asian monsoon climate simulated in the PlioMIP. *Clim. Past*. doi:10.5194/cp-9-2085-2013.
Zhang, T., and Sun, D. Z. (2014). ENSO asymmetry in CMIP5 models. *J. Clim.* 27, 4070–4093. doi:10.1175/JCLI-D-13-00454.1.
Zhang, W., and Jin, F. F. (2012). Improvements in the CMIP5 simulations of ENSO-SSTA meridional width. *Geophys. Res. Lett.* 39, 1–5. doi:10.1029/2012GL053588.
Zhang, X., Zwiers, F. W., Hegerl, G. C., Lambert, F. H., Gillett, N. P., Solomon, S., et al. (2007). Detection of human influence on twentieth-century precipitation trends. *Nature* 448, 461.
Zhang, Y., Guo, Y., Dong, W., and Li, C. (2018c). What drives the decadal variation of global land monsoon precipitation over the past 50 years? *Int. J. Climatol.* 38, 4818–4829. doi:10.1002/joc.5699.
Zhang, Y., Wallace, J. M., and Battisti, D. S. (1997). ENSO-like Interdecadal Variability: 1900–93. *J. Clim.* 10, 1004–1020. doi:10.1175/1520-0442(1997)010<1004:ELIV>2.0.CO;2.
Zhao, D. F., Buchholz, A., Tillmann, R., Kleist, E., Wu, C., Rubach, F., et al. (2017). Environmental conditions regulate the impact of plants on cloud formation. *Nat. Commun.* 8, 14067.
Zhao, F., Zeng, N., Asrar, G., Friedlingstein, P., Ito, A., Jain, A., et al. (2016). Role of CO$_{2}$, climate and land use in regulating the seasonal amplitude increase of carbon fluxes in terrestrial ecosystems: a multimodel analysis. *Biogeosciences* 13, 5121–5137. doi:10.5194/bg-13-5121-2016.
Zheng, F., Li, J., Clark, R. T., and Nnamchi, H. C. (2013). Simulation and Projection of the Southern Hemisphere Annular Mode in CMIP5 Models. *J. Clim.* 26, 9860–9879. doi:10.1175/JCLI-D-13-00204.1.
Zheng, X.-T., Gao, L., Li, G., and Du, Y. (2016). The Southwest Indian Ocean thermocline dome in CMIP5 models: Historical simulation and future projection. *Adv. Atmos. Sci.* 33, 489–503. doi:10.1007/s00376-015-5076-9.
Zhou, C., and Wang, K. (2016). Spatiotemporal Divergence of the Warming Hiatus over Land Based on Different Definitions of Mean Temperature. *Sci. Rep.* 6, 31789. doi:10.1038/srep31789.
Zhu, F., Emile-Geay, J., McKay, N. P., Hakim, G. J., Khider, D., Ault, T. R., et al. (2019a). Climate models can correctly simulate the continuum of global-average temperature variability. *Proc. Natl. Acad. Sci.* 116, 8728–8733. doi:10.1073/pnas.1809959116.
Zhu, J., Poulsen, C. J., and Tierney, J. E. (2019b). Simulation of Eocene extreme warmth and high climate sensitivity through cloud feedbacks. *Sci. Adv.* 5. doi:10.1126/sciadv.aax1874.
Zhu, Y., and Zhang, R. H. (2018). An Argo-Derived Background Diffusivity Parameterization for Improved Ocean Simulations in the Tropical Pacific. *Geophys. Res. Lett.* 45, 1509–1517. doi:10.1002/2017GL076269.
Zhu, Z., Piao, S., Lian, X., Myneni, R. B., Peng, S., and Yang, H. (2017). Attribution of seasonal leaf area index trends in the northern latitudes with "optimally" integrated ecosystem models. *Glob. Chang. Biol.* 23, 4798–4813. doi:10.1111/gcb.13723.
Zhu, Z., Piao, S., Myneni, R. B., Huang, M., Zeng, Z., Canadell, J. G., et al. (2016). Greening of the Earth and its drivers. *Nat. Clim. Chang.* 6, 791–795. doi:10.1038/nclimate3004.
Zika, J. D., Gregory, J. M., McDonagh, E. L., Marzocchi, A., and Clement, L. (submitted). Patterns of recent ocean heat content change driven by ocean circulation, not heat uptake. *Nature* (submitted).
Zika, J. D., Skliris, N., Blaker, A. T., Marsh, R., Nurser, A. J. G., and Josey, S. A. (2018). Improved estimates of water cycle change from ocean salinity: The key role of ocean warming. *Environ. Res. Lett.* 13, 074036. doi:10.1088/1748-9326/aace42.
Zika, J. D., Skliris, N., Nurser, A. J. G., Josey, S. A., Mudryk, L., Laliberté, F., et al. (2015). Maintenance and broadening of the ocean's salinity distribution by the water cycle. *J. Clim.* 28, 9550–9560. doi:10.1175/JCLI-D-15-0273.1.
Zunz, V., Goosse, H., and Massonnet, F. (2013). How does internal variability influence the ability of CMIP5 models to reproduce the recent trend in Southern Ocean sea ice extent? *Cryosph.* 7, 451–468. doi:10.5194/tc-7-451-2013.
Zuo, J.-Q., Li, W.-J., and Ren, H.-L. (2013). Representation of the Arctic Oscillation in the CMIP5 Models. *Adv. Clim. Chang. Res.* 4, 242–249. doi:10.3724/SP.J.1248.2013.242.

Figures

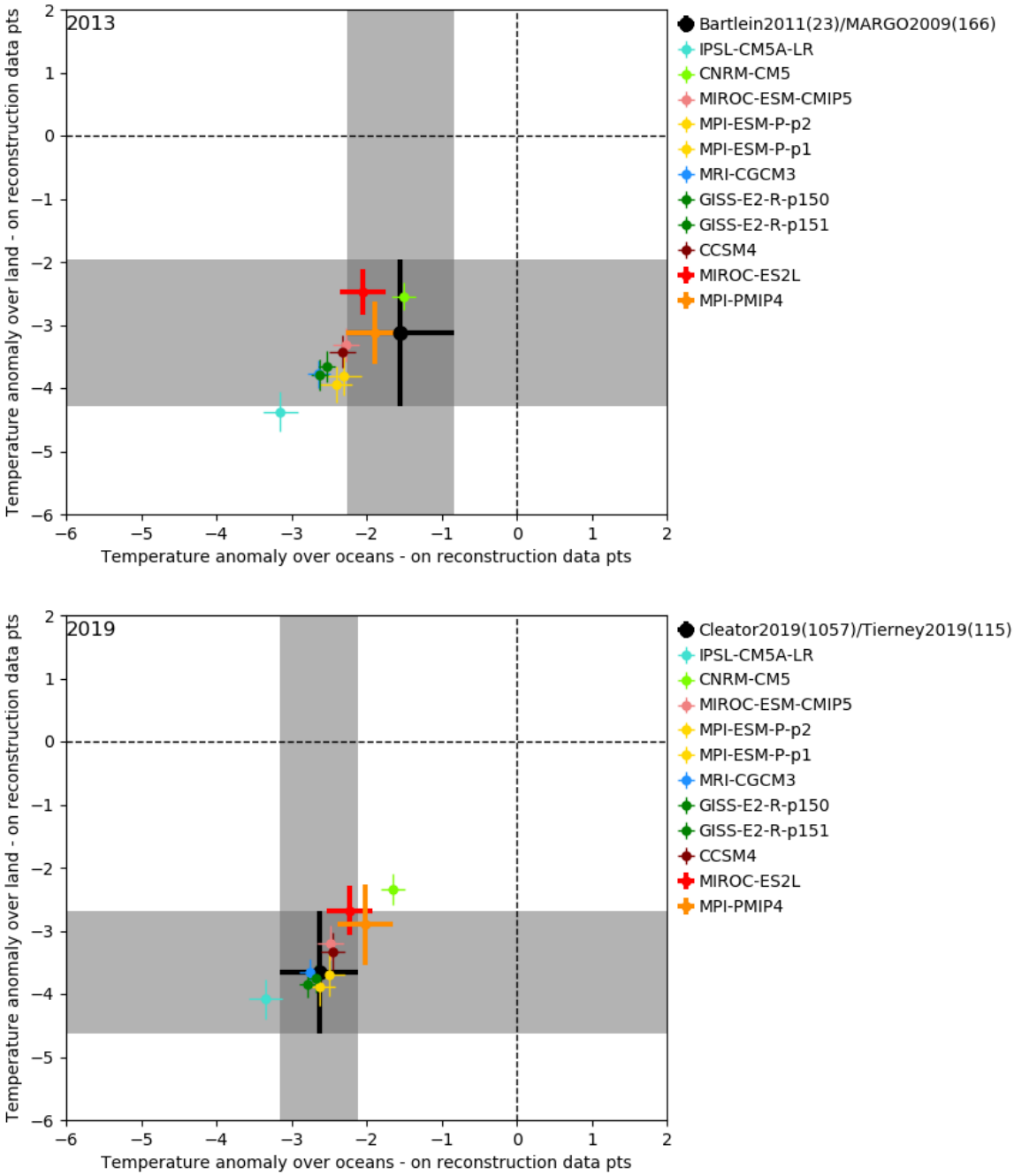

Figure 3.1: Last Glacial Maximum (LGM, 21 ka) anomalies in mean annual temperature over land and sea surface temperature in the Tropics (30S-30N) for paleoclimate reconstructions featured in AR5 (upper panel) and for updated estimates (lower panel). The coloured crosses show long-term modelled mean differences (experiment minus pre-industrial control) in the relative warming/cooling over tropical land and ocean where the model output has been sampled only at the locations for which there are temperature reconstructions. The black crosses show the paleo proxy reconstructions.

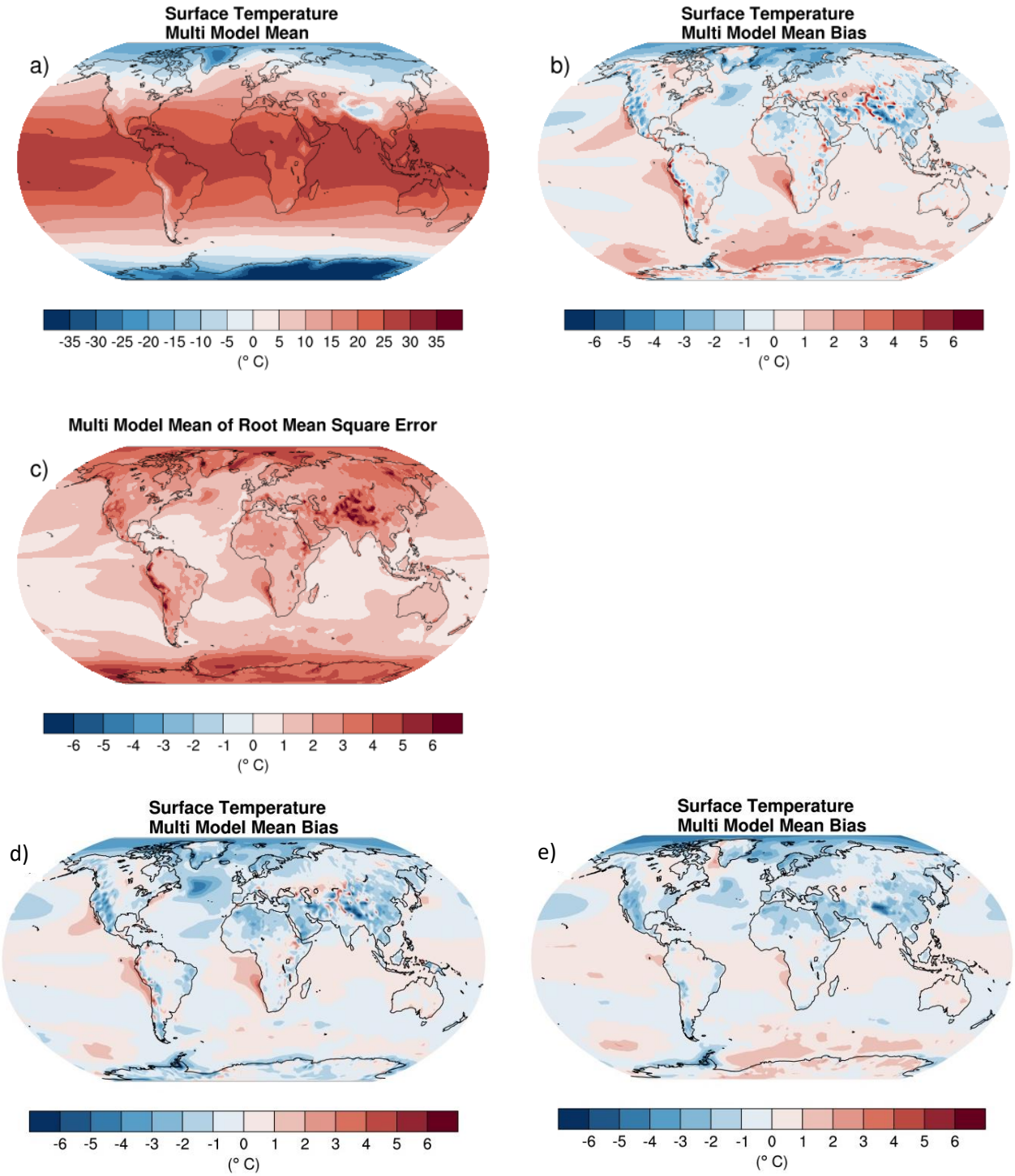

Figure 3.2: Annual-mean surface (2 m) air temperature (°C) for the period 1995–2014. (a) Multi-model (ensemble) mean constructed with one realization of CMIP6 historical experiments. (b) Multi-model-mean bias as the difference between the CMIP6 multi-model mean and the climatology from the Fifth generation of ECMWF atmospheric reanalyses of the global climate (ERA5). (c) Multi-model-mean of the root mean square error of the seasonal cycle with respect to the climatology from ERA5. Also shown is the multi-model-mean bias as the difference between the multi-model mean of (d) low resolution and (e) high resolution simulations of the HighResMIP and the climatology from ERA5. (Figure from Bock et al. (submitted), their Figure 2, produced with ESMValTool v2.0.0b3.)

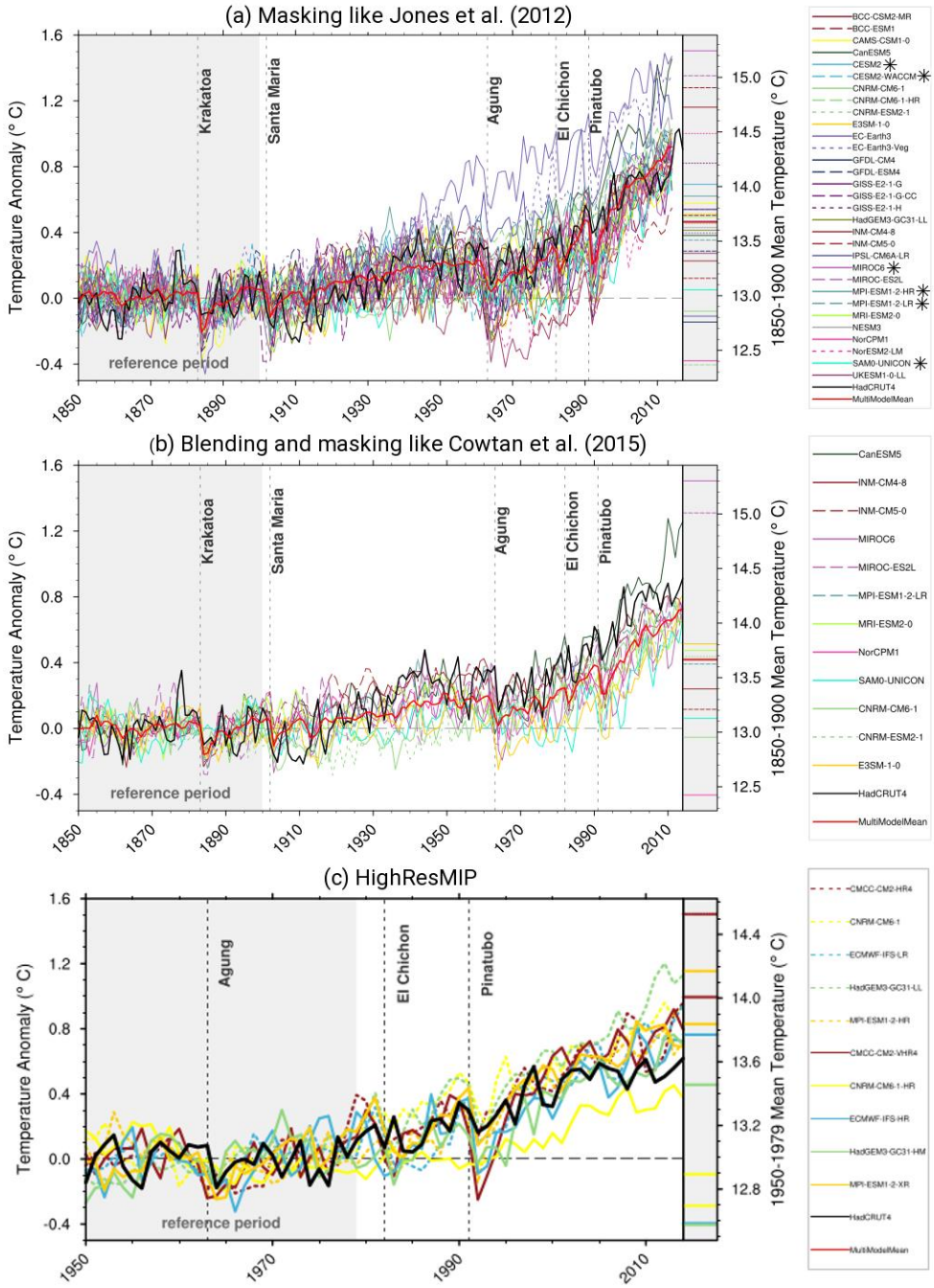

Figure 3.3: Observed and simulated time series of the anomalies in annual and global mean surface temperature. All anomalies are differences from the 1850–1900 time-mean of each individual time series. The reference period 1850–1900 is indicated by grey shading. Single simulations for CMIP6 models (thin lines); multi-model mean (thick red line). Observational data (thick black lines) are Hadley Centre/Climatic Research Unit gridded surface temperature data set 4 (HadCRUT4; Morice et al., 2012), and are merged surface temperature (2 m height over land and surface temperature over the ocean). (a) All models have been subsampled using the HadCRUT4 observational data mask (see Jones et al., 2013). (b) All models have been blended to GMST and subsampled using the HadCRUT4 observational data mask (Cowtan et al., 2015). (c) HighResMIP models are displayed with the reference period 1950-1979. Masking was done like in (a). Inset: the global mean surface temperature for the reference period of the subsampled fields. (Figure from Bock et al. (submitted), their Figure 1, produced with ESMValTool v2.0.0b3.)

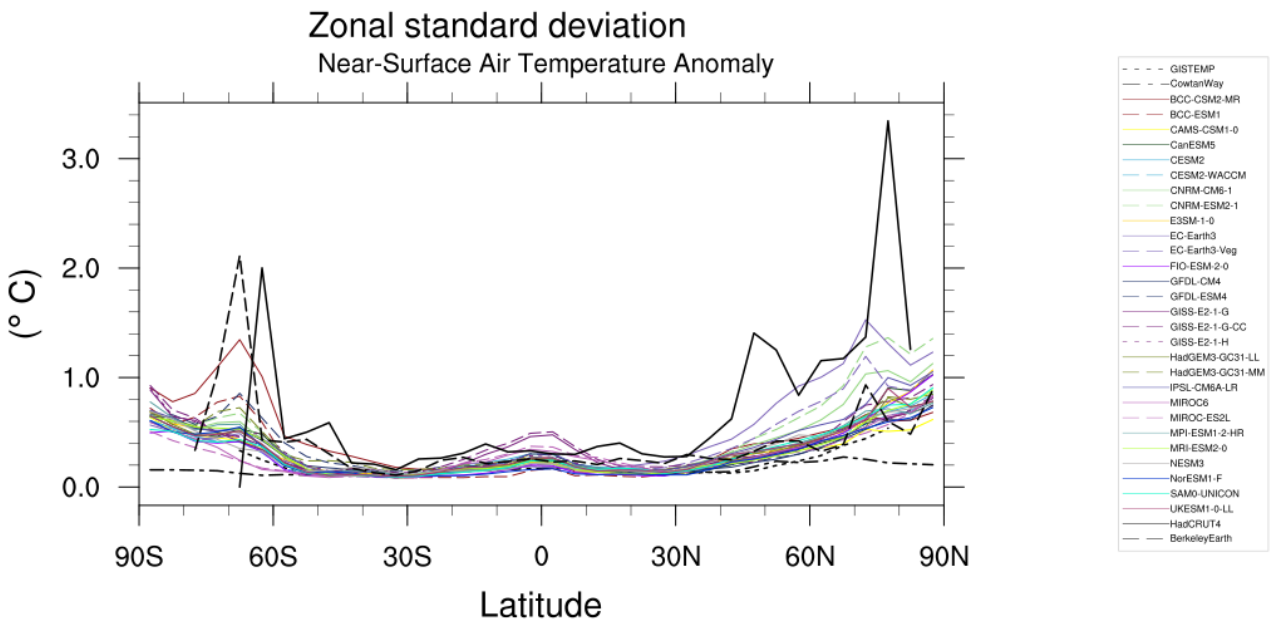

Figure 3.4: Global climate variability as represented by standard deviation of zonal-mean surface temperature of observed temperature datasets (in black: GISTEMP (dashed), Cowtan and Way (dot-dashed), HadCRUT4 (solid), and Berkeley Earth (long dashed)) and in CMIP6 pre-industrial control simulations (after Jones et al., 2013). Figure produced with ESMValTool v2.0.0b3.

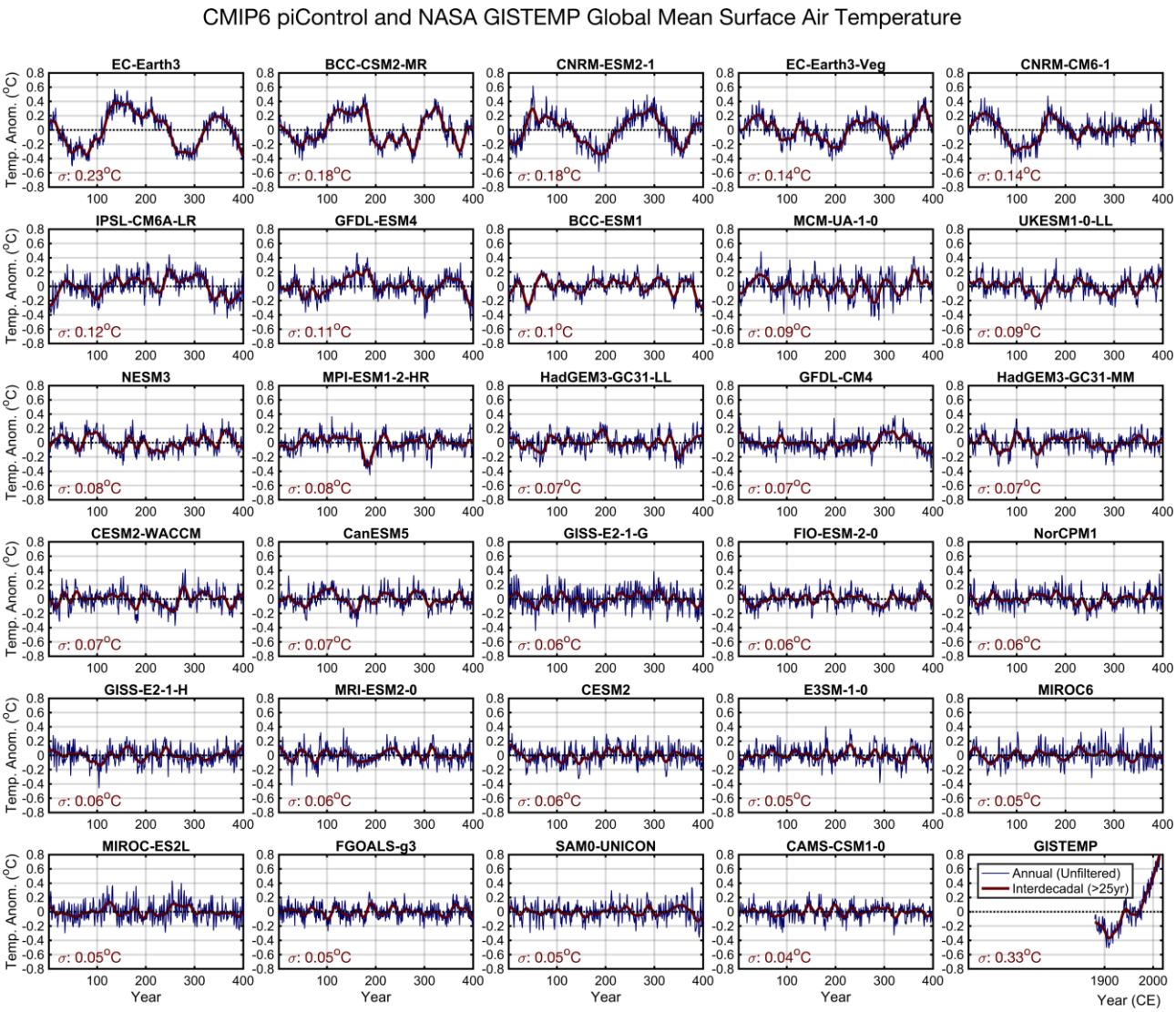

Figure 3.5: Global mean surface air temperature (GSAT) anomalies in 29 CMIP6 control simulations, compared with GISTEMP GMST observations. Blue lines show annual means, and red lines show 25-year low-pass filtered means. Red numbers show standard deviations of interdecadal GSAT/GMST variations. (From Parsons et al. (submitted), their Figure 1, updated to correct a latitude weighting error.)

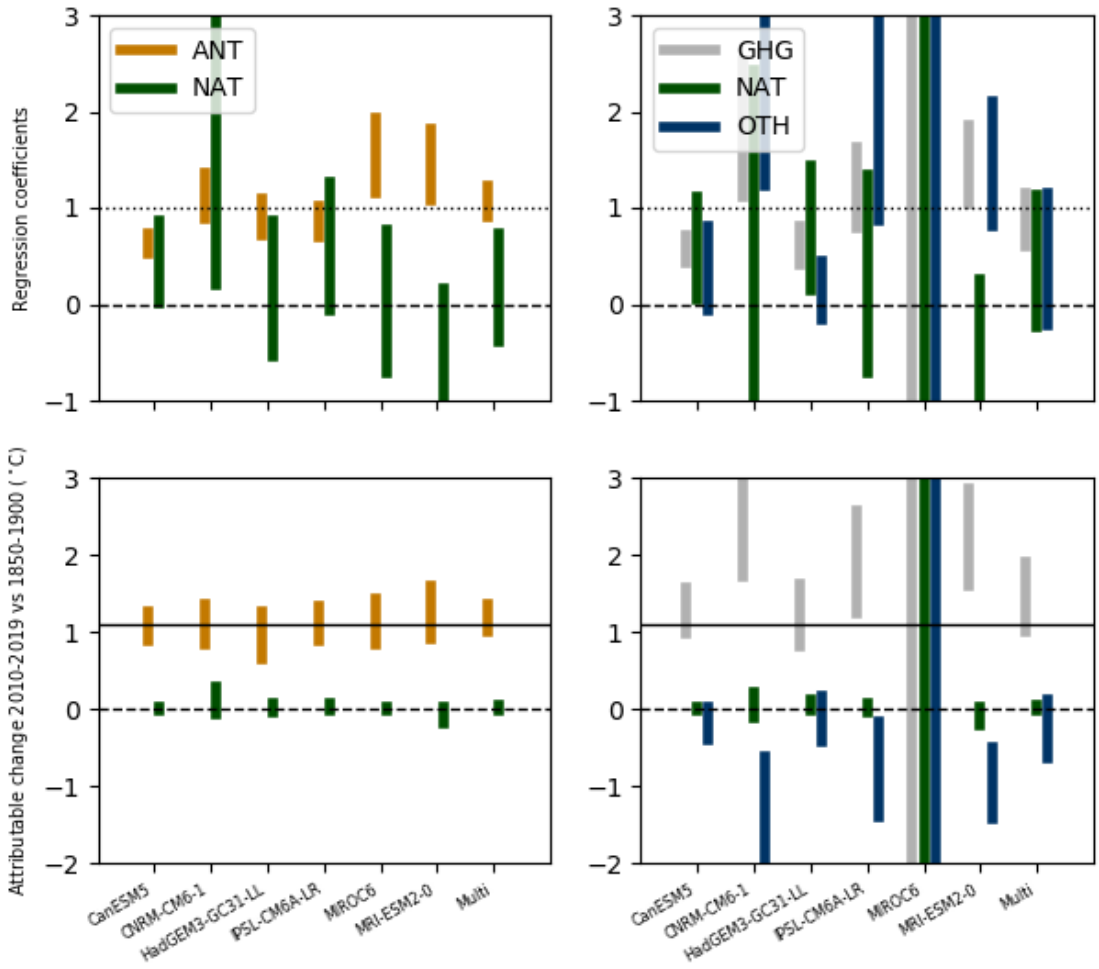

Figure 3.6: Upper panels show regression coefficients based a two-way regression (left) and three-way regression (right), of observed 5-yr mean global mean masked and blended surface temperature onto individual model response patterns, and a multi-model mean, labelled 'Multi'. Combined anthropogenic (ANT), natural (NAT), well-mixed greenhouse gases (GHG), and other anthropogenic (aerosols, ozone, land-use change, OTH) regression coefficients are shown. Regression coefficients are the scaling factors by which the model responses must be multiplied to best match observations. Regression coefficients consistent with one indicate a consistent magnitude response in observations and models, and regression coefficients inconsistent with zero indicate a detectable response to the forcing concerned. Note that three-way regression coefficients for MIROC6 are unconstrained. Lower panels show corresponding observationally-constrained estimates of attributable warming in globally-complete GSAT for the period 2010-2019, relative to 1850-1900, and the horizontal black line shows an estimate of observed warming in GSAT for this period. (Figure from Gillett et al. (submitted), their Figure S3.)

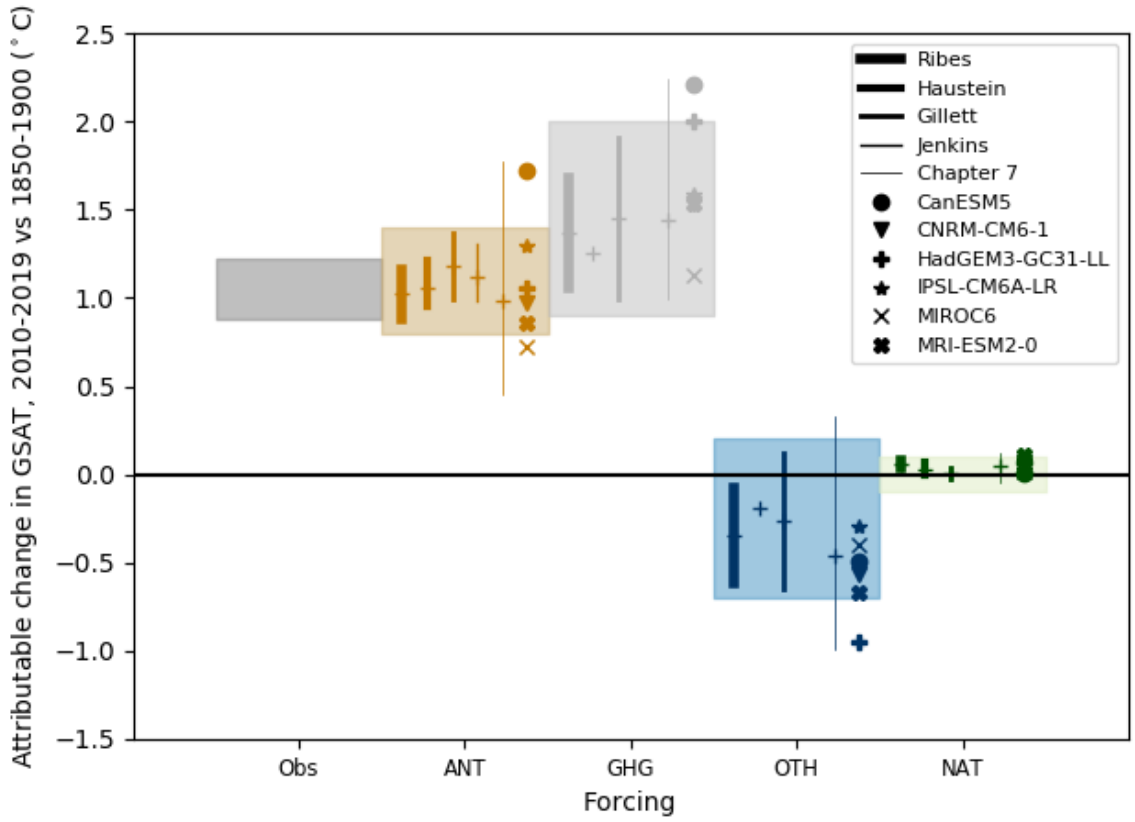

Figure 3.7: Coloured bands show assessed *likely* ranges of temperature change in GSAT, 2010-2019 relative to 1850-1900, attributable to anthropogenic forcings (ANT), well-mixed greenhouse gases (GHG), other anthropogenic forcings (aerosols, ozone, land-use change, OTH), and natural forcings (NAT), and in observations (Obs). The observed warming shown currently is for 2009-2018 but will be updated to 2010-2019 in the final draft. Bars show 5-95% ranges based on the individual studies indicated (Gillett et al., submitted; Haustein et al., 2017; Jenkins et al., 2019; Ribes et al., submitted), with the results from Gillett et al. (submitted) corresponding to the multi-model attributable warming estimates shown in Figure 3.6:. The Jenkins et al. (submitted) range shown was calculated by subtracting 0.35 times an estimated anthropogenic warming rate of 0.17°C/decade (Haustein et al., 2017) from the Jenkins et al. (submitted) reported anthropogenic attributable warming in GSAT in 2018 of 1.04-1.37°C, to account for the difference in averaging period. The Chapter 7 best estimates and ranges are derived using assessed forcing timeseries and a two-layer energy balance model as described in Section 7.3.5.4. Chapter 7 uncertainty ranges account for uncertainties in climate properties and radiative forcings, without constraints based on observed climate change, but are approximate and will be updated in the final draft. Coloured circles show the raw simulated responses to the forcings concerned in each of the models indicated.

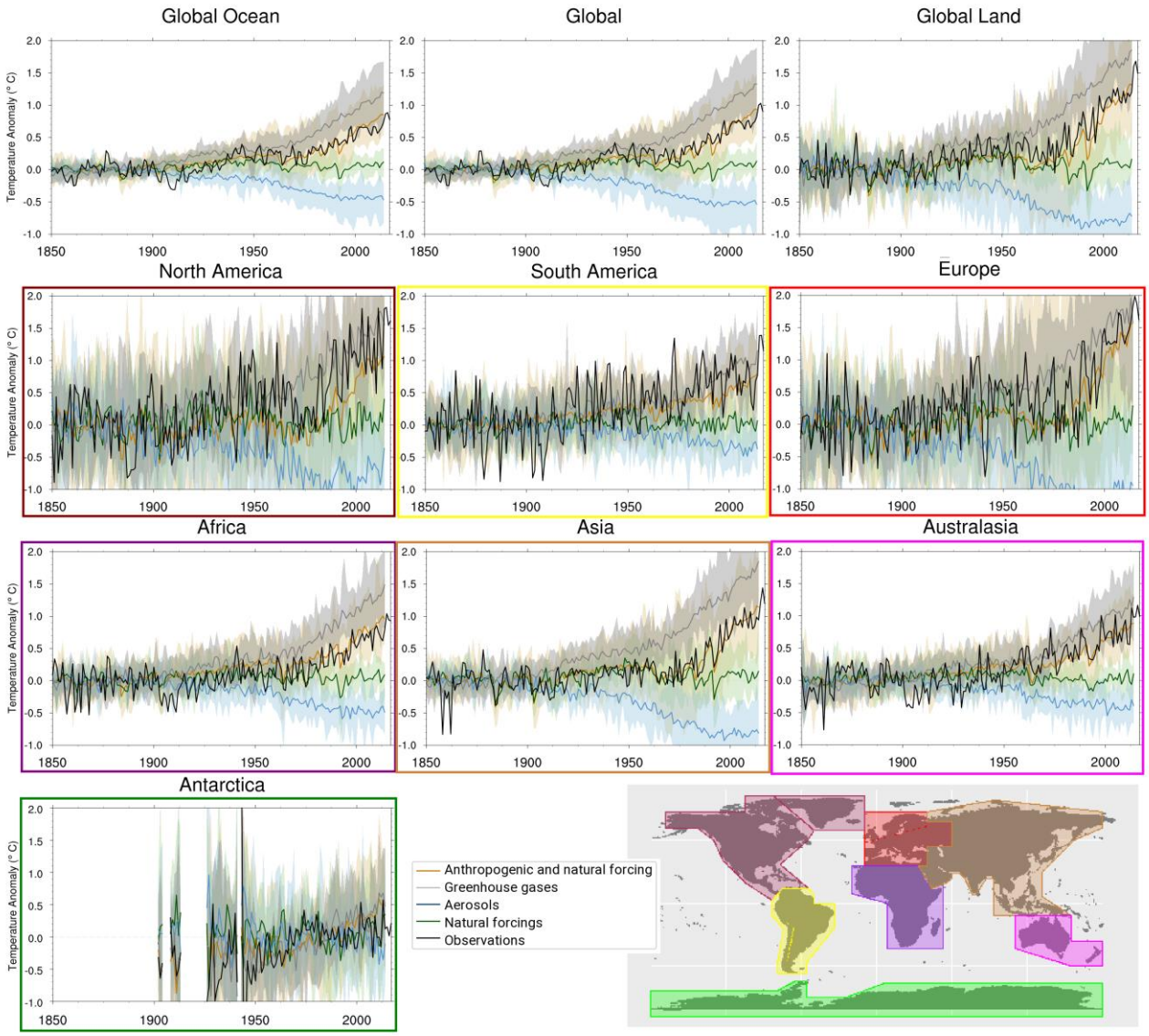

Figure 3.8: Global, land, ocean and continental annual mean temperatures anomalies for CMIP6 historical (brown) hist-nat (green), hist-GHG (grey) and hist-aer (blue) simulations (multi-model means shown as thick lines, and minimum and maximum ranges shown as shaded area) and for Hadley Centre/Climatic Research Unit gridded surface temperature data set 4 (HadCRUT4, black). All models have been subsampled using the HadCRUT4 observational data mask (see Jones et al., 2013). Temperatures are shown with respect to 1850–1900, for Antarctica with respect to 1900–2010. (Figure produced with ESMValTool v2.0.0b3).

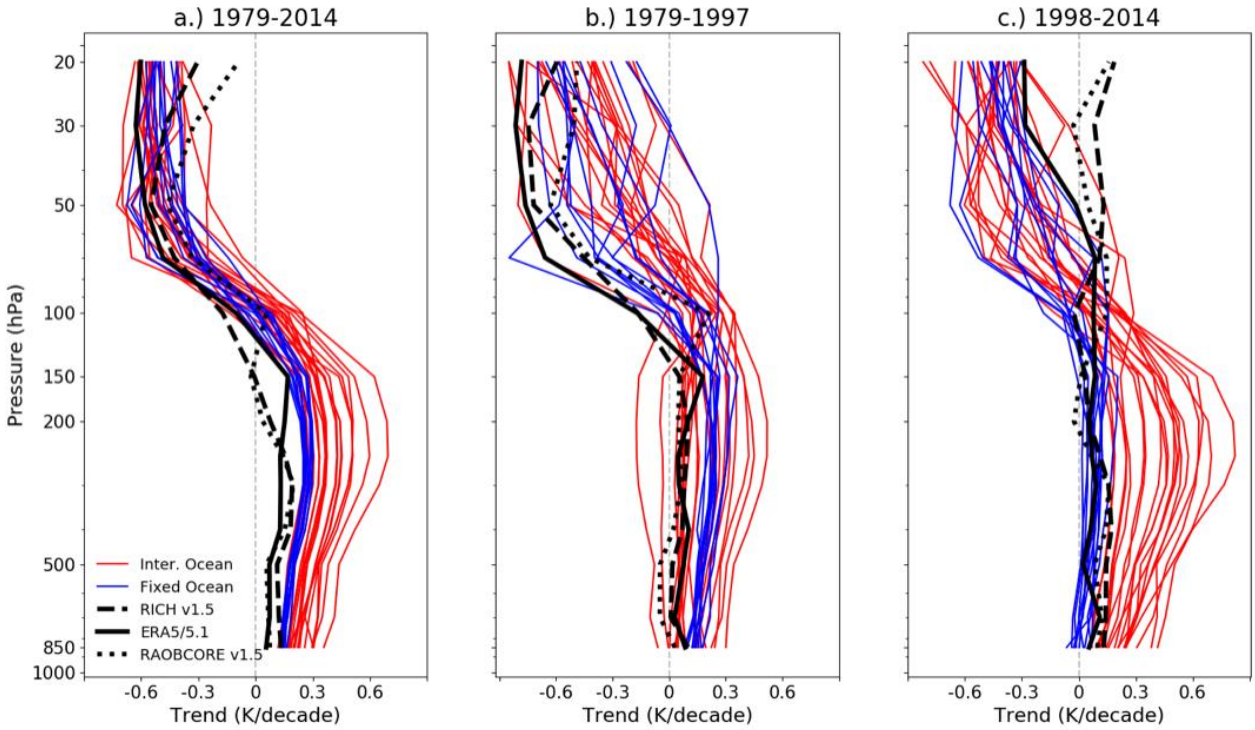

Figure 3.9: Vertical profiles of temperature trends in the tropics (20°S-20°N) for three periods between 1979 and 2014. The black lines show trends in the RICH1.5 and RAOBCORE1.5 radiosonde datasets, and ERA5/5.1 reanalysis. Red lines show trends in 18 CMIP6 models' historical simulations, and blue lines show trends in 18 CMIP6 models' simulations with prescribed sea surface temperatures. Panel a), b) and c) show trends over the periods 1979-2014, 1979-1997 (ozone depletion era), and 1998-2014 (ozone recovery era) respectively. (Figure from Mitchell et al. (submitted), their Figure 1.)

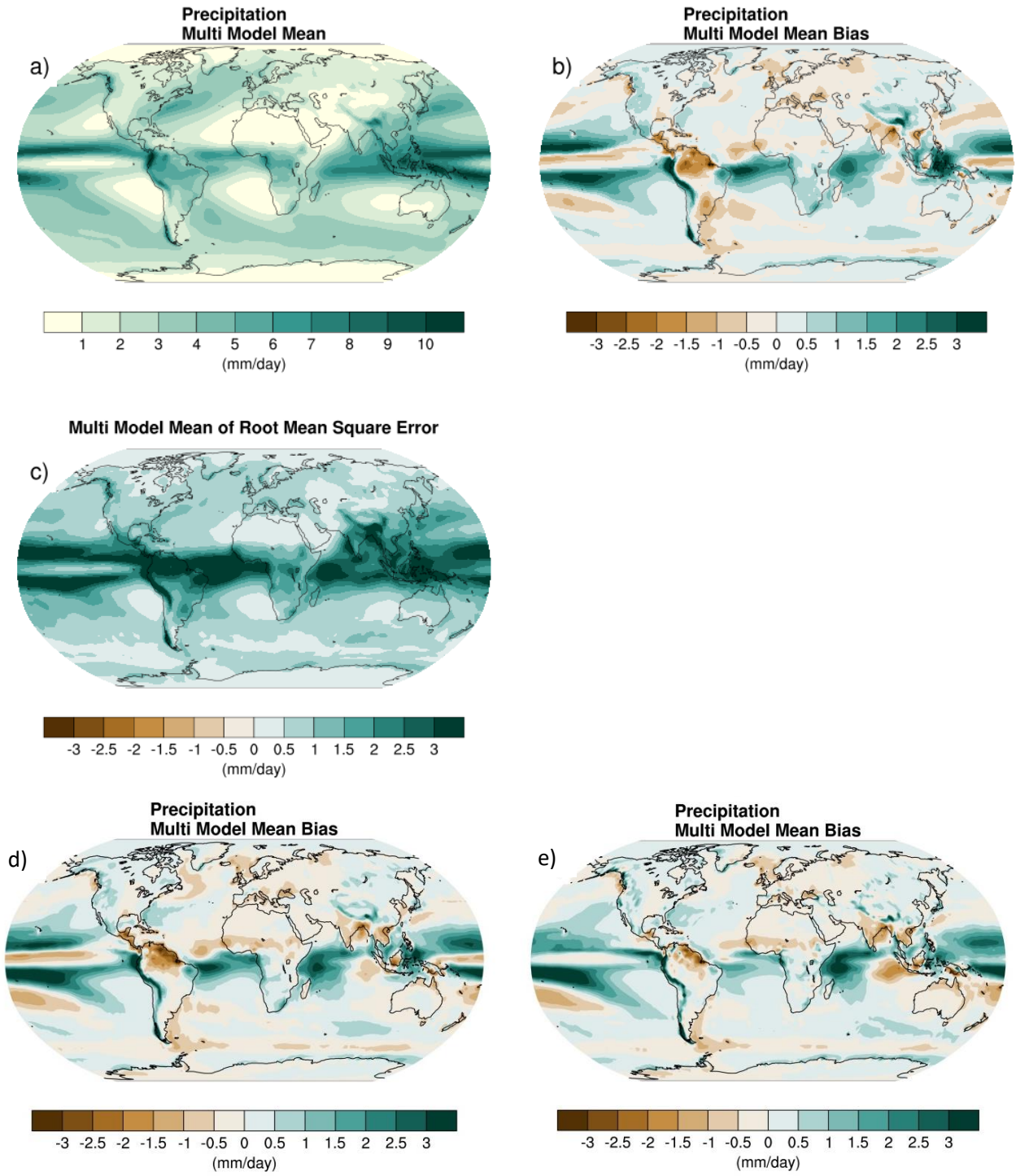

Figure 3.10: Annual-mean precipitation rate (mm day–1) for the period 1995–2014. (a) Multi-model-mean constructed with one realization of CMIP6 (included models: see Fig.3.3) historical experiments (b) Difference between multi-model mean and precipitation analyses from the Global Precipitation Climatology Project (GPCP) version 2.3 (Adler et al., 2003). (c) Multi-model-mean of the root mean square error of the seasonal cycle with respect to precipitation analyses from GPCP v2.3. Also shown is the Multi-model-mean bias as the difference between the multi-model mean of (d) low resolution and (e) high resolution simulations of the HighResMIP and precipitation analyses from GPCP v2.3. (Figure from Bock et al. (submitted), their Figure 3, produced with ESMValTool v2.0.0b3).

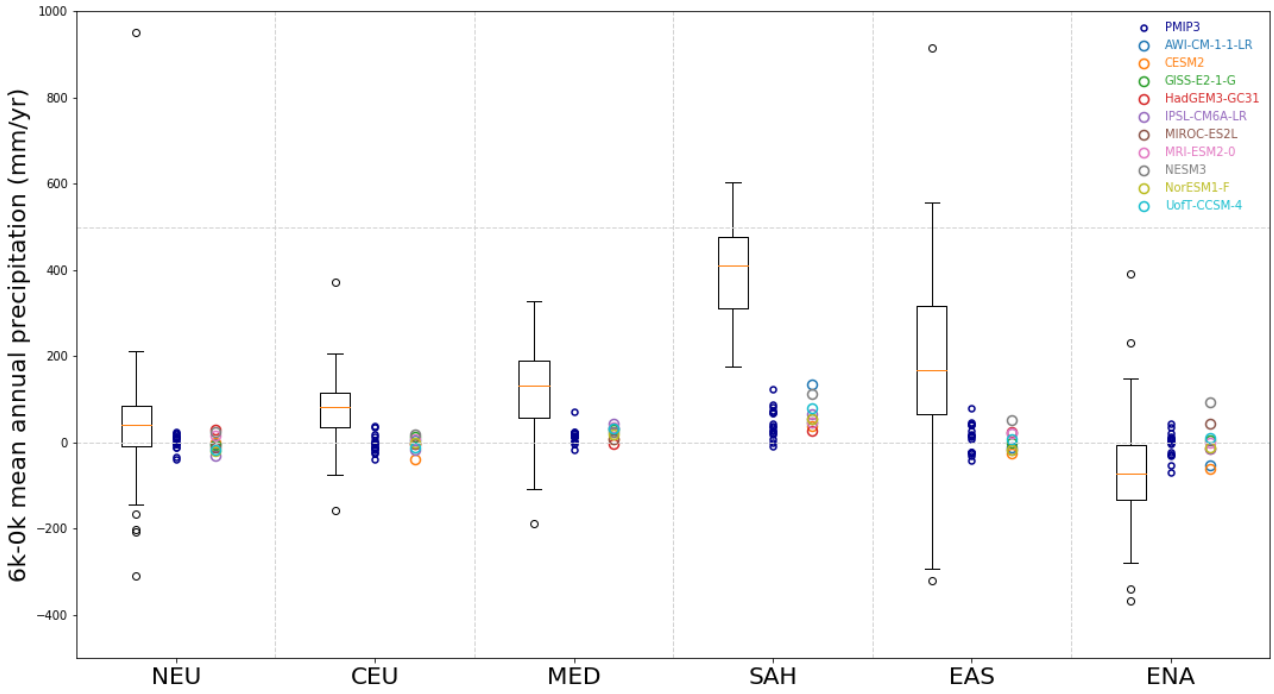

Figure 3.11: Comparison between simulated annual precipitation changes and pollen-based reconstructions. Six regions where multiple quantitative reconstructions exist are chosen. These are Northern Europe (NEU), Central Europe (CEU), the Mediterranean (MED), the Sahara/Sahel (SAH), East Asia (EAS) and Eastern North America (ENA). The distribution of reconstructions within the region are shown by boxes and whiskers. The area-averaged change in mean annual precipitation simulated by CMIP6 (individually identifiable) and CMIP5 (blue) within each region is shown for comparison. (Figure from Brierley and PMIP4 (submitted), their Figure 11).

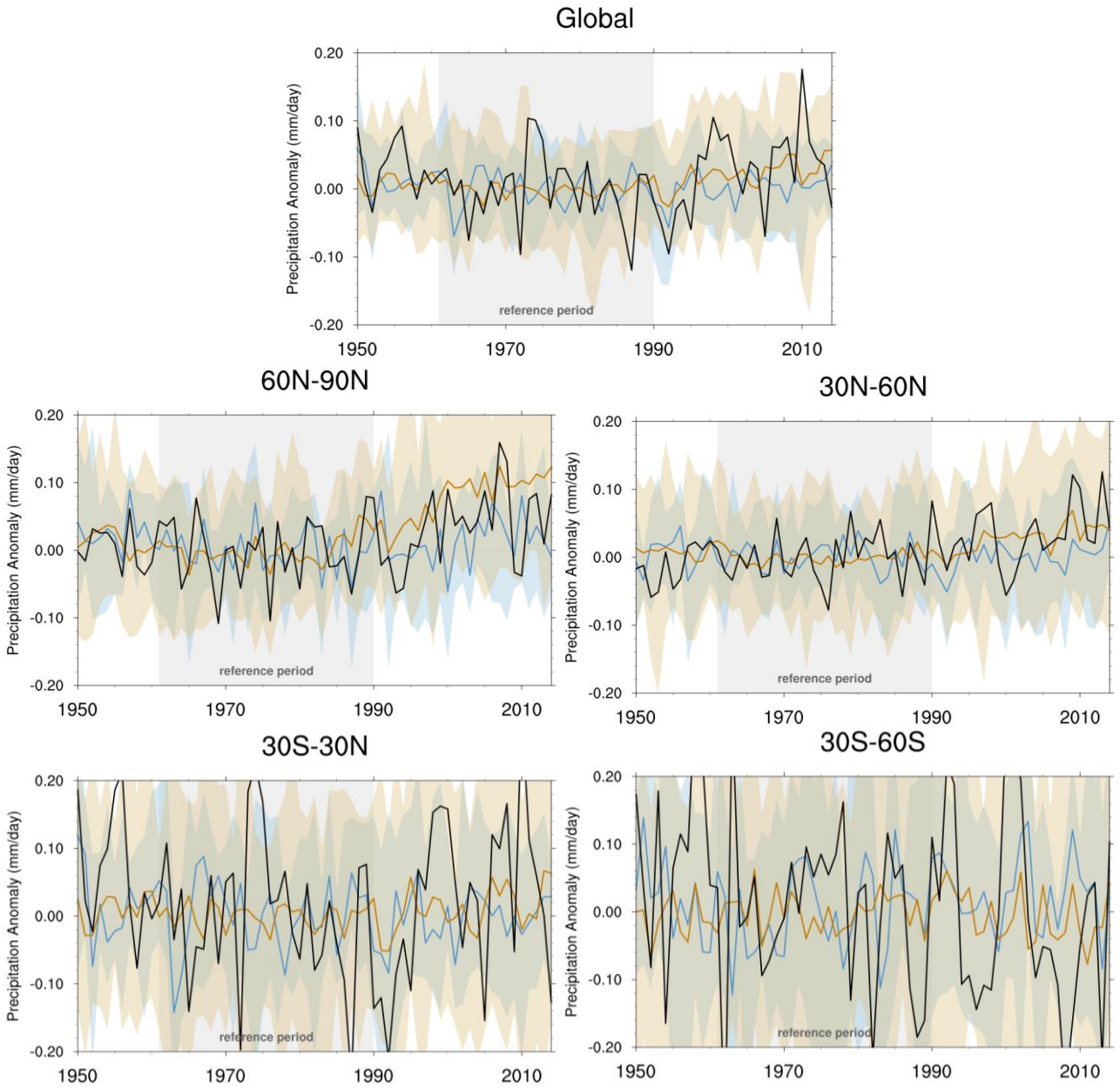

Figure 3.12: Global and zonal average changes in annual mean precipitation (mm day-1) over areas of land where there are observations, expressed relative to the base-line period of 1961–1990, simulated by CMIP6 models forced with both anthropogenic and natural forcings (brown) and natural forcings only (blue). Multi-model means are shown in thick solid lines and shading shows minimum and maximum ranges of the individual model simulations. Observations (gridded values derived from Global Historical Climatology Network station data, updated from Zhang et al. (2007) are shown as a black solid line. (Figure produced with ESMValTool v2.0.0b2.)

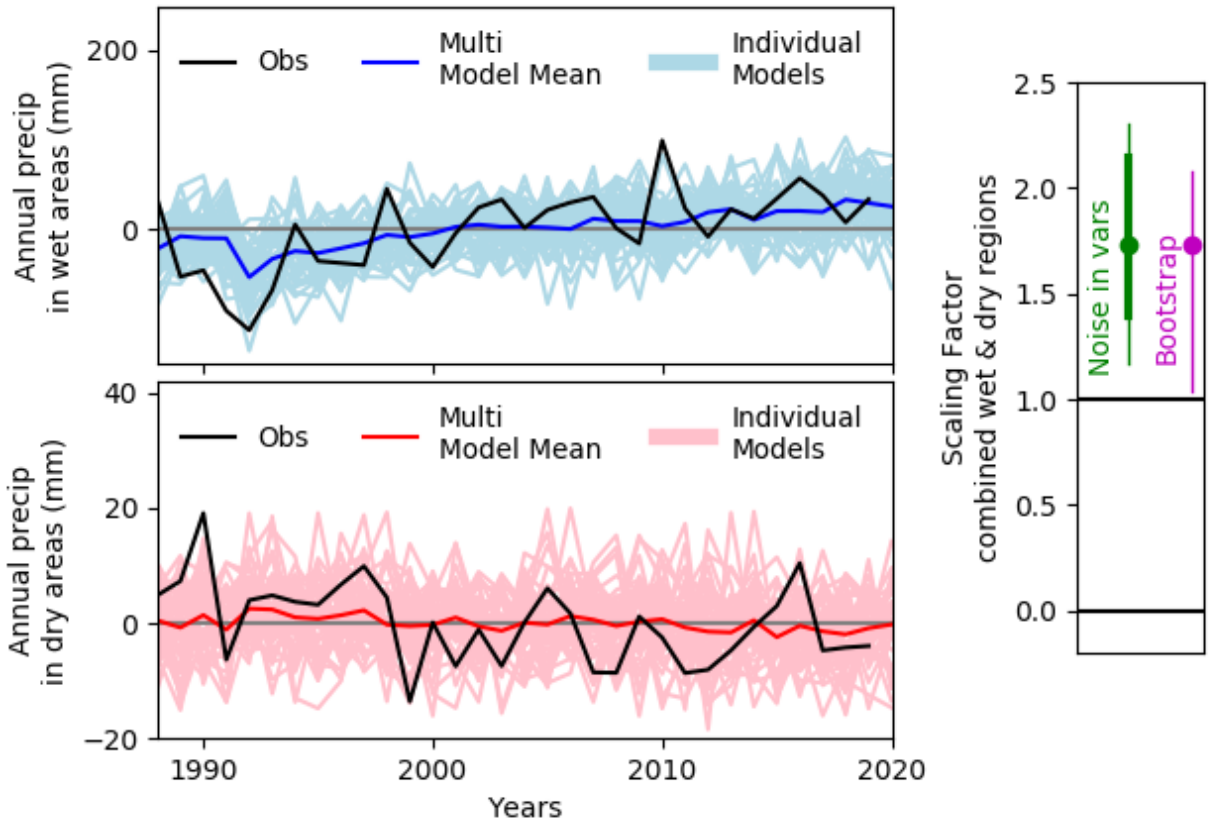

Figure 3.13: Wet (top) and dry (bottom) region tropical mean (30S-30N) annual precipitation anomalies with respect to 1988-2018 (mm) for observations (GPCP - in black) and CMIP6 model simulations (single simulations light blue/red with multi-model-mean in dark blue/red). Wet and dry region annual values are calculated as the mean over 4 seasons (OND, JFM, AMJ, JAS). The regions are defined by the wettest third and driest third by surface area, calculated for the observations and for each model separately for each season (following Polson and Hegerl 2017). Scaling factors (right) are calculated for the combination of the wet and dry region mean, where the observations and all the model simulations are first standardised using the mean standard deviation of piControl simulations. Two total least squares regression methods are used: noise in variables (following Polson and Hegerl 2017) which estimates a best estimate and a 5-95% confidence interval using the piControls (circle and thick green line) and the piControls with double the variance (thin green line); and the bootstrap method (DelSole et al., 2019a) 5-95% confidence interval purple line, best estimate purple circle.

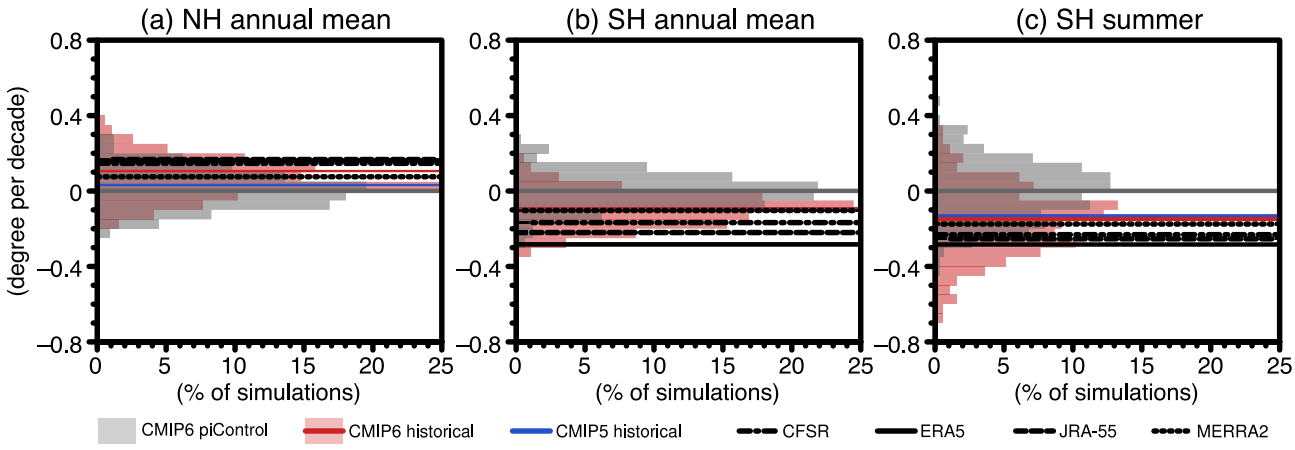

Figure 3.14: 1980-2013 trend of subtropical edge latitude of the Hadley cells in (a) the Northern Hemisphere for annual mean and (b-c) Southern Hemisphere for (b) annual mean and (c) DJF. Positive values indicate northward shifts. Histograms are based on historical (red) and 34-year segments of piControl (grey) simulations of CMIP6. Horizontal lines indicate MME means of historical simulations of CMIP6 (red) and CMIP5 (blue; extended with RCP4.5) along with reanalyses. The edge latitude is defined where the surface zonal wind velocity changes sign from negative to positive, as described in the Appendix of Grise et al., (2018). Produced with 22 CMIP6 models (192 members of historical and 338 segments of piControl simulations) and 20 CMIP5 models (99 members).

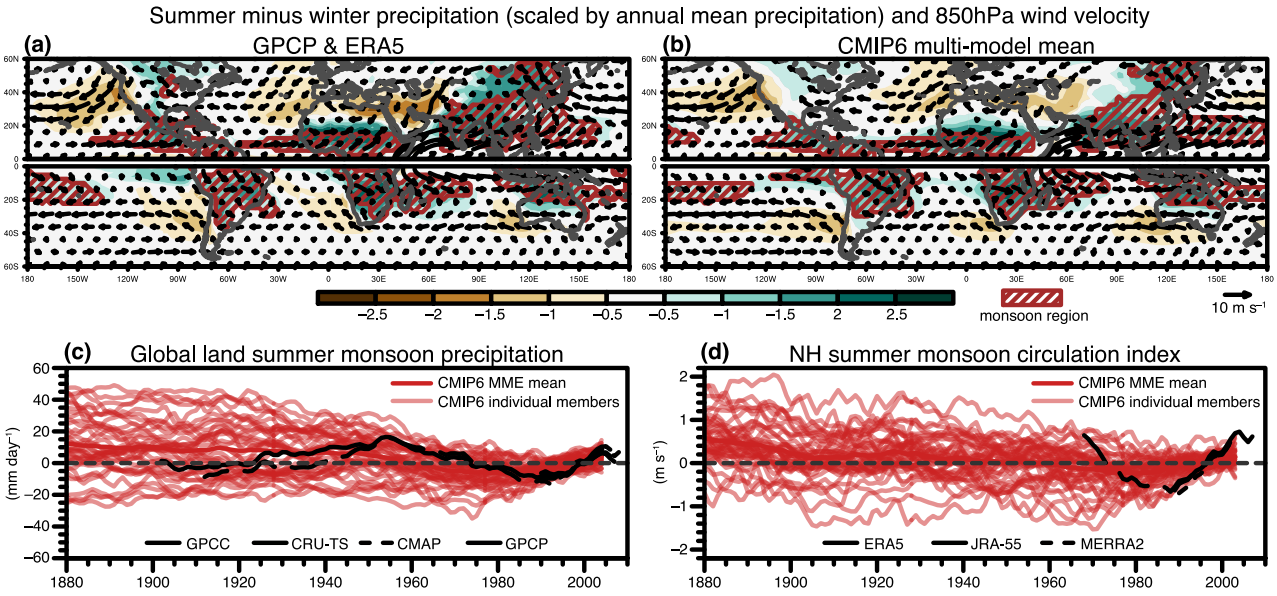

Figure 3.15: (a-b) Climatological summer-winter range of precipitation rate (scaled by annual mean precipitation rate; shading) and 850 hPa wind velocity (arrows) based on (a) GPCP and ERA5 and (b) MME mean of CMIP6 historical simulations for 1979-2014 (1 member each). Hatched regions are the monsoon domain based on the definition by (Wang and Ding, 2008) (c-d) 20-year running means of (c) summertime precipitation rate averaged over the monsoon regions over land (mm day^{-1}) and (d) the NH summer monsoon circulation index defined as the vertical shear of zonal winds between 850 and 200 hPa levels averaged over 0º-20ºN, 120ºW-120ºE (Wang et al., 2013; m s^{-1}). Summer and winter are defined for individual hemispheres: May through September for NH summer and SH winter, and November through March for NH winter and SH summer. Produced with 40 CMIP6 models (each 1 member).

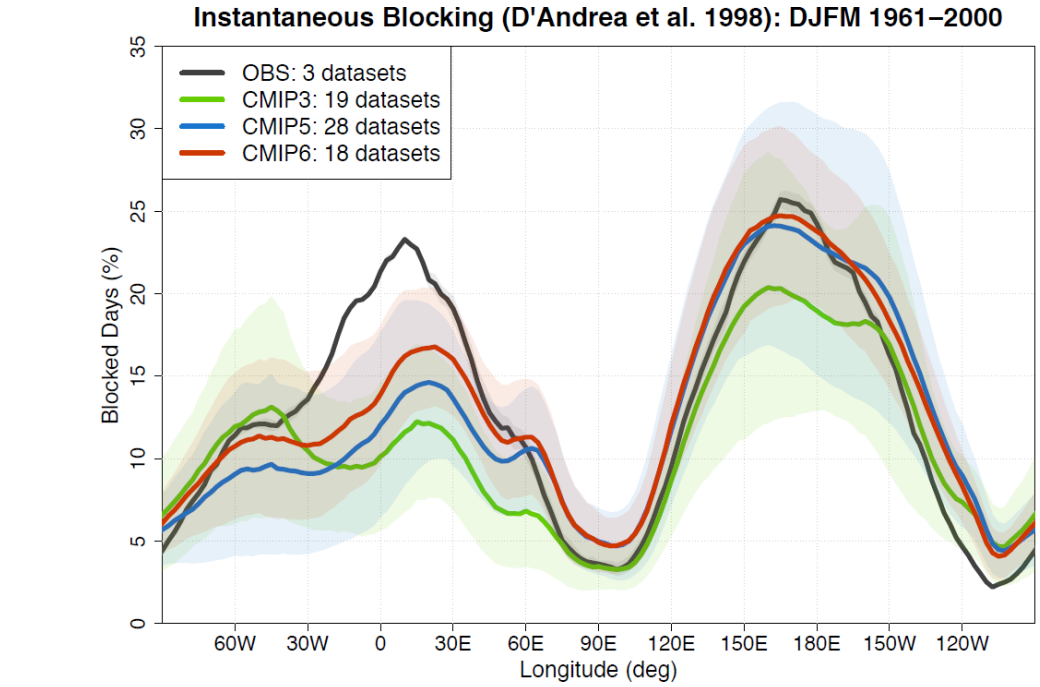

HighResMIP:

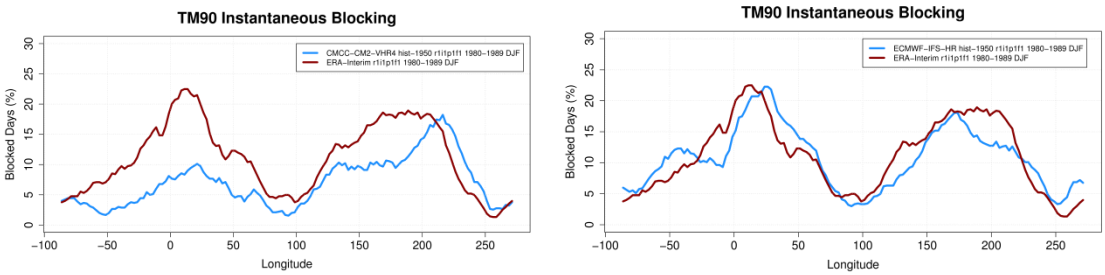

Figure 3.16: Instantaneous Northern-Hemisphere blocking frequency (% of days) in the extended northern winter season (DJFM) following the (D'Andrea et al., 1998) definition of blocking, for the years 1961-2000. Reproduced from (Davini and D'Andrea, submitted), their figure 11. Note the good simulation of Pacific blocking but a persistent remaining underestimation of the blocking frequency in the Euro-Atlantic sector. The lower two panels show the results from two HighResMIP models. (Figure produced with ESMValTool v2.0a1.)

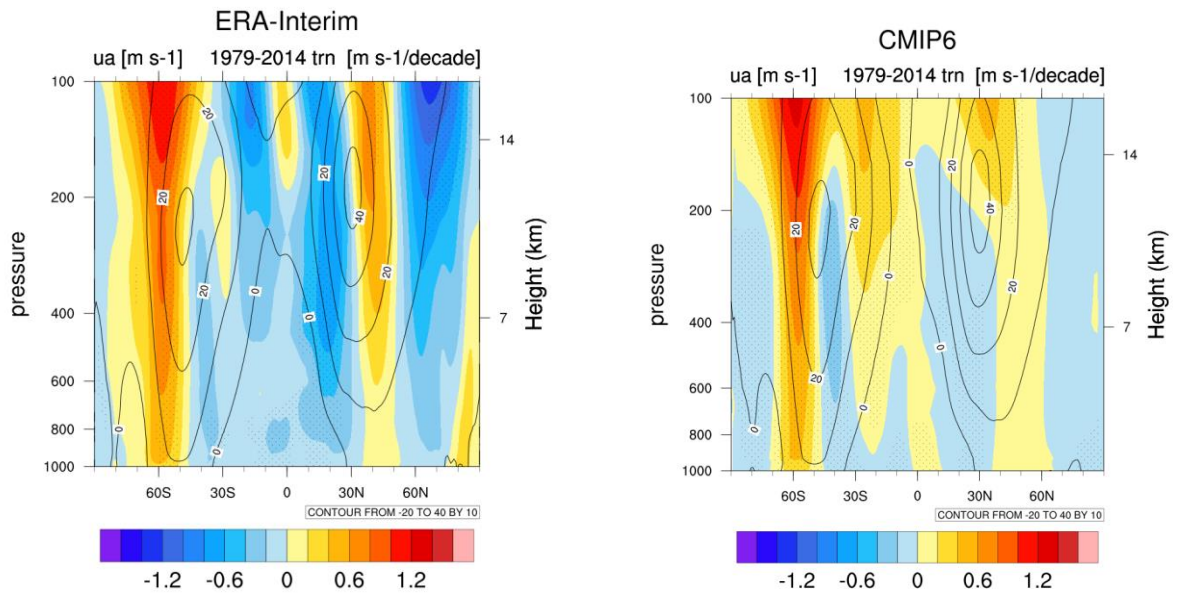

Figure 3.17: Long-term mean (thin black contour) and linear trend (colour) of zonal mean DJF zonal winds for (a) ERA-Interim and (b) CMIP6 over 1979-2014. Only one ensemble member per model is included. (Figure produced with ESMValTool v1.0.)

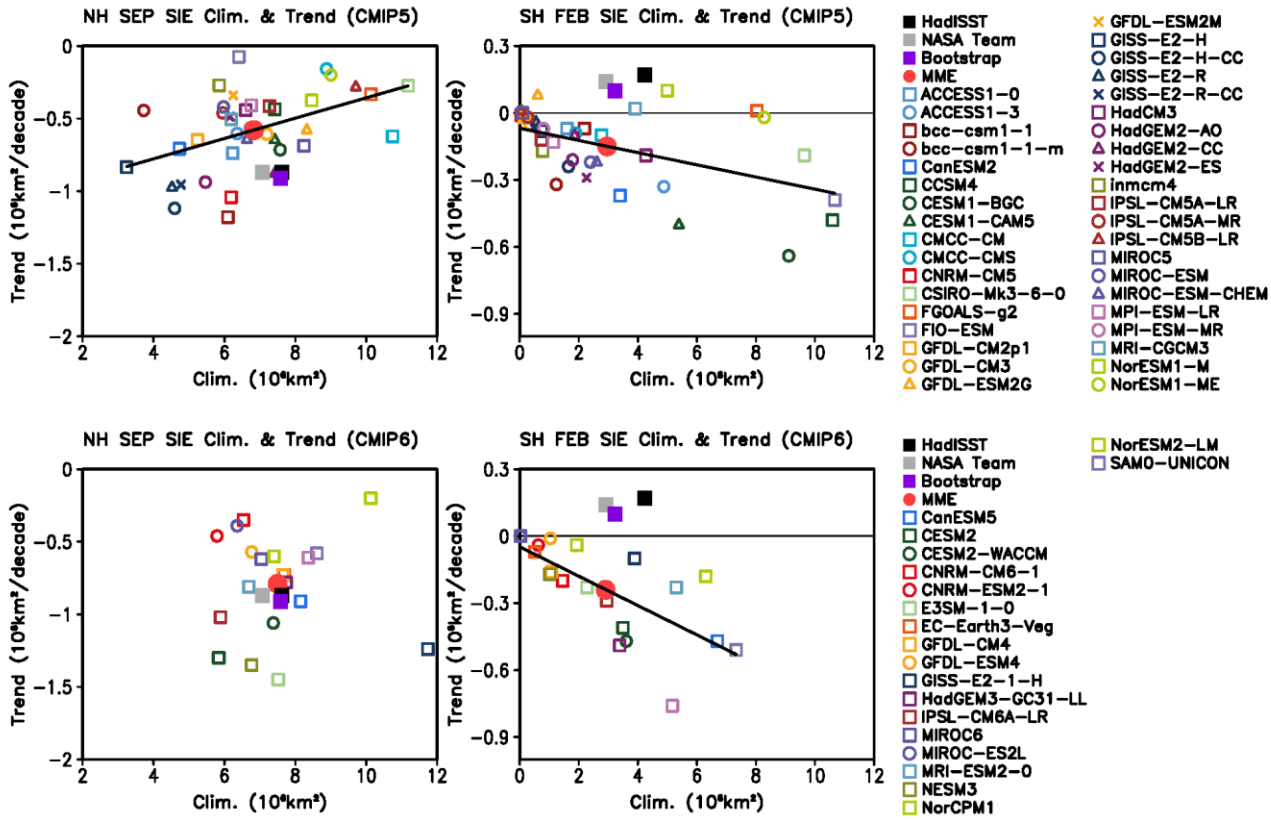

Figure 3.18: Climatology (x-axis) and trend (y-axis) in Arctic sea ice extent in September (left) and Antarctic sea ice extent in February (right) for 1979-2014 from CMIP5 (upper) and CMIP6 (lower) models. All individual models (ensemble means) and the multi-model mean values are compared with the observations (HadISST, NSIDC NASA Team, and NSIDC Bootstrap). Solid line indicates a linear regression slope which is statistically significant at 5% level.

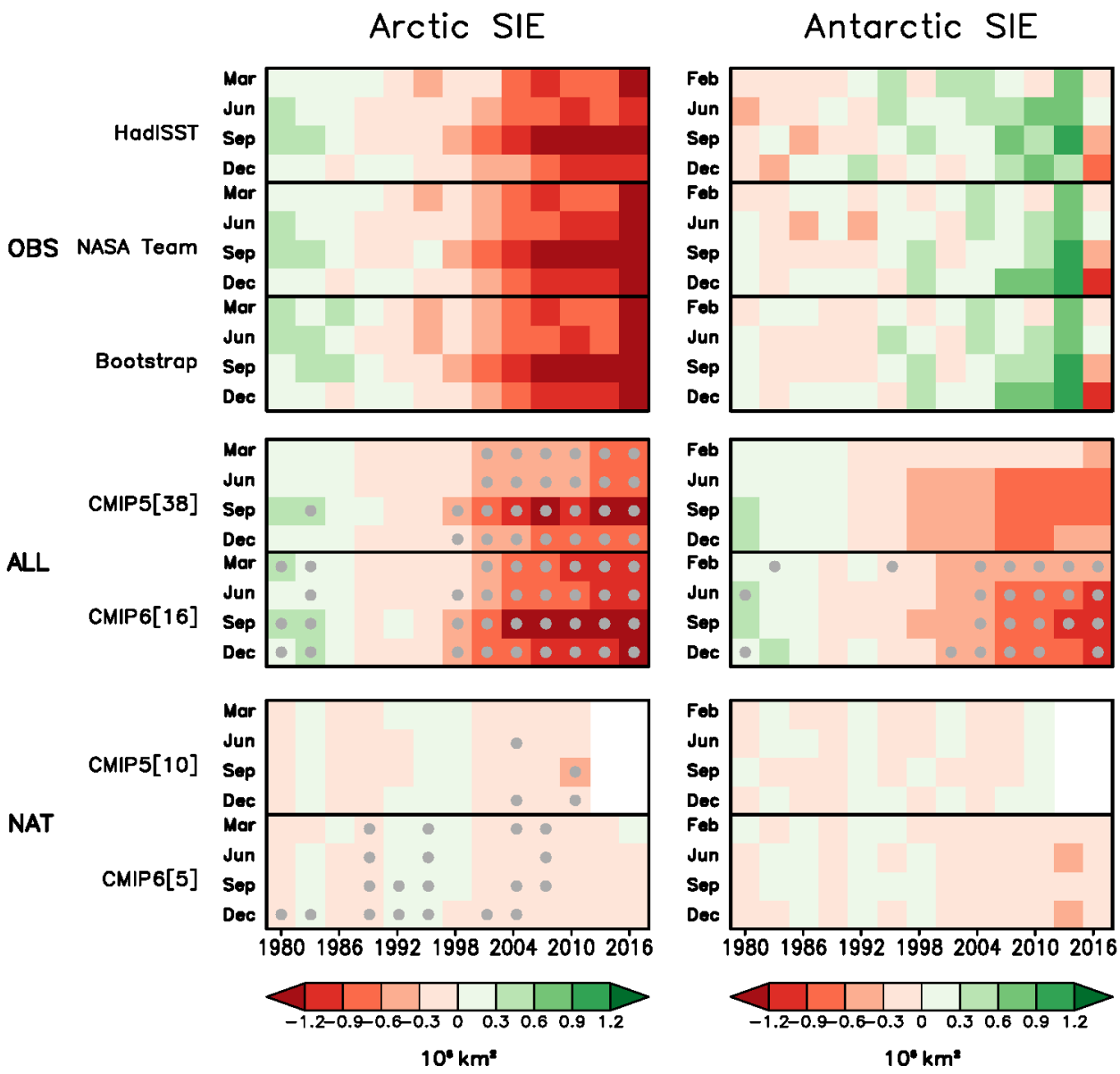

Figure 3.19: Seasonal evolution of observed and simulated Arctic (left) and Antarctic (right) sea ice extent (SIE) over 1979–2017. SIE anomalies relative to the 1979–2000 means from observations (OBS from HadISST, NASA Team, and Bootstrap, top) and historical (ALL, middle) and hist-nat (NAT, bottom) simulations from CMIP5 and CMIP6 multi-models. These anomalies were obtained by computing non-overlapping 3-year mean sea ice anomalies for March (February for Antarctic SIE), June, September, and December separately. CMIP5 ALL runs are extended by using RCP4.5 scenario runs after 2005 while CMIP6 ALL runs are extended by using SSP2-4.5 scenario runs after 2014. CMIP5 NAT runs ends in 2012. Number in bracket represents the number of models used. The multi-model mean is obtained by taking the ensemble mean for each model first and then averaging over models. Grey dots indicate multi-model mean anomalies stronger than inter-model spread (beyond ± 1 standard deviation). Units: 10^6 km^2.

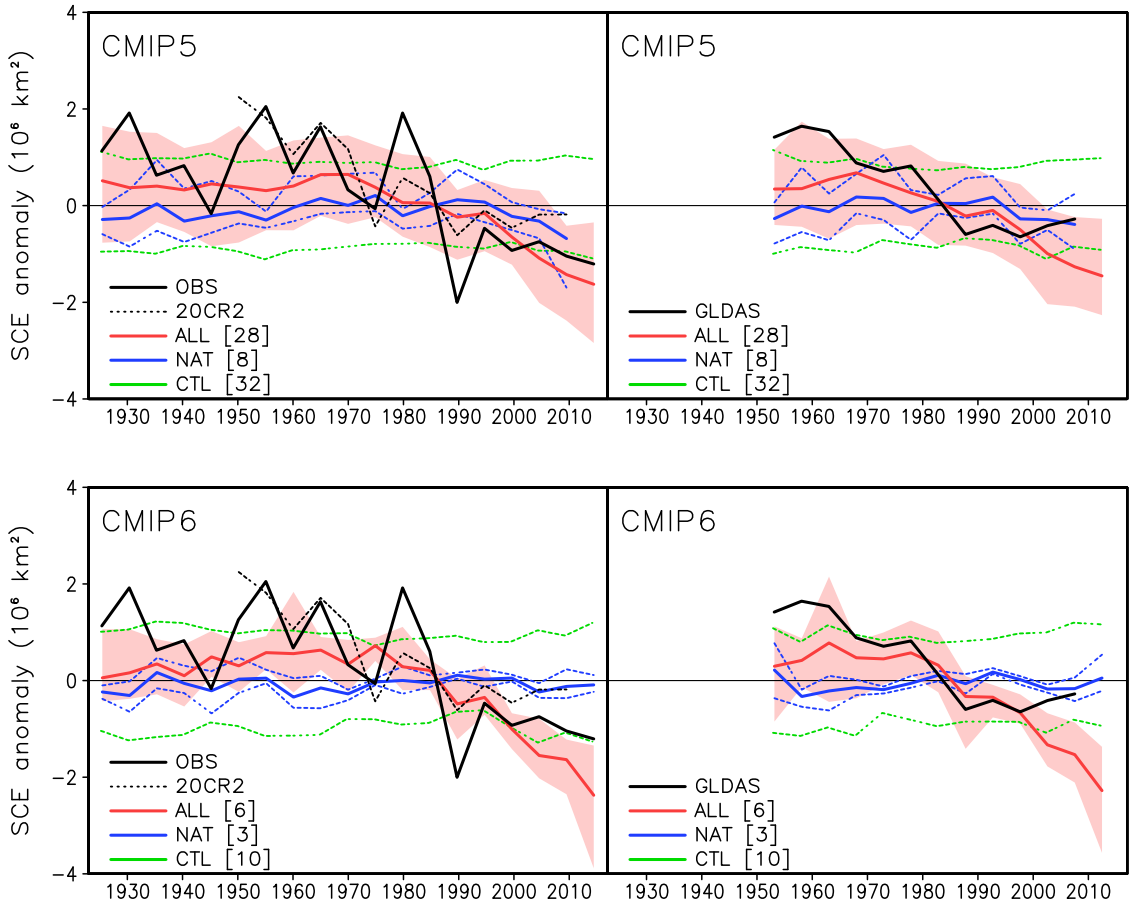

Figure 3.20: Time series of Northern Hemisphere March-April mean snow cover extent (SCE) from observations [OBS: Brown and Robinson (2011), 20CR2, and GLDAS2 data], CMIP5 (upper) and CMIP6 (lower) models' simulations of the response to natural plus anthropogenic forcing (ALL), natural forcing only (NAT), and pre-industrial control simulations (CTL). 5-year mean anomalies are shown for the 1923-2017 period (left) and 1951-2015 period (right) with the *x*-axis representing the centre years of each 5-year mean. CMIP5 ALL simulations are extended by using RCP4.5 scenario simulations after 2005 while CMIP6 ALL simulations are extended by using SSP2-4.5 scenario simulations after 2014. ALL and NAT results are based on ensemble means for each model while CTL results are based on all available non-overlapping segments. Shading indicates the 5-95% range of CMIP5 ALL simulations and min-max range of CMIP6 ALL simulations. Blue dotted lines represent min-max ranges of NAT simulations while green dotted lines indicate 5-95% ranges of CTL simulations. Number in brackets indicate the number of models used. Anomalies are relative to the average over 1971-2000. For models, SCE is restricted to ice-free land (ice-free fraction ≥ 25%). Greenland is excluded from the spatial averages as it contains essentially perennial snow cover. (Updated from Najafi et al. (2016), their Figure 3).

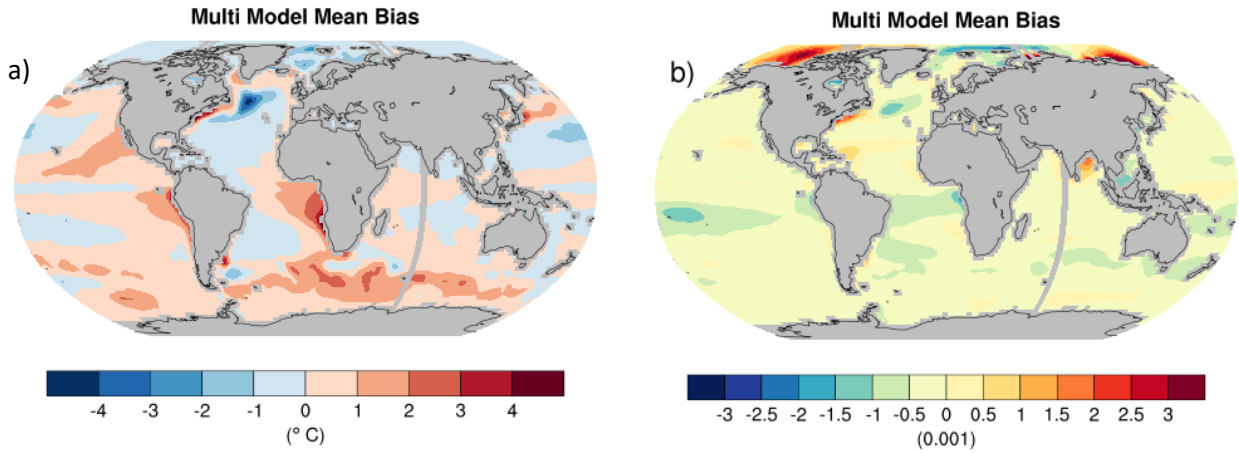

Figure 3.21: Multi-model-mean bias of (a) sea surface temperature (°C) and (b) surface salinity as the difference between the CMIP6 multi-model mean constructed with one realization of CMIP6 historical experiments and the climatology from the World Ocean Atlas 2013 for the period 1995–2014. (Figure produced with ESMValTool v2.0.0b3.)

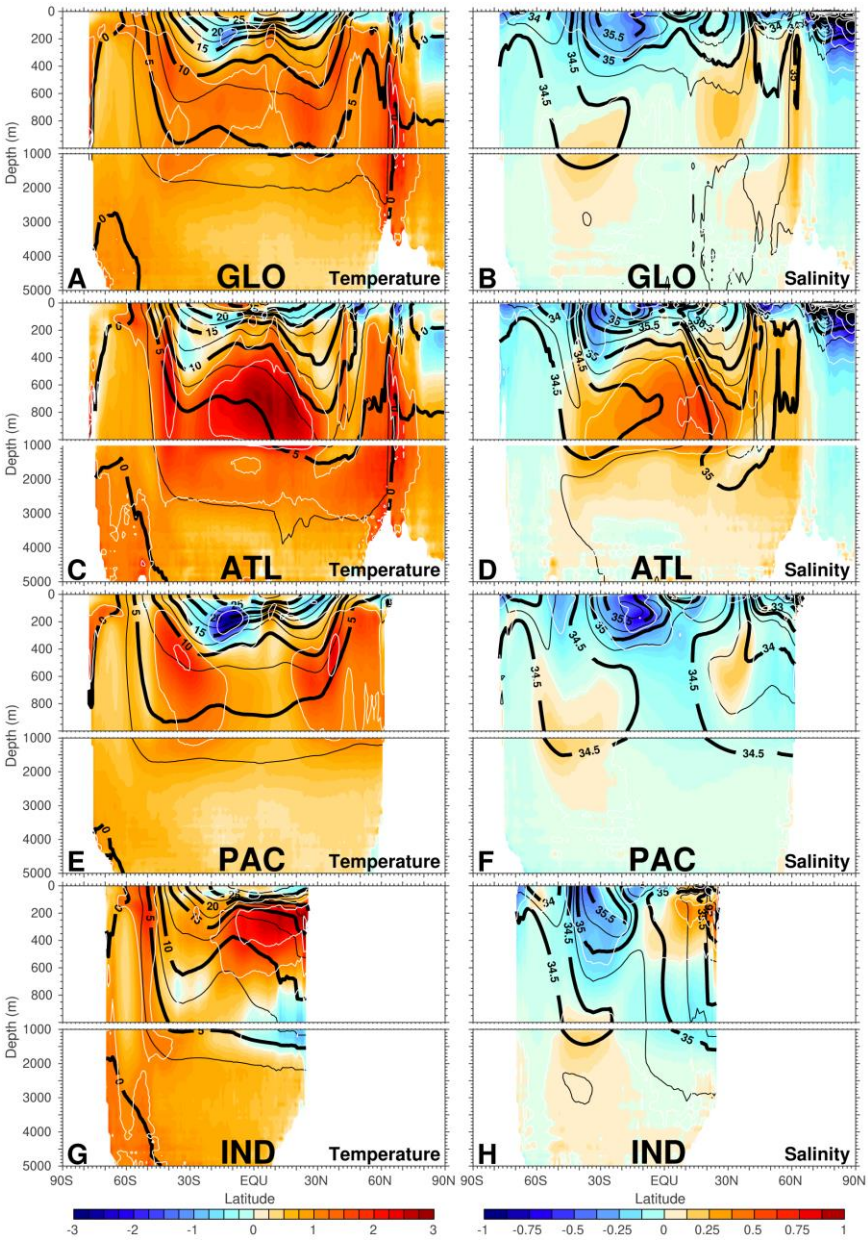

Figure 3.22: (a,c,e,g) Potential temperature (degrees C) and (b,d,f,h) salinity (PSS-78) for each of the ocean basins, global (GLO; a,b), Atlantic (ATL; c,d), Pacific (PAC; e,f) and Indian (IND; g,h). Shown in colour are the time-mean differences between the CMIP6 historical ensemble climatological mean and observations, zonally averaged for each basin (excluding marginal and regional seas). The observed climatological values are obtained from the World Ocean Atlas 2018 (WOA18; Prepared by the Ocean Climate Laboratory, National Oceanographic Data Center, Silver Spring, MD, USA), and are shown as labelled black contours for each of the basins. White contours show regions in potential temperature (left column) where the differences exceed positive or negative 1, 2, or 3 (degrees C), and regions in salinity (right column) where the differences exceed positive or negative 0.25, 0.5, 0.75 or 1 (PSS-78). The simulated annual mean climatologies are obtained for 1984 to 2014 from available CMIP6 historical simulations, whereas WOA18 synthesizes observed data from 1874 to 2018 in calculations of the decadally averaged annual mean; however, the median time for gridded observations most closely resembles the more modern era. Multiple realizations from individual models are first averaged to form a single model ensemble climatology, before construction of the CMIP6 multi-model mean from these fields. A total of 20 available CMIP6 models have contributed to the temperature panels (left column) and 21 models to the salinity panels (right column).

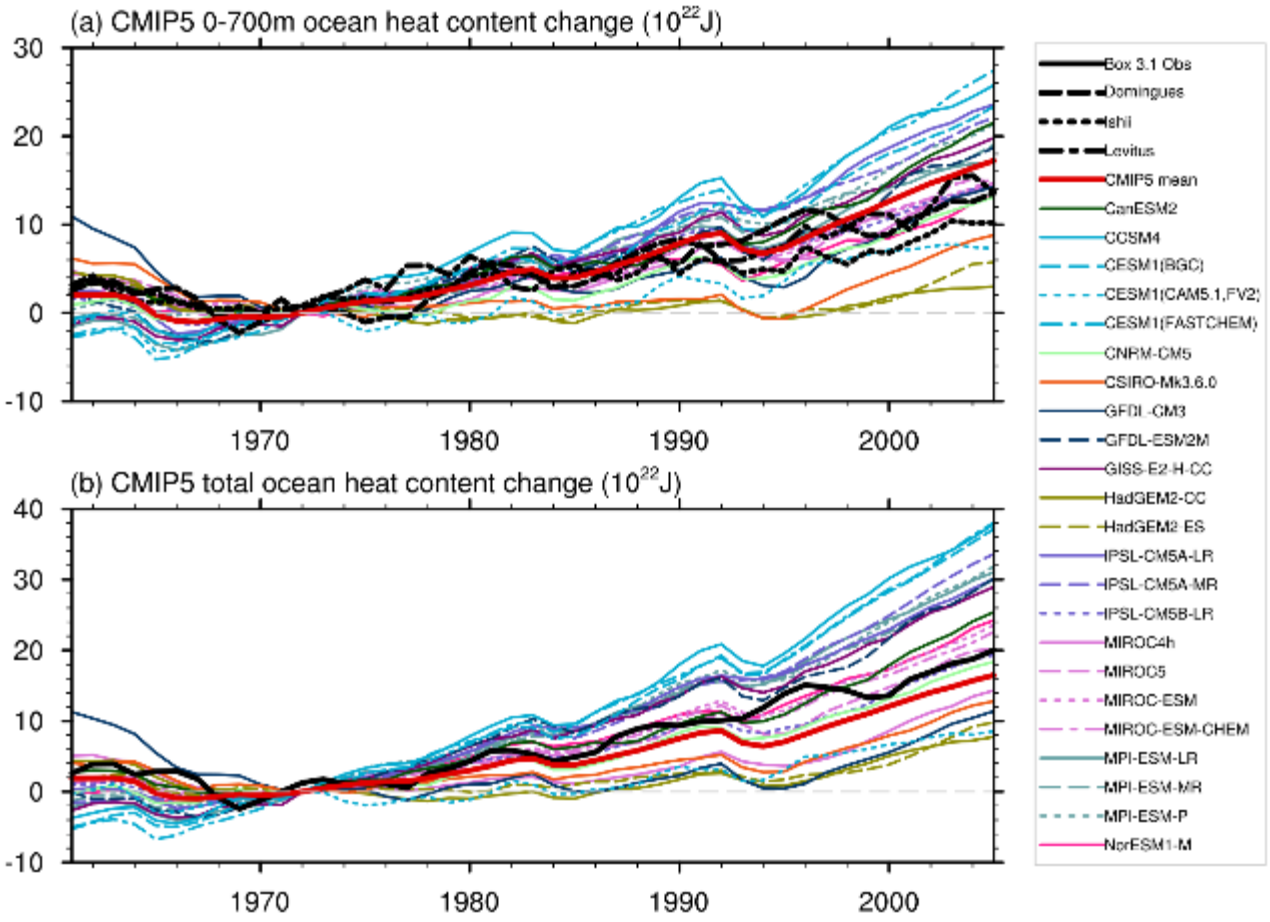

Figure 3.23: Time series of simulated and observed global ocean heat content anomalies (with respect to 1971). CMIP5 historical simulations and observations for both the upper 700 m of the ocean (a) as well as for the total ocean heat content (b). The 0 to 700 m and total heat content observational estimates (thick lines) are respectively described in AR5 Figure 3.2 and AR5 Box 3.1, Figure 1. Simulation drift has been removed from all CMIP5 runs with a contemporaneous portion of the quadratic fit to each corresponding pre-industrial control run (Gleckler et al., 2012). Units are 10^{22} Joules.

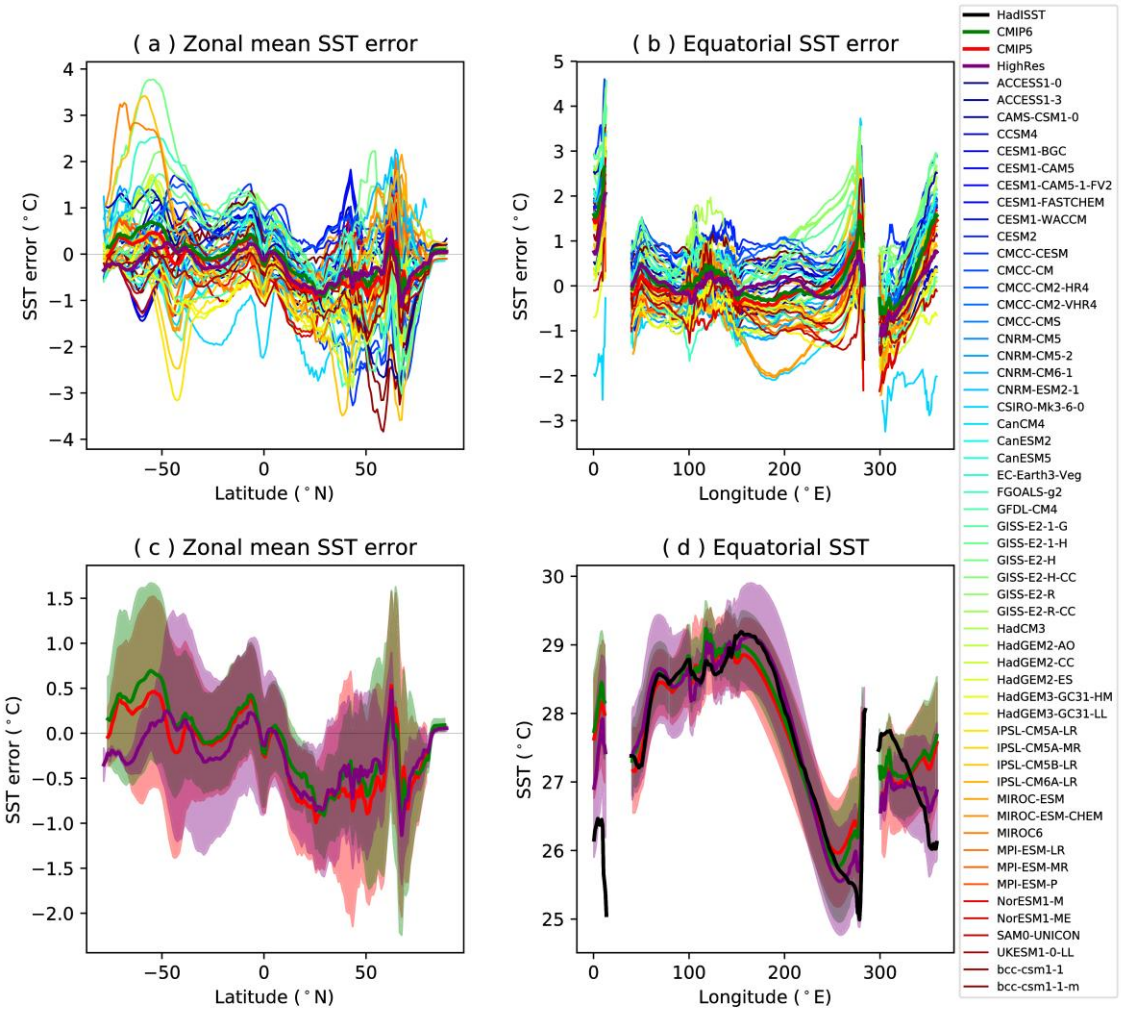

Figure 3.24: (a) Zonally-averaged sea surface temperature (SST) error in CMIP6 models. (b) Equatorial SST error in CMIP6 models. (c) Zonally averaged multi-model mean SST error for CMIP6 (green curve), CMIP5 (red curve) and HighresMIP (purple curve), together with inter-model standard deviation (shading). (d) Equatorial multi-model mean SST in CMIP6 (green curve), CMIP5 (red curve) and HighresMIP (purple curve) together with inter-model standard deviation (shading) and observations (black). Model climatologies are derived from the 1979-1999 mean of the historical simulations. The Hadley Centre Sea Ice and Sea Surface Temperature (HadISST) (Rayner et al., 2003) observational climatology for 1979-1999 is used as the reference for the error calculation in (a), (b) and (c); and for observations in (d).

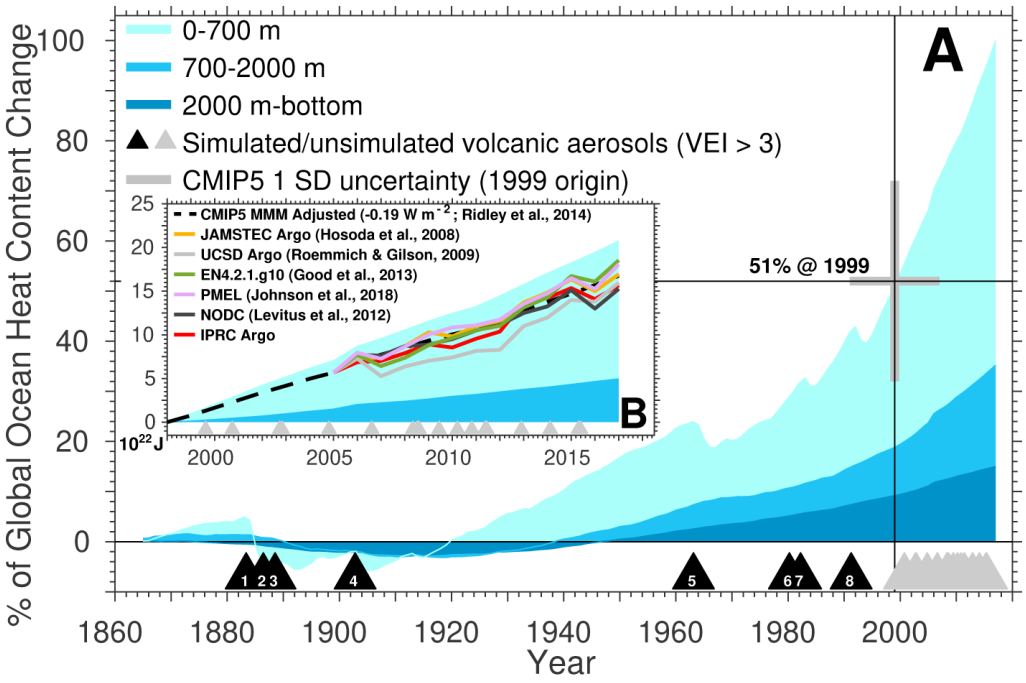

Figure 3.25: (a) Ocean heat uptake (percentage of total 1865-2017 change) for the CMIP5 multi-model mean layers. The three shaded wedges are combined similarly to the AR5 change in global inventory (Rhein et al. (2013); Box 3.1, Figure 1). The thick vertical grey bar represents a +/- one standard deviation spread from the CMIP5 simulations about the year (1999) at which the multi-model heat uptake reaches 50% of the net (1865-2017) industrial-era increase, and the thick horizontal grey bar indicates the CMIP5 +/- one standard deviation spread om the year at which 50% of the total accumulated heat is reached. Black (forcing included) and grey (forcing not included) triangles represent major twentieth- and twenty-first-century volcanic eruptions with magnitude (volcanic explosivity index [VEI] represented by symbol size. (b) The inset box displays the upper and intermediate layer warming for the years 1998 to 2017, with an adjustment for the 0 to 2000 m total warming by -0.19 W m-2, the estimated discrepancy between CMIP5 modelled and the observed volcanic forcing (Ridley et al., 2014). When observed 0 to 2000 m ocean warming is compared across five independent available estimates these rates of change are approximately equal. (Figure from Durack et al., 2018, their Figure 2).

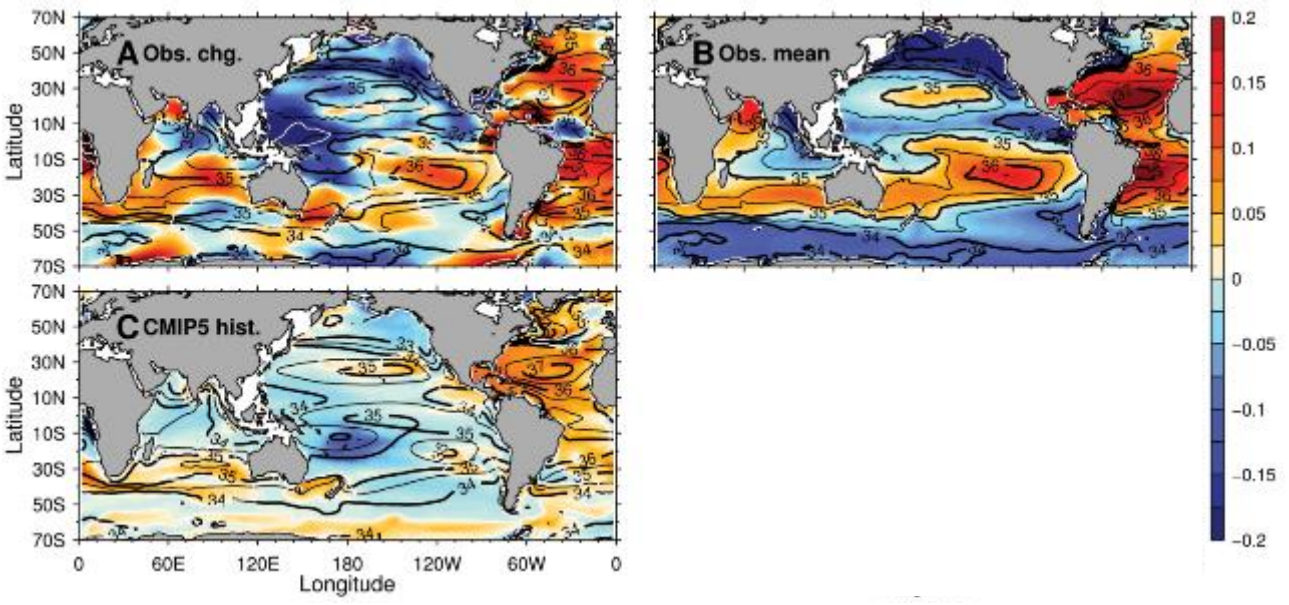

Figure 3.26: Maps of 50-year salinity trends for the near-surface ocean. (a) the 1950-2000 observational change and (b) the corresponding 1950-2000 climatological mean (Durack and Wijffels, 2010) (analysis period 1950-2008). (c) Modelled changes for the 1950-2000 period from the CMIP5 historical experiment multi-model mean. Black contours bound the climatological mean salinity associated with each map, and white contours bound the salinity trend in increments of 0.25 (PSS-78). (Figure from Durack, 2015, their Figure 7).

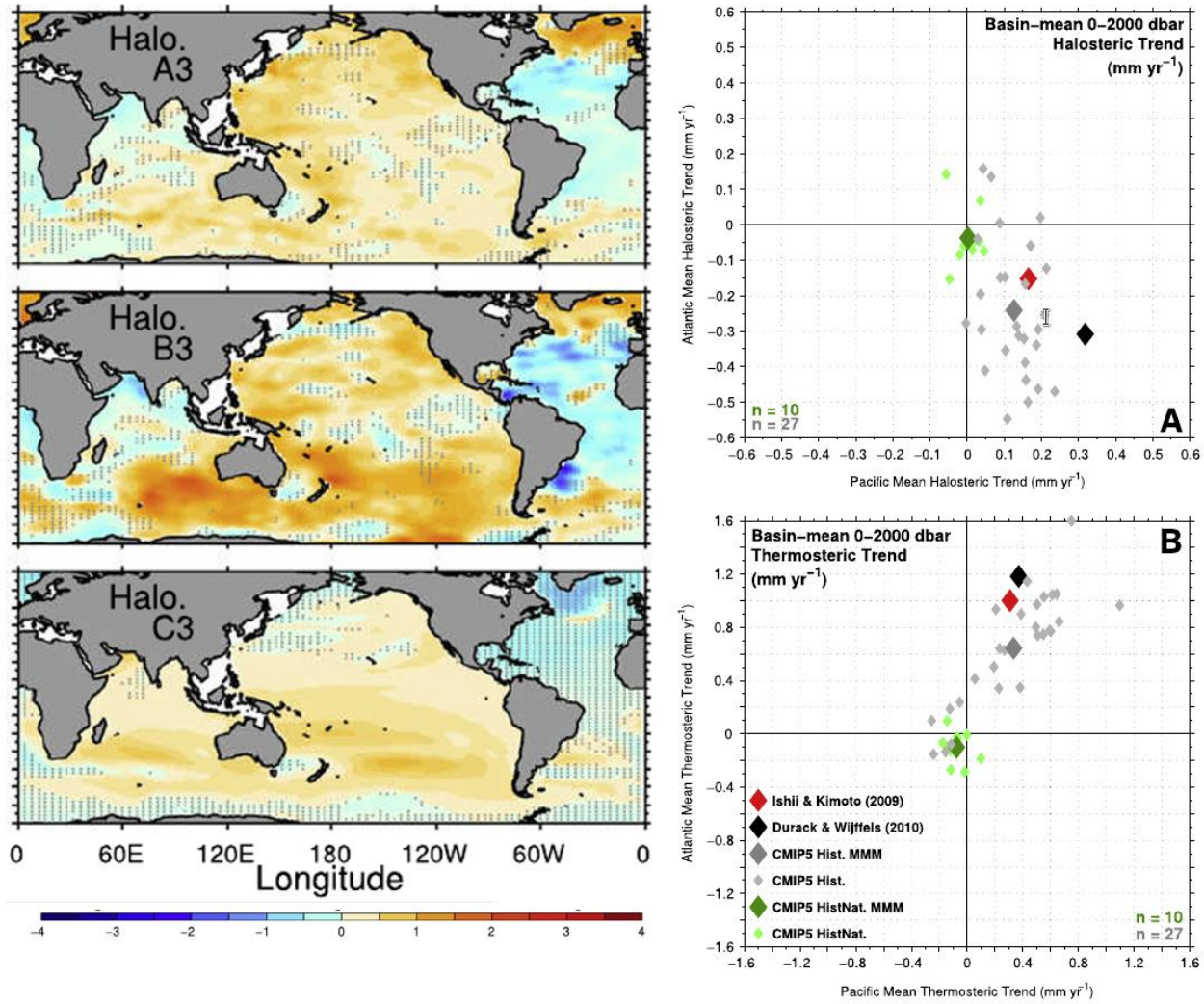

Figure 3.27: Long-term trends in 0 to 2000 dbar total halosteric (salinity-driven) sea level anomaly, and the contrast of basin-integrated results for the Pacific and Atlantic Oceans compared to CMIP5 models. Units are mm year-1. Maps of 0 to 2000 dbar halosteric anomalies (left column, a3, b3 and c3) from (Ishii and Kimoto, 2009, a3), (Durack and Wijffels, 2010, b3) and the CMIP5 historical multi-model mean (c3). Blue colours show a halosteric contraction (enhanced salinity) and orange a halosteric expansion (reduced salinity). Stippling is used to mark regions where the two observational estimates do not agree in their sign (a3, b3) and where less than 50% of the contributing models do not agree in sign with the multi-model mean map from the ensemble. Basin-integrated halosteric (right column, top panel A) and thermosteric (right column, panel B) anomalies for the Pacific, where Pacific anomalies are presented on the x-axis and Atlantic on the y-axis. Observational estimates are presented in the red (Ishii and Kimoto, 2009) and black (Durack and Wijffels, 2010) diamonds, CMIP5 historical models are shown in grey diamonds, with the multi-model mean in dark grey, and CMIP5 historicalNat models are shown in green diamonds with the multi-model mean in dark green. (Figure from Durack et al. (2014b), their Figures 1 and 4).

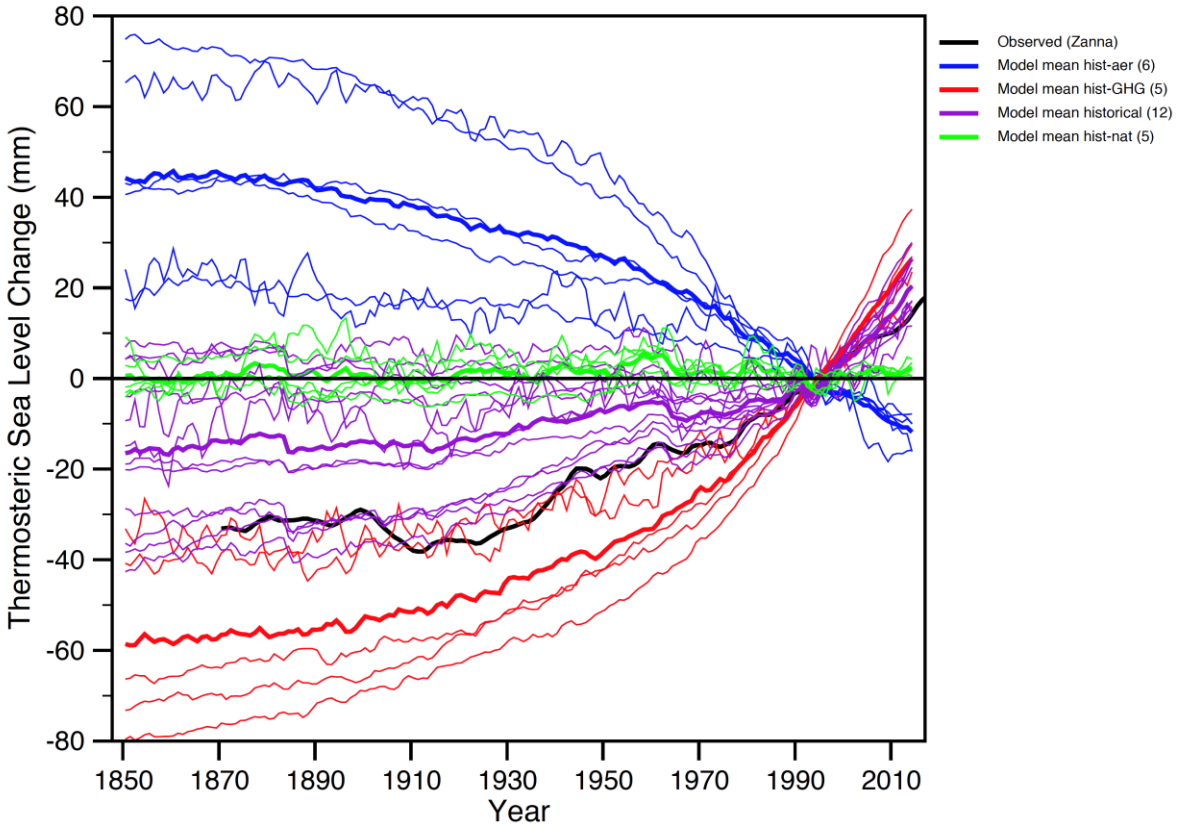

Figure 3.28: Comparison of global annual mean thermosteric sea level anomalies for CMIP6 historical (purple), natural-forcing only (green), well-mixed GHG only (red) and aerosol only (blue) simulations (multi-model means shown as thick lines, and individual model simulations as thin lines) and for observed thermosteric sea level anomalies (Zanna et al. (2019), black). Anomalies are shown with respect to1985–2004. Numbers within brackets denote number of models used in producing the multi-model mean.

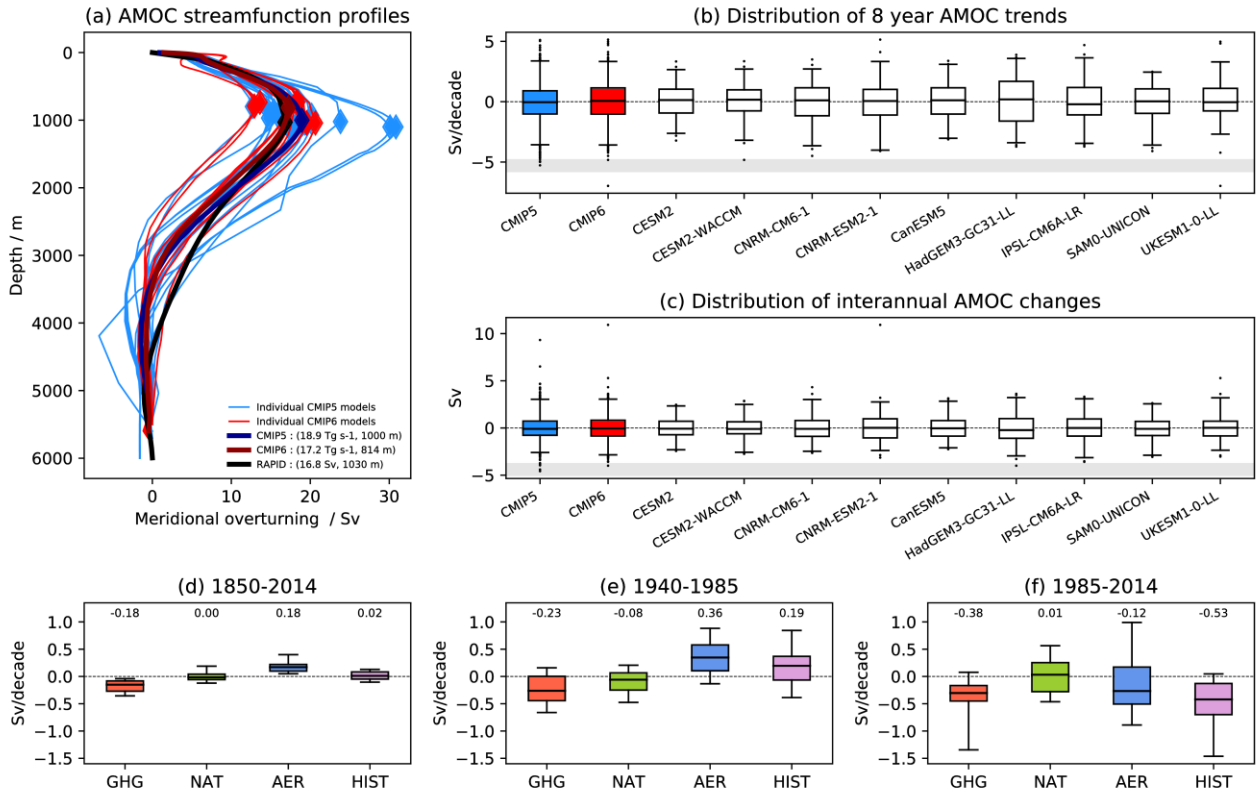

Figure 3.29: (a) AMOC streamfunction profiles at 26.5°N from the historical CMIP5 (1860-2004) and CMIP6 (1860-2014) simulations compared with the mean overturning observed with the RAPID data (2004-2018, black line). Overturning maxima are indicated by diamonds and the RAPID, CMIP5 MMM and CMIP6 MMM values are given in the legend. (b) distribution of 8-year AMOC trends from individual CMIP6 historical simulations and the observed 2004-2012 trend (grey line) (following Roberts et al., 2014). (c) Distribution of interannual AMOC variability from individual CMIP6 model historical simulations, along with the combined distributions of all available CMIP5 and CMIP6 models. The grey line is the observed value for 2009/2010 minus 2008/2009 (following Roberts et al., 2014). All annual means are for April-March. (d-f) distribution of linear AMOC trends calculated over various time periods (see panel titles) over the historical period in CMIP6 simulations forced with: Anthropogenic greenhouse gas forcing only (GHG), Natural forcing only (NAT), Anthropogenic Aerosol forcing only (AER) and all forcing combined (Historical; HIST). (b-d) Boxes indicate 25th to 75th percentile, whiskers indicate 1st and 99th percentiles, and dots indicate outliers, while the horizontal black line and text value are the multi-model mean trends. (a-c) were produced with one historical ensemble member per model where the AMOC variable was available (listed), while (d-f) were produced with the AMOC detection and attribution simulation data sets utilised by Menary et al. (submitted). (Figure produced with ESMValTool v2.0a1.)

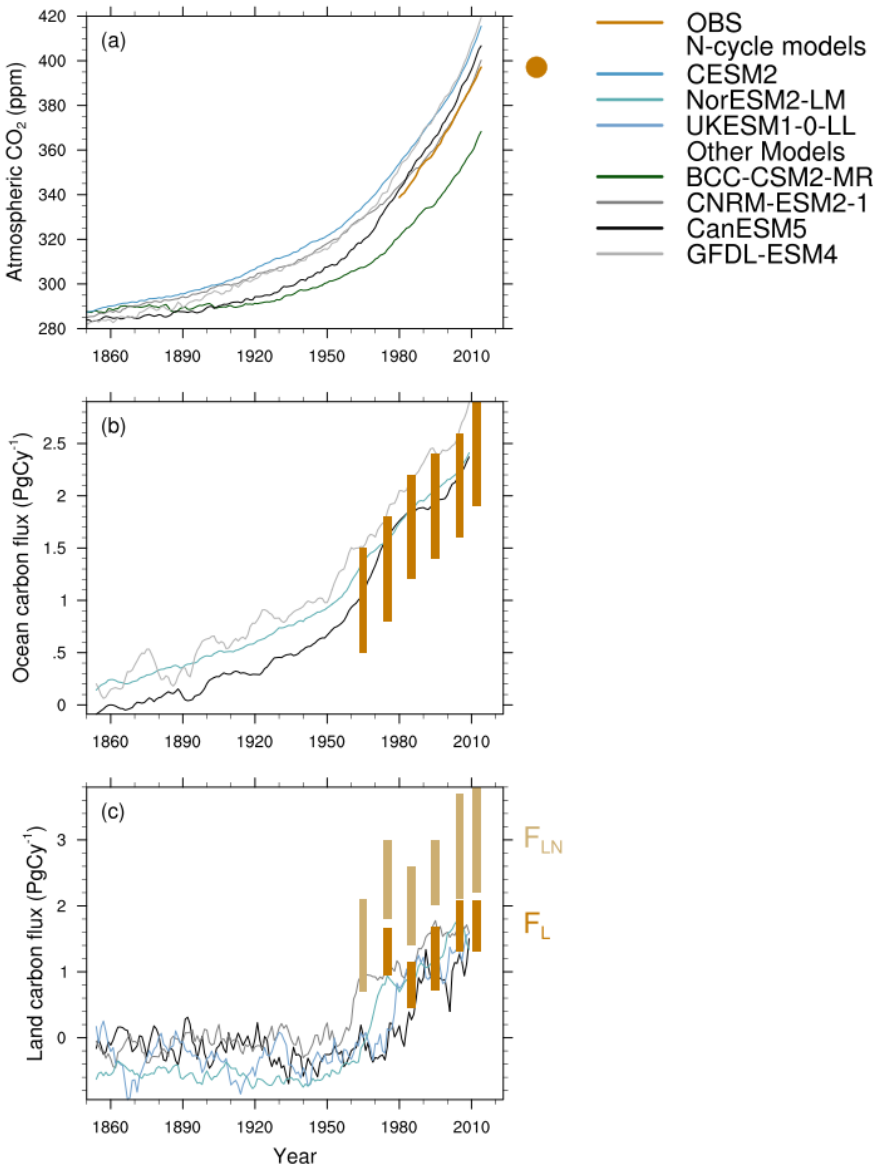

Figure 3.30: Evaluation of historical emissions-driven CMIP6 simulations for 1860-2014, against observational estimates of global mean (a) atmospheric CO_2 concentration (ppmv) (observational constraints are not yet included; red dot: 2005 Global CO_2 value) Models: BCC-CSM2-MR, CNRM-ESM2-1, (b) ocean carbon uptake (PgC yr^{-1}) Models: CanESM5, CNRM-ESM2-1, NorESM2-LM, GFDL-ESM4, (c) land carbon uptake (PgC yr^{-1}). Models: CanESM5, CNRM-ESM2-1, UKESM1-0-LL, NorESM2-LM. F_L represents the atmosphere-land CO_2 flux and can be compared with the models. F_{LN} is the residual land sink, excluding the effects of land-use change. (Figure produced with ESMValTool v2.0.0b3.)

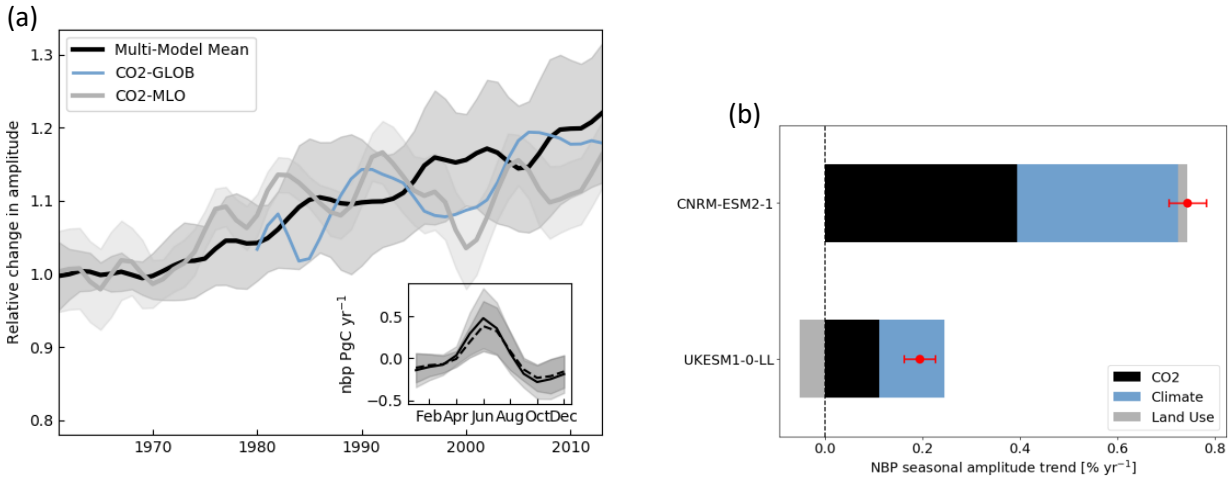

Figure 3.31: Changes of the amplitude of the seasonal cycle of global land-carbon uptake in the historical simulations from 1961-2014. (a) Net biosphere production (nbp) estimates from CMIP6 models (CanESM5, MIROC-ES2L, UKESM1-0-LL, CNRM-ESM2-1, IPSL-CM6A-LR, GISS-E2-1-G, GISS-E2-1-G-CC, GISS-E2-1-H, CESM2, CESM2-WACCM, SAM0-UNICON, in black) and atmospheric CO_2 seasonal cycle amplitude changes from observations (global in blue, Mauna Loa Observatory (MLO) in grey). Seasonal Cycle Amplitude calculated using the curve fit algorithm package (https://www.esrl.noaa.gov/gmd/ccgg/mbl/crvfit/crvfit.html) from the National Oceanic and Atmospheric Administration Earth System Research Laboratory (NOAA ESRL). Trends are relative to the 1961-1970 mean and for short time series adjusted to have the same mean as the model ensemble in the last 10 years. Interannual variation was removed with a 9-year Gaussian smoothing. Shaded areas show the 1 sigma model spread (grey) and the 1 sigma standard deviation (light-grey) for the CMIP6 ensemble and the CO_2 MLO observations respectively. Inset: average seasonal cycle of ensemble mean for 1961-1970 and its 1 sigma model spread (dashed line, light grey shading) and 2005-2014 (solid line, darker grey shading). (b) Attribution of causes of increasing amplitude from CMIP6 models using historical, hist-bgc (fixed climate in biogeochemistry) and hist-noLu (no land-use change) simulations and calculated from the amplitude trend following panel a (similar to Zhao et al., 2016, their Figures 4 and 5), Models: CNRM-ESM2-1, UKESM1-0-LL. (Figure produced with ESMValTool v2.0.0b3.)

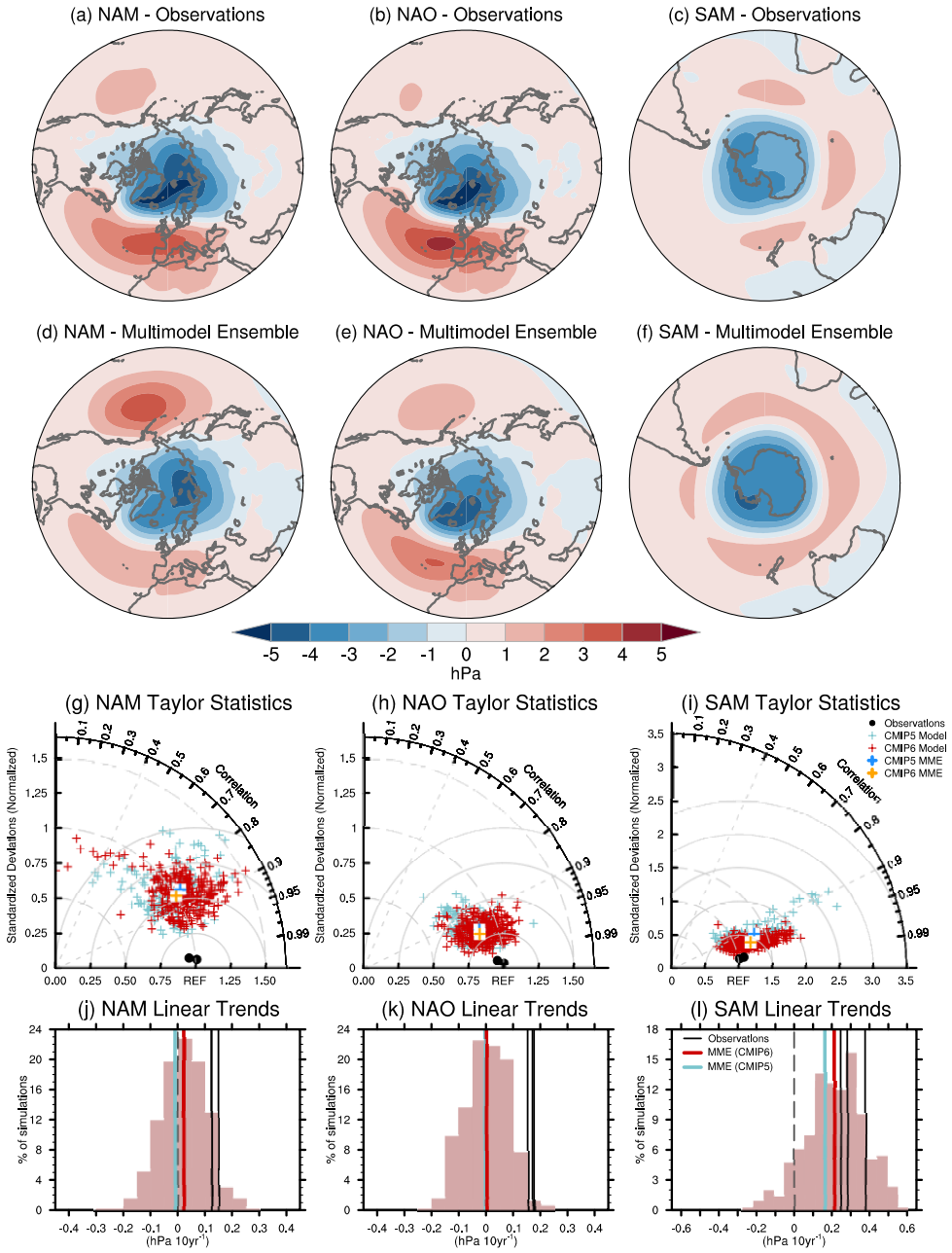

Figure 3.32: Regression of Mean Sea Level Pressure (MSLP) anomalies (in hPa) onto the normalized principal component (PC) of the leading mode of variability obtained from empirical orthogonal decomposition (EOF) of the boreal winter (Dec.-Feb) MSLP poleward of 20ºN for the Northern Annular Mode (NAM, a) over 20-80°N, 90°W-40°E for the North Atlantic Oscillation (NAO, b), and poleward of 20ºS for the Southern Annular Mode (SAM, c) for the JRA-55 reanalysis. The selected period for NAO/NAM is 1958-2014 but 1979-2014 for SAM. (d-f) Same but for multi-model multi-member ensemble mean from CMIP6 historical simulations. Models are weighted in compositing to account for differences in their respective ensemble size. (g-i) Taylor diagram summarizing the representation of the modes in models and observations following Lee et al. (2019) for CMIP5 (light blue) and CMIP6 (red). The reference pattern is taken from JRA-55 (a-c). Ratio of standard deviation (radial distance), spatial correlation (radial angle) and resulting root-mean-squared-errors (solid isolines) are given from individual members and models and for other observational products (ERA-20C combined with ERA-Interim, NOAA-20CR atmospheric reanalyses, black dots). (j-l) Histogram of the trends built from all members and all the models PCs (light pink bars). Vertical lines in black stand for all the observational estimates. The red and light blue lines indicate the multi-model multi-member ensemble mean of CMIP6 and CMIP5, respectively. A total of 293 CMIP6 historical simulations from 35 models and 152 CMIP5 historical simulation from 39 models have been used for the computation.

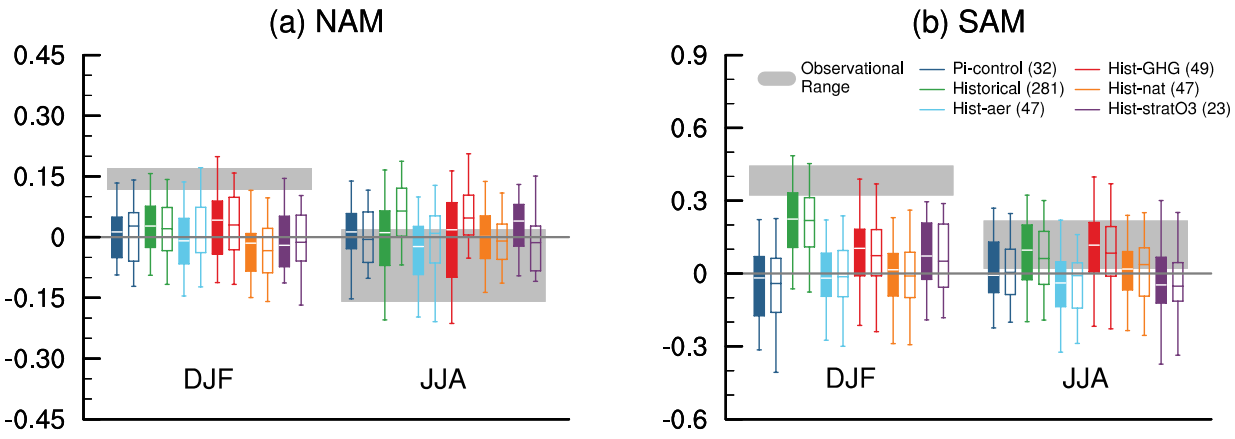

Figure 3.33: Simulated and observed trends (hPa decade^{-1}) in NAM indices over 1958-2014 (a) and in SAM indices over 1979-2014 (b) for boreal winter (December-February average; DJF) and summer (June-August average; JJA). Ensemble mean, interquartile ranges and 5th and 95th percentiles are shown by boxes and whiskers based on CMIP6 DAMIP ensembles forced by individual forcings. The number of simulations used for computing the distribution is given in brackets with the colour code of the DAMIP ensemble. For grey shading (observations) and filled boxes, the indices are based on latitudinal difference of the zonally averaged mean sea level pressure (between 35ºN and 65ºN for the NAM and between 40ºS and 65ºS for the SAM as defined in Jianping and Wang (2003) and Gong and Wang (1999), respectively). For open boxes, the indices are defined as projection coefficients onto the EOF pattern as in Figure 3.32: but defined based on the corresponding piControl simulations following Lee et al. (2019). Grey shading shows the range of observed trend among JRA-55, ERA-20C combined with ERA-Interim and NOAA-20CR.

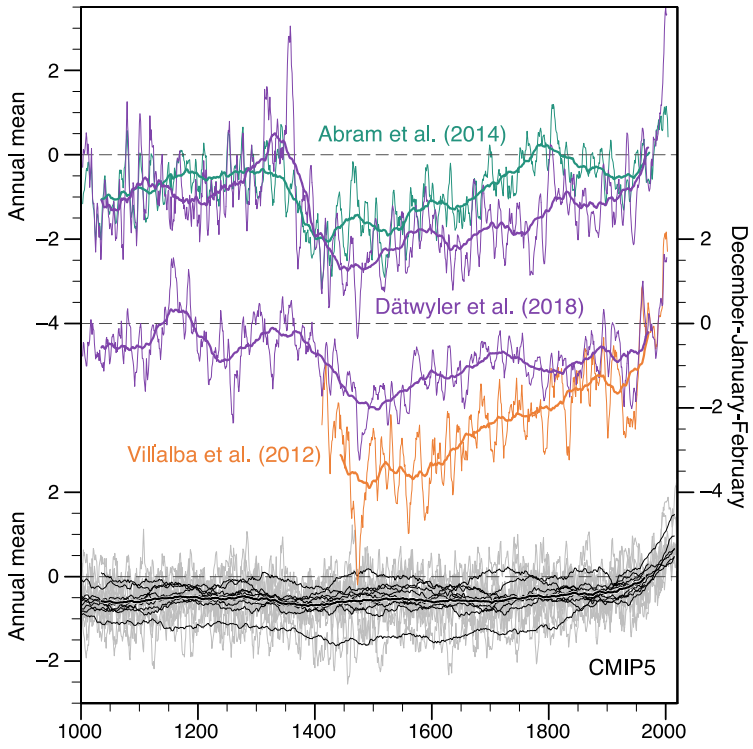

Figure 3.34: SAM indices in the last millennium. SAM reconstructions (top: annual mean, middle: December-January-February) by Abram et al. (2014), Villalba et al. (2012) and Dätwyler et al. (2018). 7-year (thin lines) and 70-year (thick lines) moving averages. (bottom) CMIP5 Last Millennium simulations extended by historical simulations. 7-year (grey lines) and 70-year (thin black lines) moving averages for individual simulations and the MME mean of the 70-year running means (thick black line). Normalized with AD 1961-1990 means and standard deviations.

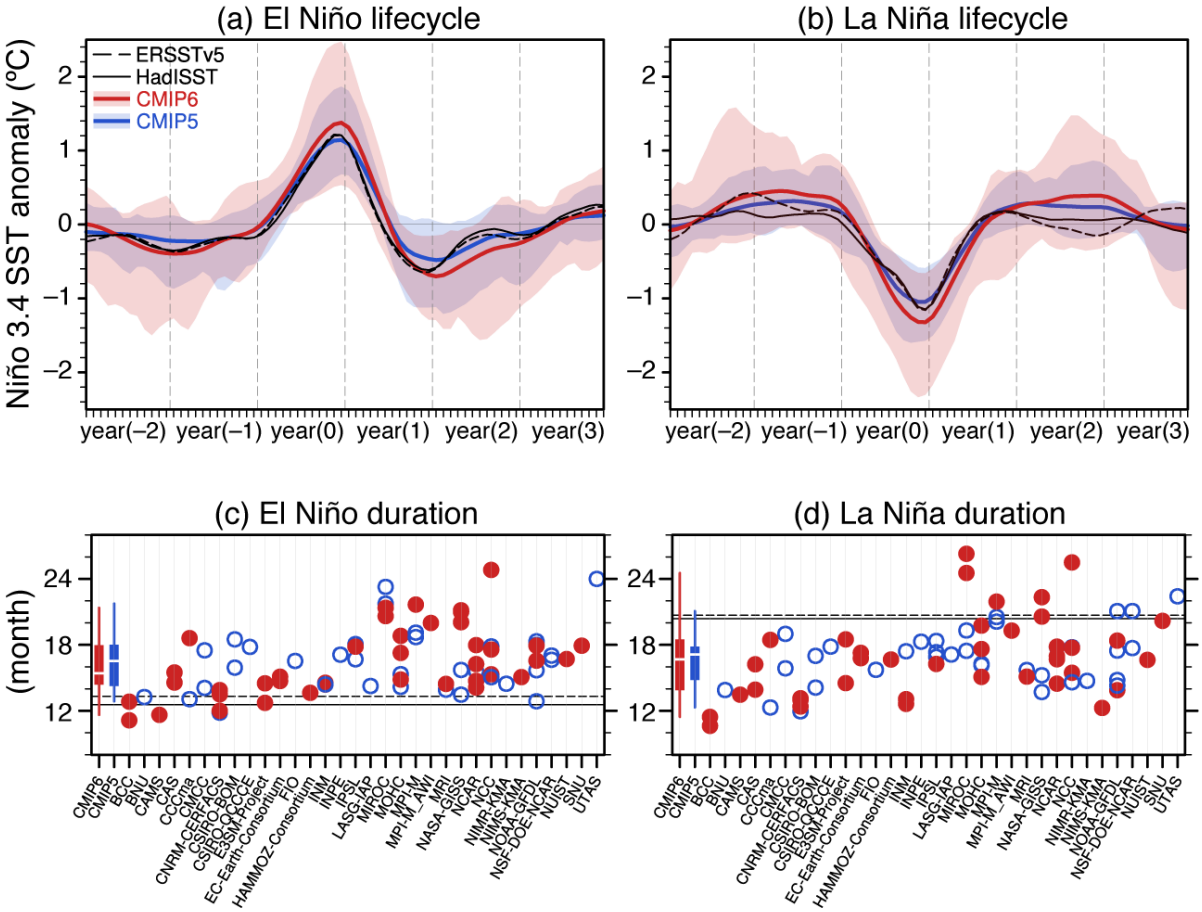

Figure 3.35: Life cycle of (left) El Niño and (right) La Niña events in observations (black) and historical simulations in CMIP5 (blue; extended with RCP4.5) and CMIP6 (red). An event is detected when December Niño 3.4 SST anomaly in year zero exceeds 0.5 times its standard deviation for 1950-2010. The horizontal axis represents month relative to the reference December, with numbers in parentheses indicating relative years. (a, b) Composites of Niño 3.4 SST anomalies (ºC). Shading and lines represent 5th-95th percentiles and ensemble means, respectively. (c, d) Mean durations (months) of El Niño and La Niña events defined as number of months in individual events for which Niño 3.4 SST anomaly exceeds 0.25 times its December standard deviation. The horizontal axis indicates modelling centres. The boxes and whiskers represent multi-model ensemble median, interquartile ranges and 5th and 95th percentiles of CMIP5 and CMIP6. All based on 5-month running mean SST anomalies with triangular-weights after linear detrending. Produced with 257 members from 38 CMIP6 models and 115 members from 35 CMIP5 models.

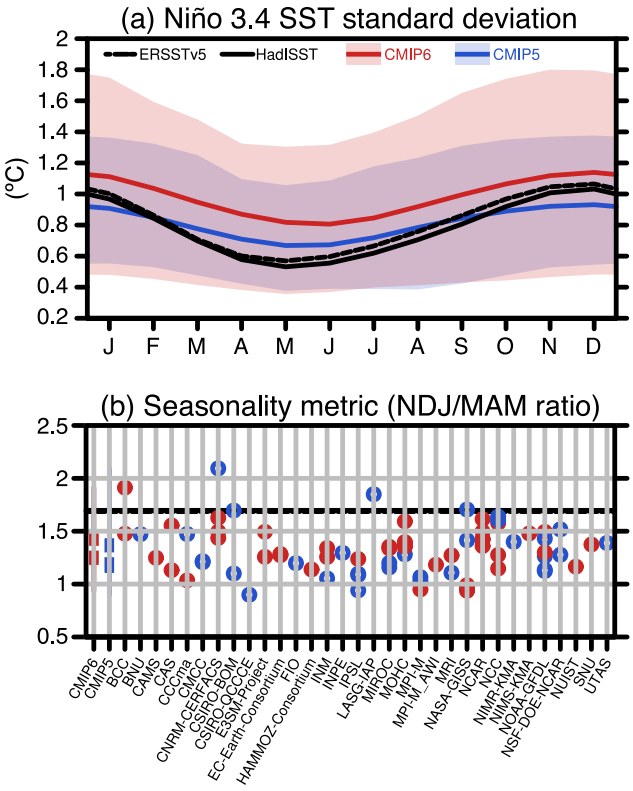

Figure 3.36: ENSO seasonality diagnosed from Niño 3.4 SST anomalies in observations (black) and historical simulations in CMIP5 (blue; extended with RCP4.5) and CMIP6 (red). (a) Climatological standard deviation of monthly Niño 3.4 SST (°C). Shading and lines represent 5th-95th percentiles and ensemble means, respectively. (b) Seasonality metric defined as the ratio of climatological standard deviation of Niño 3.4 SST between November-January (NDJ) and March-May (MAM). The boxes and whiskers represent multi-model ensemble median, interquartile ranges and 5th and 95th percentiles of CMIP5 and CMIP6 individually. Produced with 257 members from 38 CMIP6 models and 115 members from 35 CMIP5 models.

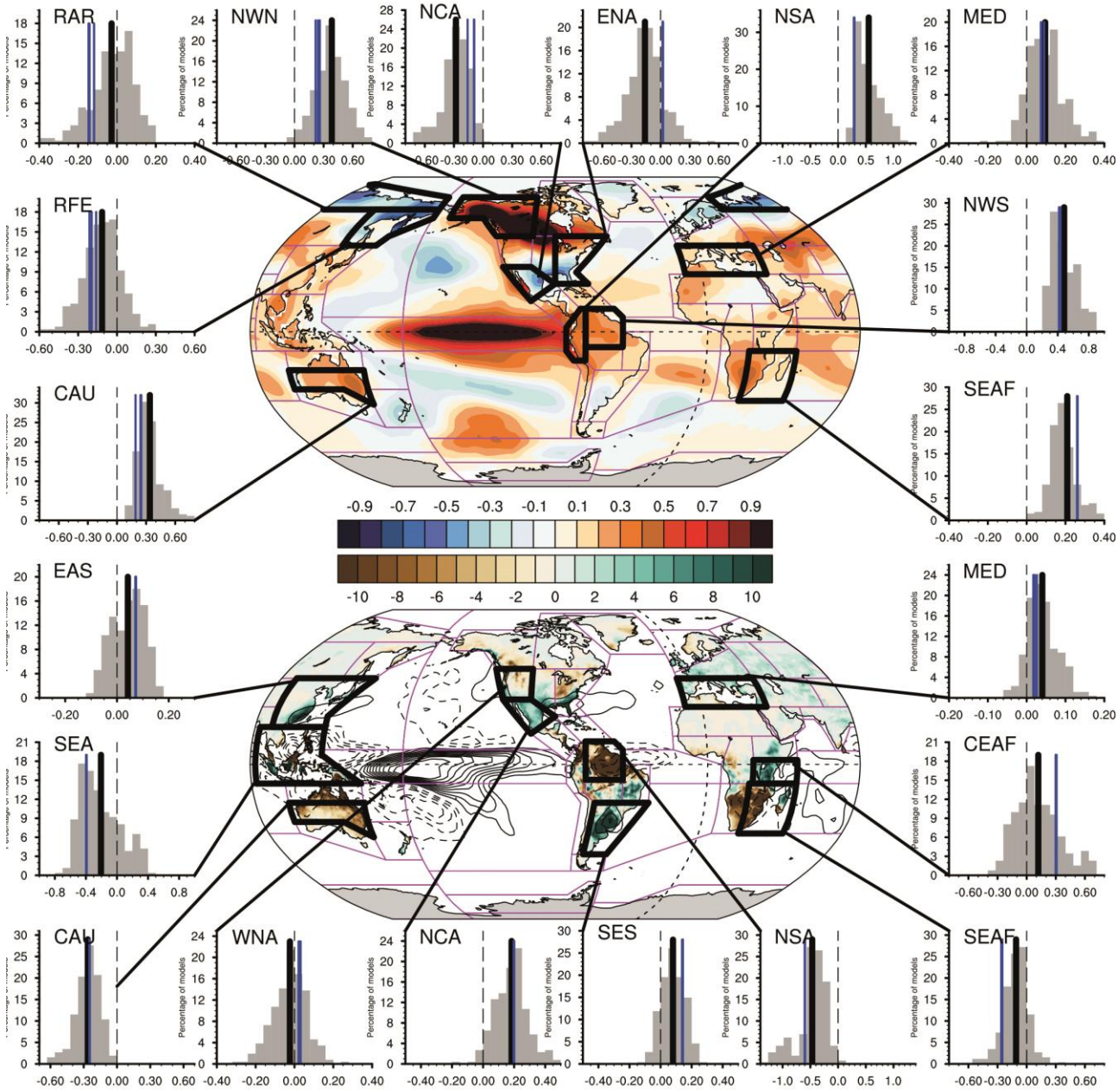

Figure 3.37: Observed and simulated ENSO teleconnections for 2m-temperature and precipitation during December-January-February. Teleconnections are identified by linear regression with the Niño 3.4 SST index based on ERSSTv5 during the period 1958-2014. Maps show observed patterns for temperature from the Berkeley Earth dataset over land and from ERSSTv5 over ocean (top) and for precipitation from GPCC over land and GPCP over ocean (contour, period: 1979-2014). Distributions of regression coefficients for regional means drawn from 261 historical simulations from 30 CMIP6 models are provided for a subset of pre-defined AR6 regions in the Atlas for temperature (light pink, top) and precipitation (green, bottom). Multi-model multi-member ensemble means are indicated by thick vertical coloured lines (red for temperature, blue for precipitation). Black vertical lines stand for observational estimates based on Berkeley Earth and GISTEMP datasets for temperature and from GPCC and GPCP datasets for precipitation.

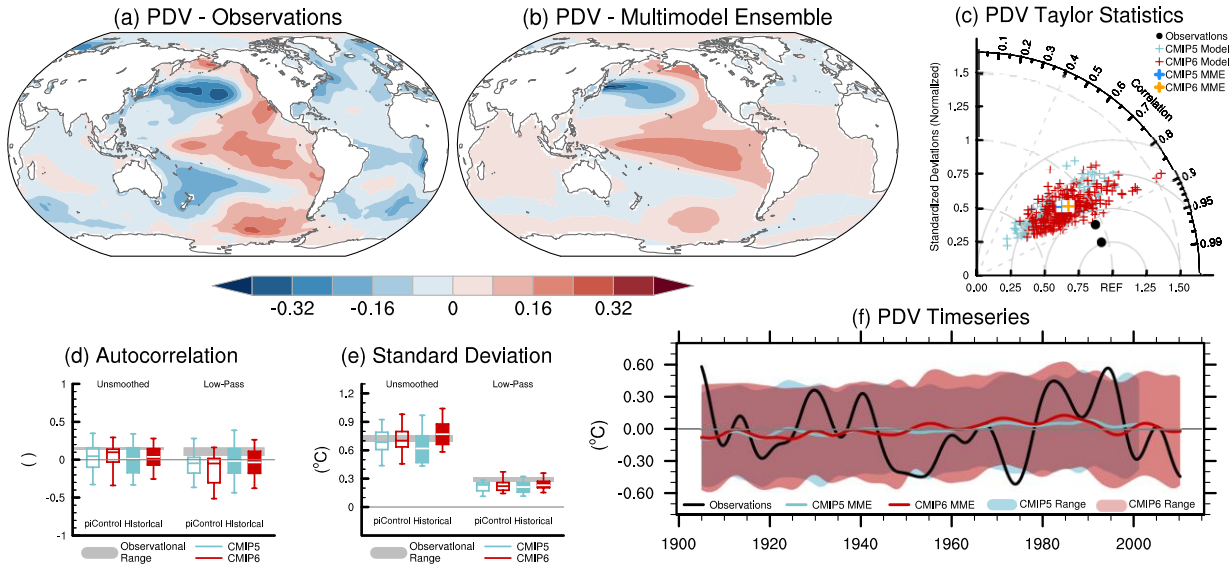

Figure 3.38: PDV spatio-temporal properties in observations and models. (a, b) SST anomalies (ºC) regressed onto the Tripole Index (TPI; Henley et al., 2015) for 1900-2014 in (a) ERSSTv5 and (b) CMIP6 historical simulations (MME composite). A 10-year low-pass filter has been applied beforehand. (c) A Taylor diagram summarizing the representation of the PDV pattern in models and observations over [40ºS-60ºN, 110ºE-70ºW] for CMIP5 (light blue) and CMIP6 (red). The reference pattern is taken from ERSSTv5. Black dots indicate other observational products (ERSSTv3b and HadISSTv1). (d) Autocorrelation of unfiltered monthly TPI at lag 1 year ("unsmoothed") and 10-year low-pass filtered TPI at lag 10 years ("Low-Pass") for observations (grey shading) and 115-year chunks of piControl simulations (open boxes) and historical ensemble simulations (filled boxes) over 1900-2014 from CMIP5 and CMIP6. (e) As in (d), but standard deviation of unfiltered and filtered TPI (ºC). Boxes and whiskers show mean, interquartile ranges and 5th and 95th percentiles. (f) Time series of 10-year low-pass filtered TPI (ºC) in ERSSTv5 (black) and CMIP5 and CMIP6 historical simulations. The thick red and light blue lines are the MME mean for the historical simulations in CMIP5 and CMIP6, respectively, and the envelopes represent the ±2 standard deviation range across ensemble members. 39 models and 149 historical members have been used for evaluation in CMIP5; 29 models and 250 historical members for CMIP6.

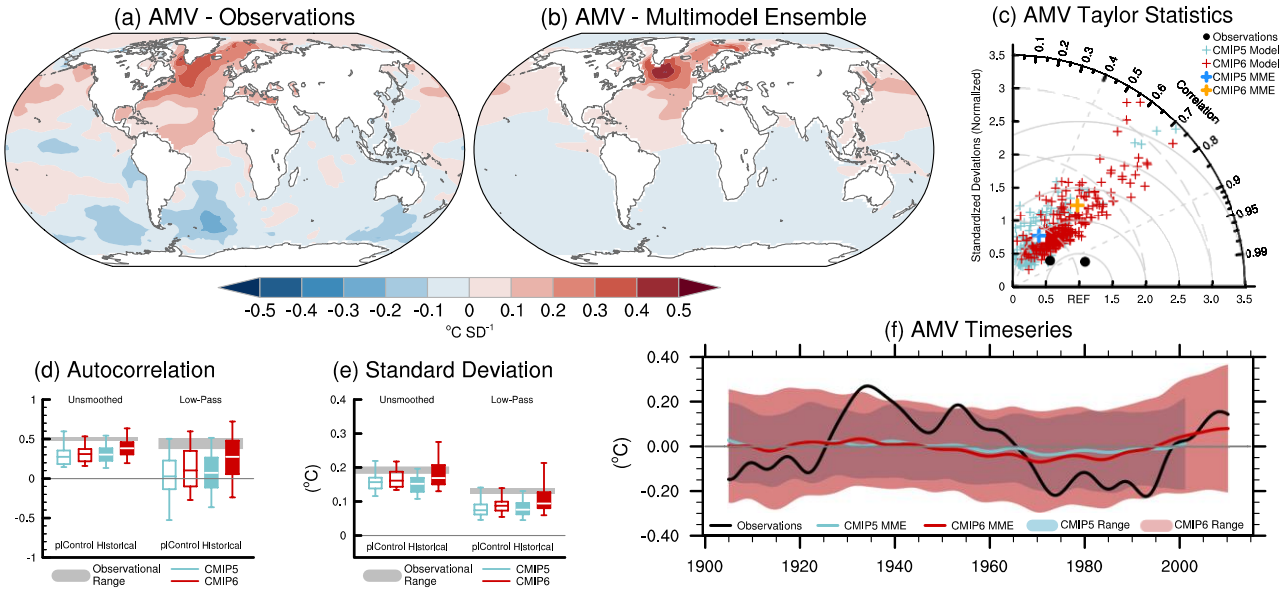

Figure 3.39: AMV spatio-temporal properties in observations and models. (a, b) SST anomalies (ºC) regressed onto the AMV index defined as the 10-year low-pass filtered North Atlantic (0º-60°N, 80°W-0°E) area-weighted SST* anomalies over 1900-2014 in (a) ERSSTv5 and (b) CMIP6 historical simulations (MME composite). Asterisk denotes that the global mean SST anomaly has been removed at each time step of the computation. (c) A Taylor diagram summarizing the representation of the AMV pattern in models and observations over [0º-60°N, 80°W-0°E] for CMIP5 (light blue) and CMIP6 (red). The reference pattern is taken from ERSSTv5. Black dots indicate other observational products (ERSSTv3b and HadISSTv1). (d) Autocorrelation of unfiltered AMV index at lag 1 year ("Unsmoothed") and 10-year low-pass filtered AMV at lag 10 years ("Low-Pass") for observations (grey shading) and 115-year chunks of piControl simulations (open boxes) and historical ensemble simulations (filled boxes) over 1900-2014 from CMIP5 and CMIP6. (e) As in (d), but standard deviation of unfiltered and filtered AMV (ºC). Boxes and whiskers show mean, interquartile ranges and 5th and 95th percentiles. (f) Time series of the AMV index (ºC) in ERSSTv5 (black) and CMIP5 and CMIP6 historical simulations. The thick red and light blue line are the MME mean for the historical simulations in CMIP5 and CMIP6, respectively, and the envelopes represent the ±2 standard deviation range across ensemble members. 39 models and 149 historical members have been used for evaluation in CMIP5; 29 models and 262 historical members for CMIP6.

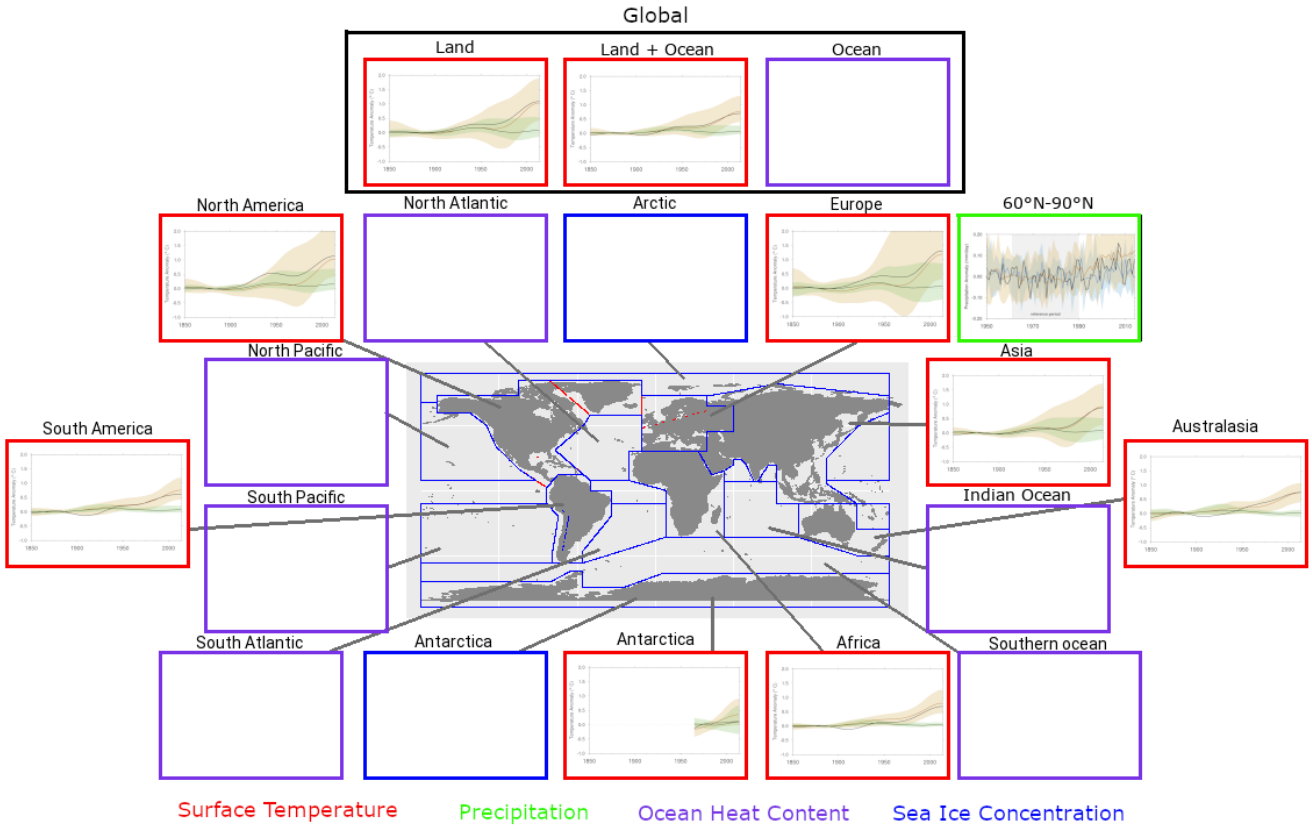

Figure 3.40: Summary figure showing simulated and observed changes in key large-scale indicators of climate change across the climate system, for continental, ocean basin and larger scales. Black lines show observations, red lines and shading show the multi-model mean and 5-95th percentile ranges for CMIP6 historical simulations including anthropogenic and natural forcing, and blue lines and shading show corresponding ensemble means and 5-95th percentile ranges for CMIP6 natural-only simulations. Temperature timeseries are as in Figure 3.8, but with smoothing by a 2-years running mean. Precipitation timeseries are as in Figure 3.12. Additional variables shown will be added in the final draft. (Figure produced with ESMValTool v2.0.0b2.)

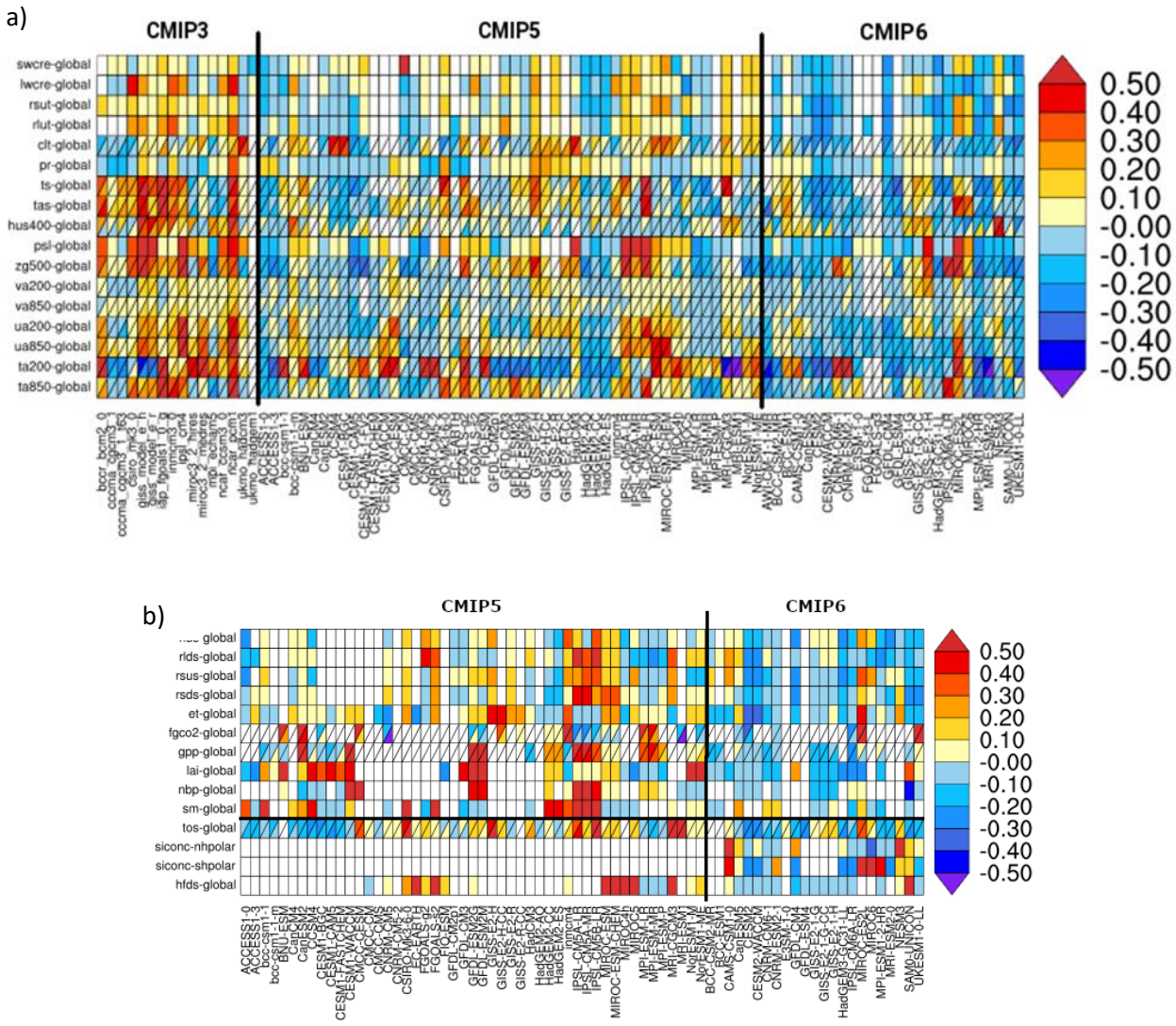

Figure 3.41: Relative space-time root-mean-square deviation (RMSD) calculated from the climatological seasonal cycle of the CMIP simulations (1980-1999) compared to observational datasets (Table 1 of the Technical Annex on Observations): (a) CMIP3, CMIP5, and CMIP6 for 17 atmospheric variables (SWCRE, LWCRE, RSUT, RLUT, CLT, PR, TS, TAS, HUS400, PSL ZG500, VA200, VA850, UA200, UA850, TA200, TA850), (b) CMIP5 and CMIP6 for 10 land variables (RLUS, RSDS, RSUS, RSDS, ET, FGCO2, GPP, LAI, NBP, SM) and four ocean/sea-ice variables (TOS, SICONC Antarctic, SICONC Arctic, HFDS). A relative performance is displayed, with blue shading indicating better and red shading indicating worse performance than the median of all model results. A diagonal split of a grid square shows the relative error with respect to the reference data set (lower right triangle) and the alternative data set (upper left triangle). White boxes are used when data are not available for a given model and variable. Updated and expanded from Figure 9.7 of Flato et al. (2013). (Figure from Bock et al. (submitted), their Figure 5, produced with ESMValTool v2.0.0b3.)

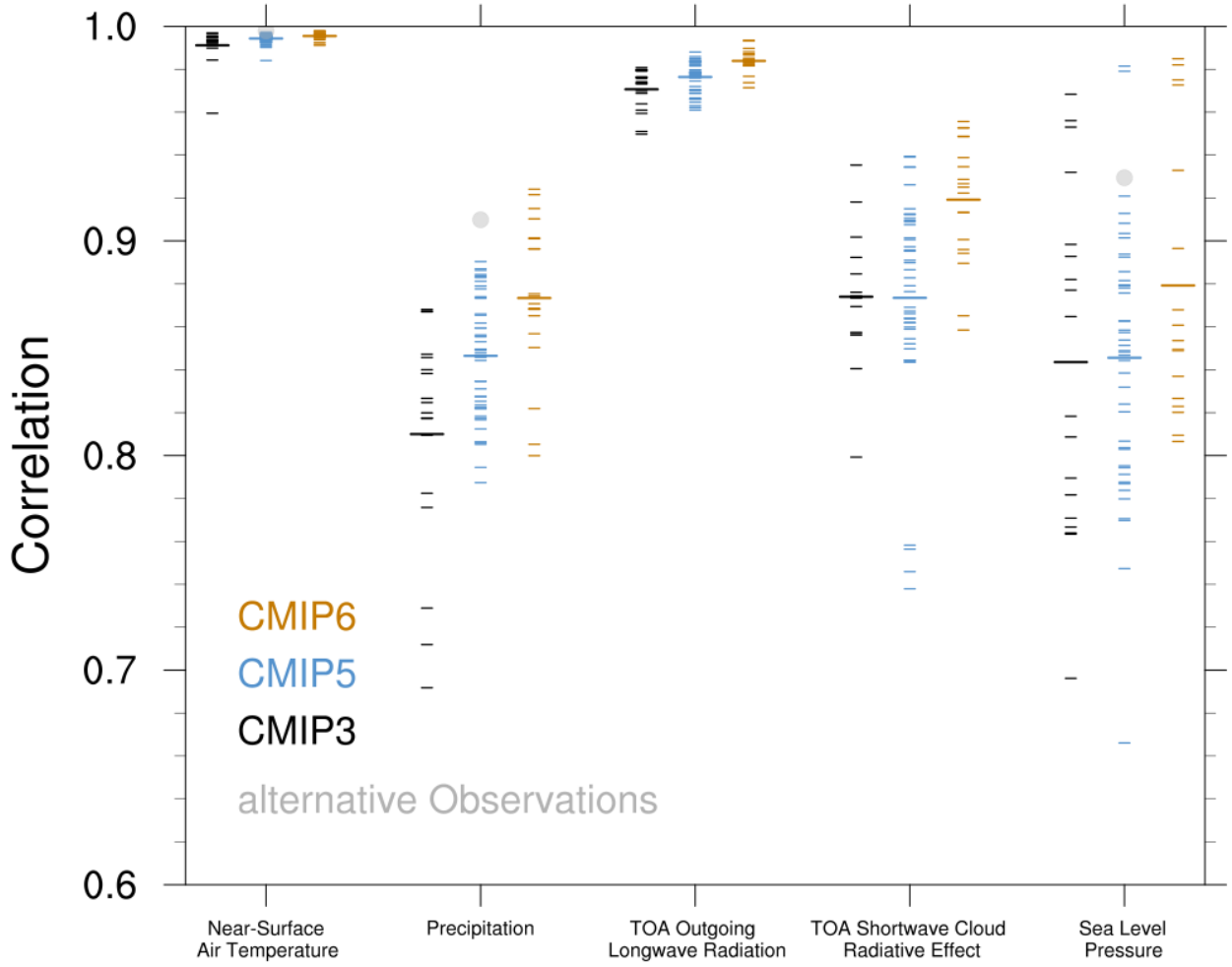

Figure 3.42: Centred pattern correlations between models and observations for the annual mean climatology over the period 1980–1999. Results are shown for individual CMIP3 (black), CMIP5 (blue) and CMIP6 (brown) models as short lines, along with the corresponding ensemble averages (long lines). The correlations are shown between the models and the reference observational data set listed in Table 5. In addition, the correlation between the reference and alternate observational data sets are shown (solid grey circles). To ensure a fair comparison across a range of model resolutions, the pattern correlations are computed after regridding all datasets to a resolution of 2.5º in longitude and 2.5º in latitude. Only one realization is used from each model from the CMIP3, CMIP5 and CMIP6 historical simulations. (Figure from Bock et al. (submitted), their Figure 6, produced with ESMValTool v2.0.0b3.)

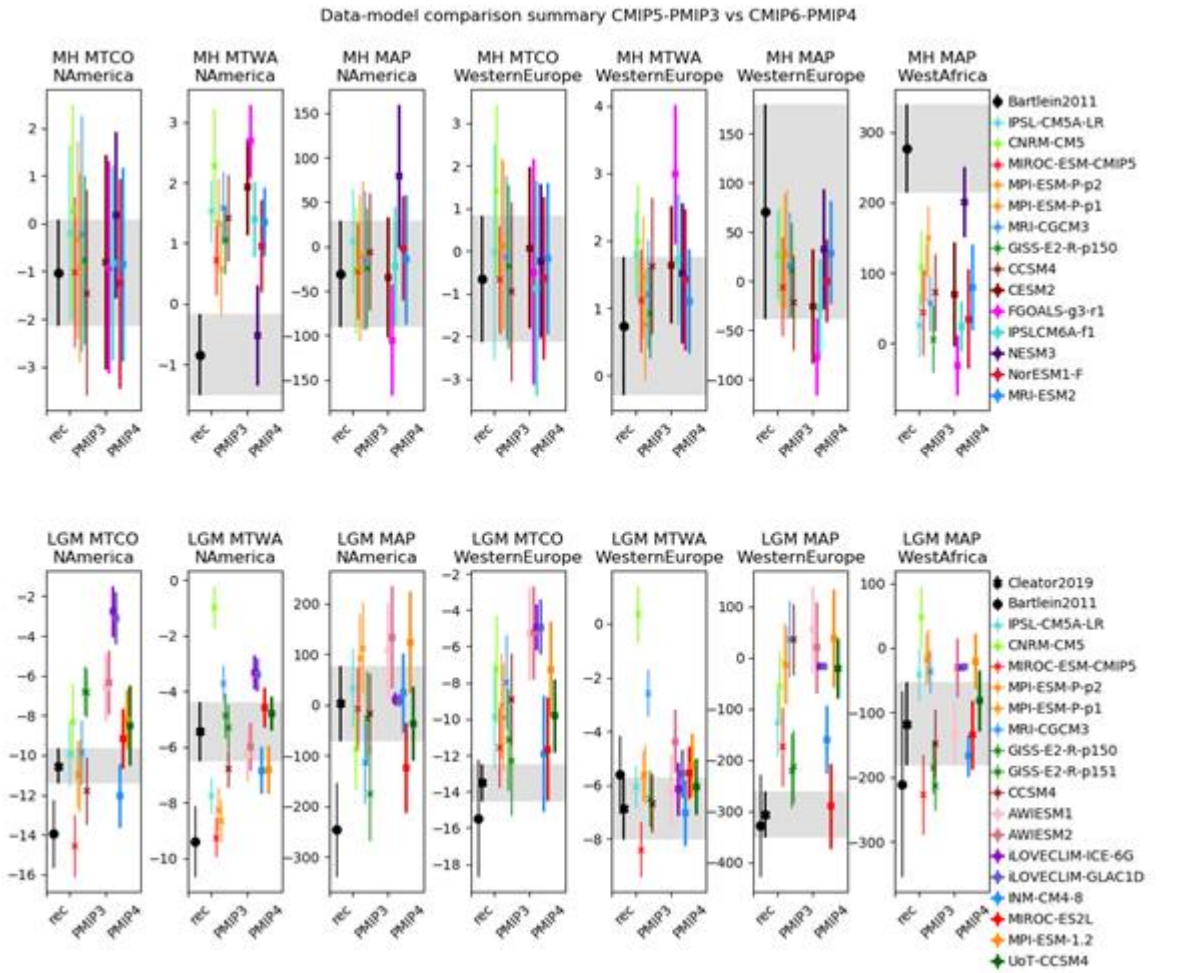

Figure 3.43: Data-model comparisons for the mid-Holocene (top line) and LGM (bottom line) periods, for PMIP3-CMIP5 and PMIP4-CMIP6 models. The figure shows the mid-Holocene - piControl (top) and LGM - piControl (bottom) averages and ranges computed for pollen-based reconstructions and model output taken over the grid points for which there are reconstructions, for the following regions: North America (20-50°N, 140-60°W), Western Europe (35-70°N, 10°W-30°E) and West Africa (0°-30°N, 10°W-30°E). MTCO: Mean Temperature of the Coldest Month (°C), MTWA: Mean Temperature of the Warmest Month (°C), MAP: Mean Annual Precipitation (mm/year). The ranges shown for the reconstructions are based on the standard error given at each site: the average and associated standard deviation over each area is obtained by computing 10000 times the average of randomly drawn values from the Gaussian distributions defined at each site by the reconstruction mean and standard error. The ranges for the model results are based on the interannual variability of the average over the area: the mean ± one standard deviation is plotted for each model. The reconstructions are from Bartlein et al. (2011) and Cleator et al. (2019). (Figure from Brierley et al. (submitted), their Figure S3 for the mid-Holocene and from Kageyama and PMIP4 (submitted), their Figure 12 for the LGM.)

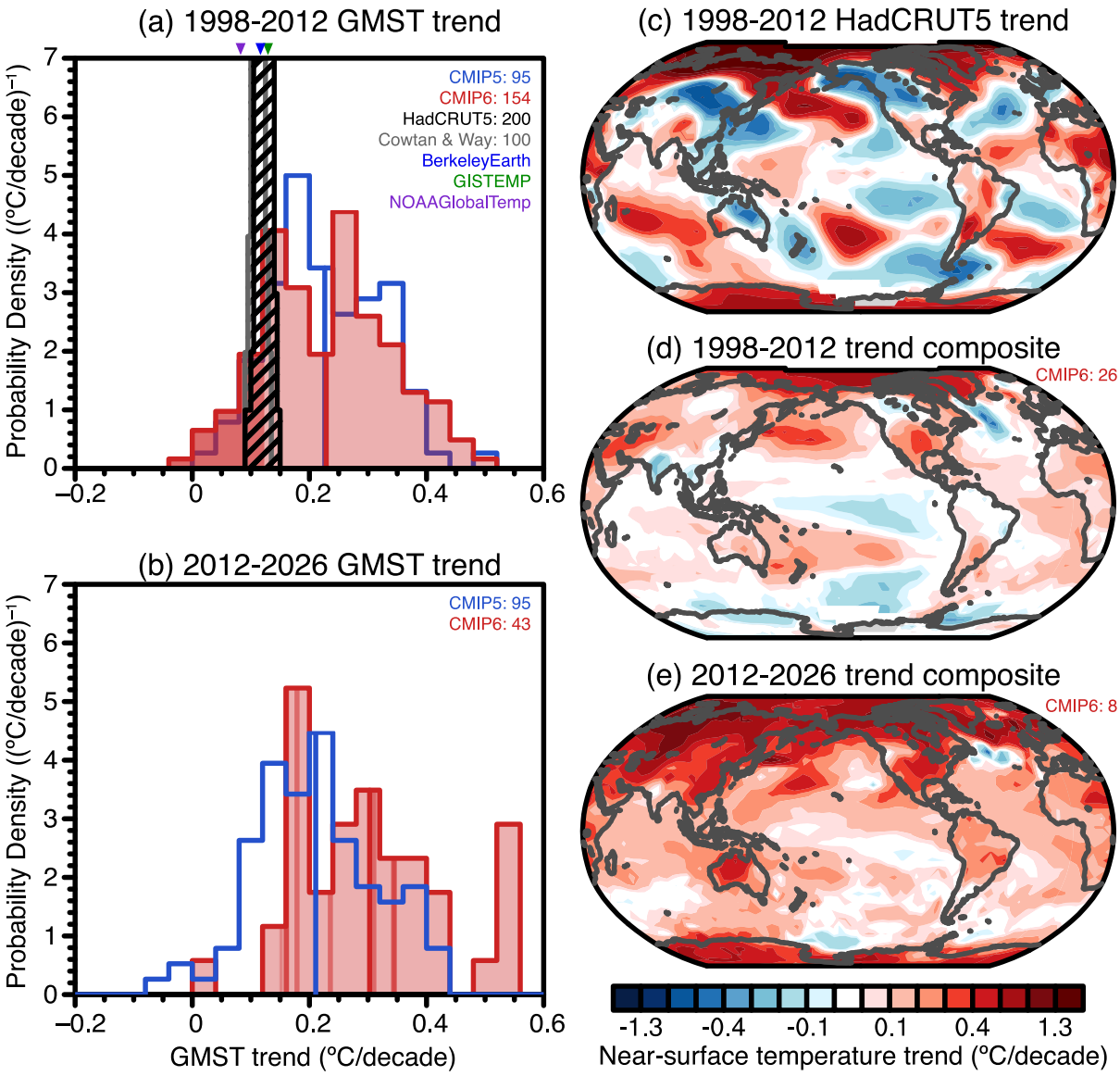

Cross-Chapter Box 3.1, Figure 1: (a, b) GMST trends for 1998-2012 (a) and 2012-2026 (b). Histograms (scaled so that the area under the curve sums to one) based on historical simulations of CMIP6 (red shading, extended by SSP2-4.5) and CMIP5 (blue outlines; extended by RCP4.5). Hatching shows histograms of HadCRUT5.0.0.0 and (Cowtan and Way, 2014). Triangles at the top of (a) represent GISTEMP, NOAAGlobalTemp and Berkeley Earth estimates. Selected CMIP6 members whose 1998-2012 trends are lower than the HadCRUT5.0.0.0 mean trend are indicated by darker shading (a) and vertical lines (b) in the histograms. Model GMST is based on a blend of SST and SAT masked to match HadCRUT data coverage, following Cowtan et al. (2015). (c-e) Trend maps of annual near-surface temperature. (c, d) 1998-2012 trends based on HadCRUT5.0.0.0 mean (c) and composited trends of subsampled CMIP6 simulations included in darker shading area in (a). (e) Corresponding composited trends but for 2012-2026 indicated by dark red lines in (b). Ensemble size used for each of the histograms and trend composites is indicated at the top right of each of panels (a,b,d,e).

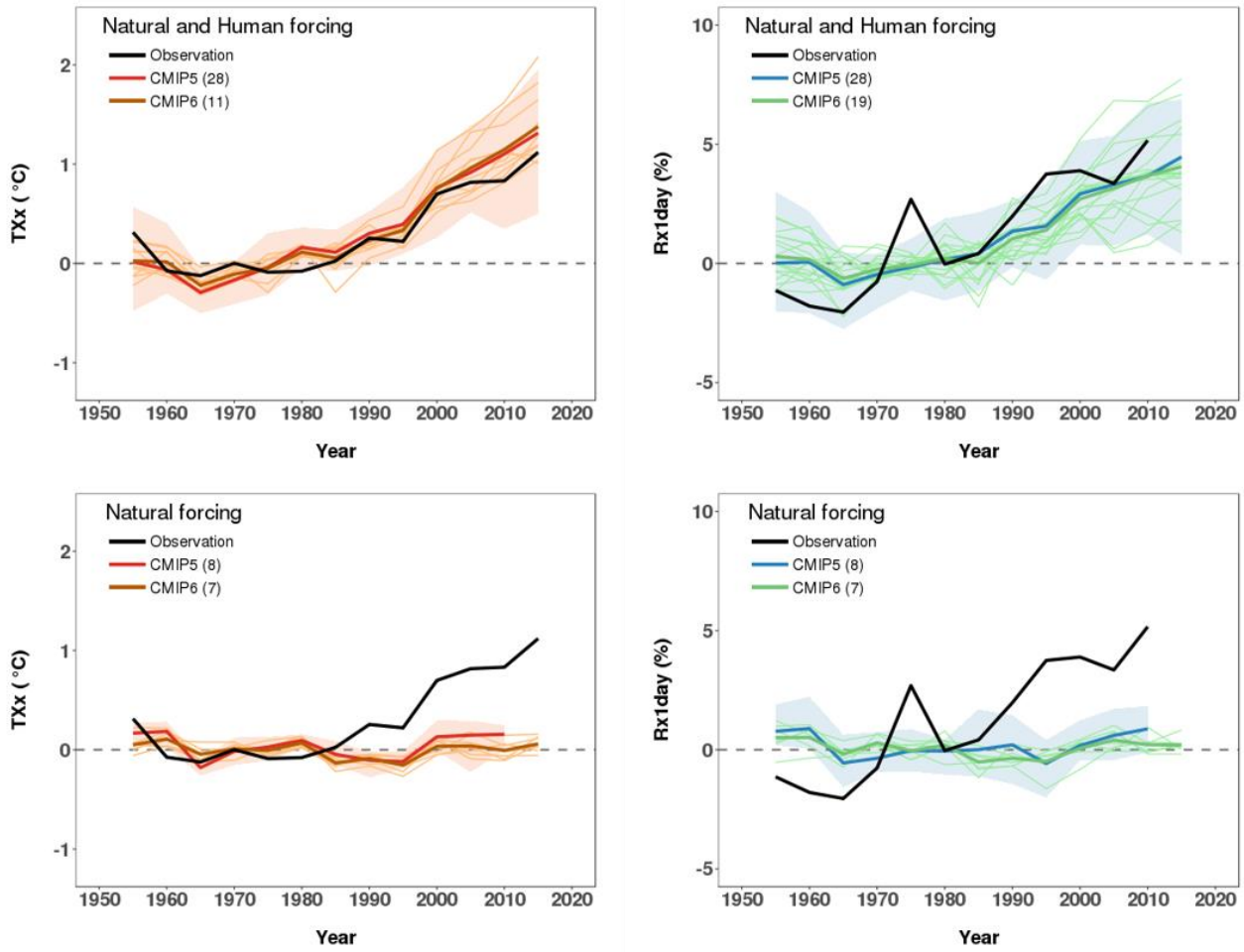

Cross-Chapter Box 3.2, Figure 1: Time series of global averaged 5-year mean anomalies of TXx (°C) and Rx1day (standardized probability index, %) during 1953-2017 from the HadEX3 observations and the CMIP5 and CMIP6 multi-models with natural and human forcing (upper) and natural forcing only (lower). For CMIP5, historical simulations for 1953-2005 are combined with corresponding RCP4.5 scenario runs for 2006-2017. For CMIP6, historical simulations for 1953-2014 are combined with SSP2-45 scenario runs for 2015-2017. Number in bracket represents the number of models used. The time-fixed observational mask has been applied to model data throughout the whole period. For TXx, grids with more than 70% data availability during 1953-2017 plus having data for at least 3 years during 2013-2017 are used. For Rx1day, grids with more than 70% data availability during 1953-2011 plus having data for at least 2 years during 2008-2011 are used. Thick coloured lines indicate multi-model means (with equal weighting given for each model). Shading represents the range of CMIP5 individual model (ensemble means) and thin lines display CMIP6 individual model ensemble means. Anomalies are relative to 1961-1990 means.

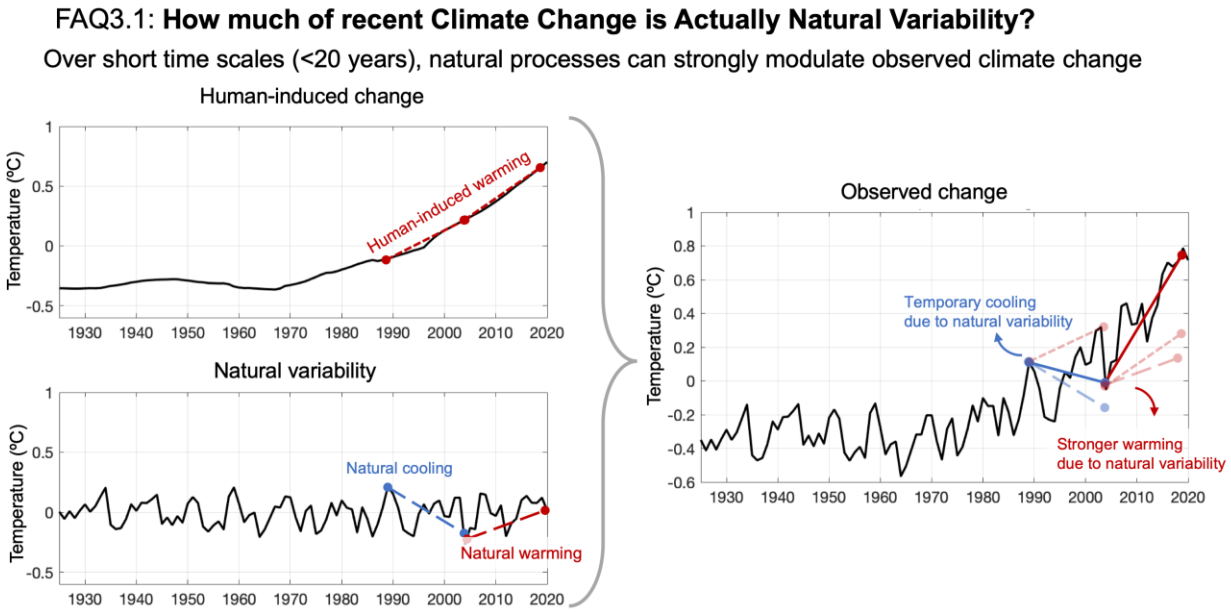

FAQ 3.1, Figure 1: (Upper left) Climate model estimate of human-induced change in global average temperature. (Lower left) Representation of natural global average temperature variability from a climate model. (Right) The combined signal, which is similar to that observed. Overlying blue lines represent temperature changes during a period with strong naturally driven cooling, while red lines represent temperature changes during a period with strong naturally driven warming.

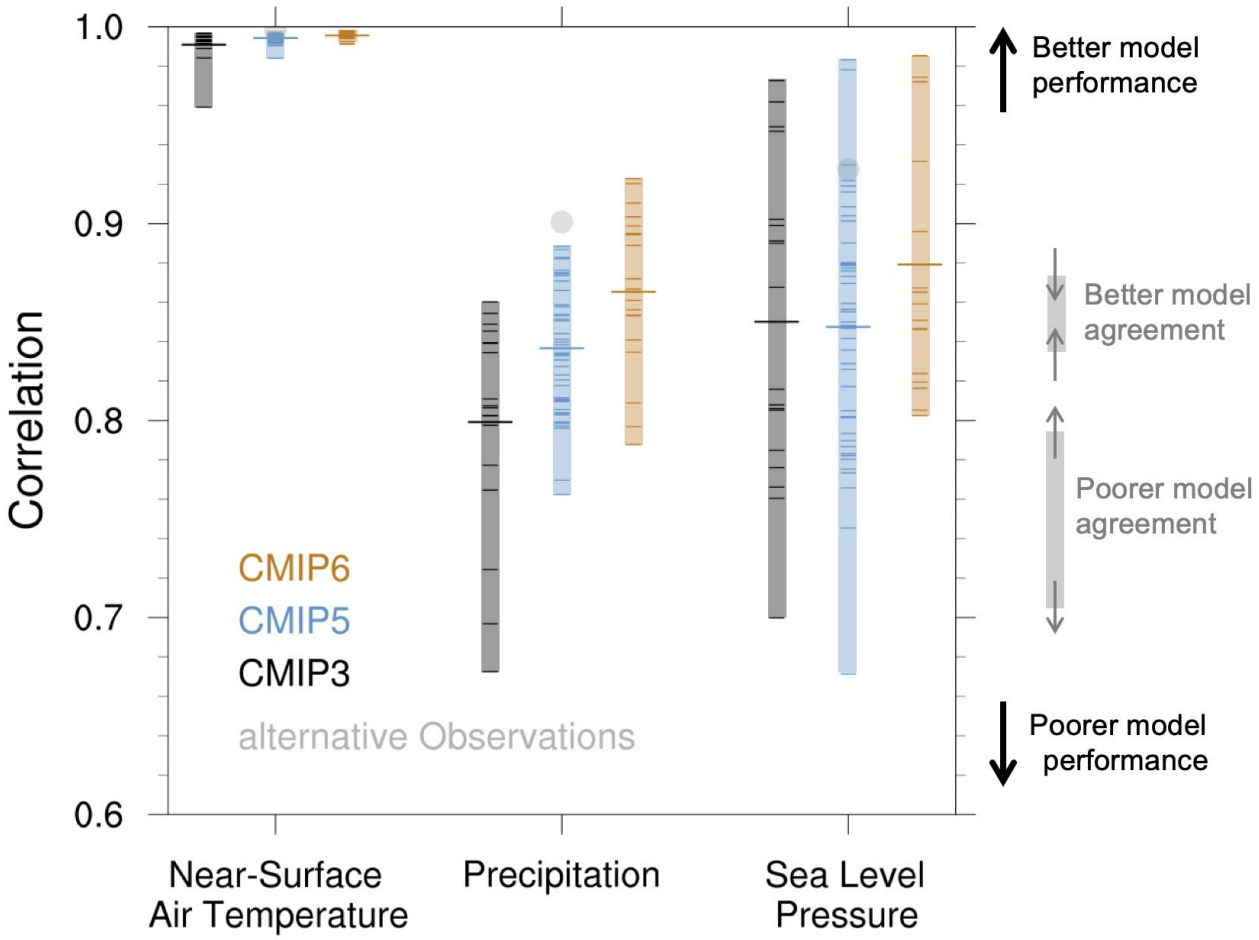

FAQ 3.2, Figure 1: Centred pattern correlations between models and observations for the annual mean climatology over the period 1980–1999 for three different variables: surface air temperature, precipitation and sea level pressure. Results are shown for individual CMIP3 (black), CMIP5 (blue) and CMIP6 (brown) models as short lines, along with the corresponding ensemble average (long line). The correlations are shown between the models and the reference observational data set. In addition, the correlation between the reference and alternate observational data sets are shown (solid grey circles). To ensure a fair comparison across a range of model resolutions, the pattern correlations are computed at a resolution of 2.5º in longitude and 2.5º in latitude. Only one realization is used from each model from the CMIP3, CMIP5 and CMIP6 historical simulations. (Figure produced with ESMValTool v2.0.0b2.)

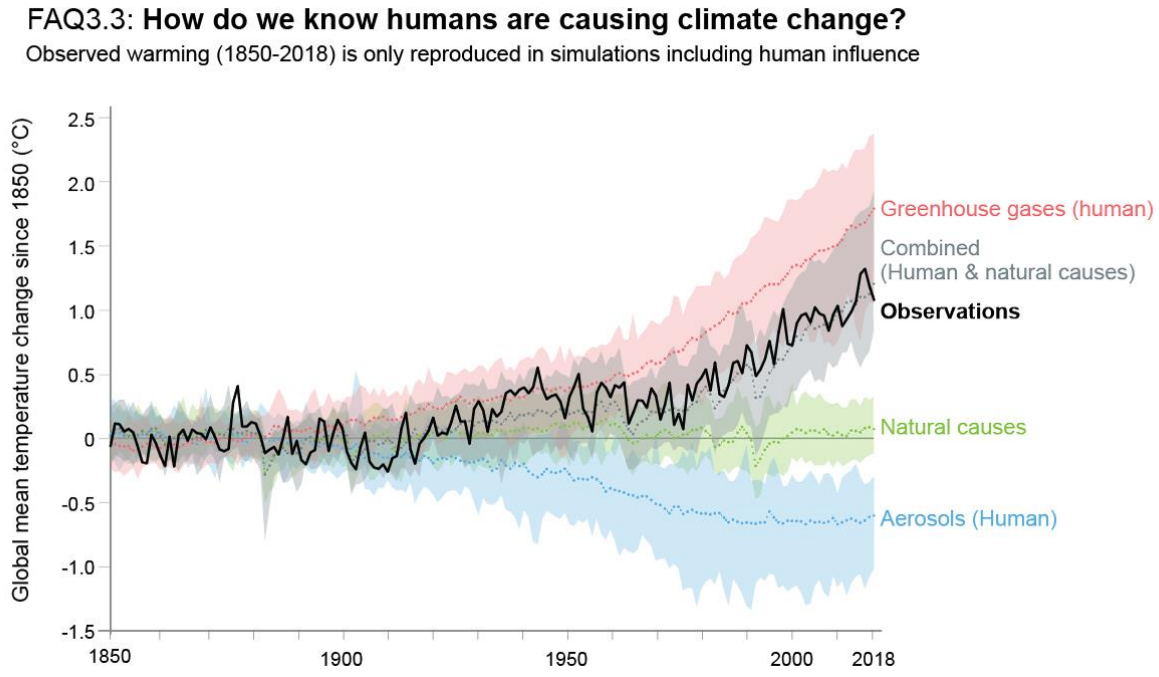

FAQ 3.3, Figure 1: Global average changes in surface air temperature in observations (HadCRUT4), compared to climate model simulations of the response to all human and natural forcings (grey band), greenhouse gases only (red band), aerosols only (blue band) and natural forcings only (green band). Solid coloured lines show the multi-model mean, and coloured bands show the 5–95% range of individual simulations.